Aerocapture Mission Analysis

Investigation and Optimisations for Earth, Mars, and Venus Trajectories

J. Engelsma

Delft University of Technology

TU Delft Delft University of Technology

Challenge the future

Aerocapture Mission Analysis

Investigation and Optimisations of Earth, Mars, and Venus Trajectories

by

J. Engelsma

to obtain the degree of Master of Science
at the Delft University of Technology,
to be defended publicly on Friday March 29, 2019 at 09:30 AM.

Student number: 4285646

Thesis committee:

Prof. dr. L.L.A. Vermeersen,	TU Delft, chair
Dr. ir. E. Mooij,	TU Delft, supervisor
Dr. ir. D. Dirkx,	TU Delft
Dr. J. Guo,	TU Delft

Cover image credit: NASA - Artist concept of aerocapture applied to enter the orbit of Mars
Available at `https://www.nasa.gov/centers/marshall/multimedia/photos/2006/photos06-098.html`

TU Delft

Preface

To obtain the degree of Master of Science in the field of aerospace engineering, an aspiring engineer has to prove that their own abilities are those that are expected and required of an engineer. As proof, the student performs a research regarding a certain topic. The student should preferably chose a topic they are sufficiently interested in, as doing so means dedicating close to a year of their lives to researching it. Lastly, the student writes a thesis in which they discuss their research and present their findings. This document is produced as the result of such a research. In this document the entirety of the conducted research is discussed, from the early stages of researching the general topic, to the final stages of drawing conclusions from the produced data, and the conclusion of the thesis.

This report will be made publicly available on the TU Delft repository[1] on the March 15, 2019. The key demographic of this report are those interested in aerocapture, or aeromanoeuvring in general, with at least a basic knowledge of spaceflight. The contents of this reports can be used as a source of information to learn about aerocapture, to set up research, to support (or refute) claims, or, simply, as an example of a thesis report.

I wish to thank my supervisor, Dr. Erwin Mooij, for his patience, encouragement, and unyielding and infectious enthusiasm for this research. Having never conducted a research at this level before, and one with such stakes attached to it, I found myself often filled with doubt regarding my own capacity as an aerospace engineer, my work-ethic, or my ability to finish the research in time and still be satisfied with the results. However, after every meeting we have had, I always left with new-found confidence and enthusiasm, regardless of how I felt regarding the progress of the research before the meeting.

Additionally, I would like to thank my parents, Geert and Mariska, for always fully supporting me in my endeavours and providing me with the opportunities in life that have led me to conduct this research in the first place. My girlfriend, Amber, for her emotional support during the stress and doubt-filled periods of my research and her willingness to be my proof-reader. Lastly, my friends for providing me with well-needed distractions from the research whenever I needed it.

J. Engelsma
Faculty of Aerospace Engineering, Delft University of Technology
March 14, 2019

[1] TD Delft repository `http://repository.tudelft.nl/`

Nomenclature

Abbreviation	Expansion
ABAM	Adams-Bashforth Adams-Moulton
CEV	Crew Exploration Vehicle
CNES	Centre National d'Études Spatiales (National Centre of Space Studies)
CNSR	Comet Nucleus Sample Return
CRM	Crew Return Mission
DOF	Degree Of Freedom
EA	Evolutionary Algorithms
EMCD	ESA Mars Climate Database
ESA	European Space Agency
EVA	Extra-Vehicular Activity
FPA	Flight-Path Angle
GRAM	Global Reference Atmosphere Model
ISAS	Institute of Space and Astronautical Science
ISS	International Space Station
JAXA	Japan Aerospace Exploration Agency
LST	Local Solar Time
MAV	Mars Ascent Vehicle
MCO	Mars Climate Orbiter
MGS	Mars Global Surveyor
MO	Mars Odyssey
MPCV	Multi-Purpose Crew Vehicle
MRO	Mars Reconnaissance Orbiter
MSR	Mars Sample Return
NASA	National Aeronautics and Space Administration
NEO	Near-Earth Object
NSGA-II	Non-Dominant Sorting Genetic Algorithm II
ODE	Ordinary Differential Equation
PaGMO	Parallel Global Multi-Objective Optimisation
RKF	Runge-Kutta-Fehlberg
RMS	Root-Mean-Square
SBX	Simulated Binary Crossover
SRM	Sample Return Missions
SZA	Solar Zenith Angle
TDB	Temps Dynamique Barycentrique (Barycentric Dynamical Time)
TPS	Thermal Protection System
Tudat	Technical University of Delft Astrodynamical Toolbox
USM	Unified State Model
USSR	Union of Soviet Socialist Republics
VIRA	Venus International Reference Area

Symbol	**Meaning** [unit]
a	Acceleration [ms^{-2}]
a	Semi-major axis [m]
a	Speed of sound [ms^{-1}]
$\mathbf{a}$	Acceleration vector [ms^{-2}]
B, E^*, k	Non-dimensional parameters [-]
C_D	Drag coefficient [-]
C_L	Lift coefficient [-]
C_S	Side force coefficient [-]
c_p	Constant pressure specific heat [-]
CR	Crossover probability [-]
D	Drag force [N]
e	Eccentricity [-]
E	Eccentric Anomaly [rad]
f	flattening [-]
$\mathbf{F}$	Force vector [N]
$\mathbf{F_A}$	Aerodynamic force vector [N]
$\mathbf{F_G}$	Gravitational acceleration vector [ms^{-2}]
g	gravitational acceleration [ms^{-2}]
h	Altitude [m]
h	Non-dimensionalised altitude [-]
h_p	Penetration depth [m]
H	Angular momentum [m^{2}s^{-1}]
H_s	Scale-height [m]
i	Inclination [rad]
K_n	Knudsen number [-]
L	Lift force [N]
L	Characteristic length [m]
L_s	Solar longitude [rad]
m	mass [kg]
m	Mutation probability [-]
M	Mach number [-]
$\mathbf{p}$	Linear momentum vector [kgms^{-1}]
q	Heat flux [Wm^{-2}]
q_∞	Dynamic pressure [Pa]
r	Radial position [m]
$\mathbf{r}$	Position vector [m]
R	Gas constant [Jkg^{-1}K]
R	Surface radius [m]
$\bar{R}_e$	Mean equatorial radius [m]
$\bar{R}_p$	Mean polar radius [m]
R_e	Reynolds Number [-]
R_n	Nose radius [m]
S	Side force [N]
S	Surface area [m^2]
S_{ref}	Reference surface area [m^2]
t	time [s]
T	Thrust force [N]
T	Temperature [K]
t_s	Switch time [s]
u	Relative velocity [ms^{-1}]
u	Non-dimensionalised velocity [-]
V	Velocity Magnitude [ms^{-1}]
$\mathbf{V}$	Velocity vector [ms^{-1}]
r	Radial position [m]
x	x-position [m]
x	Non-dimensional altitude [-]
y	y-position [m]
y	Non-dimensionalised altitude [-]
z	z-position [m]
$\mathbf{x}$	State vector

Symbol	**Meaning** [unit]
α, λ, ν	Non-dimensional parameter [-]
α	Angle of attack [rad]
α_i	i^{th} Euler angle [rad]
β	Angle of sideslip [rad]
γ	Flight-Path angle [rad]
γ	Ratio of specific heats [-]
δ	Latitude [rad]
ϵ_T	Thrust elevation [rad]
η_c	Distribution index for crossover [-]
η_m	Distribution index for mutation [-]
θ	Range angle [rad]
θ	True anomaly [rad]
μ	Standard Gravitational Parameter [m^3s^{-2}]
ν	Kinematic viscosity [m^2s^{-1}]
ρ	Density [kgm−3]
σ	Bank angle [rad], or Stephan-Boltzman Constant [$Wm^{-2}K^{-4}$]
τ	Longitude [rad]
τ	Re-written range angle [rad]
ϕ	Re-written flight-path angle [rad]
χ	Heading [rad]
ψ_T	Thrust azimuth [rad]
ω	Argument of periapsis [rad]
ω	Rotational Rate [$rads^{-1}$]
Ω	Right-ascension (or longitude) of ascending node [rad]

Contents

1 Introduction

Humanity has a inherent and continuous desire to explore. According to Olson et al. (2012), it is human nature to "push beyond boundaries and see what lies beyond the horizon" and that "our drive to explore is fueled *[sic]* by curiosity that compels us to seek and understand the unknown". Throughout history humanity has expanded its boundaries, discovered new continent, and facilitated both short and long distance travel by developing manually operated wheeled vehicles, sea and ocean faring ships, automobiles, and aeroplanes. In more contemporary history, humanities focus has turned to exploring space: "the final frontier", to help us gain insight into the history of Earth, our Solar System, the universe, and humanity itself. With the so-called "Space Race", humanity injected itself into the trajectory of becoming a space faring civilisation.

According to Siddiqi (2000), the "Space Race" brought with it many firsts in space, such as the first artificial satellite to orbit Earth (Sputnik 1, USSR, 1957), the first vehicle in heliocentric orbit (on accident) (Luna 1, USSR, 1959), the first probe on an extra-terrestrial body (Luna 2, USSR, 1959), the first animals to successfully orbit Earth (Belka and Strelka aboard Korabl-Sputnik 2, USSR, 1960), the first man in space (Yuri Gagarin aboard Vostok 1, USSR, 1961), the first Extra-Vehicular Activity (EVA) (Alexei Leonov aboard Voskhod 2, USSR, 1965), and the first humans on an extra-terrestrial body (Neil Armstrong and Edwin Aldrin Jr aboard Apollo 11, NASA, 1969).

Humanity's activity in space has not ceased since. Missions have continued to venture to extra-terrestrial bodies such as planets, Near-Earth Objects (NEOs), and into deep space. Recently the exploration, and potential colonisation, of Mars has attracted the interest of national agencies, professional industry, and the general public. Such is evidenced by national agency programs such as the European Space Agency's (ESA) Aurora programme (Gardini et al., 2003) and the National Aeronautical and Space Administration's (NASA) Constellation programmes[1], private company SpaceX's plan to facilitate the colonisation of Mars[2], and entertainment media such as books and video games concerning Mars colonisation and research such as "The Martian" (Weir, 2011) or "Surviving Mars" (Haemimont Games, 2018), respectively.

According to Olson et al. (2012) there are four main reasons for studying and exploring space, and in particular Mars. These reasons are the attempted gain in knowledge about the history and future of the Earth by studying the evolution of Mars, the advancement of the cutting edge of technology by developing technology to survive on Mars, to show the success of international cooperation in space exploration, and to advance humanity further along becoming a space faring civilisation. The first of these reasons is exclusive to Mars due to the similarity between the "Red Planet" and our own. The other three reasons however are applicable to exploration and colonisation missions on any extra-terrestrial body.

One of the main obstacles for prolific space exploration missions is the high cost of space missions. The cost of launching a vehicle is roughly proportional with the mass of the vehicle and the orbital energy of the desired orbit, a low Earth orbit being cheaper than a geosynchronous transfer orbit, and an interplanetary transfer trajectory being more expensive than both. This makes the mass of the spacecraft a driving concern in the aerospace industry.

[1] Connolly, J.F. "Constellation Program Overview", October 2006. Retrieved on March 25, 2018 from `https://www.nasa.gov/pdf/163092main_constellation_program_overview.pdf`

[2] Musk, E. "Making Humans a Multiplanetary Species", September 2016. Retrieved on March 25, 2018 from `https://youtu.be/H7Uyfqi_TE8`

To reduce the cost of missions without losing any of the payload mass, sophisticated manoeuvres have been proposed to reduce the amount of fuel required for post-launch manoeuvres. Once such manoeuvre is the aerocapture. According to Hall et al. (2005), the application of aerocapture enables large propellant mass savings. This is illustrated in Fig. 1.1, depicting the result of a first-order analysis performed by Hall et al. (2005) regarding the mass savings made possible by aerocapture.

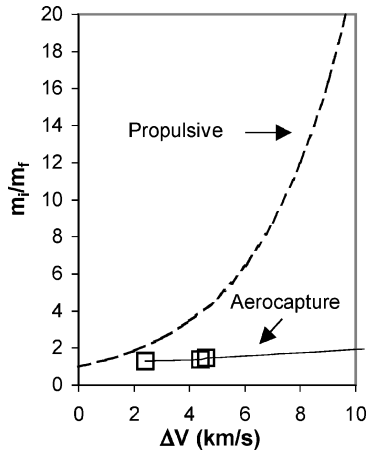

Figure 1.1: Comparison of the total to fuel mass ratios for propulsive capture and aerocapture.Hall et al. (2005)

Aerocapture is a type of aero-assist manoeuvre (hereinafter aeromanoeuvre). Aeromanoeuvres are manoeuvres that use the aerodynamic force resulting from the interaction between the vehicle and the atmosphere instead of thrust to accomplish a manoeuvre. Three types of aeromanoeuvres can be discerned: aerogravity-assist, aerobraking, and aerocapture. During aerogravity-assists the aerodynamic forces are used to further increase the energy gain or trajectory modification compared to a regular gravity-assist. During aerobraking the aerodynamic forces are used to reduce the orbital energy, lowering the apoapsis of a closed orbit. During aerocapture the aerodynamic forces are used to reduce the orbital energy of the vehicle, reducing the open hyperbolic trajectory to a closed elliptical orbit. Aerobraking and aerocapture manoeuvres are depicted schematically in Fig. 1.2.

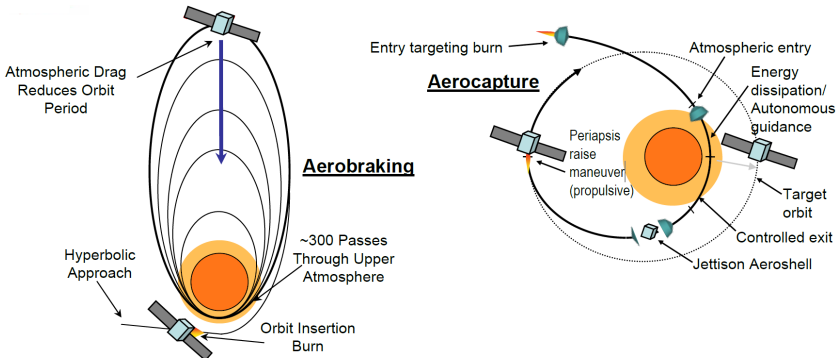

Figure 1.2: Schematic illustration of aerobraking (left) and aerocapture (right). Munk and Spilker (2008)

According to Munk and Spilker (2008) there are several additional benefits to aerocapture. These include the lowered post-launch fuel consumption and the possibility to establish an orbit after a single pass through the atmosphere, compared to the many passes required for aerobraking. However, three downsides of aerocapture are also mentioned. The first downside is the necessity to have a protective aeroshell, also known as a Thermal Protection System (TPS) against the aerothermal heating that occur during the hypersonic pass through the atmosphere. The second is the fact that it is a one-shot manoeuvre, failure most likely resulting in the loss of a vehicle, and its contents. The final downside is that due to the ionisation of the atmosphere around the vehicle, ground-based communications are not possible, making the vehicle fully dependent on on-board flight software for, for instance, guidance.

Aerocapture has never been implemented for an interplanetary mission since it was first proposed by

Cruz (1979). However, it is an often analysed and proposed manoeuvre for interplanetary missions. The studies of aerocapture are not limited to Earth centred aerocapture, but have also been performed for extra-terrestrial bodies such as Mars, Venus, Titan, and Neptune. Nevertheless, according to Munk and Spilker (2008) it is likely that the first every aerocapture mission will be an Earth-based demonstrator, stating the increase in technology readiness level as the primary reason. With large programmes such as ESA's Aurora programme and the possible scientific return from a Mars sample return mission it is also likely that the first interplanetary mission to feature aerocapture will be a Mars sample return mission, where aerocapture will be used to both capture the orbiter at Mars and to return the samples to Earth.

1.1. Research Question

The research questions were established based on the topic selected. These questions drive the direction of the research. Almost all the work performed during the research was done with the idea of answering either the primary research question, or the sub-questions. The primary research questions refer to the ultimate goal of the research, where the sub-questions provide additional insight and understanding of the problem, as well as potentially reinforcing the conclusion of the primary research question. Two primary research questions were formulated for this research:

1. *"What is the optimal aerocapture trajectory to reach the target apoapsis for the reference vehicle about the central body, arriving with arbitrary entry interface conditions."*
2. *"What are the limit entry interface conditions with which the reference vehicle can arrive at the central body, and still reach the target apoapsis after aerocapture."*

These research questions are formulated by using the general terms "central body" and "reference vehicle" in lieu of a specific celestial body or vehicle. This is done such that only two research questions had to be formed, instead of numerous that would all be slight variations of each other. Each of the specific forms of the two research questions are discussed next.

1.1.1. Research Question Variations

The first variation is the type of mission flown, and thus the type of vehicle used. In this research two difference types of missions are considered. The first type is a manned mission, and thus uses a vehicle that is representative of vehicle that are meant to be crewed and pass through atmospheres. This type of missions is hereinafter referred to a Crew Return Mission (CRM). The second type of mission is, logically, one that is unmanned, and uses a vehicle that is representative of a vehicle used for unmanned missions that pass through the atmosphere. Unmanned re-entry missions are often used for Sample Return Missions (SRM). This designation will be used hereinafter for this type of mission.

The second variation is the planet the mission is executed about. As the subtitle of this report might have already have given away, the three planets considered are Earth, Mars, and Venus. These planets were chosen as they provided an interesting spread of atmospheres in which the atmospheric portion of the flight is conducted. Mars features a very tenuous atmosphere, whereas Venus has a very dense atmosphere. Earth features an atmosphere somewhere between these two.

These two variations bring the total number of research questions up to sex variations of the same basic research question. Two different vehicles flying aerocapture trajectories about three difference planets. As a last remark, the nomenclature used for the types of missions, crew return and sample return, do not make a sense when used in the context of performing aerocapture about Mars or Venus, as this would indicate that a crew or sample collected would return to Mars or Venus. However, using this nomenclature, the major difference between the two missions can be readily understood.

1.1.2. Research Sub-questions

In addition to the two primary research questions, three additional sub-questions were formulated to further guide the research. These sub-questions deal with improving the applicability of the aerocapture manoeuvre, and demonstrating the benefit of aerocapture over regular propulsive capture.

3. *"If the reference vehicle arrives with an entry interface condition outside of the previously defined limits, what is the optimal way to salvage the aerocapture?"*
4. *"How much mass does each of the trajectories save over traditional chemical circularisation?"*

5. *"What is the limit entry interface condition for which traditional chemical circularisation becomes preferable over an aerocapture trajectory?"*

The answers to the two primary research questions and these sub-questions were obtained throughout this research. At the end of this report, while discussing the conclusions, a summary will be given of the research questions, the sub-questions, and their found answers.

1.2. Report Layout

This report is split into four parts, each part grouping together several chapters that deal with a distinct part of the research. Part I consists of Chapters 2 and 3 and provides the required background for the research. Chapter 2 provides required background information regarding aerocapture manoeuvres, and a brief history of aeromanoeuvres in general. The two reference vehicles and the requirements imposed on them are described, and the trajectory targets are established. Chapter 3 discusses the flight dynamics. The equations governing the motion and the forces that effect this motion are discussed. The reference frames in which these forces are defined are described and transformations between the various frames are determined. Lastly, the environment that is the source of these forces and the models used to approximate this environments is discussed.

Part II deals with the numerical methods and software used in this research. In Chapter 4 a description of the various used numerical methods is given. In Chapter 5, the software libraries from where these numerical methods were obtained are described, and the general architecture of the developed software is presented.

Part III deals with the results from the research. In Chapter 7 the results from evaluating the accuracy of a first-order and second-order analytical method is presented. In Chapter 8 a proposal for optimal aerocapture trajectories is investigated. In Chapter 9 the effect of varying the initial conditions and the control variables on the trajectory is investigated. In this investigation it is also determined what the best course of action is when the initial conditions violate a constraint. Lastly, in Chapter 10 the conclusions drawn throughout this part are brought together to develop entry corridors and flight envelopes that specify the boundaries for which aerocapture can be performed. The last chapter of this part, Chapter 11, discusses the methodology formulated to obtain optimal aerocapture trajectories, and the benefit of flying these trajectories compared to propulsive capture.

The last part, Part IV, concludes the research with only a single chapter, Chapter 12. In this chapter the conclusions made based on the results presented in this report are gathered, and the recommendations for future research are given.

I

Part I: Background

2

Mission Overview

As already stated in Chapter 1, an aerocapture manoeuvre has never been implemented in an interplanetary mission. However, the manoeuvre has been proposed and investigated numerous times and missions using similar mechanics, such as aerobraking and skipping, have been successfully executed in the past. Furthermore, missions that perform direct entry from an hyperbolic trajectory have also been performed. By investigating what has been previously prosed for aerocapture missions, as well as aerobraking, skipping, and hyperbolic direct entry missions, additional insight can be gained into the aerocapture manoeuvre. This insight comes in the form of possible range of initial conditions, vehicle configurations, and requirements imposed on the trajectory. In this chapter an overview is provided of missions tat fall in any of these categories.

In Section 2.1 missions that featured direct entry from an hyperbolic trajectory are discussed. This type of mission and the aerocapture shares the characteristic of entry into the atmosphere from an open orbit. In Section 2.2, missions that performed, or were able to perform, skipping flight are discussed. These missions and the aerocapture share the characteristic of skipping out of the atmosphere. The aerobraking mission also shares this characteristic, and these missions are discussed in Section 2.3. The last type of missions discussed are two mission proposals that featured aerocapture. These mission proposals are discussed in Section 2.4. Using the information obtained from these four types of missions, the possible range of initial conditions, as well as the nominal initial conditions and target apoapsis altitude and desired accuracy are established in Section 2.5. The final section, Section 2.6, the reference vehicles used throughout this report are discussed. For the reference vehicle the physical properties, such as the size, shape, and mass will be provided, as well as, the requirements imposed on the trajectory by the vehicle.

2.1. Past Hyperbolic Direct Entry Missions

A hyperbolic direct entry mission and an aerocapture manoeuvre have in common that in both cases the vehicle enters the atmosphere while on a hyperbolic (open) trajectory. In the case of the direct entry mission, during the single pass through the atmosphere, the vehicle looses all is orbital energy and results in a touch- or splash-down on the central body. In most cases, the hyperbolic direct entry is supplemented by additional force inducing elements, such as parachutes or retrorockets.

On Earth, hyperbolic direct entry has been applied by several sample return missions returning from comets and asteroids. These include Stardust and Hayabusa.

Stardust was a NASA sample return mission launched in 1999. According to Atkins et al. (1997), the objective of the mission was to approach comet Wild-2 and collect cometary and interstellar particle. These samples would then be returned to Earth. At Earth, the sample return capsule performed ballistic entry. According to Revelle and Edwards (2007) the inertial velocity of the entry was 12.9 kms^{-1} with a flight-path angle of -8.2°. During entry the vehicle encountered a peak heat flux of 12.0 MWm^{-1} and a peak mechanical load of 34g.

Hayabusa was a JAXA sample return mission launched in 2003. According to Kawaguchi et al. (2006), the objective of the mission was to rendezvous with the asteroid Itokawa, and collect samples from the asteroid surface, and return them to Earth. At Earth, the sample return capsule performed ballistic entry and according to Cassel et al. (2011), it re-entered the Earth atmosphere with an inertial velocity of 12.035 kms^{-1}

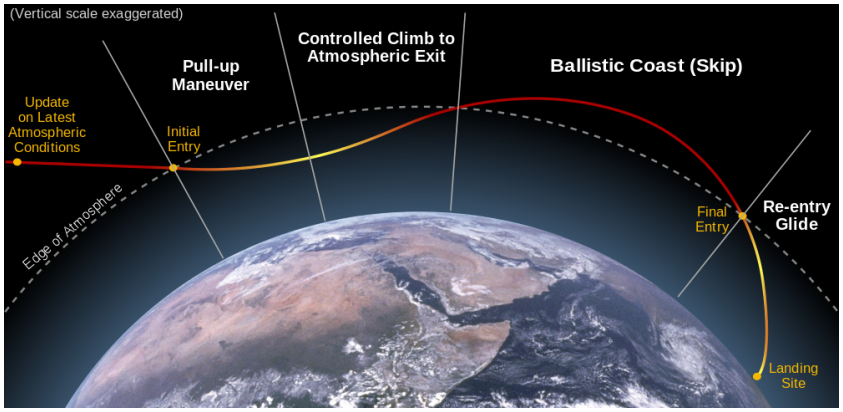

Figure 2.1: Atmospheric entry trajectory illustrating the basic phases of flight in a skip entry. Clem Tiller (2006)

and a flight-path angle of -12.35°. During entry it encountered a peak heat flux of 11.12 MWm^{-1} and a peak mechanical load of 49g. According to Watanabe et al. (2017), a follow-up to this mission, Hayabusa2 was launched in 2014, rendezvoused with asteroid Ryugy in 2018, and is expected to return to Earth in 2020. The capsule for Hayabusa2 is expected to re-enter with 12 kms^{-1}.

On Mars, missions have been performed using direct entry in more recent history. Some examples of these missions are NASA's Pathfinder (1996) landing the Sojourner rover, NASAs' Mars Exploration Rover (2003) landing the Spirit and Opportunity rovers, NASA's Mars Science Laboratory (2011) landing the Curiosity rover, and ESA's ExoMars, in particular the Schiaparelli EDM Lander (2016).

For Venus the only missions to perform hyperbolic direct entry in to the atmosphere occurred during the aforementioned space race. According to Colin (1980) these were the Soviet Verena 3 through 12 from 1966 through 1978, and NASA's Pioneer-Venus 2 in 1978. Pioneer-Venus 2 consisted of 4 probes and the spacecraft bus. The relative velocity and relative flight-path angle at entry for these four probes were 11.5377 kms^{-1} at -32.37°, 11.5372 kms^{-1} at -68.74°, 11.5371 kms^{-1} at -25.44°, and 11.5375 kms^{-1} at -41.50°. The bus entered with 11.5289 kms^{-1} at -9.38°.

The flight-path angles of these trajectories were found to be a lot steeper than those found characteristic for aerocapture, as will be discussed later. This is due to aerocapture requiring a shallower entry to manage to skip out of the atmosphere. For this reason, only the velocities at which these entries occurred were considered while formulating the nominal reference mission later in this chapter.

2.2. Past Skipping Entry Missions

A skipping entry and an altitude-targeting aerocapture manoeuvre share the similarity that during the atmospheric pass the orbital energy is lowered, and at the end of the atmospheric pass the vehicle skips back out of the atmosphere. For the aerocapture manoeuvre at this point the periapsis of the orbit would be raised to fall outside of the sensible atmosphere. For skipping entry it is more common leave the orbit intersecting the atmosphere such that the vehicle passes through the atmosphere again and the remaining orbital energy can be lost. A general skip entry manoeuvre featuring a single skip is illustrated in Fig. 2.1

Skipping entry has only been successfully performed by three of the Soviet Zond missions, namely Zond-6, -7, and -8 in 1968, 1969, and 1970, respectively (Siddiqi, 2000). According to the same source, the Apollo missions were also planned to feature a single skip during the entry during the early stages of development, and the guidance algorithm featured in Apollo was capable of executing the manoeuvre. However, because Apollo was a manned mission and that the risks associated with a skip entry were deemed too high, it never performed the manoeuvre. Regardless of the fact that Apollo never performed a skip itself, it has had a big impact on future developments in both skip and aerocapture manoeuvres. For instance the first ever aerocapture guidance algorithm by Gamble et al. (1988) is based on the Apollo guidance.

Another example of Apollo's impact is the Orion Multi-Purpose Crew Vehicle (MPCV), known as the Crew Exploration Vehicle (CEV) before cancellation of the Constellation programme. The Orion MPCV can be seen as a continuation of the technology developed for the Apollo program. This continuation is evident from both the vehicle shape and the guidance algorithm used. The vehicle shape of Orion very closely represents that of an enlarged Apollo capsule, as is illustrated in Fig. 2.2. According to Bairstow and Barton (2007), the guidance

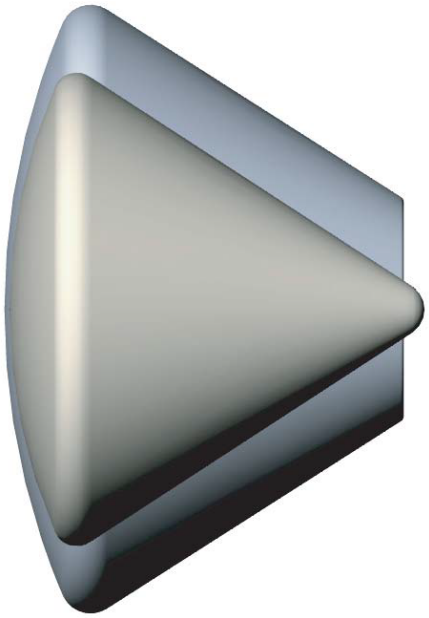

Figure 2.2: Relative size of the larger Orion Crew Exploration Vehicle (Back) to the Apollo Command Module (Front). Moss et al. (2006).

algorithm used in Orion, PredGuid, is based on the guidance algorithm from Apollo. Additionally, according to NASA (2013), another adaptation of this guidance algorithm has been developed with the capability for performing an aerocapture manoeuvre, called PredGuid+A. The Orion CEV was proposed to be used to ferry both crew and cargo to the ISS, as a crew vehicle for a lunar mission, and, since its redesign into the MPCV, a manned mission to Mars.

2.3. Past Aerobraking Missions

The similarities between aerobraking and aerocapture stem from the fact that in both missions the atmosphere is used to decrease the energy of the vehicle passing through the atmosphere. The main difference between the two manoeuvres are the types of orbit for which the manoeuvre is performed, and the depth with which the atmosphere is penetrated. Aerobraking is performed to lower the apoapsis of a closed orbit, when the vehicle has already been captured about a celestial body, whereas an aerocapture manoeuvres is performed on an open (hyperbolic) orbit with the target to obtain a closed orbit. Aerobraking would be a logical follow-up to aerocapture to lower the apoapsis further if the current apoapsis is greater than the desired apoapsis. Additionally, aerobraking commonly happens in the upper parts of the atmosphere to limit the aerodynamic forces and aerothermal load, whereas aerocapture penetrates the atmosphere deeper to make use of the increased density at lower altitudes to increase the aerodynamic forces, and decrease the orbital energy faster. Fig. 1.2 provides a schematic view of both aerocapture and aerobraking manoeuvres.

The first aerobraking manoeuvre was performed by the Japanese Institute of Space and Astronautical Science (ISAS), now a division of Japan Aerospace Exploration Agency (JAXA), mission Hiten (Uesugi, 1996) in 1991. The vehicle performed a total of two aerobraking manoeuvres about Earth, both consisting of a single pass. The details of both aerobraking manoeuvres were obtained from Uesugi (1996), and are presented in Table 2.1.

The first extra-terrestrial aerobraking manoeuvre was performed by the Magellan spacecraft on Venus. The Magellan spacecraft was tasked to map the surface and to measure the planetary gravitational field. In this mission aerobraking was used to reduce the orbital eccentricity by lowering the apoapsis altitude and thereby improving the resolution of the gravity mapping. The details of the manoeuvre were obtained from Tolson et al. (2013), Lyons (2000), and Spencer and Tolson (2007), and are presented in Table 2.1. Tolson et al. (2013) states that, based on the successful application of aerobraking for the Venus Magellan mission, aerobraking became a technology that enabled Mars orbiting missions.

The Mars Global Surveyor (MGS) was intended to map the entire Martian surface. It was the first mission that was designed with aerobraking in mind during the design. Due to the low density atmosphere surround-

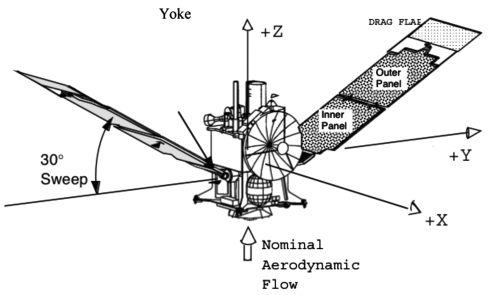

Figure 2.3: Mars Global Surveyor Spacecraft in Aerobraking Configuration. Spencer and Tolson (2007).

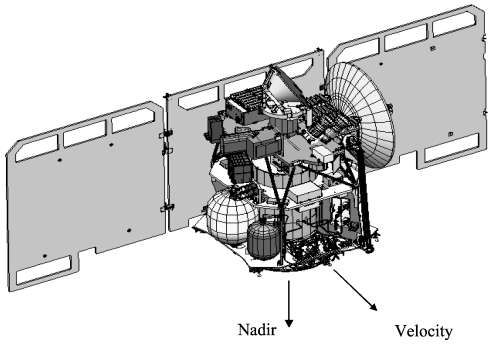

Figure 2.4: Mars Odyssey Spacecraft in Aerobraking Configuration. Smith and Bell (2005).

Table 2.1: Details from the various investigated performed aerobraking manoeuvres. The fuel saved is presented both as the actual mass of the fuel saved, as well as an approximate percentage of dry mass.

Mission	Body	r_p [km]	Passes [#]	ΔV [ms^{-1}]	Δr_a [km]	Fuel saved [kg (%Dry)]
Hiten #1	Earth	125.5	1	1.712	8 665	-
Hiten #2	Earth	120	1	2.8	14 000	-
Magellan	Venus	170	700	1 200	8 000	490 (~50%)
MGS	Mars	120	446	1 200	54 000	330 (~50%)
MO	Mars	110	332	1 080	26 000	320 (~85%)
MRO	Mars	110	420	1 200	43 500	580 (~60%)
MCO	Mars	57	$\frac{1}{2}$	-	-	-

ing Mars the MGS (and every subsequent aerobraking mission on Mars) used its solar panels to increase its surface area perpendicular to the velocity to increase the amount of drag effected. This is shown schematically for the MGS and Mars Odyssey in Figs. 2.3 and 2.4, respectively. According to Lyons (2000) the solar panels of MGS were swept back to reduce the mechanical loading during the aerobraking manoeuvre. The details of the manoeuvre were obtained from Lyons (2000) and Spencer and Tolson (2007), and are presented in Table 2.1

After MGS came 2001 Mars Odyssey (MO). MO investigated the planet's geology and radiation environment, as well as search for evidence of past or present water or ice. The details of the manoeuvre were obtained from Tolson et al. (2013) and Spencer and Tolson (2007), and are presented in Table 2.1

The Mars Reconnaissance Orbiter (MRO), launched in 2005, was designed to map the surface of Mars in a higher resolution than was done by MGS so that a landing site for future surface missions could be designated. As stated, MRO's attitude was such that its solar panels were aligned roughly perpendicular to the flow. The details of the manoeuvre were obtained from Tolson et al. (2013) and Spencer and Tolson (2007), and are presented in Table 2.1.

The first failure in an aerobraking manoeuvre occurred during the Mars Climate Orbiter (MCO) mission. This mission was launched in 1998 and was intended to investigate the Martian atmosphere. An aerobraking manoeuvre had been proposed to be used after orbit insertion about Mars to circularise the orbit. This orbit insertion is where the mission failed. The failure occurred due to a mix-up of imperial and metric units when supplying commands[1]. The insertion manoeuvre placed the vehicle in an orbit with a periapsis of 57 km, 170 km below the planned 226 km, and 23 km below the minimum altitude considered survivable by MCO of 80 km. At this altitude the atmospheric density was too high, and most likely resulted in the disintegration of the spacecraft in the Martian atmosphere.

2.4. Proposed Aerocapture Missions

As stated in Chapter 1, aerocapture was first proposed by Cruz (1979), but has never been put into practice since, not even for a demonstrator mission. Nevertheless, many studies have been performed into the use of aerocapture as a means of saving propellant and making certain far away destinations, such as Neptune,

[1] Mars Climate Orbiter Mishap Investigation Board, "Phase I Report", November 1999. Available at `https://llis.nasa.gov/llis_lib/pdf/1009464main1_0641-mr.pdf`

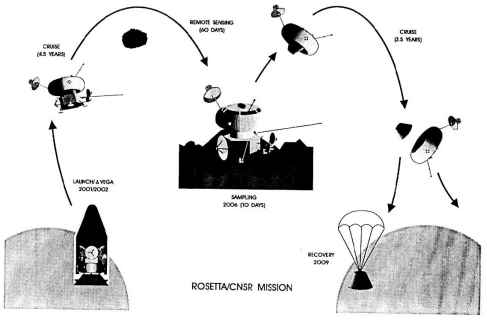

Figure 2.5: Artist's impression of the Rosetta/CNSR mission from the original proposal by Schwehm (1989)

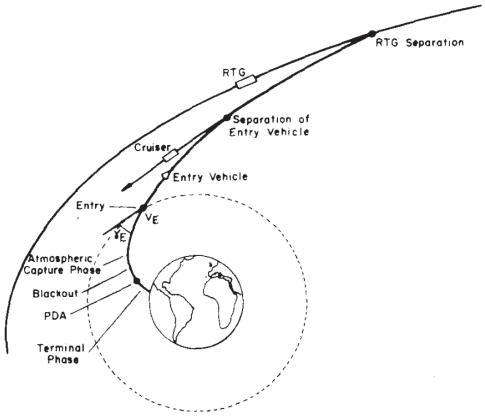

Figure 2.6: Rosetta/CNSR Earth Approach and Re-Entry Scenario. Serrano-Martinez and Hechler (1989).

feasible. In this section two types of missions that were proposed featuring aerocapture at some point as a primary method for capturing the vehicle are discussed. The two proposals are for a Mars Sample Return (MSR) mission, and the original Rosetta Comet Nucleus Sample Return (CNSR) mission.

2.4.1. Rosetta Comet Nucleus Sample Return

The original proposal for the Rosetta mission made by Schwehm (1989) was to bring back a 10 kg comet core sample, a 10 g to 100 g volatile sample, and a 1 kg to 5 kg surface sample. According to Serrano-Martinez and Hechler (1989), this mission would have a tremendous scientific return as it allowed for the analysis of the most primitive material in the solar system, which was hoped to provide insight in the chemical and physical processes that marked the beginning of our Solar System. The original proposal featured aerocapture of the sample return capsule followed by rendezvous with the International Space Station (ISS), from which the samples would have been returned to Earth via "standard" entry. This part of the mission was scrapped however, with Serrano-Martinez and Hechler (1989) citing problems with keeping the samples at the required temperature for prolonged period of time in the near Earth environment as the root of the problem. The mission was changed to feature aerocapture followed by direct entry using an low L/D, capsule-like, vehicle and guidance algorithm similar to that used for Apollo. An artist's impression of the original mission plan as presented in Schwehm (1989) is presented in Fig. 2.5, and the updated mission plan featuring direct reentry from Serrano-Martinez and Hechler (1989) is shown in Fig. 2.6.

The eight phases of the mission as proposed by Schwehm (1989) were: launch and injection into Earth-escape trajectory, heliocentric trans-comet cruise, comet approach, sample acquisition and storage, comet departure, heliocentric trans-Earth cruise, aerobraking (*[sic]*, this manoeuvre is actually an aerocapture manoeuvre as there is no other manoeuvre between the trans-Earth cruise and entry/orbiting) directly to ground or into Earth orbit, and lastly sample retrieval. Serrano-Martinez and Hechler (1989) provides more details regarding a number of the phases. The first phase of the mission was the launch using the Titan/Centaur rocket. This was followed by an Earth gravity-assist, transfer to the comet, approach of the comet, and rendezvous at its apoapsis at roughly 5 au. At the comet the samples would be gathered via drilling, after which the vehicle would depart the comet and transfer back to Earth. The final stages are the approach of Earth with an hyperbolic excess velocity (V_∞) exceeding 10 kms^{-1}, separation from the transfer vehicle, separation from the entry vehicle, and start of aerocapture in the upper atmosphere. The aerocapture was planned to start with an initial entry velocity of 15 kms^{-1} at an flight-path angle of -10.5°. The developed guidance algorithm of the the mission was reported to have a landing precision of less than 10 km, and a peak acceleration below 20g. 20g being the proposed mechanical load factor sustainable by the vehicle.

In the work by Serrano-Martinez and Hechler (1989) two vehicle shapes were analysed. The first being a low L/D vehicle modelled after Apollo, and one with ah higher ratio (Bent nose biconic type vehicle model). The result of the analysis was that the biconic vehicle showed heating problems at its small radius nose, whereas the Apollo capsule performed within acceptable limits. For this reason an Apollo shaped capsule was proposed for this mission.

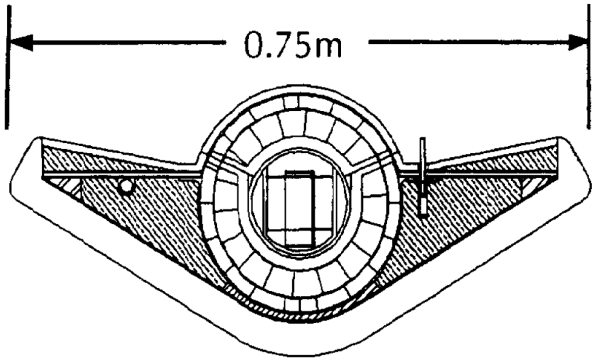

Figure 2.7: Schematic representation of the Earth entry vehicle from the NASA/CNES MSR mission proposal. O'Neil and Cazaux (2000).

2.4.2. Mars Sample Return

According to Mitcheltree et al. (1998), MSR missions had, at the time, been studied periodically for 30 years. Adding 20 years since that report, means that MSR missions have been of interest for roughly half a century. This continuous interest is because a sample return from Mars is considered the mission with the highest scientific return regarding insight into Earth's history. Bringing the sample back to Earth allows the analysis of the sample not only with the instruments on board of the lander, but with all the instruments available on Earth. This will drastically increasing the potential scientific data gathered. With Mars commonly being considered to most Earth-like planet in our Solar System, this analysis would not only provide insight into Mars, but also our own planet. In this section a MSR missions will be discussed. This mission was proposed by a team formed by NASA and the Centre National d'Études Spatiales (CNES) in France.

According to O'Neil and Cazaux (2000), the original proposal for a Mars Sample Return mission involved two separate launches. The first launch, planned for 2003, was the responsibility of NASA. This launch would launch a Mars Lander, Rover, and Mars Ascent Vehicle (MAV). The second launch was planned for 2005 and was the responsibility of CNES. This launch would carry another lander, rover, and MAV, an orbiter, and an Earth entry Vehicle. This Earth entry vehicle had an empty weight of 23 kg, and would weigh 3.6 kg heavier upon entry due to the stowed samples. The maximum diameter of the vehicle is 0.75 m, but no figure was provided regarding the deflection angle or nose radius. An illustration of this vehicle is provided in Fig. 2.7.

When arriving at Mars, the orbiter would have performed aerocapture to be captured at Mars without the use of a propulsive system. It would penetrate the Martian atmosphere with an altitude of 40 km, resulting in an elliptical orbit with an apoapsis of roughly 1500 km. After the aerocapture, rockets would be used to raise the periapsis outside of the sensible atmosphere. After this, the orbiter would attempt to locate the 2003 sample capsules put in orbit by the MAVs. After locating the capsules, the orbit of the orbiter is altered to match the orbital plane of the sample and its orbit is circularised. This procedure would be repeated with the 2005 sample canisters. By 2007 it was expected that all samples are captured and stowed in their respective Earth Entry Vehicles. The orbiter would depart from Mars and start along its trans-Earth orbit. Approaching Earth, a gravity-assist would be performed to allow for landing sites on the northern hemisphere. At Earth, the Earth entry vehicles would re-enter the Earth's atmosphere on a ballistic trajectory with a velocity of 11.5 kms^{-1}.

2.5. Reference Mission

In this section the nominal initial conditions for each of the three planets are discussed. The nominal initial condition was selected based on proposed and executed missions that had the same planet as their target. After the nominal state is established, the accuracies required from the interplanetary guidance, navigation, and control subsystems are stated.

Following this, the target of the trajectory, the the requirements that the trajectory has to adhere to, and the guidance and control accuracies are formulated. In the next section, Section 2.6, the two vehicles, and the requirements imposed on the trajectory flown by the vehicle to ascertain the safety of the vehicle and its contents, are discussed. Additionally, in the final subsection of the next section, the requirements are formally formulated and grouped together.

Table 2.2: Nominal Entry Interface Vehicle State for all three planets.

Central Body	Altitude [km]	Velocity [kms^{-1}]	Flight-Path Angle [°]
Earth	125	11.5	-7.4
Mars	125	8.2	-11.5
Venus	250	11.25	-6.1

2.5.1. Nominal Initial State

For the first two missions, the transfer from Earth to Mars and back from Mars to Earth, the MSR mission was selected as a reference mission. For this mission an entry velocity on Earth of 11.5 kms^{-1} was proposed, at an altitude of 125 km. According to Lyne (1992), this value is representative for a conjunction class transfer from Mars to Earth. Lyne (1992) states that conjunction class transfers result in entry velocities of 11 kms^{-1} to 12 kms^{-1}, and that opposition class transfers result in a higher velocity of 13 kms^{-1} to 15 kms^{-1}. Wooster et al. (2006) reports a broader range for conjunctions class missions from 11.5 ms^{-1} to 14.7 ms^{-1}. The difference between conjunction and opposition class transfers is not of import to this research and will not be touch upon. Mitcheltree et al. (1998) and Robinson et al. (2009) further corroborate these statements.

Mitcheltree et al. (1998) reports a lower bound on the entry velocity of 11 kms^{-1} at an altitude of 125 km, and uses a value of 11.46 kms^{-1} at an altitude of 125 km with a flight-path angle (FPA) of -12° in its research. Robinson et al. (2009) presents a range of different initial velocities and FPAs for both Earth aerocapture and Earth direct entry at Mars return conditions at an altitude of 122 km. For aerocapture the velocities and flight-path angles range from 12 kms^{-1} to 16 kms^{-1}, and -5° to -10°, respectively. For the direct entry the velocities and flight-path angles range from 12 kms^{-1} to 16 kms^{-1}, and -5° to -7.4°, respectively.

Based on this information the nominal initial state of the vehicle are as follows. The inertial velocity of the vehicle will be taken as 11.5 kms^{-1} as to mimic the discussed MSR mission and the research by Mitcheltree et al. (1998), and to have an average value for a conjunction type transfer as presented by Lyne (1992), while still falling within the range reported by Wooster et al. (2006). For the flight-path angle an inertial angle of -7.4° will be used. While this angle is on the high end of the spectrum for direct entry as proposed by Robinson et al. (2009), it is average for the proposed aerocapture values. The nominal initial altitude of the vehicle is set to 125 km, again following the design of Mitcheltree et al. (1998), and being similar to the initial altitude altitude used by Robinson et al. (2009). The nominal initial states for Earth is tabulated in Table 2.2.

For the Mars entry velocity from Earth, there were no entry values presented in the MSR mission proposal. However, according to Lyne (1992), the probable range of entry speeds ranges from 6 kms^{-1} to 10 kms^{-1}. This was again corroborated by Wooster et al. (2006), who reports a possible range between 5.5 kms^{-1} and 9.5 kms^{-1}. They also report a possible range of flight-path angles ranging from -8° to -13°. Based on these ranges, nominal values for the velocity and flight-path angle that were used in this research were selected. For both variables, nominal values above the average (at roughly the two-thirds mark of the ranges) were selected. This was to obtain high energy nominal trajectories, that would make the research more interesting to perform. The nominal initial velocity was set to 8.2 kms^{-1}, and the flight-path angle to -11.5°. The nominal initial states for Mars is tabulated in Table 2.2.

For the Venus entry from Earth, the work by Munk and Spilker (2008) uses an inertial entry velocity range from 10.5 kms^{-1} to 14.0 kms^{-1}, with a nominal entry velocity and flight path angle of 11.25 kms^{-1} and -6.12°, respectively. Craig and Lyne (2002) presents a range for the entry velocity between 11.0 and 14.0 kms^{-1}, and for entry angles between -6.5° and -11°. Due to the late inclusion of this mission, and the infrequency the nominal initial conditions were used throughout this research, it was decided to not expend more time into finding other references for Venus entries, and to use the values as proposed by Munk and Spilker (2008) as the nominal entry state, as they are similar to the lower bound presented by Craig and Lyne (2002). The nominal initial states for Venus is tabulated in Table 2.2.

In this research the interest lays on investigating the feasibility and applicability of the aerocapture manoeuvre. The interplanetary trajectory leading up the the aerocapture is not of interest outside of potential discrepancies with the nominal initial conditions. However, when the impact of varying the initial conditions on the feasibility and applicability of the aerocapture manoeuvre is evaluated, this will be done by setting different initial conditions, instead of applying a random error. Doing so allows for greater control over the evaluated range of initial conditions. For this reason it is assumed that the interplanetary guidance, navigation, and control subsystems are perfect, resulting in initial conditions that exactly match the specified initial conditions.

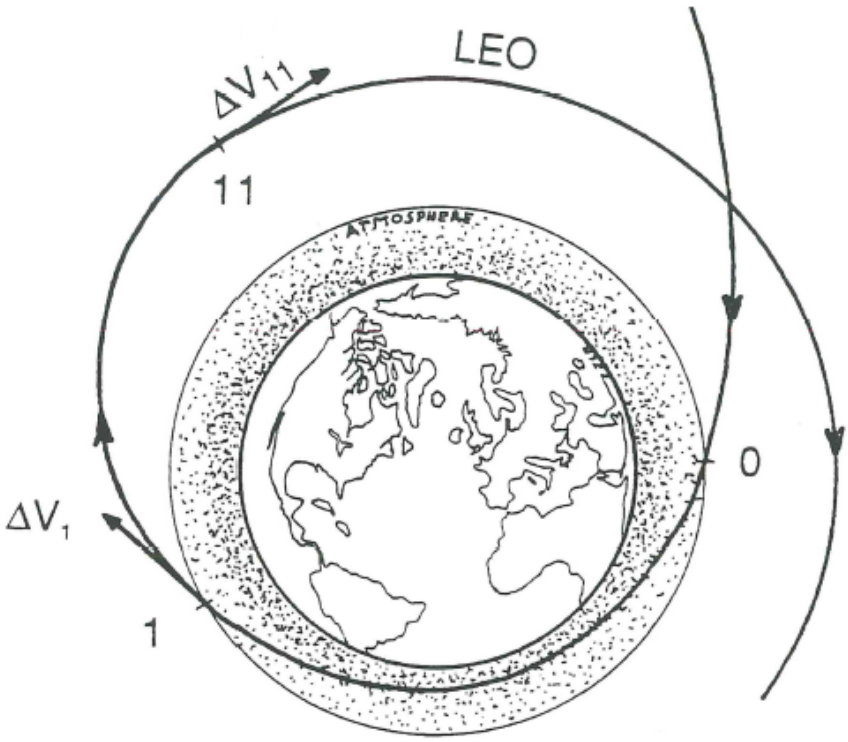

Figure 2.8: Illustration of an aerocapture manoeuvre resulting in a parking orbit about the central body. ΔV_{11} is used to circularise the orbit, and ΔV_1 is attempted to be minimised during the optimisation. ACRI/LAN (1992).

2.5.2. Target Orbit

The aerocapture manoeuvre attempts to use a single pass through the atmosphere to transition from a hyperbolic orbit to a closed orbit with its apoapsis at the desired altitude. After the apoapsis is reached, the periapsis can be circularised, or raised to any other desired altitude. This type of mission is schematically depicted in Fig. 2.8. In the optimal solution, the ΔV_1 manoeuvre is zero.

The original Rosetta CNSR, as proposed by Schwehm (1989), is an example of a mission where the final target was an orbit at a particular altitude. In this particular example the target orbit was placed at the altitude of the ISS, at an altitude of 400 km. In the study of Robinson et al. (2009) the target of the aerocapture analysis was an orbit with an apoapsis of 500 km. Based on these two missions, it was opted to follow the study by Robinson et al. (2009) and make the target orbit an orbit with an altitude of 500 km. The target altitude of the trajectory was not changed for Mars or Venus, and thus the 500 km apoapsis altitude is also the target for these two missions. Using the mean volumetric radii for Earth[2], Mars[3], and Venus[4], of 6371.0 km, 3389.5 km, and 6051.8 km, respectively, the target apoapsis radii and semi-major axes (after circularisation), are 6871.0 km, 3889.5 km, and 6551.8 km, respectively.

In this research, planar changes are not considered. Therefore the inclination of the target orbit will be the same as that of the initial orbit. Neglecting the inclination of the orbital planes with respect to the ecliptic, and assuming that the transfer orbits happen fully within the ecliptic, the initial and target inclinations are equal to the tilt of the central body's rotational axis with respect to the ecliptic. For Earth, Mars, and Venus, this tilt is equal to 23.44°, 25.19°, and 2.64°, respectively.

After the target apoapsis is reached, the orbit is circularised, thus an eccentricity of zero is desired. The longitude of the ascending node, the argument of periapsis, and the true anomaly of the target orbit are not important for this research as no actual rendezvous is planned. A summary of the orbital elements considered is provided in Table 2.3.

As it is impossible to obtain the exact target values in reality, for each of the target variables an allowable error margin is defined, and these error margins are subsequently formulated into requirements to which the trajectory has to adhere. However, the error margin does not have to apply directly to the variable. For

[2]NASA Earth Fact Sheet, available at `https://nssdc.gsfc.nasa.gov/planetary/factsheet/earthfact.html`
[3]NASA Mars Fact Sheet, available at `https://nssdc.gsfc.nasa.gov/planetary/factsheet/marsfact.html`
[4]NASA Venus Fact Sheet, available at `https://nssdc.gsfc.nasa.gov/planetary/factsheet/venusfact.html`

Table 2.3: Overview of the orbital elements of the target orbit for the orbit targeting mission.

Central body	Apoapsis radius [km]	Eccentricity [-]	Inclination [°]
Earth	6871 km	0	23.44
Mars	3889.5 km	0	25.19
Venus	6551.8 km	0	2.64

instance, instead of defining an error margin on the apoapsis radius, it is possible to define an allowed corrective ΔV that adjusts the apoapsis radius post aerocapture.

In addition to the required target accuracy, the accuracy of the atmospheric flight guidance, navigation, and control system need to be defined. Similar to its interplanetary counterpart, this subsystem is assumed to be perfect. This means that the navigation provides the exact current state to the guidance system, and that the control perfectly executes the manoeuvre dictated by the guidance system. As in this research only the bank angle is considered a control variable, the control subsystem only controls the bank angle.

As stated, in the optimal situation, the ΔV_1 required to reach the target apoapsis is zero. However, a error margin is provided in which the burn required to reach the apoapsis is sufficiently small. As in this situation a circularisation burn is also performed, it was decided to consider the apoapsis altering burn sufficiently small if ΔV_1 was negligible compared to the ΔV required for the circularisation. A ratio of 1:20, or 5%, was chosen to be considered negligible.

The eccentricity of the orbit is the result of the two ΔV manoeuvres post aerocapture. In this research, the ΔV manoeuvres are assumed to be executed instantaneously and with perfect accuracy. As the ΔV magnitudes are determined analytically, the resultant eccentricity can be set to match zero exactly.

Lastly, a requirements detailing maximum allowed angle between the initial and final orbit, which is be referred to as the wedge angle. The maximal value for the wedge angle used in ACRI/LAN (1992) was 0.1°. However, as in this research perfect guidance and control is assumed, it was decided to take a more driving constraint by halving this value. This resulted in a maximal wedge angle of 0.05°.

2.6. Reference Vehicle

In this section the two reference vehicles used in the research are described. One vehicle is used as a template for a Crew Return Mission vehicle, and one is used as a template for a Sample Return Mission vehicle. After describing the dimensions and physical properties of the vehicles that are used in the research, the requirements imposed on the vehicles to ensure safe passaged through the atmosphere are stated.

2.6.1. Nominal Vehicle Configuration

Two different vehicles are required, one for the manned flight and one for the unmanned flight. It was noticed while consulting literature that the Apollo Command Module, or vehicle similar to it, was used often as a baseline vehicle for both studies. This was the case in studies such as Serrano-Martinez and Hechler (1989), Lyne (1992), Robinson et al. (2009), and Zucchelli (2016). The often quoted reason for this is the fact that for the Apollo CM a plethora of other studies and extensive databases are available, facilitating finding required information regarding, for instance, the aerodynamics of the the vehicle, very quickly. Additionally, the Apollo capsule was capable of performing skip entry, as reported by Siddiqi (2000), and was found to be capable of aerocapture based on the work of Gamble et al. (1988). Furthermore the Apollo CM was used as a reference vehicle for the design of the Orion MPCV, indicating that its design is still relevant for the design of new vehicles today. The combination of available information and relevance drove the selection of the Apollo CM as a reference vehicle for the CRM.

In Fig. 2.9 a schematic cross-section of the nominal Apollo CM is provided. The nominal mass of the command module is 5500 km, and, based on the diameter of 3.9116 m, the aerodynamic reference area is 12.017 m^2. The nose radius of the Apollo CM is 4.694 m, and the ratio between the diameter and the nose radius is 1.2 m. The trim attitude and aerodynamic coefficients of the Apollo CM as a function of Mach number were found quickly in the work by Graves and Harpold (1970), the effects of the Mach and Reynolds number on the attitude and aerodynamic coefficients were found in the work by DeRose (1969), and the effect of the Knudsen number on the aerodynamics was investigated by Moss and Bird (1984). These relations will be further discussed in Section 3.6.1.

For the SRM vehicle two vehicles that were used for interplanetary SRM missions were investigated, namely NASA's Stardust and JAXA's Hayabusa. According to Willcockson (1999), the Stardust sample return

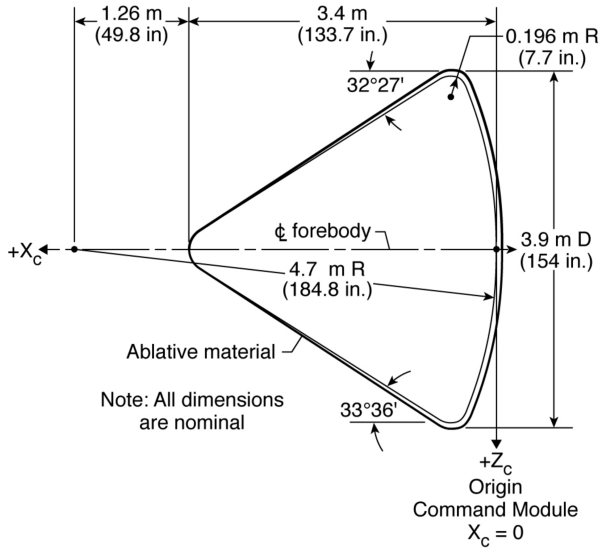

Figure 2.9: Geometry of the Apollo CM. Robinson et al. (2009).

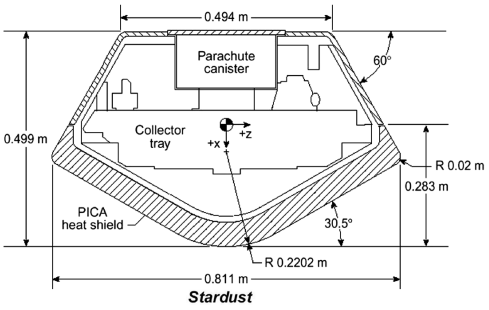

Figure 2.10: Geometry of the Stardust return capsule. Boyd et al. (2010).

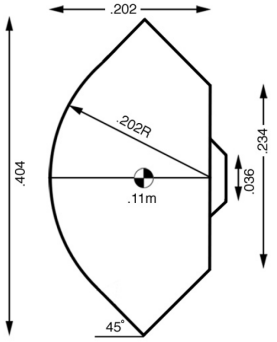

Figure 2.11: Geometry of the Hayabusa return capsule. All measurements are given in meters. Davies and Arcadi (2006).

capsule is a 81.1 cm diameter capsule with a blunt 60° half angle sphere-cone nose for the forebody heatshield and a 30° truncated afterbody cone. The capsule weighed a total of 45.6 kg and is 49.9 cm deep. A schematic cross-section of the Stardust capsule is shown in Fig. 2.10. As reported by Grindstead et al. (2011), the Hayabusa sample return capsule is a 40 cm diameter capsule with a blunt 45° half angle sphere-cone noes for the forebody heatshield, and a 45° truncated cone afterbody. The entire capsule was 20 cm deep and weighed 16.3 kg. A schematic cross-section of the Hayabusa capsule is shown in Fig. 2.10. From the description and the illustrations it can be seen that both of these vehicles differ significantly from the Apollo CM in both shape and size. Regardless of this, a scaled version of the Apollo CM was used for the analysis of the SRM. The main reason for this is that the search for aerodynamic models for these vehicles proved unfruitful. Since excellent resources for the Apollo CM were already obtained, it was decided to scale down the Apollo CM to the size of the capsule proposed in the above discussed MSR mission. The diameter of this capsule was 0.75 m. This falls between the diameter of Stardust of 0.81 m and Hayabusa of 0.40 m. This is roughly 19% of the size of the Apollo capsule. Using the diameter of 0.75 m, an aerodynamic reference area of 1.76 m^2 is found. Preserving the ratio between the nose radius and the diameter results in a nose radius of 0.9 m. If a linear relation between the volume and the mass of the capsule is assumed (assuming the density of the capsule to be homogeneous), and the volume of the capsule is approximated by a cone with a base equal to the diameter and height equal to the nose radius, a nominal mass for the SRM vehicle of 38.77 kg is found. This is slightly heavier than both the discussed MSR and Hayabusa vehicle, but less than the Stardust capsule. A table containing the diameter, nose radius, and mass values for both the SRM and CRM vehicles is provided in Table 2.4.

Table 2.4: Nominal values for the physical properties of the CRM and SRM entry vehicles. Both vehicle designs are shaped like the Apollo CM depicted in Fig. 2.9.

Mission	Diameter [m]	Aerodynamic Reference Area [m^2]	Nose Radius [m]	Mass [kg]
CRM	3.9116	12.017	4.694	5500
SRM	0.75	0.441	0.90	38.77

2.6.2. Crew Return Vehicle Requirements

While performing any entry, requirements are put on the trajectory to ensure the safe passage of the vehicle and its contents. Since the vehicle for the manned mission is based on the Apollo CM, it is logical to also take the requirements imposed on this vehicle. The two requirements that were considered throughout this research are the peak mechanical load factor and the peak heat flux. From Pavlosky and Leger (1974), it was found that the design requirements for the maximum heat flux on the Apollo CM was 700 $Btu.ft^{-2}s^{-1}$, or 7.95 MWm^{-2}. For the maximum mechanical load factor, the work by Graves and harpold (1972) was consulted. In this work a maximum aerodynamic load factor of 12g is stated for the Apollo Entry. Whether this value was driven by mechanical failure or the human-rating of the spacecraft was not mentioned. However, after finding the values for the mechanical load imposed on the SRM vehicles, and consulting NASA (2010), it was concluded that the 12g mechanical load limit was driven by the fact that the vehicle was intended to ferry humans on board.

2.6.3. Sample Return Vehicle Requirements

While the design and the aerodynamic model for the SRM vehicle is based on the Apollo CM, it was decided to compromise the requirements for the peak heat load and the peak acceleration more in line with those of other sample return missions. According to Willcockson (1999), the peak load factor allowable for the Stardust capsule was 40g, and the peak heat flux was 11 MWm^{-2}. Cassel et al. (2011) states similar values for Hayabusa, namely a peak deceleration of 49g, and a peak heat flux of 11.12 MWm^{-2}. In the proposal for the Rosetta mission, Serrano-Martinez and Hechler (1989) states a peak mechanical load factor of 20g. Since the vehicle itself is still based on the Apollo CM, and theoretically would use the same TPS, the value for the peak heat flux was taken to be the same as that for the CRM. For the value of the peak load factor, the most driving value, namely 20g from Rosetta, was chosen.

2.7. Requirements Overview

In the previous two sections the requirements imposed on the trajectory due to either a desired accuracy or vehicle limitations were discussed. Based on these discussions, a set of formal requirements were formulated. Each of these requirements is given a unique designation that will be used to refer back to it where needed later in this report.

The first two set of requirements is obtained from Section 2.5. The first set deals with the requirements for the interplanetary guidance, navigation, and control subsystem, regarding the nominal entry interface state, and the required accuracy of this state:

- **[GNC-Earth-01]** For an Earth-based mission, the interplanetary flight guidance, navigation, and control subsystem shall ensure a relative velocity of 11.5 kms^{-1} at 125 km altitude with perfect accuracy
- **[GNC-Earth-02]** For an Earth-based mission, the interplanetary flight guidance, navigation, and control subsystem shall ensure a relative flight-path angle of -7.4° at 125 km altitude with perfect accuracy
- **[GNC-Mars-01]** For a Mars-based mission, the interplanetary flight guidance, navigation, and control subsystem shall ensure a relative velocity of 8.2 kms^{-1} at 125 km altitude with perfect accuracy
- **[GNC-Mars-02]** For a Mars-based mission, the interplanetary flight guidance, navigation, and control subsystem shall ensure a relative flight-path angle of -11.5° at 125 km altitude with perfect accuracy
- **[GNC-Venus-01]** For a Venus-based mission, the interplanetary flight guidance, navigation, and control subsystem shall ensure a relative velocity of 11.25 kms^{-1} at 125 km altitude with perfect accuracy
- **[GNC-Venus-02]** For a Venus-based mission, the interplanetary flight guidance, navigation, and control subsystem shall ensure a relative flight-path angle of -6.1° at 125 km altitude with perfect accuracy

The second set of requirements deals with the guidance, navigation, and control subsystem during atmospheric flight. These requirements regard the accuracy of the state provided to the guidance system, the accuracy with which the target is reached, and the accuracy and speed with which the commanded bank angle is set:

- **[NAV-01]** The atmospheric flight navigation subsystem shall provide the current vehicle position to the guidance subsystem with perfect accuracy.
- **[NAV-02]** The atmospheric flight navigation subsystem shall provide the current vehicle attitude to the guidance subsystem with perfect accuracy
- **[GUID-01]** The ΔV manoeuvre needed to reach the desired apoapsis after the aerocapture manoeuvre shall not exceed 5% of the ΔV required for circularisation.
- **[GUID-02]** The wedge angle between the final and target orbit shall be less than 0.05°.
- **[CTRL-01]** The atmospheric flight control subsystem shall set the bank angle as commanded by the guidance system with perfect accuracy.
- **[CTRL-02]** The atmospheric flight control subsystem shall change the bank angle instantaneously.

The final two sets were obtained from Section 2.6. The first of these sets deals with the requirements imposed on the physical vehicle itself, on the weight, and the loads it and its subsystems have to be able to withstand:

- **[CRM-MASS-01]** The crew return vehicle shall have a mass of 5500 kg at an altitude of 125 km.
- **[CRM-MECH-01]** The crew return vehicle shall be able to withstand a load factor of 12g.
- **[CRM-TPS-01]** The thermal protection system of the crew return vehicle shall be able to withstand a heat flux of 7.95 MWm^{-2}.
- **[SRM-MASS-01]** The sample return vehicle shall have a mass of 38.77 kg at an altitude of 125 km.
- **[SRM-MECH-01]** The sample return vehicle shall be able to withstand a load factor of 20g.
- **[SRM-TPS-01]** The thermal protection system of the sample return vehicle shall be able to withstand a heat flux of 7.95 MWm^{-2}.

The last set deals with requirements on the trajectory due to vehicle constraints, such as the mechanical load factor and the heat flux. These requirements are similar to those in the previous set, expect in the context of the trajectory instead of the vehicle.

- **[TRJ-01]** The trajectory shall induce have a peak heat flux smaller than 7.95 MWm^{-2}.
- **[TRJ-CRM-01]** For the crew return vehicle, the trajectory shall induce have a maximum load factor smaller than 12g.
- **[TRJ-SRM-01]** For the sample return vehicle, the trajectory shall induce have a maximum load factor smaller than 20g.

3

Flight Dynamics

A stated in Section 1.1, the goal of this research is to study aerocapture trajectories about various planets and the potential benefits they can offer. To study these trajectories, the equations governing the motion of the vehicle and the dynamics involved during the flight need to be understood. This chapter serves the purpose of provided the needed background into the flight dynamics, and provides the exact models and equations used in the simulation of the motion of the vehicle and study of the trajectories.

As the goal of the research is only to study the trajectories, only the translational motion of the centre-of-mass of the vehicle is of interest. As such, the change in attitude of the vehicle during the flight can be ignored. This results in a three-degree-of-freedom (3dof) simulation. Only the motion in three directions needs to be considered, and thus only the equations governing the motion in these directions are needed. The equations governing the motion are aptly named the equations of motion, and can be defined in any coordinate system.

To evaluate the equations of motion, the forces that act on the body need to be known. The effected motion depends on both the attitude and the magnitude of the force. Therefore both need to be defined. The attitude of the force can be defined as acting along an axis in a particular reference frame. By subsequently defining the attitude of this reference frame with the reference frame of the motion, the attitude of the force is known. To express the attitude of one frame with respect to another, a set of angles is required. The magnitude of the forces depend on the current state of the vehicle, such as the altitude and velocity, and the environment in which the vehicle is located.

In this chapter all the above stated items will be considered. First, in Section 3.1, the various reference frames that are used in this research to define the motion and the forces are discussed. Following this, in Section 3.2 the definition of the angles used the express the attitude between two frames, and the static transformation to go from one frame to another is presented. Then the state variables, the set of variables that fully define the current state of the vehicle are established in Section 3.3, and the equations of motion that define the motion of the vehicle according the the current state are presented in Section 3.4. In Section 3.5 the spherical equations of motion are approximated using first- and second-order analytical expressions. Lastly, in Section 3.6, the environment that effects the forces based on the current state is described. Both the numerical or mathematical models that are used to model the environment and the equations that need to be applied to determine the force resulting from the interaction between the vehicle and the environment are discussed.

3.1. Reference Frames

Reference frames are used to define the origin and direction of vectors. Vectors are used to represent amongst others, forces, positions, velocities, and rotational axes. The reference frames required to be defined depends on the vectors required to be expressed. For this research the vectors required to be expressed are the position and velocity of the vehicle, and the gravitational and aerodynamic forces acting on the vehicle. All reference frames described here are right-handed reference frames, and often only two of the three axes will be described in detail with the third complementing these two. The system descriptions discussed here were taken from Mooij (1994) unless state otherwise.

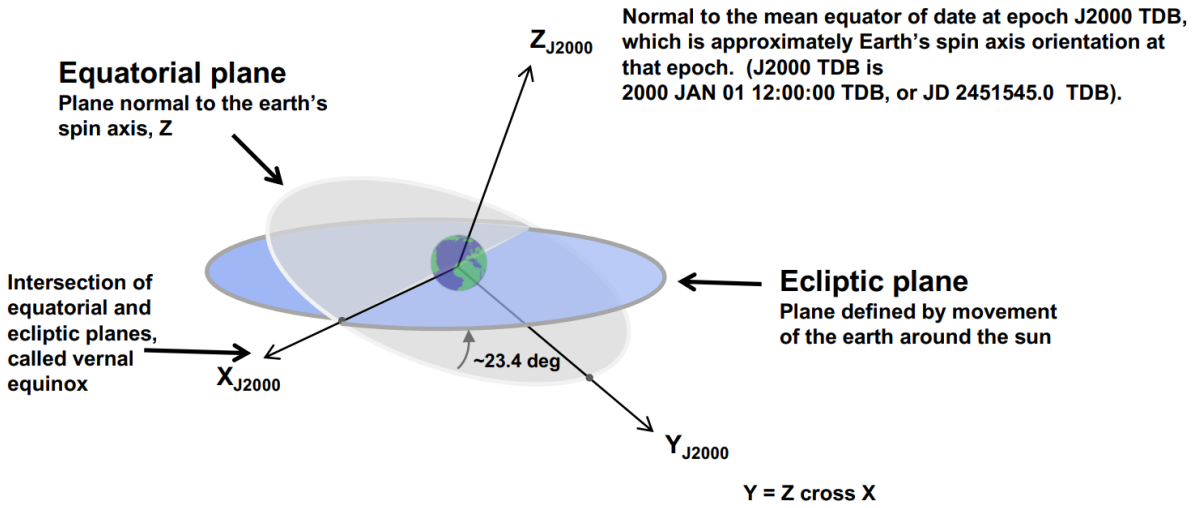

Figure 3.1: Illustration of the J2000 Inertial Planetocentric reference frame.

Inertial Planetocentric Reference Frame (Index I, $OX_IY_IZ_I$) The origin of this reference frame is located in the centre of mass of the central body. The OX_IY_I-plane coincides with the equatorial plane, and the Z_I-axis is aligned with the rotational axis of the central body. The X_I-direction is determined by a reference meridian at zero time. This reference frame therefore does not rotate together with the central body. Throughout this research the J2000 frame definition will be used to define the direction of the X_I-axis for Earth. In the J2000 frame, the X_I-axis is determine by the intersection of the equatorial and ecliptic plane, and the zero time is January 01, 2000 12:00:00 Barycentric Dynamical Time (TDB from the French Temps Dynamique Barycentrique)[1]. An illustration of the J2000 reference frame is provided in Fig. 3.1. For the planets Mars and Venus analogous definitions were used to define the X_I-axis and the Z_I-axis is defined the same.

Contrary to the name of this reference frame, it is actually a pseudo-inertial reference frame. Wakker (2015) defines and inertial reference frame as follows: "An inertial reference frame is a reference frame with respect to which a particle remains at rest or in uniform rectilinear motion if no resultant force acts upon that praticle". In other words, inertial reference frames are all frames that perform constant rectilinear motion and experience no rotational motion. In reality, the selected origin of this reference frame, the centre of the central body, does not experience constant rectilinear motion as it is in orbit about the centre of mass of the Solar System, which is in turn in orbit around the centre of mass of the Milky Way galaxy, etcetera. Therefore a particle also does not experiences uniform rectilinear motion with respect to this reference frame if no other force was acting upon it.

However, due to the close proximity of the vehicle to the central body and the relatively short duration of the manoeuvres considered (relative to the orbital period of the central bodies), the centre of the central body is assumed to be stationary, and therefore a pseudo-inertial reference frame can be attached to it. For the purpose of this research, there exists no difference between a true inertial and pseudo-inertial reference frame. Therefore, hereinafter, the pseudo-prefix will be omitted. Another illustration of this reference frame is provided in Fig. 3.2 together with the rotating and vertical reference frames.

Rotating Planetocentric Reference Frame (Index R, $OX_RY_RZ_R$) This reference frame is fixed to the centre of mass of the central body and is chosen to coincide with the inertial planetocentric reference frame at zero time. This reference frames co-rotates with the central body about the Z_R-axis, keeping the X_R-axis aligned with its initial longitude. The importance of this frame stems from the fact that the atmosphere of the central body is assumed to co-rotate with it, and the motion of the vehicle is expressed relative to this rotating atmosphere. This reference frame is illustrated in Fig. 3.2 together with the inertial reference frame and vertical reference frame.

[1] NAIF, "An Overview of Reference Frames and Coordinate Systems in the SPICE Context", January 2018. Available from `https://naif.jpl.nasa.gov/pub/naif/toolkit_docs/Tutorials/pdf/individual_docs/17_frames_and_coordinate_systems.pdf`

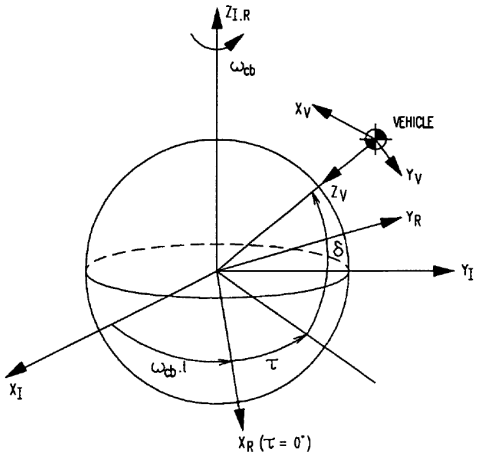

Figure 3.2: Illustration of the inertial, rotating, and vertical reference frames, together with the angles used in the transformations. Mooij (1994).

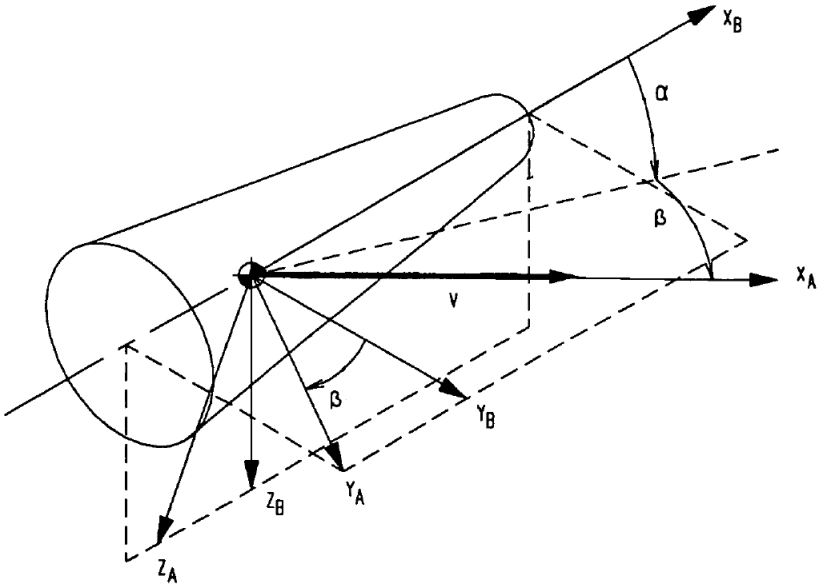

Figure 3.3: Illustration of the body fixed and aerodynamic reference frames. Mooij (1994).

Vertical Reference Frame, (Index V, $\mathbf{OX_VY_VZ_V}$) This reference frame is fixed to the centre of mass of the vehicle. The Z_V-axis pointed towards the centre of mass of the central body. The X_V-axis is parallel to the meridian and due north. Together with the the Y_V-axis, the OX_VY_V-plane forms the local horizontal plane. This frame is important as it serve as a link between the rotating reference frame and the body fixed reference frames. This reference frame is illustrated in Fig. 3.2 together with the inertial reference frame and rotating reference frame and in Fig. 3.4 together with the trajectory reference frame.

Body Fixed Reference Frame (Index B, $\mathbf{OX_BY_BZ_B}$) This reference frame is fixed to the centre of mass of the vehicle. The X_B-axis falls in the plane of symmetry of the vehicle and is defined positive forwards (towards the nose of the vehicle, similar to an aircraft). The Z_B axis is also located in the symmetry plane and is defined positive "downward". For capsule-like vehicles performing aerodynamic entry the attitude of the vehicle is usually reversed, entering with its rear first, where the thermal protection system (TPS) is located. In this case, the X_B-axis is still towards the nose of the vehicle (now aimed away from the central body). As a consequence of this the Z_B-axis is now pointing "upward". This reference frame is important as it allows for the definition of the three aerodynamic attitude angles. This reference frame is illustrated in Fig. 3.3 together with both the aerodynamic reference frame and in Fig. 3.5 together with the trajectory and aerodynamic reference frames.

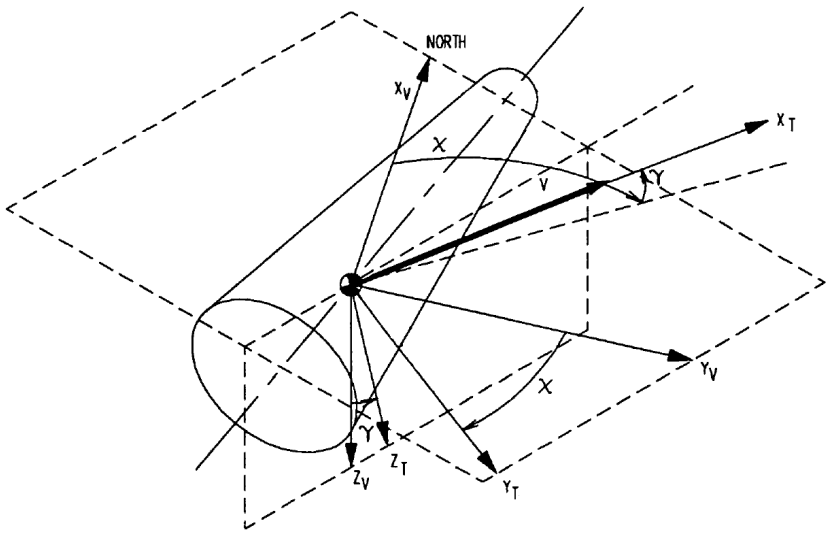

Figure 3.4: Illustration of the trajectory and vertical reference frames. Mooij (1994).

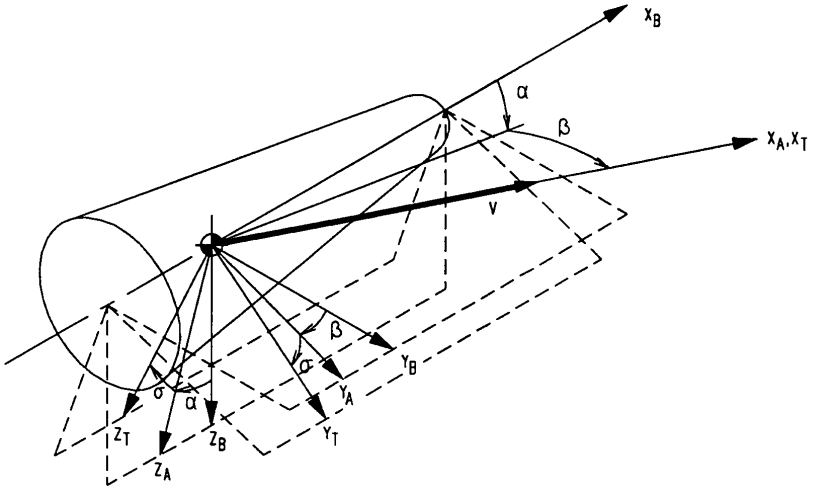

Figure 3.5: Illustration of the trajectory, aerodynamic, and body fixed reference frames. Mooij (1994).

Trajectory Reference Frame (Index T, $\mathbf{OX}_T\mathbf{Y}_T\mathbf{Z}_T$) This reference frame is fixed to the centre of mass of the vehicle. The X_T- axis is defined positive along the velocity vector of the vehicle relative to the atmosphere. Therefore the velocity expressed in this reference frame is the relative velocity, not the inertial velocity. The Z_T-axis is located in the vertical plane, pointing "downwards". The main use for this reference frame is the definition of the flight-path angle (FPA), and the heading, relative to the rotating atmosphere. Additionally, it provides a frame with respect to which the bank angle can be defined. This reference frame is illustrated in Fig. 3.4 together with the vertical reference frame and in Fig. 3.5 together with the body and aerodynamic reference frame. The definition of the flight-path, heading, and bank angles is also present in these figures, and will be further discussed in Section 3.2.

Aerodynamic Reference Frame (Index A, $\mathbf{OX}_A\mathbf{Y}_A\mathbf{Z}_A$) This reference frame is fixed to the centre of mass of the vehicle. The X_A-axis is defined along the velocity vector of the vehicle relative to the atmosphere. Therefore the velocity expressed in this reference frame is again the relative velocity, not the inertial velocity. The Z_A-axis is collinear with the aerodynamic lift force, but in opposite direction. This reference frame defines each of the three main aerodynamic forces and has an axis is opposite direction of the force, as drag is always opposite direction of velocity. The T-frame and A-frame coincide when the vehicle is not banking. This reference frame is illustrated in Fig. 3.3 together with the body fixed reference frame and in Fig. 3.5 together with the body and trajectory reference frames.

3.2. Frame Transformations

Frame transformations are used to transform a vector expression from one frame to an expression in another frame. The main purpose of establishing frame transformations is to obtain the force vectors in the reference frame with respect to which the vehicle's motion is simulated. For the purpose of expressing the attitude of one frame with respect to another the Euler angles were used. The information presented next regarding the Euler angles was obtained from Diebel (2006), unless stated otherwise.

3.2.1. Euler Angles

The orientation of any frame with respect to another can be described by at most three angles. By describing these angles in a particular way, one can describe the transformation from any frame to another by first rotating about one of the three axes of the original frame, followed by a second and, if necessary, third rotation about one of the axes of the intermediate frames. The angles which are used for each of these rotations are the so-called Euler angles. Since each of the rotations is performed about one of the three axes of a Cartesian reference frames, one can define unit rotation matrices that describe the effect of a single rotation about a single axis. The three unit rotation matrices for rotations about the X-, Y-, and Z-axes, respectively, are defined as followed:

$$\mathbf{R}_X(\alpha_1) = \begin{bmatrix} 1 & 0 & 0 \\ 0 & \cos\alpha_1 & \sin\alpha_1 \\ 0 & -\sin\alpha_1 & \cos\alpha_1 \end{bmatrix} \tag{3.1}$$

$$\mathbf{R}_Y(\alpha_2) = \begin{bmatrix} \cos\alpha_2 & 0 & -\sin\alpha_2 \\ 0 & 1 & 0 \\ \sin\alpha_2 & 0 & \cos\alpha_2 \end{bmatrix} \tag{3.2}$$

$$\mathbf{R}_Z(\alpha_3) = \begin{bmatrix} \cos\alpha_3 & \sin\alpha_3 & 0 \\ -\sin\alpha_3 & \cos\alpha_3 & 0 \\ 0 & 0 & 1 \end{bmatrix} \tag{3.3}$$

Here the angles α_1, α_2, and α_3 are the Euler angles. By multiplying the matrices required for a particular transformation, one obtains the corresponding transformation matrix. According the Wertz (1978), there are a total of 12 unique matrix multiplication sequences to represent the three rotations . Six sequences, where each rotation is about a different axis, are the so called type-1, or asymmetrical, rotations. The remaining six, where the first and last rotation are about the same axis, are the so called type-2 or symmetrical, rotations.

Singla et al. (2005) states that, according to Euler's Rotation Theorem (Euler, 1775), Euler angles, and all other parametrisations that use three values to describe the attitude, suffer from singularities. Singularities occur when it is attempted to determine the attitude of the vehicle with respect to the some reference frame, and there are an infinite number of rotations possible to express the rotation. This can cause an error between the actual and commanded values for the rotation. For Euler angles these singularities occur when the second rotation aligns the first and third rotational axis. For the asymmetrical type-1 rotations this occurs when the second rotation is ±90°, and for the symmetrical type-2 rotation this occurs when the second rotation is 0° or 180°.

Singularities primarily pose a problem for spacecraft attitude determination and control. In this research however, they do not pose a problem, as the attitude of the vehicle will not be determined and changed through rotations, but is set based on a model in the case of the angle of attack and angle of side-slip, or commanded to achieve lift modulation in the case of the bank angle.

If one desires to reverse the rotation, the order of the rotations and the sign of each of the Euler angles must be flipped. Alternatively, one can take the transpose of the resulting transformation matrix. The notation for a rotation from the **A** frame to the **B** frame requiring rotations about the Z-, Y-, and X-axes, in that order, with the Euler angles α_3, α_2, and α_1, respectively, can be written as:

$$\mathbf{B} = \mathbf{R}_X(\alpha_1)\mathbf{R}_Y(\alpha_2)\mathbf{R}_Z(\alpha_3)\mathbf{A} = \mathbf{C}_{B,A}\mathbf{A} \tag{3.4}$$

Where $\mathbf{C}_{B,A}$ represents the transformation matrix for the rotation going from the **A** frame to the **B** frame. Using this transformation matrix, it is now possible to transform a vector defined in the **A** frame, $\mathbf{r}_A$, into the vector $\mathbf{r}_B$, defined in the **B** frame using $\mathbf{r}_B = \mathbf{C}_{B,A}\mathbf{r}_A$.

3.2.2. Static Transformations

Using the Euler angles to express the orientation of one reference frame with another, the required transformations between the frames discussed in Section 3.1 can be formulated. Unless specified otherwise, the transformation matrices obtained here based on the work of Mooij (1994) and Mooij (2017).

Rotating Planetocentric to Inertial Planetocentric, $\mathbf{C}_{I,R}$ As stated in the description of the R frame, the R- and I-frame are chosen to coincide at time zero. The rotating frame rotates with the central body about the Z_R-axis, which was the defined to coincide with the rotational axis of the central body, with the same angular motion of the central body. Therefore the only rotation required to go from the R- to the I-frame is a rotation about the Z_R-axis with an angle equal to the negative angle rotated since the start of the simulation. This angle is equal to $-\omega_{cb}t$. The transformation matrix therefore becomes:

$$\mathbf{C}_{I,R} = |_I\mathbf{R}_Z(-\omega_{cb}t)|_R \tag{3.5}$$

Here t represents the arbitrary time since the start of the simulation at which the two frames coincided, ω_{cb} is the angular velocity of the central body, and $\mathbf{R}$ is the same unit rotation matrix as was presented in the discussion of the Euler angles in Section 3.2.1. The frames and angles used for this transformation are illustrated in Fig. 3.2 together with the angles used to express the attitude of the vertical frame with respect to the rotating reference frame, which is discussed next.

Vertical to Rotating Planetocentric, $\mathbf{C}_{R,V}$ As stated in the description of the V-frame, the Z_V-axis is pointed towards the CoM of the central body, and the X_V-axis is parallel to the local meridian due North. By first rotating about the Y_V-axis with an angle equal to the planetocentric latitude δ, the OY_VZ_V-plane is parallel to the OX_RY_R-plane, and the X_V axis is parallel to the Z_R-axis. Rotating an additional 90° or $\frac{\pi}{2}$ radians about the Y_V-axis, the OX_VY_V-plane is parallel to the OX_RY_R-plane, and the Z_V axis is parallel to the Z_R-axis All that remains to be done now is to rotate about the $Z_{V'}$-axis with an angle equal to the negative planetocentric longitude $-\tau$. In unit rotation matrix form this equation can be represented by:

$$\mathbf{C}_{R,V} = |_R\mathbf{R}_Z(-\tau)|_{V'}\mathbf{R}_Y(\frac{\pi}{2}+\delta)|_V \tag{3.6}$$

Trajectory to Vertical, $\mathbf{C}_{V,T}$ To go from the trajectory to that vertical frame the Flight-Path Angle (FPA, γ) and heading angle (χ) are used. Since the definition of these angles is the same for both the airspeed- and groundspeed-based reference frames, they will both be treated simultaneously. In this they will both be represented by a single shared index T. The FPA is the angle between the velocity vector and the local horizontal plane. This angle is defined positive when the velocity has a component along the radial position vector away from the central body (In other words, when the velocity is pointed away from the central body). The heading is the angle between the projection of the velocity on the local horizontal plane and the X_V-axis, which indicates the "northward" direction. An illustration of this is provided in Fig. 3.4. One can go from the T-frame to the V frame by first rotating about the Y_T-axis with the negative FPA, and subsequently about the $Z_{T'}$ with the negative heading angle.

$$\mathbf{C}_{V,T} = |_V\mathbf{R}_Z(-\chi)|_{T'}\mathbf{R}_Y(-\gamma)|_T \tag{3.7}$$

Aerodynamic to Trajectory, $\mathbf{C}_{T,A}$ Similar to the previous case, again both groundspeed and airspeed will be treated simultaneously under a single index A. As explained in the definition of the aerodynamic frames, they only differ from the trajectory frames when the vehicle is banking. The bank angle, σ, is defined as the angle between the Z_T- and Z_A-axis. As a reminded, the Z_T-axis is located in the local vertical plane, and the Z_A-axis is in direction opposite of the lift vector. The bank angle can therefore be defined as the angle between the lift vector and the local vertical. To go from the aerodynamic to the trajectory frame only a single rotation about the X_A-axis equal to the bank angle. An illustration of this is provided in Fig. 3.5. In matrix form rotation matrix form:

$$\mathbf{C}_{T,A} = |_T\mathbf{R}_X(\sigma)|_A \tag{3.8}$$

Body to Aerodynamic, $\mathbf{C}_{A,B}$ With the transformation from the body the the aerodynamic frame the last two aerodynamic angles are introduced. The first of these is the angle of attack, α. The second is the angle of side-slip, β. Again, both of these angle are different for the airspeed and groundspeed, but will be treated here as one as their definition remains the same. These two angles are illustrated in both Fig. 3.5 and Fig. 3.3. Note that in the configuration depicted in these figures the angle of attack is closer to 0° than to 180°. During entry this angle would be closer to 180° to have the TPS forward.

$$\mathbf{C}_{A,B} = |_A\mathbf{R}_Z(\beta)|_{B'}\mathbf{R}_Y(\alpha)|_B \tag{3.9}$$

However, due to the 3dof simulation the angle of side-slip is 0°, which reduces the above equation to:

$$\mathbf{C}_{A,B} = |_A\mathbf{R}_Y(-\alpha)|_B \tag{3.10}$$

3.3. State Variables

With the reference frames and frame transformations defined, the state variables that are used to describe the position and velocity of the vehicle during the simulation are discussed. As stated at the start of this chapter, only a 3dof simulation will be performed, so the entire vehicle state can be described by its position and velocity.

3.3.1. Available State Variable Sets

Three well-established methods for describing the vehicle state, that can be found in almost any literature regarding astrodynamics such as Wakker (2015), are the Cartesian, Keplerian, and spherical components. A fourth, more novel, parameter set is the unified state model (USM) originally proposed by Altman (1972), reinvigorated by Vittaldev (2010), and recently investigated by Facchinelli (2019).

The claimed benefit of the USM is that it has better accuracy compared to Cartesian integration. This was, however, drawn into question based on the work by Facchinelli (2019). Facchinelli (2019) compared the accuracy and computation time of integrating Cartesian coordinates using an RKF5(6) method and the USM for various cases, including aerocapture. In this particular case the conclusion could be drawn that for sufficiently high tolerances, resulting in small step-sizes, the accuracy of the Cartesian coordinate integration surpasses that of the USM. Facchinelli (2019) draws the same conclusion stating that for a step-size smaller than 1s, the accuracy benefit of USM becomes negligible, and the additional complexity (resulting in additional computational time) make the USM less desireable.

Furthermore the error of the USM plateaus, whereas that of the Cartesian integration kept reducing, meaning that certain level of accuracy were not attainable by the USM. Additionally, instead of a single-step method such as the Runge-Kutta family of numerical integrators, a multi-step method could be used to decrease the computational time. However, the comparison between a multi-step method and the USM was not made. As will be discussed in Section 4.3, using a linear multi-step method with fixed step size was found to increase the computational time by a factor 3 compared to RKF4(5), and a factor 6 for RKF7(8).

The decisive argument against the use of the USM is that it requires the use of more complex parameters than Euler angles to describe the attitude of the vehicle. In the works by Vittaldev (2010) and Facchinelli (2019), three versions are proposed, using quaternions, modified Rodrigues parameters, or exponential modeling. Combining the increased complexity with the fact that a certain level of accuracy is unobtainable if desired lead to the decision to not use the USM model for the integration.

Another possibility for the simulation parameter set are the spherical components. In the work by **?**, it is shown that using Taylor series integration is faster at simulating reentry problems than integrating the Cartesian state variables using RKF5(6). In this work, for a tolerance of $1 \cdot 10^{-8}$, a computational time decrease of a factor 3.28 was found. However, the same comment can be made as before. A multi-step method can significantly decrease the computational time of the Cartesian integration. The decisive reason against using Taylor series integration is again the required complexity of the method compared to Cartesian integration, as for every desired modification made to the environment, new equations of motion have to be established.

The three parameter sets that are used, together with their purpose and reason for selection are:

- **Cartesian components:** used to simulate the trajectory. This parameter set is chosen as the equations of motion using these variables are very modular by allowing the fast removal or addition of terms without affecting other parts of the equations. This modularity makes the software very flexible.

- **Spherical components:** used for post-processing of the simulated trajectories. This parameter set is very intuitive which makes them idea for analysis and visualisation of the orbit.

- **Keplerian components:** used for the definition of the target orbit, and for determining the ΔV after the aerocapture manoeuvre.

In the next three subsections each of these three parameter sets is discussed in more detail, providing the definition and the method to convert between the various sets.

3.3.2. Cartesian Components

The Cartesian components define the position and velocity vector in three-dimensional space using three components for each vector, each component aligned with one axis in the Cartesian coordinate system. The position of the vehicle is defined by the x, y, and z, components. The velocity is expressed as the time rates of change of the positional component along each axis, or the derivative of position. Similarly, in the state derivative, the acceleration is not written as components of acceleration, nor as time rates of change of the velocity components, but as time rates of change of time rates of change of the positional component along each axis, or, simply, the second-derivative of position. The state and state derivative are thus define as:

$$\mathbf{x} = \left(x, y, z, \dot{x}, \dot{y}, \dot{z}\right)^T \tag{3.11}$$

$$\dot{\mathbf{x}} = \left(\dot{x}, \dot{y}, \dot{z}, \ddot{x}, \ddot{y}, \ddot{z}\right)^T \tag{3.12}$$

3.3.3. Spherical Components

In the spherical state variables the position and velocity are defined in the form of two vectors. The positional vector has a magnitude r and is defined as the distance between the centres of mass of the vehicle and the central body. The direction of the position vector is defined by the two angles, the latitude, δ, and longitude, τ. The latitude angle is defined with along a great-arc with respect to the equatorial plane of the central body, positive on the Northern hemisphere. The longitude is defined with respect to a reference meridian, positive Eastward. The velocity is similarly defined by a magnitude (V) and two angles (FPA, γ, and the heading χ, both of which have been defined in Section 3.2). The state derivative in spherical components is simply the derivative of each of the six components. The vehicle state and state derivative in spherical components are:

$$\mathbf{x} = \left(r, \tau, \delta, V, \chi, \gamma\right)^T \tag{3.13}$$

$$\dot{\mathbf{x}} = \left(\dot{r}, \dot{\tau}, \dot{\delta}, \dot{V}, \dot{\chi}, \dot{\gamma}\right)^T \tag{3.14}$$

The transformation between the Cartesian and spherical positional parameters can be done using the following equations:

$$r = \sqrt{x^2 + y^2 + z^2} \tag{3.15}$$

$$\tau = \text{atan2}(y, x) \tag{3.16}$$

$$\delta = \text{atan2}(z, \sqrt{x^2 + y^2}) \tag{3.17}$$

The transformation between the Cartesian and spherical velocity parameters can be done is almost the exact same way:

$$V = \sqrt{\dot{x}^2 + \dot{y}^2 + \dot{z}^2} \tag{3.18}$$

$$\chi = \text{atan2}(\dot{y}, \dot{x}) \tag{3.19}$$

$$\gamma = -\text{atan2}(\dot{z}, \sqrt{\dot{x}^2 + \dot{y}^2}) \tag{3.20}$$

3.3.4. Keplerian Elements

The Keplerian components use five components to describe the size, shape, and orientation of the orbit, and a sixth component to define the position of the vehicle within the orbit. The five Keplerian elements describing the size, shape, and orientation are the semi-major axis (a), the eccentricity (e), the inclination (i), the right-ascension (or longitude) of the ascending node (Ω), and the argument of periapsis (ω). The element describing the position of the vehicle is the true anomaly (θ).

The semi-major axis defines the size of the orbit and is defined as the mean value of the periapsis and apoapsis distance. The eccentricity defines the shape of the orbit. The inclination defines the tilt of the orbital plane with respect to a reference plane (generally the rotational plane of the central body). The right-ascension defines the rotation of the orbital plane with respect to a reference direction. The argument of periapsis defines the rotation of the orbit within the orbital plane, defined as the angle between the ascending node and the periapsis. The true anomaly is the position of the orbiting body in the orbit, defined as the angle from the argument of periapsis.

The Keplerian elements are used to determine if requirements **GUID-01** and **GUID-02** are met at the atmospheric exit. Using the semi-major axis and the eccentricity, the apoapsis and periapsis radii after atmospheric exit can be determined. From here the required ΔV to correct and circularise the orbit is determined. The difference between the target and final inclination can also be determined. The remaining three elements that specify the orientation and vehicle position were not used in this research.

The semi-major axis can be computed by using

$$a = \frac{r}{2 - \frac{rV^2}{\mu}} \tag{3.21}$$

where the spherical radial position r and velocity V can be computed using Eq. (3.15) and Eq. (3.18) respectively. The flight-path angle can either be computed using Eq. (3.20) or

$$\gamma = \arcsin \frac{x\dot{x} + y\dot{y} + z\dot{z}}{rV} \tag{3.22}$$

Since -90°$\leq \gamma \leq$90°, this last equation defines the flight-path angle unambiguously.

With the semi-major axis, radial position, and flight-path angle known, the eccentricity can be determined using either

$$e^2 = 1 - \frac{rV^2}{\mu}\left(2 - \frac{rV^2}{\mu}\right)\cos^2\gamma \tag{3.23}$$

or by solving the following two equations simultaneously for the eccentricity and eccentric anomaly (E).

$$e\cos E = 1 - \frac{r}{a} \tag{3.24}$$

$$e\sin E = \sqrt{\frac{1}{\mu a}}(x\dot{x} + y\dot{y} + z\dot{z}) \tag{3.25}$$

To determine the inclination, first the angular momentum is required. The angular momentum can either be determined straight from the spherical components using

$$H = \sqrt{\mu a(1 - e^2)} \tag{3.26}$$

or by determining the three individual components using the Cartesian components using

$$\begin{aligned} H_x &= x\dot{y} - y\dot{x} \\ H_y &= x\dot{z} - z\dot{x} \\ H_z &= y\dot{z} - z\dot{y} \\ H &= \sqrt{H_x^2 + H_y^2 + H_z^2} \end{aligned} \tag{3.27}$$

Using the angular momentum, finally the inclination can be determined using

$$i = \arccos\left(\frac{x\dot{y} - y\dot{x}}{H}\right) \tag{3.28}$$

from which the inclination can be determined unambiguously as per definition 0°$\leq i \leq$180°.

3.4. Equations of Motion

In this section the equations of motion that are integrated to simulate the motion of the vehicle will be defined. In the simulation environment these equations are integrated in the inertial planetocentric reference frame using Cartesian coordinates. Since motion of a physical (massive) body is dealt with, both kinematics and dynamics are of importance to the derivation of the equations of motion. Dynamics treats the motion of a vehicle due to forces acting on it and the connection between these forces and the velocity of the vehicle. Kinematics provides information regarding the position and attitude of a vehicle based on these velocities. In addition to the formation used in the numerical simulation, a simpler formulation of the equations of motion is also desired to be approximated in the analytical approach. For this, simplified equations of motion will be described in a rotating planetocentric reference frame using spherical coordinates.

3.4.1. Fundamentals

The first to describe (or, at least popularise) the relation between forces acting on a body, and the resultant motion of the body, was Newton. Therefore the study of the interaction between forces, massive bodies, and their motion is referred to as classical, or Newtonian mechanics. Newton's Laws of Motion are well known and often repeated, and will thus not all be reproduced here. Newton's second law of motion relates the change in momentum of a vehicle to the forces acting on the vehicle according to:

$$\mathbf{F} = \frac{d\mathbf{p}}{dt} = \frac{d(m\mathbf{v})}{dt} = \frac{m d\mathbf{v}}{dt} + \frac{\mathbf{v} dm}{dt} \tag{3.29}$$

where $\mathbf{p}$ represent the momentum, the product of mass and velocity.

In this research the vehicle was assumed to not use any propulsion, and thus no propellant, during atmospheric flight. Therefore the vehicle is considered a constant-mass vehicle, allowing for the second term in the right-hand side of the above equation to be omitted. In reality, the vehicle considered might not have a constant mass due to the potential usage of an ablative TPS that losses mass as material is ablated ("burned-up") throughout the entry. However, the effect on the motion of the vehicle due to the loss of mass of an ablative TPS is insignificant compared to the aerodynamic forces acting on the vehicle. By removing the variable mass term, and rewriting the change in velocity as the acceleration acting on the body, a more recognisable version of Newton's second law is obtained. However, by writing the velocity as the rate of change of position, a more suitable form of the equation that will be used throughout the rest of this report is obtained.

$$\mathbf{F}_I = m\mathbf{a}_I = m \left. \frac{d^2\mathbf{r}}{dt^2} \right|_I \tag{3.30}$$

Here the sum of all forces acting on the vehicle is represented by $\mathbf{F}$, and $\mathbf{r}$ is the positional vector. The potential forces which are known to act upon an entry vehicle are the gravitational, aerodynamic, and propulsive forces. In this research however, the propulsive forces will not be taken into account.

For the equations of motion in an inertial, Cartesian reference frame, the above equations for the motion can be directly applied. By additionally formulating the kinematics law which relates the change in position to the velocity, the following two relations are obtained, of which the first is a reordered version of Eq. (3.30), and the second is the kinematic equation:

$$\begin{aligned} \left. \frac{d^2\mathbf{r}}{dt^2} \right|_I &= \frac{\mathbf{F}_I}{m} \\ \frac{d\mathbf{r}}{dt} &= \mathbf{V}_I \end{aligned} \tag{3.31}$$

Both of these equations have a total of three components, resulting in a total of six differential equations as is required to describe the motion of a body in three-dimensional space.

3.4.2. Relative Spherical Equations

The equations of motion used for the analytical approach are be defined in a rotating planetocentric reference frame using spherical coordinates. The definition of the spherical coordinates has already been given in Section 3.3.3. However, instead of the full equations of motion, simplified versions are used. The applied assumptions simplify the equations of motion sufficiently for them to be used analytically, instead of requiring numerical integration.

In total five assumptions are made. The first assumption is that no propulsion will be used during atmospheric flight, $T = 0$. The non-propulsive nature of the flight was already state before. In the analytical approach the gravity field is approximated by a central gravitational field model, meaning only the radial component of gravity is considered, $g_\delta = 0$. Furthermore, the central body is considered non-rotating, $\omega_{cb} = 0$, ignoring the effect of the apparent forces. The flight is assumed to be symmetrical, resulting in the omission of side force, $S = 0$. The final simplification is that only full-lift up flight is considered, resulting in $\sigma = 0°$. Using these four simplifications, the equations of motion become:

$$\frac{dV}{dt} = -\frac{D}{m} - g\sin\gamma \tag{3.32}$$

$$V\frac{d\gamma}{dt} = \frac{L}{m} - g\cos\gamma + \frac{V^2}{r}\cos\gamma \tag{3.33}$$

$$V\frac{d\chi}{dt} = \frac{V^2}{r}\cos^2\gamma\tan\delta\sin\chi \tag{3.34}$$

Similar to the Cartesian case, in addition to three equations expressing the dynamics of the vehicle, three kinematic relations are also required to fully define the motion in three-dimensional space. The three kinematic relations are:

$$\frac{dr}{dt} = V\sin\gamma \tag{3.35}$$

$$\frac{d\tau}{dt} = \frac{V\sin\chi\cos\gamma}{r\cos\delta} \tag{3.36}$$

$$\frac{d\delta}{dt} = \frac{V\cos\chi\cos\gamma}{r} \tag{3.37}$$

The major benefit of these representations over the Cartesian version is that their results are intuitive and easily understood. They directly provided the a value for the change in velocity, flight-path angle, altitude, etcetera, where these parameters need to be determined using additional computations when using Cartesian coordinates.

With the establishment of the equations of motion both in the inertial Cartesian and the rotating spherical system, all that remains to be done before both sets of equations can be evaluated is the definition of the forces. The forces are effected by the interaction of the vehicle with the environment. Therefore, to obtain expressions for the magnitude of the forces, the environment needs to be modelled. The models used for the environment in both the numerical simulation and the analytical approximation is discussed next.

3.5. Analytical Approximation Spherical Equations of Motion

In this section the first- and second-order approximation of the spherical equations of motion are discussed. The goal of analytical approximations is to obtain analytical expressions that can provide insight into the trajectory, such as approximations of the peak loads and terminal conditions. This information can subsequently be used as the basis for a guidance application. The guidance application can make a prediction of the peak loads and terminal conditions based om the current vehicle state, command appropriate corrections to ensure the target is reached and the requirements are not violated.

3.5.1. First-Order Approximation

For the first-order approximation the equations of motion presented in the previous section are further simplified by assuming the effects of drag and lift to be far greater than the effect of gravity. This results in Eqs. (3.32) and (3.33) to be further reduced to:

$$\frac{dV}{dt} = -\frac{D}{m} \tag{3.38}$$

and

$$V\frac{d\gamma}{dt} = \frac{L}{m} \tag{3.39}$$

By dividing one equation by the other, reordering the terms, and integration from entry to an arbitrary point in trajectory, the following expression can be obtained relating the velocity at an arbitrary point in the trajectory to the flight-path angle:

$$\frac{V}{V_E} = e^{-\frac{\gamma-\gamma_E}{L/D}} \tag{3.40}$$

The actual derivation from Eqs. (3.38) and (3.39) to this final equation will not be repeated here as it does not add any relevant insight, and can be found in numerous places, such as Mooij (2017), or worked out by oneself. The four points in the trajectory that are of interest are the lowest point in the trajectory, where $\gamma = \gamma_E = 0°$, the point in the trajectory where the peak heat flux and peak acceleration occur, $\gamma = \gamma_{q,max}$ and $\gamma = \gamma_{a,max}$, respectively, and the point in the trajectory where the vehicle exits the atmosphere $\gamma = \gamma_F$.

By using Eq. (3.39), the hydrostatic equation, and the exponential atmosphere model to approximate the relation between altitude and density, the following expression can be obtained relating the flight-path angle at an arbitrary point in the trajectory to the density (and thus the altitude):

$$\cos\gamma - \cos\gamma_E = \frac{\frac{1}{2}\rho S C_L}{m} H_s \tag{3.41}$$

By solving this equation using $\gamma = 0°$, indicative of the lowest point in the trajectory, and rewriting it as a function of altitude using the exponential atmosphere model, the following relation can be obtained for the atmospheric penetration depth:

$$h_p = -H_s \ln\left(\frac{2}{H_s}\frac{m}{\frac{1}{2}\rho_0 S C_L}\sin^2\frac{\gamma_E}{2}\right) \tag{3.42}$$

Alternatively, by solving Eq. (3.41) for γ by setting the local density to zero, indicative of the vehicle reaching the end of the atmosphere, two solutions can be obtained, namely $\gamma = \gamma_E$, or $\gamma = -\gamma_E$. Since γ_E is the flight path of the vehicle entering the atmosphere, in the first solution the vehicle is moving downwards, entering the atmosphere, and in the second solution, the vehicle is moving upwards, leaving the atmosphere. Therefore $\gamma_F = -\gamma_E$, according to this approximation.

The equations to obtain the normalised aerodynamic acceleration component that is collinear with the velocity as a function based on the entry conditions and the local flight conditions is:

$$\frac{a_v}{g_0} = \frac{V_E^2}{g_0 H_s}\frac{D}{L}(\cos\gamma - \cos\gamma_E)e^{-\frac{2(\gamma-\gamma_E)}{L/D}} \tag{3.43}$$

where, a_v is the aerodynamic acceleration component collinear with the velocity, g_0 is the mean surface gravity of Earth, V is the velocity relative to the atmosphere, H_s is the scale-height of an exponential atmosphere model, D and L are the drag and lift forces, respectively, and their ratio is the lift-over-drag ratio, γ is the flight-path angle, and the subscribe E denotes values that are taken at the entry interface. Regardless of which body is the actual central body, the acceleration always gets non-dimensionalised by dividing it by the mean surface gravity of Earth. This ensures that the values obtained from different central bodies can be compared easily.

By evaluating this equation with the flight-path angle at which the maximum acceleration occurs, the maximal acceleration component collinear with the velocity can be found. By using

$$\frac{a_{\text{res}}}{g_0} = \frac{a_v}{g_0}\sqrt{(1+\frac{L}{D}^2)} \tag{3.44}$$

the maximal total (resultant) aerodynamic acceleration can be found. This equations uses the fact that the aerodynamic acceleration collinear and perpendicular to the velocity are proportional to the drag and lift forces, respectively, and the basic Pythagorean theorem, to determine the resultant aerodynamic acceleration. The flight-path angle at which the peak acceleration occurs can be found using:

$$\gamma_{a,max} = 2\arctan\left[\frac{\frac{L}{D}}{2(1+\cos\gamma_E)}\left(1-\sqrt{1+\frac{4\sin^2\gamma_E}{\frac{L}{D}^2}}\right)\right] \tag{3.45}$$

3.5.2. Second-Order Approximation

After analysing the first-order approximations for aerocapture trajectories, the assumption that the gravitational effect was negligible was found to be invalid. This evaluation is discussed in Chapter 7. In an attempt to find analytical expressions for the equations of motion that took into account the effect of gravity, the works by Chapman (1958), Loh (1968), and Vinh et al. (1993) were found.

A common threat through these works is that new dependent and independent variables and constants are introduced to non-dimensionalise the equations. Due to this non-dimensionalsiation process, the equations lose their intuative nature and become increasingly complex. Nevertheless, the non-dimensionalisation and rewriting process is solely a mathematical operation, and the obtained equations of motion still produce the exact results also obtained from standard equations of motion. For a more detailed description of this process the reader is encouraged to attempt the rewriting process themselves, and is directed to the work by Vinh et al. (1993) where it is performed in full.

The first step is to introduce a new dependent variable, the range angle. The range angle is a measure for the ground distance travelled by the vehicle. The expression for the range angle is

$$\frac{d\theta}{dt} = \frac{V\cos\gamma}{r} \tag{3.46}$$

By dividing Eqs. (3.32), (3.33) and (3.35) by Eq. (3.46) the independent variable is switched from time to the range angle.

Following this, non-dimensional variants for the radial position and velocity are introduced. The radial position is non-dimensionalised by first subtracting the entry radius to obtain the penetration depth, and subsequently dividing by the entry radius, resulting in

$$h = \frac{r - r_E}{r_E} \tag{3.47}$$

Note that the subscript $_E$ denotes entry interface. At the entry interface, the values of h, and later y and v, are zero, one, and zero, respectively. At the start of entry $h = 0$, it decreases until it reaches a minimum at the lowest point in the trajectory, after which it increases again until it reaches the atmospheric exit, where, again, $h = 0$.

The velocity is non-dimensionalised by first considering the squared velocity, and dividing it by the square of the circular velocity at the entry altitude. For convenience in the further derivation, the square of the circular velocity is expressed as the product of the entry radius and the gravitational acceleration at this position, such that

$$u = \frac{V^2}{V_{c,0}^2} = \frac{V^2}{g_E r_E} \tag{3.48}$$

Furthermore, three constants are introduced to further "simplify" the equations of motion. While these equations do indeed make writing the equations easier by removing terms, they in fact make understanding the equations harder and obfuscate the physics. The first constant expresses the maximum lift-to-drag ratio and is defined as

$$E^* = \frac{1}{2\sqrt{KC_{D_0}}} \tag{3.49}$$

where K and C_{D_0} are related to the parabolic drag polar according to

$$C_D = C_{D_0} + KC_L^2 \tag{3.50}$$

A warning before continuing, the K in this equation is explicitly a capital K. This is important as later in the derivation a lower-case k, and a lower-case k_1 will be introduced, leading to potential confusion. The second constant specifies the entry altitude and physical characteristics of the vehicle. This constant is B, and is defined as

$$B = \frac{\rho_E S r_E}{2m}\sqrt{\frac{C_{D_0}}{K}} \tag{3.51}$$

The third and last new constant is the lift-control, and allows for lift-modulation. The lift-control is defined as

$$\lambda = \frac{C_L}{\sqrt{C_{D_0}/K}} \tag{3.52}$$

and is equal to one when the vehicle is flying at maximum lift-to-drag ratio, zero for ballistic entry, and anything in between for modulated lift. While not stated in any of the sources, one can even use negative values for the lift-control to model lift-down flight, with negative one for flight with full lift-down, or a bank angle of 180°. Using varying this parameter, lift modulation due to continuous or discrete bank angle control can approximated. Note however that te induced side force and the motion because of this force are not modelled, as these equations are only for planar flight.

The next step is to again change the dependent and independent variable. The new independent variable is still a measure for the range angle, but this time with information regarding the atmosphere ingrained into it. The new independent variable is

$$\tau = \sqrt{\frac{r_E}{H_s}}\theta \tag{3.53}$$

where part under the square provides the information regarding the atmosphere. At the start of entry, $\tau = \theta = 0°$. The new dependent variable for altitude is

$$y = e^{-\frac{R_E h}{H_s}} = \frac{\rho}{\rho_E} \tag{3.54}$$

At atmospheric entry $y = 1$, after entry, y increases until it reaches y_{max} at the point of deepest penetration, from which it decreases back down to to $y = 1$ at atmospheric exit. Note that for this to be true, the density at the atmospheric entry and exit cannot be considered zero. The new dependent variable for velocity is

$$v = \frac{1}{\eta}\ln\frac{V_E^2}{V^2} \tag{3.55}$$

As already stated, at atmospheric entry $v = 0$, and as the velocity decreases it becomes negative. If for some reason the velocity would increase beyond atmospheric entry, the value would become positive. In this equation V_E is the entry speed, and the constant η is defined as

$$\eta = \frac{B}{E^*\sqrt{\frac{r_E}{H_s}}} = \frac{\rho_E S C_{D_0}}{m}\sqrt{H_s r_E} \tag{3.56}$$

Lastly, the new dependent variable for the flight-path angle is

$$\phi = -\sqrt{\frac{r_E}{H_s}}\sin\gamma \tag{3.57}$$

In addition to the introduction of η, two other new constants are introduced, again to "simplify" the equations. The two constants are

$$k = \frac{2E^*}{\sqrt{\frac{r_E}{H_s}}B} \tag{3.58}$$

$$\alpha = \frac{g_E r_E}{V_E^2} \tag{3.59}$$

Doing all these steps eventually leads to a new system of three non-dimensional equations of motion that still produce the exact results, matching those of the regular equations of motion when evaluated. However, due to the large amount of mathematical operations and introduction of new variables and constants, they are much less intuitive than the original equations. Written out, the new equation for the non-dimensional altitude is

$$\frac{dy}{d\tau} = \frac{1+h}{\cos\gamma}y\phi \tag{3.60}$$

The equation for the non-dimensional velocity is

$$\frac{dv}{d\tau} = \frac{1+h}{\cos\gamma}\left(1+\lambda^2\right)y - \frac{k\alpha\phi e^{v\eta}}{(1+h)\cos\gamma} \tag{3.61}$$

Lastly, the equation for the non-dimensional flight-path angle is

$$\frac{d\phi}{d\tau} = -(1+h)B\lambda y + \frac{\cos\gamma}{1+h}\alpha e^{\eta v} - \cos\gamma \tag{3.62}$$

As stated, these equations are still the same equations as the original equations of motion, only rewritten. No simplifications or assumptions have been made in obtaining these expressions, and they will therefore result in the exact solutions.

Before analytical equations can be obtained from these rewritten equations of motion however, two simplifications are introduced. The first of these simplifications is the small-angle assumption. By assuming the flight-path angle to be small, the geometric relations involving the cosine of the flight-path angle can be simplified to $\cos(\gamma) \approx 1$. The second simplification is to with the non-dimensional variable h. As entry into the atmosphere if a planet is considered, the altitude of the vehicle above the surface is negligible compared to the radius of the planet. Mathematically: $r - r_E \approx 0$, therefore $h \approx 0$, and thus $1 + h \approx 1$. Additionally, k_1, a new constant, is introduced, defined as

$$k_1 = B\lambda \tag{3.63}$$

Using the two simplifications, and introducing the newly defined constant, the above exact equations of motion can be simplified down to

$$\frac{dy}{d\tau} = y\phi \tag{3.64}$$

$$\frac{dv}{d\tau} = \left(1+\lambda^2\right)y - k\alpha\phi e^{\eta v} \tag{3.65}$$

$$\frac{d\phi}{d\tau} = -k_1 y - \left(1 - \alpha e^{\eta v}\right) \tag{3.66}$$

These simplified versions of the non-dimensionalised equations of motion are the starting equations for the development of the analytical expressions.

The first step in the development in the second-order analytical approximations is to develop first-order approximations from Eqs. (3.64) to (3.66). This is done by ignoring the variation in speed in the $e^{\eta v}$ term. By keeping the velocity equal to the entry velocity we obtain $e^{\eta v} = \exp\left(\eta/\eta \ln\left(V_E^2/V_E^2\right)\right) = 1$. This is the same as taking the first term of the Taylor series expansion, resulting in the following first-order approximations:

$$\frac{dy}{d\tau} = y\phi \tag{3.67}$$

$$\frac{dv}{d\tau} = \left(1+\lambda^2\right)y - k\alpha\phi \tag{3.68}$$

$$\frac{d\phi}{d\tau} = -k_1 y - (1-\alpha) \tag{3.69}$$

By dividing the third equation by the first, using the product rule to obtain an explicit equation, integrating the equation from $y(0) = 1$, $\phi(0) = c$ to an arbitrary point in the trajectory, and introducing a new independent variable x, an expression for ϕ^2 against x can be obtained. This process is shown in mathematical steps below First, the division of the third equation by the first:

$$\frac{d\phi}{d\tau}\frac{d\tau}{dy} = \frac{d\phi}{dy} = \frac{-k_1 - (1-\alpha)\frac{1}{y}}{\phi} \tag{3.70}$$

The application of the product rule to obtain an explicit relation:

$$\frac{d\phi^2}{dy} = \frac{d(\phi\cdot\phi)}{dy} = \frac{\phi d\phi + \phi d\phi}{dy} = \frac{2\phi d\phi}{dy} = 2\phi\frac{d\phi}{dy} = -2k_1 - 2(1-\alpha)\frac{1}{y} \tag{3.71}$$

The result of integration from atmospheric entry to arbitrary point in trajectory, and introduction of the new independent variable x, together with the definition of x:

$$\phi^2 = c^2 - 2k_1\left(e^x - 1\right) - 2(1-\alpha)x \tag{3.72}$$

$$x = \log(y) = -\frac{(r_E h)}{H_s} = \frac{r_E - r}{r_E} \tag{3.73}$$

The new independent variable x is yet another measure for the altitude of the vehicle throughout the entry. At the start of the entry, $x = 0$, after entry x increases to x_{max}, but remains relatively small. After reaching the deepest point in the atmosphere, x decreases again back down to 0. The constant $c = \phi_E$.

By replacing y in Eq. (3.67) by the newly defined independent variable x, and using the definition for ϕ from Eq. (3.72), the following relation can be obtained

$$d\tau = \frac{dx}{\phi} = \frac{dx}{\pm\sqrt{c^2 - 2k_1\left(e^x - 1\right) - 2(1-\alpha)x}} \tag{3.74}$$

which can be used to obtain an expression relating x to τ. However, to facilitate obtaining this expression, Vinh et al. (1993) approximates ϕ^2 as a second-order polynomial with x as the independent variable. The general form of this approximating trinomial is

$$\phi_a^2 = a_1 x^2 + a_2 x + a_3 \tag{3.75}$$

which results in the relation between x and τ taking the form

$$x = -\frac{a_2}{a_1} - \frac{\sqrt{a_2^2 - 4a_1 a_3}}{2a_2} \sin\left(\sqrt{-a_1}\tau - \beta\right) \tag{3.76}$$

where β is defined as

$$\sin\beta = \frac{a_2}{\sqrt{a_2^2 - 4a_1 a_3}} \tag{3.77}$$

At this point Vinh et al. (1993) states that the three coefficients are to be determined though any approximation scheme. Later in the paper however, Vinh et al. (1993) gives an analytical solution for the three coefficients of the approximate trinomial, namely

$$a_1 = \frac{3}{x_1}\left(2(1-\alpha) - \frac{c^2 + 4k_1}{x_1} + \frac{4k_1\left(e^{x_1} - 1\right)}{x_1^2}\right) \tag{3.78}$$

$$a_1 = -6(1-\alpha) + \frac{2\left(c^2 + 6k_1\right)}{x_1} - \frac{12k_1\left(e^{x_1} - 1\right)}{x_1^2} \tag{3.79}$$

$$a_3 = c^2 \tag{3.80}$$

In these three equations, x_1 is the value for x at the lowest point in the trajectory. At the point in the paper where these analytical formulations of the coefficients are given, Vinh et al. (1993) states that x_1 can be computed by solving Eq. (3.72) for $\phi^2 = 0$, which occurs at the lowest point in the trajectory, when $x = x_1$. Due to the nature of this equation, an exact solution was not found. Therefore, the solution had to be otherwise obtained. One method of doing this was to use a numerical root-finding scheme. The other method was to use an approximation. Since an first-order approximation for the altitude of the deepest point in the trajectory was already obtained in Eq. (3.42), this approximation was used to approximate x_1. Using this approximate, the coefficients of the approximate trinomial can be obtained.

Thus far, a first-order approximation for the flight-path angle as a function of the altitude (Eq. (3.72)) and for the altitude as a function of the range angle (Eq. (3.76)), which can easily be inverted to obtain the range angle as a function of altitude, has been obtained. The only thing missing now is a first-order approximation of the velocity. This can now be readily obtained by first inverting Eq. (3.69) to obtain an expression for y, and inserting this into Eq. (3.68), followed by inserting the expression for ϕ as shown in Eq. (3.74), and lastly integrating the resulting equation from atmospheric entry to an arbitrary point in the trajectory. This ultimately results in the following first-order approximation for the velocity as a function of altitude and range angle

$$v = \frac{\left(1+\lambda^2\right)}{k_1}(c - \phi) - k\alpha x - \frac{(1-\alpha)\left(1+\lambda^2\right)}{k)1}\tau \tag{3.81}$$

It should be noted that this is the first equation where the flight-path angle ϕ is required, and not ϕ^2. Since Eq. (3.72) provides us with ϕ^2, the solution to this is $\pm\phi$. Since ϕ is the negative sin of the flight-path angle,

and the sin operation retains the same sign as its argument for the range of angles considered valid for the flight-path angle (±90°), the sign of ϕ is positive for the descending leg of the trajectory, and negative for the ascending leg.

With the first-order approximations developed, Vinh et al. (1993) continues by improving the accuracy of the system by taking into account the $e^{\eta v}$ term. However, to still allow the development of the second-order analytical equations, the $e^{\eta v}$ term is approximated by the first two terms if its Taylor series, resulting in $e^{\eta v} \approx 1 + \eta v$. This results in the second-order approximations of the non-dimensionalised equations of motion:

$$\frac{dy}{d\tau} = y\phi \tag{3.82}$$

$$\frac{dv}{d\tau} = \left(1+\lambda^2\right)y - k\alpha\phi - \eta k\alpha\phi v \tag{3.83}$$

$$\frac{d\phi}{d\tau} = -k_1 y - (1-\alpha) + \eta\alpha v \tag{3.84}$$

Following the same procedure as before, the third equation is divided by the first, and the independent variable y is replaced by x. Due to the inclusion of the second term of the Taylor series expansion, now v appears. Fortunately, Eq. (3.89) can be used to obtain a relation that only depends on x and ϕ. By again integrating this solution from atmospheric entry to an arbitrary point in the trajectory, an improved approximation for ϕ^2 can be obtained. The majority of this integration is the same as was performed previous, only Eq. (3.89) has to be integrated. Unfortunately, this integration leads to the most terms. This improved approximation for the flight-path angle as a function of altitude and range angle is

$$\phi^2 = c^2 - 2k_1\left(e^x - 1\right) - 2(1-\alpha)x + 2\eta\alpha I(x) \tag{3.85}$$

where $I = \int_0^x v dx$, which, when worked out, results in

$$I = \frac{\left(1+\lambda^2\right)}{k_1}cx - \frac{1}{2}k\alpha x^2 - \frac{(1-\alpha)\left(1+\lambda^2\right)}{k_1}\tau x - \frac{\left(1+\lambda^2\right)}{k_1}I_1(x) + \frac{(1-\alpha)\left(1+\lambda^2\right)}{k_1}I_2(x) \tag{3.86}$$

where $I_1 = \int_0^x \phi dx \approx \int_0^x \phi_a dx$, and $I_2 = \int_0^x \frac{x dx}{\phi} \approx \int_0^x \frac{x dx}{\phi_a}$, which, when worked out, result in

$$I_1 = \frac{1}{2}\phi_a x - \frac{a_2}{4a_1}(c - \phi_a) + \frac{\left(4a_1a_3 - a_2^2\right)}{8a_1}\tau \tag{3.87}$$

$$I_2 = -\frac{1}{a_1}(c - \phi_a) - \frac{a_2}{2a_1}\tau \tag{3.88}$$

In these equations the trinomial coefficients determined previously return. To obtain the second-order approximation for the non-dimensionalised velocity, the same procedure as as used to obtain the first-order approximation is applied. As was the case for the flight-path angle, the resulting equation is the same as the first-order equivalent with the addition of a term involving v. The first-order approximation for this variable is used to obtain an evaluable expression. After integration, the final second-order analytical expression for the velocity as a function of altitude and range angle is

$$v = \frac{\left(1+\lambda^2\right)}{k_1}(c - \phi) - k\alpha x - \frac{(1-\alpha)\left(1+\lambda^2\right)}{k_1}\tau - \eta k\alpha I(x) + \frac{\eta\alpha\left(1+\lambda^2\right)}{k_1}J(x) \tag{3.89}$$

where I is the same as before, and $J(x) = \int_0^x v d\tau$, which, when worked out, results in

$$J = \frac{\left(1+\lambda^2\right)}{k_1}c\tau - \frac{\left(1+\lambda^2\right)}{k_1}x - \frac{(1-\alpha)\left(1+\lambda^2\right)}{2k_1}\tau^2 - k\alpha I_2(x) \tag{3.90}$$

where I_2 is the same as before.

An improved expression for the altitude as a function of the range angle is obtained by using the same three equations for the trinomial coefficients as used before, but this time by calculating the values using a better approximation of x_1. Since now a second-order approximation of the flight-path angle is available, this approximation should be used instead of a first-order approximation. At this point, a root-finding scheme is required to for which value of x: $\phi^2(x) = 0$. Vinh et al. (1993) notes that for low L/D vehicles a problem

arises with the new approximation. They state that the first-order approximation for the lowest point in the trajectory will be smaller than the more accurate second-order value, and therefore during the root-finding scheme, values for x will be tested that are above x_1. As a reminder, a larger value of x indicates deeper penetration. Therefore, stating that the value obtain for x_1 from the first-order estimate is smaller than the more accurate second-order value infers that in reality the vehicle dives deeper into the atmosphere than expected from the first-order estimate. This is not the case for the vehicle considered in this research, as has been shown in Fig. 7.1, where it can be seen that the first-order estimate puts the vehicle deeper into the atmosphere.

Regardless, the problem Vinh et al. (1993) mentions is that, because x values are tested that are in excess of x_1, the normally positive $\phi_a^2(x)$ becomes 0 at x_1, become negative for values in excess of x_1, leading to erroneous results. As a remedy for this it is proposed that, whenever a value of x above x_1 is tested, the value for x used in the $2\eta\alpha I(x)$ term should be held constant at x_1. As a precaution, this remedy was added when implementing the algorithm to obtain the analytical expressions, even though it was expected to never be needed.

Using this updated value of x_1, the trinomial coefficients can be re-calculated, and the updated versions of these trinomials can be used in place of the old versions, to obtain improved versions of the second-order approximations. In theory this cycle of computing an updated x_1, recalculating the trinomial coefficients, and updating the second-order approximations could be continued ad infinitum. However, no significant increase in accuracy was obtained by repeating this cycle any additional amounts.

The last tasks undertaken when implementing these equations was to make τ the only independent variable, and to obtain expressions for the aerodynamic forces and heat load that use the same independent variables and constants as the rest of the second-order analytical equations such that all the equations could be evaluated at once. Obtaining the above equations with τ as the independent variable was a simple matter of rewriting and defining the expressions. The analytical forms of the aerodynamic equations and the heat flux were obtained by staring from the basic form of the equation for the aerodynamic force as given in Section 3.6.1, and the general form for heat flux as obtained in Section 3.6.4, and rewriting them using the constants that were introduced in this derivation. The final set of second-order analytical equations as implemented for this research, and the rewritten equations for the aerodynamic forces and a general expression for the heat loading are:

$$x(\tau) = -\frac{a_2}{2a_1} - \frac{\sqrt{a_2^2 - 4a_1a_3}}{2a_1}\sin\left(\sqrt{-a_1}\tau - \arcsin\frac{a_2}{\sqrt{a_2^2 - 4a_1a_3}}\right) \tag{3.91}$$

$$\phi_a^2(\tau) = a_1x(\tau)^2 + b_2x(\tau) + a_3 \tag{3.92}$$

$$\phi_a(\tau,\delta) = \delta\sqrt{\phi_a^2(\tau)} \tag{3.93}$$

$$I_1(\tau,\delta) = \frac{1}{2}\phi_a(\tau,\delta)x(\tau) - \frac{a_2}{4a_1}(c - \phi_a(\tau,\delta)) + \frac{\left(4a_1a_3 - a_2^2\right)}{8a_1}\tau \tag{3.94}$$

$$I_2(\tau,\delta) = -\frac{1}{a_1}(c - \phi_a(\tau,\delta)) - \frac{a_2}{2a_1}\tau \tag{3.95}$$

$$I(\tau,\delta) = \frac{\left(1+\lambda^2\right)}{k_1}cx(\tau) - \frac{1}{2}k\alpha x(\tau)^2 - \frac{(1-\alpha)\left(1+\lambda^2\right)}{k_1}\tau x(\tau) - \frac{\left(1+\lambda^2\right)}{k_1}I_1(\tau,\delta) + \frac{(1-\alpha)\left(1+\lambda^2\right)}{k_1}I_2(\tau,\delta) \tag{3.96}$$

$$J(\tau,\delta) = \frac{\left(1+\lambda^2\right)}{k_1}c\tau - \frac{\left(1+\lambda^2\right)}{k_1}x(\tau) - \frac{(1-\alpha)\left(1+\lambda^2\right)}{2k_1}\tau^2 - k\alpha I_2(\tau,\delta) \tag{3.97}$$

$$\phi^2(\tau,\delta) = c^2 - 2k_1\left(e^{x(\tau)} - 1\right) - 2(1-\alpha)x(\tau) + 2\eta\alpha I(\tau,\delta) \tag{3.98}$$

$$\phi(\tau,\delta) = \delta\sqrt{\phi^2(\tau,\delta)} \tag{3.99}$$

$$\nu(\tau,\delta) = \frac{\left(1+\lambda^2\right)}{k_1}(c-\phi(\tau,\delta)) - k\alpha x(\tau) - \frac{(1-\alpha)\left(1+\lambda^2\right)}{k_1}\tau - \eta k\alpha I(\tau,\delta) + \frac{\eta\alpha\left(1+\lambda^2\right)}{k_1}J(\tau,\delta) \tag{3.100}$$

$$\frac{D}{g_E}(\tau,\delta) = \frac{\left(1+\lambda^2\right)Be^{x(\tau)-\eta\nu(\tau,\delta)}}{2\alpha E^*} \tag{3.101}$$

$$\frac{L}{g_E}(\tau,\delta) = \frac{\lambda Be^{x(\tau)-\eta\nu(\eta,\delta)}}{\alpha} \tag{3.102}$$

$$q(\tau,\delta,C,a,b,M) = CR_n^a\rho_E^b V_E^M e^{bx(\tau)-\frac{M\eta\nu(\tau,\delta)}{2}} \tag{3.103}$$

where all the equations are only dependent on the fixed entry conditions, range-angle τ, and δ, which has a value of 1 or -1, and specifies whether the flight is in the downwards or upwards leg, respectively. As stated, the value of x starts at zero at atmospheric entry, then increases up to a maximum at the deepest point in the atmosphere, and decreases back down to zero at atmospheric exit. With this known, the range of τ for which these equations can be evaluated can be determined by determining values of τ for which $x(\tau) = 0$. The first root is known from previously given definitions. At $\sqrt{-a_1}\tau = 0$, at atmospheric entry, $x(\tau) = 0$. By considering the cyclic behaviour of the sin function, one set of roots can be expressed as $\sqrt{-a_1}\tau = 2\pi k$, where k is any integer, or, $k \in \mathbb{Z}$. The first root is part of this set. Similarly, a second set of roots can be expressed as $\sqrt{-a_1}\tau = (1+2k)\pi + 2\beta$, where $\beta = \arcsin\frac{a_2}{\sqrt{a_2^2-4a_1a_3}}$, and again $k \in \mathbb{Z}$. As only the first and second roots are of interest (atmospheric entry and exit), the smallest two roots described by these two sets are of interest. These roots are, for atmospheric entry and exit, respectively, $\tau = 0$ and $\tau = \pi + 2\arcsin\frac{a_2}{\sqrt{a_2^2-4a_1a_3}}\frac{1}{\sqrt{-a_1}}$.

When the above equations are evaluated from atmospheric entry to exit, values are obtained that are not easily understood. These values are still in the non-dimensionalised and rewritten form. Therefore, the last part of the implementation process are the equations needed to transform back to the relative spherical component. These equations are listed below for the radial distance, velocity, flight-path angle, and aerodynamic loads.

$$r(\tau) = -H_s x(\tau) + r_E \tag{3.104}$$

$$V(\tau,\delta) = \sqrt{\frac{V_E^2}{e^{\eta\nu(\tau,\delta)}}} \tag{3.105}$$

$$\gamma(\tau,\delta) = \arcsin\left(\frac{\phi(\tau,\delta)}{-\sqrt{\frac{r_E}{H_s}}}\right) \tag{3.106}$$

$$\begin{aligned}\frac{D}{g_E}(\tau,\delta) &= \frac{D}{g_E}(\tau,\delta)\frac{g_E}{g_E}\\ \frac{L}{g_E}(\tau,\delta) &= \frac{L}{g_E}(\tau,\delta)\frac{g_E}{g_E}\end{aligned} \tag{3.107}$$

3.6. Forces and Environment

Two forces are considered to act on the vehicle, effecting the motion. These forces are gravitational and aerodynamic forces. Gravitational and aerodynamic forces are so called external forces, as they are effected due to the environment in which the vehicle is present. To obtain a value for these forces the environment has to be modelled in addition to having to obtain expressions for the forces. In this section each both the definition of the aerodynamics and the gravitational forces, and the corresponding models are treated.

To determine the aerodynamic force, a model of the atmosphere is required to approximate the density at the current altitude. To obtain the current altitude, a central body shape model is needed to determine the surface radial based on the current latitude. For the gravitational force a model for the gravity field of the central body is required. In both cases, a version of the model to be used in the numerical simulation and

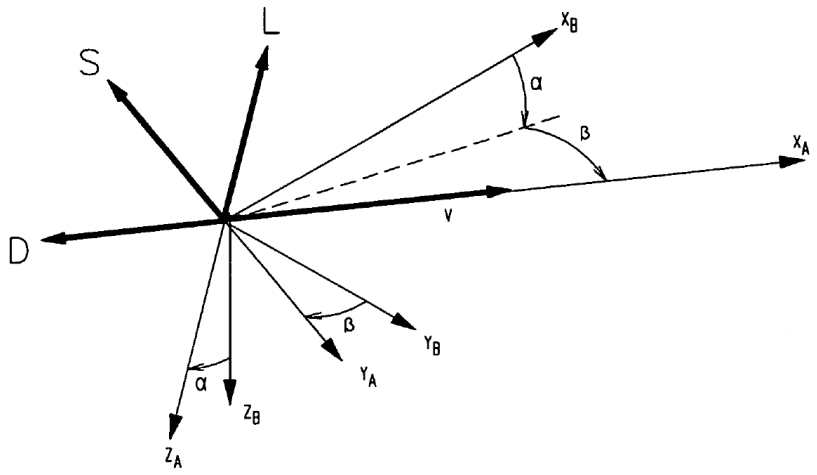

Figure 3.6: Definition of the aerodynamic forces in the airspeed-based aerodnamic reference frame. Also depicted are the body fixed axis, the groundspeed-based velocity, windspeed, and the airspeed-based velocity. Mooij (1994).

a version to be used for the analytical approximations is desired. First the aerodynamics are discussed, followed by the atmosphere and the central body shape. After this, a side effect of atmospheric flight, aerothermal heating, and the methods used to model this are presented. Lastly, the gravitational model used will be discussed.

3.6.1. Aerodynamics

As stated by Anderson (2006), any object surrounded by a medium that has a relative velocity with respect to the object experiences a force due to the interaction between the medium and the object. In this research the interaction between the atmosphere and the vehicle results in an aerodynamic force. The magnitude and orientation of this force is dependent on the size, shape, and attitude of the body, the dynamic pressure and density of the surrounding medium, and three non-dimensional parameters, the Mach, Knudsen, and Reynolds numbers.

First, some brief information regarding the aerodynamic force, and how it is determined from the aerodynamic properties of the vehicle are discussed. Following this, the model used to obtain the aerodynamic properties of the vehicle and its dependencies are discussed. Lastly, the three non-dimensional parameters are discussed, together with their impact on the aerodynamic properties of the considered vehicle.

Aerodynamic forces are, as stated, the forces that result from the interaction between the vehicle and the surrounding atmosphere. This force is the result of the surface pressure and surface shear stress distribution over the surface of the vehicle, and can be determined by integrating this pressure and stress over the entire surface. In common practice, instead of considering a single resultant force acting with a specific attitude on the vehicle, the total aerodynamic force is usually split into components along specific axis. When the aerodynamic force acting on a specific point on the surface of a vehicle is considered, the force is usually split into a tangential and a normal force, with the tangential force acting collinear with velocity. When the aerodynamic forces acting on a vehicle as a whole are considered, the force is usually split up into the more familiar drag, side-slip, and lift force. Considering that the interest of this research lays with the motion of a vehicle, and not a study of the aerodynamics about this vehicle, the latter three components are used. The drag acts collinear with, but in the opposite direction, of the velocity, the lift acts in the plane of symmetry of the vehicle, if it has any, perpendicular to the velocity, and the side-slip falls perpendicular to both the lift and drag. This is illustrated in Fig. 3.6.

Instead of having to determine the aerodynamic forces by integrating over the entire surface of the vehicle, it is customary to describe the aerodynamic forces as the produce of the dynamic pressure of the medium, which is a parameter related to the density and the relative velocity between the surface and the medium, the surface over which the medium travels, and a dimensionless force coefficient. The following relations were obtained from Anderson (2006), and are repeated here.

$$D = q_\infty S_{ref} C_D \tag{3.108}$$

$$S = q_\infty S_{ref} C_S \tag{3.109}$$

$$L = q_\infty S_{ref} C_L \tag{3.110}$$

In the above equations D, S, and L, and C_D, C_S, and C_L represent the drag, side, and lift force and dimensionless force coefficients, respectively, S_{ref} is the vehicles reference surface, and q_∞ the dynamic pressure which his defined according to $q_\infty = \frac{1}{2}\rho_\infty V_\infty^2$. Since the value of q_∞ depends on the local density and free-stream velocity, an model of the atmosphere is needed to obtain the aerodynamic forces acting on the vehicle. The expanded version of these expressions for the drag and lift force were already used in the simplified relative spherical equations of motion. Previously, and going forward, the subscript from S_{ref} was, and will be, omitted. The subscript ∞ indicates that the values are taken for the undisturbed upstream flow. As will be discussed more next, in this research a symmetrical vehicle is considered, that flies with zero angle of sideslip throughout the flight. This results in no side-force acting upon the vehicle. Therefore both S and C_S are considered zero hereinafter. The rationale for this is explained in the next section.

To facilitate the translation of these aerodynamic forces to the inertial reference frame, they are provided in vector format:

$$\mathbf{A}|_A = \left(-D, 0, -L\right)^T = -q_\infty S_{ref} \left(C_D, 0, C_L\right)^T \tag{3.111}$$

In this format all the forces are preceded by a minus sign. This is due to the definition of the axes in the aerodynamic reference frame in which these forces are defined and the orientation of these forces. The X_A-axis is defined positive in direction of the velocity vector, whereas the drag always acts opposite of the velocity, resulting in the drag force acting along the negative X_A-axis. The Z_A-axis is defined collinear with the lift-force, but in opposite direction, thus naturally the lift force acts along he negative Z_A-axis. This is illustrated in Fig. 3.6.

By using the frame transformations as discussed in Section 3.2.2, the aerodynamic force vector can be transformed from the aerodynamic reference frame to th inertial reference frame such that they can be used in the equations of motion. This full transformation is:

$$\mathbf{A}|_I = |_I\mathbf{R}_Z(-\omega_{cb}t)|_R\mathbf{R}_Z(-\tau)|_{V'}\mathbf{R}_Y(\frac{\pi}{2}+\delta)|_V\mathbf{R}_Z(-\chi)|_{T'}\mathbf{R}_Y(-\gamma)|_T\mathbf{R}_X(\sigma)\mathbf{A}|_A \tag{3.112}$$

Vehicle shape, size, and attitude determine the value for the non-dimensional force coefficients. The shape and size of the vehicle has already been discussed in Section 2.6, and is considered to be constant throughout the flight. If an ablative TPS were used, this could potentially have an impact on the shape, size, and mass of the vehicle over the duration of the flight, but this is not considered in this research.

As discussed in Section 3.2, the attitude of the vehicle with respect to the velocity is determine by three angles, namely the angle of attack, the angle of sideslip, and the bank angle. The bank angle rotates the orientation of the aerodynamic force with respect to the local horizon, but apart from that it has no impact on the magnitude of the force. Additionally, the bank angle will be fully controlled in the simulation by an ideal controller. The angle of attack and the angle of sideslip have a larger impact on the aerodynamics as it impacts the orientation of the shape of the vehicle with respect to the flow velocity. As in this research the attitude of the vehicle is not of interest, it was decided to set the angle of attack and angle of side-slip within the simulation based on a model for the equilibrium trim condition.

The equilibrium trim attitude is the attitude at which the resultant aerodynamic moment about the centre of mass of the vehicle is zero. For a symmetrical vehicle, as is considered in this research, the equilibrium trim angle for the angle of sideslip is zero, justifying the assumption to set the angle of side slip, and the side force to zero, and ignoring them for the rest of the research.

As in this research a vehicle very similar to the Apollo CM in terms of shape and mass is considered, the aerodynamics were also modelled after this vehicle. The aerodynamic model for the Apollo CM was obtained from Robinson et al. (2009), and is reproduce in Table 3.1. This data was obtained by interpolating the results found in NASA BUT REALLY IMPROVE THIS ONE (1965). This model provides, for a wide range of Mach numbers, the corresponding equilibrium trim angle of attack, lift coefficient, and drag coefficient.

With this model, the assumptions made regarding symmetric flight with a symmetric vehicle, and the perfect control of the bank angle, the entire attitude of the vehicle, and all the aerodynamic force coefficients can be determined based solely of the Mach number.

Table 3.1: Apollo Command Module Aerodynamic Model. Graves and Harpold (1970)

Mach no. [-]	Angle of Attack [°]	C_L [-]	C_D [-]
0.4	167.14	0.24465	0.85300
0.7	164.38	0.26325	0.98542
0.9	161.70	0.32074	1.10652
1.1	154.87	0.49373	1.16970
1.2	155.13	0.47853	1.15600
1.35	154.01	0.56282	1.27880
1.65	153.22	0.55002	1.26570
2.0	153.14	0.53247	1.27210
2.4	153.62	0.0740	1.24120
3.0	154.14	0.47883	1.21670
4.0	156.12	0.44147	1.21480
10.0	156.79	0.42856	1.2246
≥ 29.5	160.06	0.38773	1.28910

Mach number is a dimensionless parameter that expresses the ratio between the velocity of the body relative to a medium, and the speed of sound in a medium. The Mach number can be calculated according to:

$$M_\infty = \frac{V_\infty}{a_\infty} = \frac{V_\infty}{\sqrt{\gamma RT}} \tag{3.113}$$

In this equation V_∞ is the free-stream velocity, and a is the speed of sound. γ represents the ration of specific heats of the medium, R is the gas constant, and T is the temperature.

Knudsen number is a measure for how rarefied a medium is. It represents the ratio between the mean free path length (the mean distance travelled by a particle before colliding with another) and a reference length based on the vehicle moving through the medium. A larger Knudsen number is the result of a long mean free path length, which occurs when the medium is of low density. Because the density of an atmosphere decreases as the altitude increases, the Knudsen number of the medium increases as the altitude increases.

Moss and Bird (1984) analysed the effect of the Knudsen number on the Apollo CM for a large range of free-stream Knudsen numbers. In Fig. 3.7 the impact of the Knudsen number on the aerodynamic coefficients and the resulting L/D-ratio is graphed. From this graph it can be determined that for very high and low Knudsen numbers, there seems to be little to no impact on the aerodynamic coefficients. Moss and Bird (1984) states that in the regime $0.03 < K_n < 1.0$ the impact of the Knudsen number on the aerodynamic forces is the most significant.

In Fig. 3.8 the results of a lift-up CRM entry staring from the nominal entry conditions on Earth are shown. From this figure it can be seen that it spends roughly half of the orbit below 75 km. Additionally, only during this flight through the "lower" part of the atmosphere are the aerodynamic forces significant. At 75 km, on the downwards leg, the G-load is approximately 0.75g, and on the upwards leg, the G-load is approximate 0.5g. The peak g-load is reached at roughly 60 km.

From Fig. 3.7 it can be determined that an altitude of 75 km corresponds to a Knudsen number of $\mathcal{O}(10^{-3})$. At this value of the aerodynamic coefficients are already almost constant. The peak g-load occurs at an altitude where $K_n \leq 10^{-4}$. Above the value of 90 km, where the aerodynamic coefficients start to be affected significantly, the aerodynamic force is sufficiently small that the impact on the coefficients has a negligible effect. Because of this, it was decided to neglect the effect on the Knudsen number on the aerodynamics to allow for a simpler analysis.

The Martian atmosphere is more tenuous and colder compared to the Earth atmosphere, resulting in a larger mean free path length (less amount of particles, and less energetic particles), and thus a larger Knudsen number. It is therefore expected that the impact of the Knudsen number on the aerodynamics is larger on Mars than it is on Earth. However, the aerodynamic forces on Mars are also much smaller due to the tenuous atmosphere. The opposite is true for Venus however, where, due to its very dense and hot atmosphere, the the Knudsen number is much smaller compared to Earth and the aerodynamic forces are much greater.

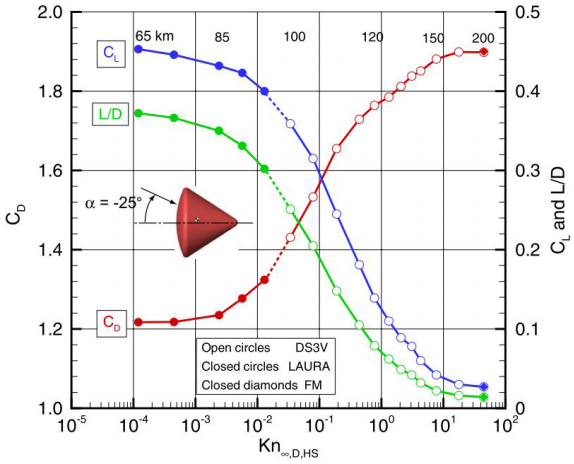

Figure 3.7: Lift-over-drag ratio and the aerodynamic coefficients for the Apollo Command Module as a function of Knudsen number. Also indicated are the altitudes corresponding to the Knudsen number based on Earth's atmosphere. Moss et al. (2006).

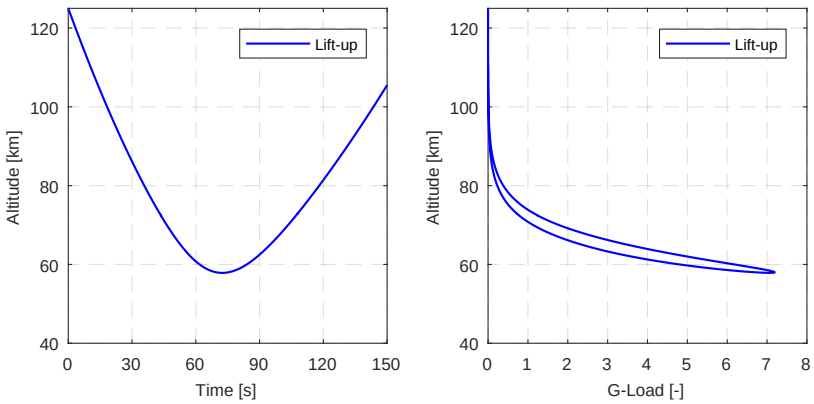

Figure 3.8: Lift-up trajectory and corresponding aerodynamic load factor for an entry performed on Earth with the nominal entry conditons by the CRM vehicle.

However, due to te Mars and Venus cases being added late into the research, no further analysis was performed regarding the Knudsen number on these planets or their effect on the aerodynamics, no concrete conclusion can be drawn. For now , the effect of the Knudsen number on Mars and Venus was ignore entirely, like it was for Earth. It is expected that this will have a negligible impact on the Venus case. If future research is done regarding aerocapture on these planets, especially Mars, this effect should be further investigated to determine the error induced by this assumption.

Reynolds number is a dimensionless parameter which expresses the ratio between the inertial and viscous forces. In less scientific words, the Reynolds number expresses the ratio between the mediums resistance to change due ot the passing of the body (inertia) and its desire to stick (viscosity) to the body and travel with it. The Reynolds number expresses how much the medium is effected by the passing of the body, and can be used as a measure for the size of the layer "sticking" to the body, also called the boundary layer. A very high Reynolds number means that flow is largely unaffected by the body, and a very thin boundary layer, whereas a low Reynolds number means the flow is highly disturbed by the presence of the body, and results in a thick boundary layer. The Reynolds number can be calculated according to:

$$Re = \frac{uL}{\nu} \tag{3.114}$$

In this equation u is the relative velocity between the body and the medium in ms^{-1}, L is a characteristic length in m, and ν is the kinematic viscosity of the medium in m^2s^{-1}. The characteristic length of both the SRM and CRM vehicle were taken as their diameter and are $\mathcal{O}(10^0)$, as stated in Table 2.4. Based on the reference missions discussed in Section 2.5, the relative velocity is approximately $\mathcal{O}(10^3)$ to $\mathcal{O}(10^4)$. The order of the kinematic viscosity for the Earth atmosphere was found to be $\mathcal{O}(10^{-3})$ at 175K, with it decreasing as the temperature increased. According to Petrosyan et al. (2011), the kinematic viscosity for Mars is $\mathcal{O}(10^{-3})$. Additionally, Petrosyan et al. (2011) states a value for Earth of $\mathcal{O}(10^{-5})$. It should be noted that, due to the late inclusion of the Venus case, no kinematic viscosity value was found for the Venusian atmosphere. Whatever conclusion was drawn based on the Earth and Mars atmosphere was also applied to the Venus atmosphere. Using these orders of magnitude, the order of the Reynolds number can be estimated to exceed $\mathcal{O}(10^6)$.

From this it can be concluded that the inertial forces are dominant in the considered case. According to Anderson (2006), the viscous interaction effects between the medium and the body can be neglected at such high Reynolds numbers. The effect of the flow viscosity was therefore ignored during this research for all trajectories, regardless of vehicle and planet.

3.6.2. Atmosphere Model

In the previous section it was made apparent that the aerodynamic forces depend on the local atmospheric conditions, and that thus an model of the atmosphere is needed to estimate these conditions. As atmospheres are unique to each planet, an individual model is needed for each of the three planets considered. Additionally, as in this research the analytical evaluation of the equations of motion is also considered, simple, analytical versions of the atmosphere models are required. In this research, the primary and single use of the atmosphere models is to determine the local atmospheric density such that the aerodynamic forces can be determined. While most atmosphere models provided additional information, such as atmospheric pressure, temperature, speed of sound, and molecular composition, our only interest is the density profile.

As stated, in addition to the three accurate atmosphere models for the three planets, three analytical approximations of the the density profiles are desired. In the next three sections, additional information regarding each of the atmosphere models, and the approximate analytical density profile will be presented.

Earth Atmsphere models For Earth the NRLMSISE-00 atmosphere model as selected. NLMSISE-00 is a empirical latitude, longitude, time (solar zenith angle, or local solar time, and solar-longitude), and altitude dependent atmosphere model. This model was selected as it is a highly accurate model and based on empirical density measurement data from a variety of satellites orbiting the Earth, that comes pre-installed with Tudat, the toolkit used during this research to facilitate the development of the numerical trajectory simulator. NRLMSISE-00 is a tabulated atmosphere model, meaning that the values are given at discrete states, and that values at intermediate states have to be obtained via interpolation. It is based on two older models, namely the MSIS-86 and MSISE-90 models. The model and appropriate unit-tests to ascertain the proper implementation are included in Tudat. As it comes pre-installed with Tudat, the interface between the model

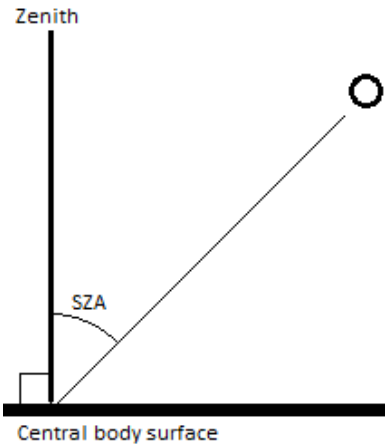

Figure 3.9: Schematic illustration of the Solar-Zenith-Angle

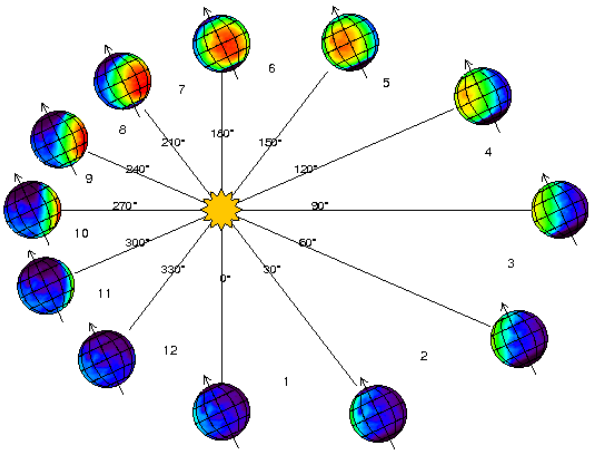

Figure 3.10: Schematic illustration of the Solar Longitude using Mars as an example[a]

. However, the definition is analogous to all planets.

[a]Retrieved from `http://www-mars.lmd.jussieu.fr/mars/time/solar_longitude.html`, accessed on 2019-01-31

and the simulation environment was already present and did not have to be produced. Additionally, as the interface was present, this model was kept as a latitude, longitude, time, and altitude dependent model.

Before continuing, some additional information regarding the dependent variables of the atmosphere model. The definition of the latitude and longitude have been given in Section 3.1, and the altitude will be further discussed in Section 3.6.3. The solar zenith angle (SZA) is a measure for the angle between a vector normal to the surface of the planet at a particular position, and the incoming solar rays. This is illustrated in Fig. 3.9. The SZA is measured positive westward to match the motion of the Sun through the sky. As the SZA depends on the normal vector of the planet's surface, it depends on the position of measurement. Hereinafter, unless otherwise specified, the SZA is always measured at zero-latitude-longitude. The Local Solar Time (LST) is a related concept that expresses the same angle, but expressed in time. For example, a LST of 00:00 (midnight), 06:00 (dawn), 12:00 (midday/noon), and 18:00 (dusk) correspond roughly to SZAs of 270° (or -90°), 0°, 90°, and 180°. it should be noted that, for the definition of LST, the hour on a planet (just like their Earth counterparts) is defined as lasting 1/24th of a solar day. Therefore, on any planet a LST of 12:00 corresponds to the Sun being directly overhead.

The last parameter to discuss is the solar-longitude. The solar longitude is the angle between the central body's northern hemisphere spring equinox and the current body-Sun position vector. This is illustrated in Fig. 3.10 for the planet Mars, but is analogous for all celestial bodies. This angle is a measure for the current season on the planet on the Northern Hemisphere. A solar longitude $L_s = 0°$ corresponds to the spring equinox (start of spring), $L_s = 90°$ corresponds to summer solstice (start of summer), $L_s = 180°$ corresponds to the autumn equinox (start of autumn), and $L_s = 270°$ corresponds to the winter solstice (start of winter).

With the definitions of the independent variables given, we return to discussing NRLMSISE-00. This model will be kept as it is available in Tudat. However, it is desired to have an idea of the variation to be expected from the model, as well as to investigate how well the exponential atmosphere, to be used for the analytical analysis, matches with this model.

In Fig. 3.11 the average is taken over latitude and longitude, leaving only the temporal variations. This time is varied over four different local solar times (00:00, 06:00, 12:00, and 18:00 GMT), and four different solar longitudes (0°, 90°, 180°, and 270°), resulting in a total of 16 atmosphere profiles from NRLMSISE-00. In addition to these averaged profiles, one profile is shown that is only altitude dependent, obtained by averaging over latitude, longitude, and time, two extreme profiles are shown, obtained by taking the minimal and maximal density value at each altitude, and an exponential atmosphere profile is shown.

In Fig. 3.12, the average is taken over the latitude and the times, leaving the longitudinal variation. In total the profile at 61 equally spaced longitude values between -180° and 180° are depicted in this figure. However, because of the minimal impact the longitude has on the density, this variation is imperceptible in this figure. Lastly, in Fig. 3.13, the average it taken over the longitude and time, leaving only the latitudinal variation. The

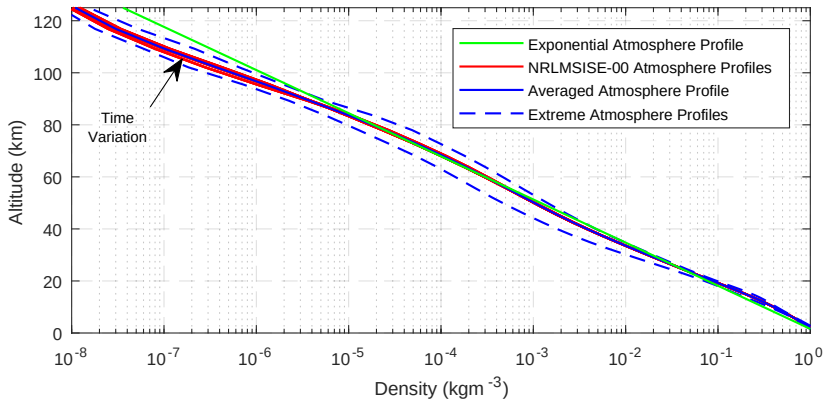

Figure 3.11: Time variation, extreme, and averaged density profiles of the NRLMSISE-00 atmosphere model.

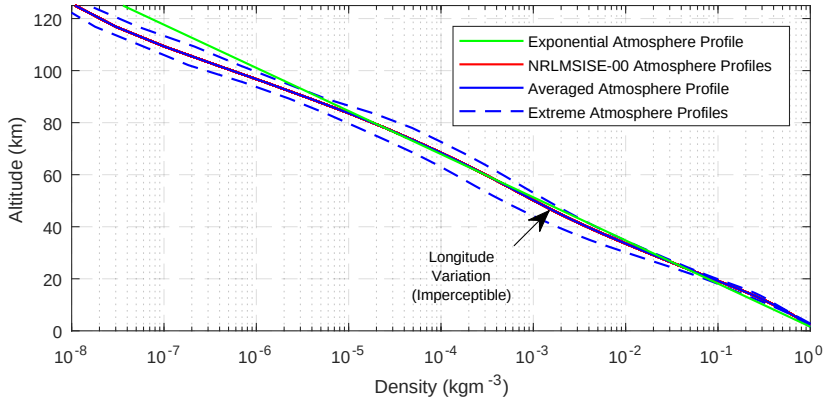

Figure 3.12: Longitude variation, extreme, and averaged density profiles of the NRLMSISE-00 atmosphere model.

profile at 31 equally spaced latitudes between -90° and 90° are shown.

By inspecting these figures the following conclusions can be drawn. The first conclusion is the remarkably good agreement between this exponential atmosphere model and the averaged NLRMSISE-00 profile, especially for the low and middle altitudes. The parameters of this exponential atmosphere model are provided in Table 3.2. Note that this is only one particular implementation of exponential atmosphere. Other exponential atmospheres can be developed when desired, as will be demonstrated later. However, form the remarkably good agreement between the average profile and the exponential atmosphere, especially at the lower altitudes where the aerodynamic forces effected by the density are dominant, this was deemed unnecessary.

The second observation is regarding the effect of the longitude, latitude, and time on the density profile. The fact that the longitude variations are so small that they are imperceptible in the above figure leads to the conclusion that for Earth's atmosphere any longitudinal dependency can be ignored with negligible error. Next, it was observed that the latitude dominates the variations in density for the lower altitude, whereas the time dominates the density variation at higher altitudes.

The single scale height exponential atmosphere was obtained by setting the mean density as 1.225 kgm^{-}3, and the scale height to 7.2 km[2].

[2]NASA Earth Fact Sheet, available at `https://nssdc.gsfc.nasa.gov/planetary/factsheet/earthfact.html`

Table 3.2: Earth exponential atmosphere model parameters

Model	scale-height (H_s) [m]	ρ_0 [kgm^{-3}]
Exponential Atmosphere	7200	1.245

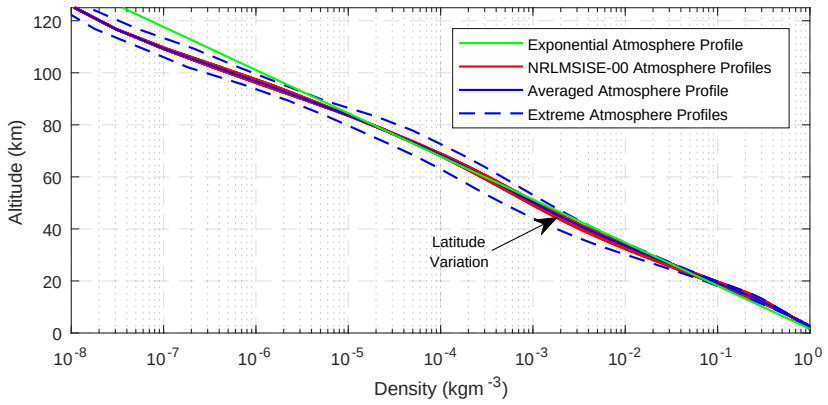

Figure 3.13: Latitude variation, extreme, and averaged density profiles of the NRLMSISE-00 atmosphere model.

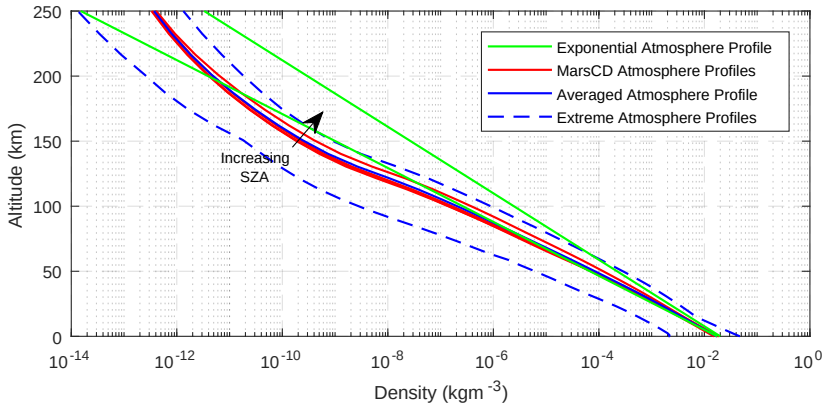

Figure 3.14: Solar zenith angle variation, extreme, and density averaged profiles of the ESA Mars Climate Database model.

Mars Atmosphere model For Mars a simplified version of the ESA Mars Climate Database (EMCD) was used. EMCD is also an latitude, longitude, time (solar zenith angle, or local solar time, and solar-longitude), and altitude dependent atmosphere model. According to Millour et al. (2018), the database is derived from numerical simulations using general circulation models, and subsequently validated using empirical data. This database did not come included in Tudat, and therefore had to implemented prior to use.

This was done primarily by Facchinelli (2019). A script was developed that would access the EMCD web interface and download a file that included the global atmospheric properties for the specified altitude and solar-longitude. Additionally, a new general interface in Tudat was created for loading multi-dependent variable tabulated atmosphere models from multiple data files, such as the script produced. By modifying the script, the ability to additionally specify the local solar time was added, the zero-altitude was changed from mean "sea"-level to surface level, and the altitudes for which the data was obtained was changed into something more appropriate for this research. Unfortunately, the interface was developed for an updated version of Tudat, and was not supported by the version of Tudat that was used during this research. Therefore, the EMCD had to be simplified down from a altitude, latitude, longitude, and time dependent model to just an altitude-dependent atmosphere model.

This was done by taking the average of the database over the longitude, latitude, and time. The results of this process can be seen in Figs. 3.14 to 3.16. In Fig. 3.14 the average is taken over the latitude and longitude, leaving only the time variations. In Fig. 3.15 the average of the time and latitude is taken, leaving the longitude variation. Lastly, in Fig. 3.16, the average of the time and longitude is taken leaving only the latitude variation. Additionally, in each graph the average profile obtained by averaging the the, latitude, and longitude, is shown, together with the two extreme profiles, and two exponential atmosphere profiles.

Three things can be noted from these figures. The first is that latitude, as expected, has the most significant impact on the density. The second is that the margins presented by the extremes are much wider than

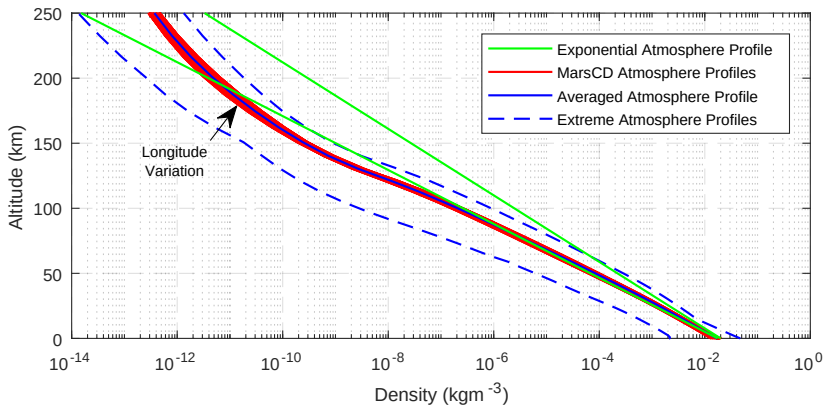

Figure 3.15: Longitude variation, extreme, and averaged density profiles of the ESA Mars Climate Database model.

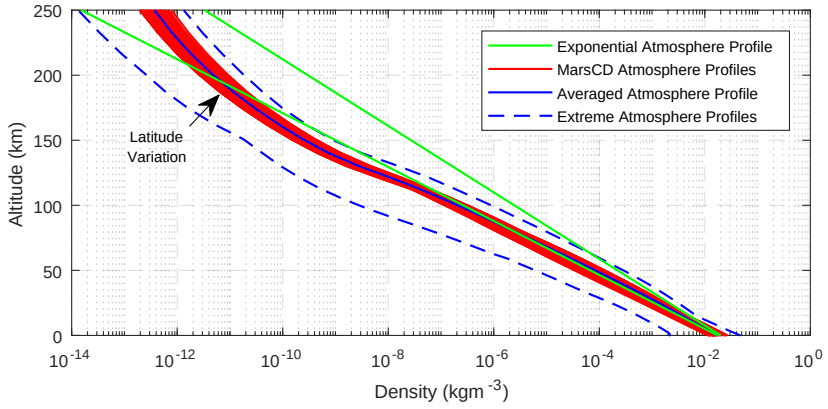

Figure 3.16: Latitude variation, extreme, and averaged density profiles of the ESA Mars Climate Database model.

Table 3.3: Mars exponential atmosphere model parameters

Model	scale-height (H_s) [m]	ρ_0 [kgm^{-3}]
Standard Exp. Atmosphere	11100	0.020
Custom Exp. Atmosphere	9000	0.01753

any of the individual contributions, and even all contributors summed together. These extreme profiles are the direct result of various surface feateurs on Mars, such as the tall volcanoes (Olympus Mons) and the deep Mare (Mare Erythraeum). Whiles these features are protruding or recessed compared to the mean surface, the surface value for the density is still taken with respect to them. This means that, for instance, for Olympus Mons, the surface density is taken nearly 25 km above the mean surface altitude, leading to a much lower density value at zero-altitude. A similar reasoning can be found for the maximum density profile. As in each of the graphs presented either the latitude, longitude, or both are averaged, the effect of these local features are largely removed from the density profile.

The third observation is that there is a reasonably well agreement between the steeper exponential atmosphere profile for the low to middle altitudes, whiles the higher exponential atmosphere starts deviating after the first approximately 20 km. As the majority of the trajectory, or at least the portion of the trajectory were the aerodynamic forces are dominant, will occur at these low to middle altitudes, the inaccuracy at the higher altitudes is not important. Additionally, at these higher altitudes, the absolute density is already sufficiently small that there the aerodynamic forces at these altitudes become negligible. The surface density and scale heights for the higher-density profile are those commonly reported for the Martian atmosphere[3]. However, it was found that the custom fitted atmosphere profile fits better for the purposes of this research, as it closer resembles the EMCD data. Therefore this custom exponential atmosphere model will be used for the analytical evaluation. The surface density and the scale height for both exponential atmosphere models are presented in Table 3.3

According to González-Galindo et al. (2009), the main limitation from the EMCD is the fact that no measurements are available above an altitude of 250 km. This however poses no issues for this research as the altitude range considered is far below this altitude. To improve the robustness of the simulator, above an altitude of 250 km, density value will be obtained by using the exponential atmosphere model. At an altitude of 250 km and above, the density values are already negligibly small, such that any aerodynamic force produced by them will also be negligible. Therefore, whilst the accuracy of the atmosphere model above 250 km is debatable, the introduce error will be insignificant.

Venus Atmosphere Model For Venus, a simplified version of Venus Global Reference Atmosphere Model, or VenusGRAM was used. VenusGRAM is an amalgamation of three other atmosphere profiles for different altitude ranges, based on the Venus International Reference Atmosphere (VIRA) profiles for those ranges. The profile for low altitudes, between the surface and 100 km altitude is altitude and latitude dependent. The profiles for the mid altitudes, between 100 km and 150 km, is altitude and local solar time dependent. Lastly, the profile for the high altitudes, between 150 km and 250 km, is altitude and solar zenith angle dependent. As the only shared dependency between the three profiles is their altitude dependence, it was opted to remove all dependencies but the altitude dependence, and create a single altitude dependent tabulated atmosphere model, similar to what had been done for the EMCD.

The atmosphere model was simplified down to an altitude-dependent profile by averaging the low profile over all latitudes, the middle profile over all solar-times, and the high profile over the zenith-angles. The latitude, local-solar-time, or solar-zenith-angle dependent profiles, together with the average profile, and two exponential atmosphere profiles are presented in Fig. 3.17.

In this image it two exponential atmosphere profiles are given. The first of these exponential atmosphere profiles uses only a single value for the surface density and scale-height. These values are reproduced in Table 3.4. However, it can immediately be noticed that, above approximately 50 km, this exponential atmosphere profile and the data obtained from VenusGRAM start to diverge significantly by multiple orders of magnitude. This is particularly bad as the expected altitudes flown by the trajectory are 50 km to 150 km. For this reason, a custom exponential atmosphere profile was fitted to closer match the data from VenusGRAM. This custom fit was made by approximating the averaged profile by three segments with constant scale height. As can be seen from the figure, this gives a much closer agreement with the averaged profile.

[3]NASA Mars Fact Sheet, available at `https://nssdc.gsfc.nasa.gov/planetary/factsheet/marsfact.html`

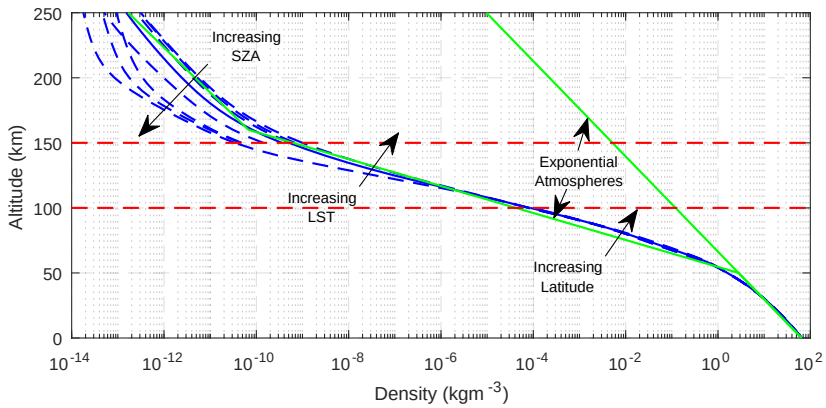

Figure 3.17: Original and averaged profiles of the Venus Global Reference Atmosphere Model.

Table 3.4: Venus exponential atmosphere model parameters

Model	scale-height (H_s) [m]	ρ_0 $[kgm^{-3}]$	h_0 [m]	ρ_0^* $[kgm^{-3}]$
Standard Exp. Atmosphere	15900	64.79	0	64.79
Low Altitude Exp. Atmosphere	15900	64.79	0	64.79
Mid Altitude Exp. Atmosphere	4500	2.7913	50000	186765.3
High Altitude Exp. Atmosphere	15000	$6.7594 \cdot 10^{-11}$	160000	$2.8986 \cdot 10^{-6}$

Initially the segments were fitted using he standard formulation for a part of the standard atmosphere with consistent scale-height, starting at a particular altitude, for which the equation is:

$$\rho = \rho_0 e^{-\frac{h-h_0}{H_s}} = \rho_0 e^{\frac{h_0}{H_s}} e^{-\frac{h}{H_s}} = \rho_0^* e^{-\frac{h}{H_s}} \tag{3.115}$$

where ρ_0 is the starting density for that layer of the atmosphere, h_0 the starting altitude of that layer of the atmosphere, h the altitude with respect to the surface, and H_s the scale height. ρ_0^* is the density at the surface if one would use the profile described by the scale-height for all altitudes. By describing the exponential atmosphere this way, and considering that it is expected that only altitudes in the range of 50 km to 150 km will be encountered, this single exponential atmosphere model can be used during the analytical approximation, without having to switch exponent or constant based on altitude. The parameters of the custom fitted exponential atmosphere model are also tabulated in Table 3.4. Note that using an exponential atmosphere model that features these discontinuities can lead to problems when designing guidance and control systems. The sudden change in slope of the density profile can, for instance, cause a spike in a given control. One way to circumvent this is to ensure a continuous derivative, and maybe even second derivative. This can be achieved by either fitting a second-order polynomial, or by using cubic splines to splice two sections with constant slopes. However, as in this research we are not dealing with control (perfect control assumed), this is not a problem.

From Fig. 3.17 it can also be seen that for the lower part of the atmosphere, there seems to be little latitude variation. Only halfway through the middle altitude profile and above can a "significant" dependency of density be observed. Whilst the deviation seems large, it should be noted that at this point, the density is already approximately a hundred-millionth of the surface density of Venus, or a millionth of the Earth's surface density. While the proportional error might be large, the absolute error is sufficiently small that the actual impact on the, potentially negligibly, small aerodynamic forces at these altitude will be negligible themselves. This is furthermore illustrated in Fig. 3.18. In addition to the error between the average profile and the dependent profiles is the error between the average profile and the custom fitted exponential atmosphere profile.

One last consideration for this atmosphere model is the limitation in its altitude. As was already stated the highest altitude supported bu the VIRA model is 250 km. Above this no data is available, similar to the case for EMCD. Above this altitude, values for the density will be obtained by using the exponential atmosphere model discussed. This causes the accuracy for the atmospheric model to drop considerably after 250 km. However, as can be seen from Fig. 3.17, at this altitude the density is already negligibly small. Therefore at these altitudes the resulting aerodynamic forces will also be negligibly small, and thus the introduced error

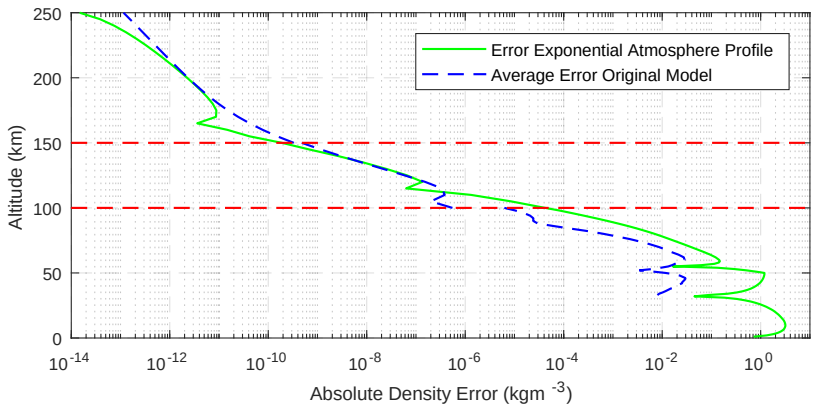

Figure 3.18: Absolute density error between the averaged Venus atmosphere profile and the custom fit exponential atmosphere model and the average error between the averaged Venus atmosphere profile and the original model.

in the simulation can be considered insignificant.

3.6.3. Central Body Shape

As mentioned in the discussion of the atmosphere model, the height at which the atmospheric conditions are estimated is based off of a reference surface. As planets are in reality not perfect spheres but rather oblique spheroids, the error in the estimation of the surface height can impact the estimation of the atmospheric conditions. For Earth the difference difference between the polar and equatorial radius is roughly 20 km[4]. If a spherical model for the Earth was used with a radius equal to the mean equatorial radius, the altitude of a vehicle above a pole would in reality be roughly 20 km higher. The vehicle would than be surrounded by less dense air. The relation for determining the central body's radius as a function of latitude provided by Mooij (2017) is

$$R(\delta) \approx \bar{R}_e(1 - f\sin^2\delta) \tag{3.116}$$

In this equation R is the body's radius at latitude δ, $\bar{R}_e$ is the mean equatorial radius, and f is the flattening parameter defined by

$$f = \frac{\bar{R}_e - \bar{R}_p}{\bar{R}_e} \tag{3.117}$$

here $\bar{R}_p$ is the mean polar radius. The altitude of the vehicle above the surface of the central body can be determined using the following equation

$$h(r,\delta) \approx r - R_e(1 - f\sin^2\delta) \tag{3.118}$$

where h represent the altitude of the vehicle above the surface of the body and r the magnitude of the positional vector of the vehicle with respect to the centre-of-mass of the body. By consulting the **?**, it was found that a built-in method for specifying the body shape as an oblate spheroid exists within the standard Tudat libraries.

The mean polar and equatorial radii for Earth[5] are 6356.752 km and 6378.137 km, respectively, resulting in a flattening parameter of 0.003353. For Mars[6], these values are 3376.2 km, 3396.2 km, and 0.005889, and for Venus[7], they are 6051.8 km, 6051.8 km, and 0.0. From these values it can be seen that for Mars the usage of a oblique spheroid model is even more important then it is for Earth. As for Venus, the mean polar and equatorial radius are the same, at least to the precision given in the source. Therefore an oblique spheroid model is not needed, as a circular body assumption would be accurate. However, as the shape model will be used for Earth and Mars, it will also be used for Venus.

[4]NASA Earth Fact Sheet, available at `https://nssdc.gsfc.nasa.gov/planetary/factsheet/earthfact.html`
[5]NASA Earth Fact Sheet, available at `https://nssdc.gsfc.nasa.gov/planetary/factsheet/earthfact.html`
[6]NASA Mars Fact Sheet, available at `https://nssdc.gsfc.nasa.gov/planetary/factsheet/marsfact.html`
[7]NASA Venus Fact Sheet, available at `https://nssdc.gsfc.nasa.gov/planetary/factsheet/venusfact.html`

Table 3.5: Mean equatorial and polar radii, the volumetric radius, and the resulting flattening parameter for Earth, Mars, and Venus.

Central Body	Mean equatorial [km]	Mean polar [km]	Volumetric [km]	flattening [-]
Earth	6378.137	6356.752	6371.000	0.003353
Mars	3396.2	3376.2	3389.5	0.005889
Venus	6051.8	6051.8	6051.8	0.0

Table 3.6: Constant and exponent vaues for three different convective heating models

Model	Constant C	Exponent M
Detra and Hidalgo (1961)	$5.16 \cdot 10^{-5}$	3.15
Sutton and Graves (1971)	$1.73 \cdot 10^{-4}$	3
Tauber and Meneses (1986)	$1.83 \cdot 10^{-4}$	3

In addition to having the more accurate oblique spheroid model to be used in the simulation, values for the surface radius of the central bodies are also required to determine that altitude of the vehicle above the surface in the analytical approximation. In these cases, the volumetric radius will be used to represent the mean surface radius of the central body. The volumetric radius is defined as the radius of a perfect sphere that has the same volume as the body it is supposed to model. The value of the volumetric radius will be somewhere in between the equatorial radius and the polar radius. The values of the volumetric radii were obtained from the same sources as the equatorial and polar radii. The mean equatorial and polar radii, the volumetric radius, and the resulting flattening parameter for each of the bodies are summarised in Table 3.5.

3.6.4. Aerodynamic Heating

Aerodynamic heating or aeroheating is a important factor in atmospheric hypersonic flight. Due to the high velocity, amount of heat can be generated during entry. An excessive amount of heat being generated can cause failure of the vehicle. It therefore forms a strong constraint. Unfortunately, most relations used to obtain an estimate that do not rely on full computational fluid dynamics are empirical, and thus not exact. Because of this, it is desired to find a conservative relation that most likely overestimates the heat flux, but ensures that the constraint is never violated.

According to Anderson (2006), aeroheating takes two forms. Heat is either transferred from the hot boundary layer surrounding the vehicle to the cooler vehicle surface via convective heating, or heat is transferred from the hot shock-layer that has a high enough temperature to emit thermal radiation, causing radiative heating. As these two modes of heat transfer differ, a model is required for both to obtain the total heat flux.

Convective heat flux can be approximate analytically by the following relation proposed by Sutton and Graves (1971)

$$q_w = C\sqrt{\frac{\rho_\infty}{R_n}}V_\infty^M \tag{3.119}$$

to estimated the heat flux due to convective heat transfer for an axisymmetric blunt body. Carandente et al. (2013) compares three popular sets of coefficients, namely those reported by Sutton and Graves (1971), Tauber and Meneses (1986), and Detra and Hidalgo (1961). The coefficients proposed by each of them is tabulated in Table 3.6. The results obtained by Carandente et al. (2013) are presented in Fig. 3.19.

From this it can be seen that the model proposed by Detra and Hidalgo (1961) is the most conservativ. Additionally, Carandente et al. (2013) states that the model proposed by Detra and Hidalgo (1961) has an accuracy of 10% for velocities between 1.8 kms^{-1} and 8 kms^{-1} and for altitudes up to 70 km when compared to an accuracy CFD analysis. For these reasons this model will be used for the estimation of the convective heat loading.

However, one modification must be applied before the equation can be used. The relation provided by Sutton and Graves (1971) is for analysis of heat transfer to a cold war. During reentry, the surface of the vehicle will heat up relatively fast. Therefore a conversion should be added to taken into account the wall temperature. By using the relation proposed by Anderson (2006) and the coefficients from Detra and Hidalgo (1961), the relation as initially proposed by Sutton and Graves (1971) for a cold wall becomes

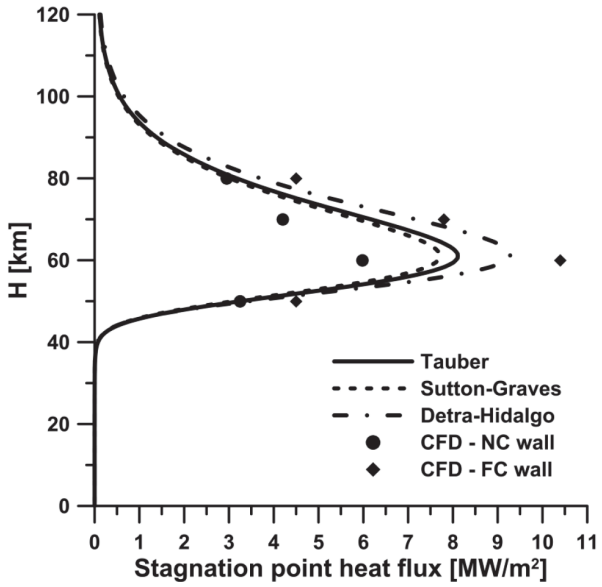

Figure 3.19: Results of the comparison between the Detra and Hidalgo (1961), Sutton and Graves (1971), and Tauber and Meneses (1986) models, and two CFD models. From this graph it can clearly be seen that of the three models tested, the model proposed by Detra and Hidalgo (1961) is the most conservative. Carandente et al. (2013).

$$q_{conv} = 5.16 \cdot 10^{-5} \sqrt{\frac{\rho_\infty}{R_n}} V_\infty^{3.15} \left(1 - \frac{h_w}{h_0}\right) \tag{3.120}$$

In this relation q represents the heat transferred, R_n the nose radius of the capsule, and h_w and h_0 the enthalpy at the wall and total enthalpy, respectively. By using the linear relation between the enthalpy and the temperature, the fractions of enthalpies can be rewritten to a fraction of temperatures. Subsequently assuming that the total temperature is the same as the adiabatic wall temperature, the equation can be rewritten into

$$q_{conv} = 5.16 \cdot 10^{-5} \sqrt{\frac{\rho_\infty}{R_n}} V_\infty^{3.15} \left(1 - \frac{T_w}{T_{w_{ad}}}\right) \tag{3.121}$$

where the wall temperature T_w is determined by satisfying thermal equilibrium. This will be discussed last, after radiative heat transfer has been discussed. The adiabatic wall temperature $T_{w_{ad}}$ can be approximated by by

$$T_{W_{ad}} \approx \frac{V_\infty^2}{2c_p} \tag{3.122}$$

Radiative heat flux is heat transferred from the hot shockwave through the means of radiation. This type of heat transfer only occurs for entries at very high velocities, such as the hypersonic entry considered in this research. According to Tauber and Sutton (1991), an approximation for radiative heating in the stagnation-point of a vehicle in the Mars or Earth atmospheres is given by:

$$q_{rad_{stag}} = C R_n^a \rho^b f(V) \tag{3.123}$$

In this equation $f(V)$ is a function of velocity for which the values can be obtained by interpolating a table with velocities ranging between 9 kms^{-1} and 16 kms^{-1} for Earth, and between 6 kms^{-1} and 9 kms^{-1} for Mars. Above these values the value of $f(V)$ is taken as constant, and below these values it is assumed there is no radiative heat transfer. These values are presented in Table 3.7 and Table 3.8 for Earth and Mars, respectively. Below a velocity of 9 kms^{-1} for Earth, and 6 kms^{-1} for Mars, radiative heat transfer is assumed to be negligibly small. Tauber and Sutton (1991) also reports values for the coefficients in his formula. For Earth these coefficients are

Table 3.7: Radiative heating functions for Earth entry. Tauber and Sutton (1991)

V [kms^{-1}]	9	9.25	9.5	9.75	10	10.25	10.5	10.75	11	11.5
f_E(V)	1.5	4.3	9.4	19.5	35	55	81	115	151	238
V [kms^{-1}]	12	12.5	13	13.5	14	14.5	15	15.5	16	
f_E(V)	359	495	660	850	1065	1313	1550	1780	2040	

Table 3.8: Radiative heating functions for Mars entry. Tauber and Sutton (1991)

V [kms^{-1}]	6	6.15	6.3	6.5	6.7	6.9	7	7.2	7.4
f_M(V)	0.2	1.1	1.95	3.45	5.1	7.1	8.1	10.2	12.5
V [kms^{-1}]	7.6	7.8	8	8.2	8.4	8.6	8.8	9	
f_M(V)	14.8	17.1	19.2	21.4	24.1	26.0	28.9	32.8	

$$\begin{aligned} C &= 4.736 \cdot 10^4 \\ a &= 0.6 \\ b &= 1.22 \end{aligned} \tag{3.124}$$

and for Mars these coefficient are

$$\begin{aligned} C &= 2.35 \cdot 10^4 \\ a &= 0.526 \\ b &= 1.19 \end{aligned} \tag{3.125}$$

For the radiative heat flux for Venusian entry, a method used by Craig and Lyne (2002) was used. This method provides a single base equation that is to be evaluated using different coefficients. The value of the coefficients depend on the velocity. The base equation proposed is

$$q_{rad_{stag}} = C R_n^{0.49} \rho^{1.2} V^M \tag{3.126}$$

where the constant C and the exponent M are to be determined based on the current relative velocity according to the velocity ranges tabulated in Table 3.9. For velocities above 12 kms^{-1}, the radiative heat flux is approximated by evaluating the form of the equation at 12 kms^{-1}. Similarly, for velocities above 16 kms^{-1} for Earth, and 9 kms^{-1} for Mars, their respective radiative heat flux is approximated by using $f_E(16)$ and $f_M(9)$, respectively.

By comparing this equation to the one used for the Earth and Mars based radiative heat flux, and even the cold-wall convective heat flux, it was noticed that a single general expression can be developed that fits all these models, only with different constants and coefficients. The general equation for heat load is:

$$q_{\text{general}} = C R_n^a \rho^b V^M f(V) \tag{3.127}$$

By setting the constant C, the exponents a, b, and M, and the function f to their respective values as reported throughout this section, each of the four different models for convective and radiative heat flux can be obtained from this one expression, with the caveat that the convective heat loading is for a cold-wall and not a hot wall. This, however, might be beneficial as the cold wall assumption makes the approximation more conservative. The adiabatic wall temperature is larger than the equilibrium wall temperature. Therefore the ratio between the two is smaller than one, and one minus this ratio is positive but less than one, resulting in a lower convective heat flux estimate.

Table 3.9: Radiative heating functions for Venus entry, as reported by Craig and Lyne (2002)

Velocity range [kms^{-1}]	Constant C	Exponent M
≤8	$3.33 \cdot 10^{-34}$	10.0
8 - 10	$1.22 \cdot 10^{-16}$	5.5
10 - 12	$3.07 \cdot 10^{-34}$	1.2

Table 3.10: Spherical harmonics coefficients for the EGM96 Earth gravitational potential model, truncated at (4, 0).

n	m	$J_{n,m}$ [-]	$\Lambda_{n,m}$ [°]
2	0	-0.48417·10^{-3}	0
2	1	-0.18699·10^{-9}	0.11953·10^{-8}
2	2	0.24391·10^{-5}	-0.14001·10^{-5}
3	0	0.95725·10^{-6}	0
3	1	0.20300·10^{-5}	0.24851·10^{-6}
3	2	0.90463·10^{-6}	-0.61902·10^{-6}
3	3	0.72107·10^{-6}	0.14143·10^{-5}
4	0	0.53987·10^{-6}	0

Table 3.11: Spherical harmonics coefficients for the JGMRO120d Mars gravitational potential model, truncated at (4, 0).

n	m	$J_{n,m}$ [-]	$\Lambda_{n,m}$ [°]
2	0	-0.87502·10^{-3}	0
2	1	0.40223·10^{-9}	0.23032·10^{-10}
2	2	-0.84633·10^{-4}	0.48939·10^{-4}
3	0	-0.11897·10^{-4}	0
3	1	0.38050·10^{-5}	0.25177·10^{-4}
3	2	-0.15947·10^{-4}	0.83624·10^{-5}
3	3	0.35056·10^{-4}	0.25571·10^{-4}
4	0	0.51290·10^{-5}	0

Thermal equilibrium is that state in which all the heat transferred to the wall is radiated back out of the wall to the environment. By assuming thermal equilibrium one can equate the outbound radiation to the inbound convection and radiation. The equation for the thermal equilibrium is

$$q_{conv} + q_{rad} = C\sqrt{\frac{\rho_\infty}{R_n}}V_\infty^3\left(1 - \frac{T_{w,eq}}{T_{w_{ad}}}\right) + q_{rad} = \sigma\epsilon T_{w,eq}^4 \tag{3.128}$$

where σ is the Stefan-Boltzmann constant and ϵ is the emissivity of the surface. The current estimate for the Stefan-Boltzmann constant is 5.670367·10^{-8} $Wm^{-2}K^{-4}$, and the emissivity of the Apollo CM was roughly 0.8 according to Robinson et al. (2009). The purpose of assuming a thermal equilibrium is that it allows for the calculation of the equilibrium wall temperature, which was needed in a previous equation.

3.6.5. Gravitational Model

The last environmental model to be considered is that for the gravitational field. The gravitational field model is used to determine the strength and direction of the gravitational acceleration dependent on the position of the vehicle. For Earth and Mars, gravitational field models that come pre-defined with Tudat were used. For Venus no standard gravitational field model was available within Tudat. Because of the later inclusion of the Venus case in the research, a simpler central gravity field model was selected for Venus. The models in Tudat for Earth and Mars are spherical harmonic models.

The first several coefficients for the spherical harmonics models available in Tudat for Earth and Mars are tabulated in Table 3.10 and Table 3.11, respectively. From these tables it can be concluded that the $J_{2,0}$, or simply J_2 term is the most significant by almost two orders of magnitude for both the Earth and Mars case. For this reason only the effect of the J_2 term on of the spherical harmonics will be included in the simulation by specifying the model to be truncated there.

Expressions for the gravitational acceleration along each axis in Cartesian coordinates perturbed by the J_2 term of the spherical harmonics model were obtained from Wakker (2015):

$$\begin{aligned} g_x &= -\frac{3}{2}\mu J_2\frac{R^2}{r^5}x(1-\frac{z^2}{r^2}) \\ g_y &= -\frac{3}{2}\mu J_2\frac{R^2}{r^5}y(1-\frac{z^2}{r^2}) \\ g_z &= -\frac{3}{2}\mu J_2\frac{R^2}{r^5}z(1-\frac{z^2}{r^2}) \end{aligned} \tag{3.129}$$

Table 3.12: Tabulation of the standard gravitational parameters for the three considered central bodies. These values were obtained from Wakker (2015)

Central body	Standard gravitational parameter [m^3s^{-2}]
Earth	$3.9860044188 \cdot 10^{14}$
Mars	$4.2828372 \cdot 10^{13}$
Venus	$3.248599 \cdot 10^{14}$

The benefit of expressing the gravitation acceleration in an inertial reference frame is that it can be directly added to the equations of motion without needing to first be transformed to the inertial reference frame. Writing these three in the vector notation as was used in the description of the Cartesian dynamic equation, the following form is obtained:

$$\mathbf{G}|_I = \left(g_x, g_y, g_z\right)^T \tag{3.130}$$

As was stated, for Venus no spherical harmonic model was used, but a central gravity field model was applied. In the case for Venus, and the analytical approximations where the central gravity field model is also used, the following equation can be evaluated to obtain the radial component of the gravitational acceleration:

$$g = \frac{\mu}{r} = g_0 \frac{R_0^2}{r^2} \tag{3.131}$$

In this equation, μ is the standard gravitational parameter, for which the values are tabulated in Table 3.12. Using the central gravity field model only a radial component of acceleration is considered, so the above equation is the only equation for this model.

II

Part II: Software

4

Numerical Methods

In this chapter the diirfferent numerical methods that are used throughout the research are discussed. For each numerical method an overview of the purpose and functionality (often in mathematical terms) of the algorithm is provided. The methods discussed in this chapter, in the order that they are discussed are root-finding in Section 4.1, interpolation in Section 4.2, integration in Section 4.3, and optimisation in Section 4.4.

4.1. Root-Finding Routine

A root-finding algorithm can be used to determine the value(s) of the arguments of a function f, for which $f = 0$. The primary purpose of root-finding in this research was to determine the value for the switch-time for the lift-up lift-down bang-bang trajectory for which $\Delta V_2 = 0$. In this research only the very rudimentary bisection method for root-finding was used. The reason for this will be discussed in Section 9.2.

4.1.1. Bisection Method

The bisection method is one of the simplest root finding schemes available. While it is possible to use a bisection method for two- or multidimensional functions, this significantly increases the complexity of the method. Those interested are referred to the works by Martin and Rayskin (2016) and Bachrathy and Stepan (2012), respectively. In this section only the application of the bisection method for one-dimensional functions is considered.

This scheme can be used for any function for which two values with the opposite sign are known. This method uses the fact that a function must cross the zero-axis for the function to transition from positive to negative, or from negative to positive. The intersection with the zero-axis is estimated to fall on the centre of the interval between the two nodes. If the value of the function at the centre is positive, than the node that previously corresponded to the positive values is replaced by the value of the central node. Likewise, if the function was evaluated to be negative at the central node, the negative node is replaced. In mathematical terms, the algorithm can be expressed as follows:

$$x_0 < x_1$$
$$f(x_0) < 0$$
$$f(x_1) > 0$$
$$x_2 = \frac{x_1 - x_0}{2}$$
$$x_3 \begin{cases} \frac{x_2 - x_0}{2} & \text{if: } f(x_2) > 0 \\ \frac{x_1 - x_2}{2} & \text{if: } f(x_2) < 0 \end{cases}$$

These steps are repeated until the size of the interval is sufficiently small such that a sufficiently accurate estimate is obtained. The accuracy of this method doubles with every iteration. The absolute error in the estimate of the root, as a function of the initial interval and the number of iterations is:

$$\epsilon = \frac{(x_1 - x_0)}{2^n} \tag{4.1}$$

where x_0 and x_1 are the two original nodes, n is the number of iterations performed, and ϵ is the absolute error.

There are two benefits to using this method. The first is that it is very simple to implement, requiring only one equation to obtain the centre of the interval, and an if-statement to replace the upper or lower bound of the interval.

The second benefit is that it does not rely on the derivative of the function of which the root is desired. This is beneficial for this research, as the derivative of the apoapsis altitude with respect to the switch-time is unknown, but the value can be obtained by simply simulating the trajectory using a particular switch time.

Technically the local derivative could be approximated by slightly varying the switch time and determining the derivative by assuming a constant slope during the interval. However, this method runs into problems when no value for the apoapsis altitude is available, such as when the trajectory results in the vehicle never leaving the atmosphere. In these cases, the value set for the apoapsis altitude is that for the lower termination altitude. Varying the switch-time slightly will most likely result in the same value, resulting in a zero derivative.

For the bisection method, the apoapsis altitude at the lower termination altitude simply counts as an undershoot, a negative value. This causes the particular switch time value to replace the previous switch-time, delaying the switch for the next iteration, resulting in the vehicle potentially leaving the atmosphere.

4.2. Interpolation Routine

Interpolation is needed when data is only available at discrete nodes, and values are desired that are not available on these nodes. Interpolation is the process of approximating the value of the dataset for these internodal values. In this research interpolation is used primarily with the environmental models, the aerodynamic model, and the aeroheating function for the radiative heat flux proposed by Sutton and Graves (1971). Unless otherwise specified, the information regarding and description of the interpolation methods is obtained from Kress (1991), and Klees and Dwight (2018).

Two types of interpolation are used in this research. For instance, the interface in Tudat that interpolates the aerodynamic model to obtained the value of the aerodynamic coefficients at unspecified values of the Mach number is a linear interpolator. For the aeroheating models a cubic Hermite spline interpolation method is used.

A final consideration is what happens at the boundary of the data set. While normally the approximation of data outside of the given set is a matter of extrapolation, it will be treated here as it does not warrant its own section. When a value is desired that exceed the dataset, the value is set to equal the closest node. Consider, for instance, the aerothermal model discussed in Section 3.6.4. For Earth, if the velocity exceeds 16 kms^{-1}, the value of f_E will be set equal to 2040.

4.2.1. Linear Interpolation

Linear interpolation is one of the simplest for of interpolation. This method connects adjacent nodes using linear relations. The value for a point between two nodes is determined by evaluating the linear relation connecting the two nearest nodes. The one-dimensional linear interpolation estimate $\phi(x)$ of the function $f(x)$ between the two known data points x_i and x_{i-1} is

$$\phi(x) = f(x_i) + \big(f(x_{i-1}) - f(x_i)\big)\frac{x - x_i}{x_{i+1} - x_i} \tag{4.2}$$

4.2.2. Cubic Spline Interpoplation

Similar to the linear interpolation, the spline interpolation connects adjacent nodes and uses the connection to approximate the value between the nodes. As the name implies, a cubic spline interpolation uses cubic (third-order/degree) polynomials. By using third-order polynomials the first and second-order derivatives of two adjacent splines can be made to match at the node at which they meet, in addition to having matching values.

For a data set consisting of $p+1$ nodes, a total of p polynomials P_i can be fitted between the nodes. Defining that the polynomial fitted between the first two points (x_0 and x_1) is P_0, results in the definition that $i = 0, 1, \ldots, p-1$ for $p+1$ nodes. The equations of a polynomial P_i that is fitted between the i^{th} and $i+1^{\text{th}}$ node, and its first two derivatives are

$$P_i(x) = a_i(x - x_i)^3 + b_i(x - x_i)^2 + c_i(x - x_i) + d_i \tag{4.3}$$

$$P_i'(x) = 3a_i(x-x_i)^2 + 2b_i(x-x_i) + c_i \tag{4.4}$$

$$P_i''(x) = 6a_i(x-x_i) + 2b_i \tag{4.5}$$

When $P_i(x)$ is evaluated at the node x_i, $x - x_i = 0$. This means that $P_i(x_i) = d_i = f_i$, where f_i is the value of the function at node i. A relation between the coefficient a_i and b_i can be obtained using the fact that $P_i''(x) = P_{i+1}''(x)$ where $i \neq p$, or $P_i''(x) = P_{i-1}''(x)$ where $i \neq 0$. The resultant relation is

$$a_i = \frac{b_{i+1} - b_i}{3(x_{i+1} - x_i)} = \frac{b_{i+1} - b_i}{3h_i} \tag{4.6}$$

where $h_i = x_{i+1} - x_i$. By inserting this result into the equation for P_i together with $d_i = f_i$, the following relation for the coefficient c_i and b_i can be obtained:

$$c_i = \frac{f_{i+1} - f_i}{x_{i+1} - x_i} - \frac{x_{i+1} - x_i}{3}\Big(2b_i + b_{i+1}\Big) = \delta_i - \frac{1}{3}h_i\Big(2b_i + b_{i+1}\Big) \tag{4.7}$$

where h_i has the same definition as before and δ_i is given by:

$$\delta_i = \frac{f_{i+1} - f_i}{h_i} \tag{4.8}$$

Using the above relations for the coefficient together with the condition that $P_i'(x) = P_{i+1}''(x)$ where $i \neq p$, or $P_i'(x) = P_{i-1}'(x)$ where $i \neq 0$, the following system of equations in terms of b_i can be obtained:

$$h_{i-1}b_{i-1} + 2(h_{i-1} + h_i)b_i + h_i b_{i+1} = 3(\delta_i - \delta_{i-1}) \tag{4.9}$$

For a data set with $p+1$ nodes, and thus $p+1$ unknowns, a system of $p-1$ equations is obtained. To obtain sufficient number equations, the values for a_0 and a_{p-1} are assumed to equal those of the adjacent polynomial, thus $a_0 = a_1$ and $a_{p-1} = a_{p-2}$, which results into two additional equations:

$$h_1 b_0 - (h_0 + h_1)b_1 + h_0 b_2 = 0 \tag{4.10}$$

$$h_{p-1}b_{p-2} - (h_{p-2} + h_{p-1})b_{p-1} + h_{p-2}b_p = 0 \tag{4.11}$$

With these two additional equations, a set of $p+1$ linear equations for $p+1$ unknowns is obtained. This set of equations can be expressed in matrix form as $\mathbf{HB} = 3\delta$, where $\mathbf{H}$ is a matrix containing linear combinations of the values for h, δ contains the difference between δ of two sequential nodes, and $\mathbf{B}$ contains the coefficients b_i. This linear system can easily be solved to obtain the coefficients b_i, which can in turn be used to calculate a_i, and c_i.

Hermite Splines

One issue with spline interpolation is the apparition of overshoots in the interpolating splines. These overshoots are often caused by rapid changes of the derivative of the original data. According to Fritsche and Carlson (1980), a modification on the general cubic splines with the purpose of tackling these overshoots are the Hermite splines. The Hermite splines ensure that on any particular interval (not just the interval between two points, but an interval across multiple points), the fitted spline respects any monotonicity the data exhibits. If the data on a particular interval is ever decreasing, all polynomials $P_i(x)$ on that interval show the same behaviour. If the node i represents a local extreme so does the end $P_i(x)$ and the start of $P_{i+1}(x)$.

Hermite splines are polynomials that match the value, and the value of the first $k_j - 1$ derivatives of a function f at the adjacent nodes, according to:

$$P^{(k)}(x_i) = f^{(k)}(x_i) \tag{4.12}$$

where $k = 0, 1, \ldots, k_j$. If only the value needs to be matched, two conditions are imposed on the spline. If also the first derivative needs to be matched, four conditions, and so forth. To satisfy these $p+1$ conditions, a p^{th}-order polynomial is needed. By that logic, a cubic (3^{rd}-order) Hermite polynomial can satisfy $3+1$ conditions; a matching value, and matching first-order derivative at each node.

The expression for the cubic Hermite polynomial P_i that is fitted between the i^{th} and $i+1^{\text{th}}$ node is:

$$P_i(x) = f_i\left(1+2\frac{x-x_i}{x_{i+1}-x_i}\right)\left(\frac{x-x_{i+1}}{x_i-x_{i+1}}\right)^2 + f_i'\left(x-x_i\right)\left(\frac{x-x_{i+1}}{x_i-x_{i+1}}\right)^2 + f_{i+1}\left(1+2\frac{x-x_{i+1}}{x_i-x_{i+1}}\right)\left(\frac{x-x_i}{x_{i+1}-x_i}\right)^2 + f_i'\left(x-x_{i+1}\right)\left(\frac{x-x_i}{x_{i+1}-x_i}\right)^2 \tag{4.13}$$

This equation can be written in the same polynomial form as was used previous, in terms of coefficient a through d, through the following definitions:

$$a_i = 2\frac{f_i - f_{i+1}}{h_i^3} + \frac{f_i' + f_{i+1}'}{h_i^2} \tag{4.14}$$

$$b_i = 3\frac{f_{i+1} - f_i}{h_i^2} - 2\frac{f_i' + f_{i+1}'}{h_i} \tag{4.15}$$

$$c_i = f_i' \tag{4.16}$$

$$d_i = f_i \tag{4.17}$$

where h_i is again defined as $h_i = x_{i+1} - x_i$. The downside of this method is that it requires the values of the derivative of the function insead of just the value itself. Kahaner et al. (1988) propose a method to obtain estimates for the derivative.

As stated, if the node represents a local extremum, so will the two polynomials attached to this node. This means that at this node, the derivative is zero, or $f_i' = 0$. Recalling the definition of $\delta_i = (f_{i+1} - f_i)/h_i$, if f_i' represents a local maxima, then δ_{i-1} and δ_i will have opposite signs. Additionally, it was stated that monotonicity is attempted to be preserved. If two sequential nodes have the same value, either δ_{i-1} or δ_i will be zero. In this case too, $f_i' = 0$.

In the other cases, where δ_{i-1} and δ_i are non-zero and have the same sign, a value for f_i' is computed using a linear combination of δ_{i-1} and δ_i:

$$f_i' = \frac{3(h_{i-1} + h_i)}{\frac{2h_{i-1}+h_i}{\delta_i} + \frac{h_{i-1}+2h_i}{\delta_{i-1}}} \tag{4.18}$$

At the first and last points, $i = 0$ and $i = p+1$, the values for δ_{i-1} and δ_i cannot be calculated due to missing data. If $\delta_0 = 0$, $f_0' = 0$, else:

$$f_0' = \frac{(2h_0 + h_1)\delta_0 - h_0\delta_1}{h_0 + h_1} \tag{4.19}$$

except for the situation where the sign of the calculated f_0' is opposite to the sign of δ_i, in which case $f_0' = 0$, or when $f_0' > 3\delta_0$, in which case $f_0' = 3\delta_0$. Similarly, for f_{p+1}':

$$f_{p+1}' = \frac{(2h_p + p_{p-1})\delta_p - h_p\delta_{p-1}}{h_p + h_{p-1}} \tag{4.20}$$

unless the sign of f_{p+1}' is opposite to δ_p or $\delta_p = 0$, in which case $f_{p+1}' = 0$, and $f_{p+1}' <= 3\delta_p$.

4.3. Numerical Integration Routine

Numerical integration is the process of solving ordinary differential equations (ODEs) that are subject to either initial or boundary values. According to Kress (1991), in general no explicit solutions exist to solve differential equations, and numerical methods are required to do so. The equations of motion that govern the trajectories that are desired to be simulated are ODEs. Therefore, to simulate the trajectories, a numerical integration method is needed.

For this research two numerical integration methods were needed. One relatively simple integration method was desired for the first- and second-order analytical approach and was selected primarily for its simplicity. The second integration method was used in the numerical simulation to obtain accuracy trajectory simulations. For this method both accuracy and speed were desired.

In this section first the trade-off between single-step or multi-step numerical integrators is made. Following this, a trade-off is made to evaluate if the use of an adaptive order and step-size is advantageous in terms of computational time, while not detracting from the accuracy of the method.

Table 4.1: Computational times and RMS differences for three single-step and a multi-step numerical integration method.

Method	C.Time [ms]	RMS Position Difference [m]	RMS Velocity Difference [ms^{-1}]
RKF4(5)	3325	0.0002	0.0000
RKF5(6)	4429	0.0004	0.0000
RKF7(8)	6776	-	-
ABAM(4)	1270	0.7122	0.0008
ABAM(6)	1246	0.7122	0.0008
ABAM(8)	1275	0.7124	0.0008

4.3.1. Integrator Type Trade-Off

In general, two types for numerical integration can be distinguished, single-step and multi-step. The distinction is made depending on how the method advances to the next state. The single-step methods only uses the current node, determines a number of intermediate nodes, and uses a linear combination of these intermediate nodes to advance to the next state. The multi-step method on the other hand uses a linear combination of a number previous states to advance to the next.

According to Kress (1991), the primary advantage of multi-step methods over single-step methods, such as the Runge-Kutta family of methods, is that for an arbitrary convergence order, each new step only requires a single evaluation of the function (two evaluations if a predictor-corrector is used), whereas for the single-step method a number of evaluations is required. This results in multi-step methods generally being faster than single-step methods for the same convergence order.

Two things have to be taken into consideration when regarding the history required for the linear multi-step method. The first is the availability of the state history. At the start of the integration, only the initial value is available. At this point, one can either lower the order (and thus the required history) of the multi-step method to the available history size or use a single-step method until sufficient history has been generated. When sufficient history has been generated, the desired order multi-step method can be used from that point onward.

The second consideration is that the history is required to be consistently space. This means that if a variable step-size method is used and the step-size is changed, the history has to be regenerated. However, by carefully changing the step-size, a portion of the existing history can be used for the new step-size. For instance, if the step-size is multiplied by an integer value, for instance three, every third node in the previous history can be reused. If the stored history is of sufficient size, the step-size could increase without having to generate any additional nodes.

When lowering the step-size, a portion of the history can be reused similarly. If, for instance, the step-size is halved, every other node is still part of the new required history. In this case however, in between each available node a new node is required. These new nodes could be obtained from single step integration from the node ahead of it, or by interpolating between the two adjacent nodes. The effect of using an adaptive step-size will be discussed in the next subsection.

To evaluate the computational speed and comparative accuracy of the single-step and multi-step method, both methods were used to simulate the nominal Earth-CRM trajectory up to a specific time, in this case 150s after entry, using a fixed step size of 0.01s. The final Cartesian state was recorded, and the root-mean-square (RMS) difference in terminal position and velocity was determined. For the single-step methods, the Runge-Kutta-Fehlber (RKF)45, RKF56, and RKF78 methods were used. These three methods were used to evaluate the effect of increasing order on the accuracy and computational time. For the multi-step method a fourth, sixth, and eighth-order Adams-Bashforth Adams-Moulton was used. The results from this effort are tabulated in Table 4.1.

From this table it can be seen that indeed the multi-step method is much faster than the single-step methods, almost outperforming the fastest single-step method by a factor three. Additionally, it can be seen that the computational speed of the multi-step method does not depend on the order of the method used. Regarding accuracy, it is clear that differences exists between the two methods. However, from this evaluation it cannot be determined which of the two is more accurate. The only reason why the RKF methods have smaller RMS differences than the ABAM methods in this table, is because the RKF7(8) method was used as the reference to determine the difference. If the ABAM(8) method was chosen as the reference, the values for the differences would be flipped. It can therefore not be determine which of these two methods is more accurate. Based on this, it was decided to use the multi-step method to take advantage of the increase in speed.

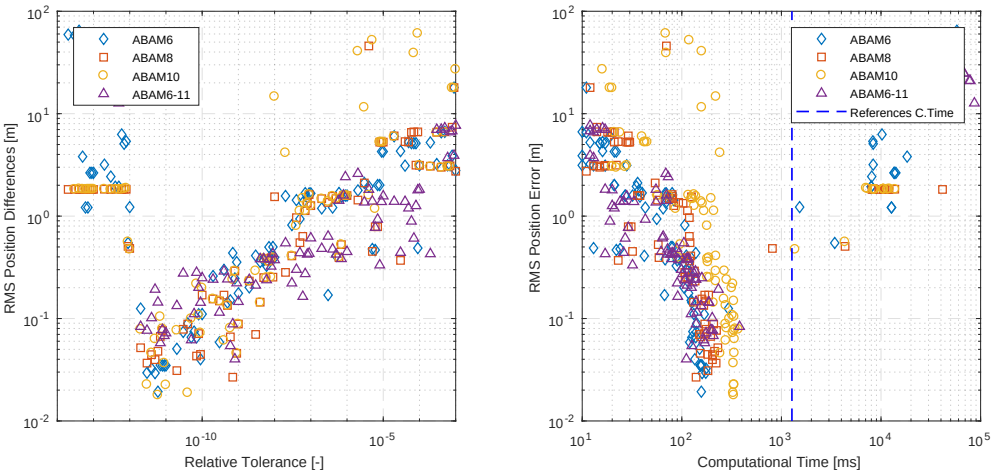

Figure 4.1: Position RMS difference and computation time forthree fixed order, variable step-size, and one variable order, variable step-size Adams-Bashforth Adams-Moulton method.

4.3.2. Adaptive Order and Step Size Trade-off

The next trade-off was regarding the use of an adaptive order and/or step-size. This trade-off was performed by simulating the same nominal Earth-CRM trajectory as for the previous trade-off using ABAM methods with various orders and relative tolerances.

From these simulations the RMS position error with respect to the fixed step-size ABAM8 method was used as an indication for the achieved accuracy. In Fig. 4.1 the result from three fixed-order and a single variable-order method are shown. The left graph shows the RMS position differences as a function of the relative tolerance, and the right graph shows the corresponding computational time. Additionally, in the right graph the computational time required by the fixed step-size ABAM method from the previous trade-off is indicated as a references.

Regarding the position accuracy, it can be observed that for relatively large allowed relative tolerances the variable order method performs best. However, as the relative tolerance decreases, the accuracy of the three fixed order methods surpasses the variable order method. The tolerance for which the accuracies of all four shown methods are approximately equal at approximately 10^{-8}, providing an RMS position differences of 0.3-0.4m. This shows that the best way to control the accuracy of the ABAM method is to control the allowed relative tolerance, as changing the order has a much weaker impact on the resultant RMS position difference.

An intersting observation is made for the relative tolerances smaller than 10^{-12}. Beyond this, the position accuracy of all method suddenly changes. This change is accuracy comes together with a significant increase in computational time. After further investigation it was found that this was due to a step-size used during the simulation smaller than the step-size used in the previous trade-off.

Regarding the computational time, it was found that for the fixed order methods, for a particular RMS position differences, the ABAM6 method was generally the fastest, followed by ABAM8 and ABAM10. The variable order ABAM6-11 method varied between being roughly as fast as the ABAM6 method, to falling between the ABAM8 and ABAM10 method. A similar conclusion can be drawn as for controlling the accuracy of the method, namely that changing the allowed relative tolerances is the best option of affect the computational time of the method.

It can also be observed that for an RMS position differences between approximately 0.3-0.4m and approximately 0.02m, the computational time for all four methods is approximately constant. Considering that the accuracy of the three constant order methods at small relative tolerances is approximately the same, and better than that of the adaptive order method, and considering that between a relative order of 10^{-8} and 10^{-11} the computational time remains approximately constant while decreasing the RMS position differences by an order of magnitude, it was decided to use a constant order, variable step-size ABAM method with an order of 6 and a relative tolerances of 10^{-11}.

To conclude this trade-off, it should be noted that this analysis was only performed considering a single aerocapture case. Before generalising these results, a more thorough investigation should be performing taking into account different initial conditions, perturbations to the atmosphere model during the trajectory,

Table 4.2: Coefficients for the Adams-Bashforth method up to six steps, corresponding to an order of six.

s	b_0	b_{-1}	b_{-2}	b_{-3}	b_{-4}	b_{-5}
1	1					
2	3/2	-1/2				
3	23/12	-4/3	5/12			
4	55/24	-59/24	37/24	-3/8		
5	1901/720	-1387/360	109/30	-637/360	251/720	
6	4277/1440	-2641/480	4991/720	-3649/720	959/480	-95/288

different atmosphere models altogether, and different vehicles. However, to perform such an analysis there is not sufficient interest nor time in this research.

4.3.3. Forward Euler

The Euler methods is the simplest form of numerical integration. This method is an explicit method, as it only relies on data that is already known at the time of evaluation. The Euler method simply takes the instantaneous derivative of the considered function y, and multiplies this instantaneous derivative by a (small) time-step h to obtain an approximation for the change to the function value. Then, the change is added to the previous value to obtain an approximation of the next value. In mathematical terms, the Euler method is:

$$y_{n+1} = y_n + y'_n h \tag{4.21}$$

where y_n and y'_n are the value and derivative of the function at point n, and h is the time-step.

The Euler method is a first-order method, meaning that the local error (error made in a single step) is proportional to h^2, and the global error (error at a fixed time, regardless of steps) is proportional to h. This means that a small step-size is required for the Euler method to run accurate. In this research, the Euler method was used only for the first-order analytical approach because of it ease of implementation.

4.3.4. Adams-Bashforth-Adams-Moulton

The Adams-Bashforth Adams-Moulton method is an implicit linear multi-step method. This method is formed by the combination of the explicit Adams-Bashforth method, and the implicit Adams-Moulton method. The method first uses the explicit Adams-Bashforth method to obtain an approximation of the next state, and then corrects this estimate using the implicit Adams-Moulton method. The mathematical description of the explicit Adams-Bashforth methods is as follow:

$$\mathbf{x}_{n+1} = \mathbf{x}_n + h\Sigma_{i=0}^{i=s-1} b_{i-s+1}\dot{\mathbf{x}}_{i-s+1} \tag{4.22}$$

In this equation $\mathbf{x}$ and $\dot{\mathbf{x}}$ represent the state and state derivative, h the step-size, s the number of steps involved in the method, and b_i the weighting coefficient which uniquely defines the AB method. Those coefficients are defined by solving:

$$b_{s-j-1} = \frac{(-1)^j}{j!(s-j-1)!}\int_0^1 \Pi_{i=0,i\neq j}^{s-1}(u+i)\,du, \text{ for } j = 0,...,s-1 \tag{4.23}$$

Two similar expressions can be obtained for the Adams-Moulton method. First, the expression for the function evaluation:

$$\mathbf{x}_{n+1} = \mathbf{x}_n + h\Sigma_{i=0}^{i=s} b_{i-s+1}\dot{\mathbf{x}}_{i-s+1} \tag{4.24}$$

And the equation to determine the coefficients:

$$b_{s-j} = \frac{(-1)^j}{j!(s-j)!}\int_0^1 \Pi_{i=0,i\neq j}^{s}(u+i-1)\,du, \text{ for } j = 0,...,s \tag{4.25}$$

The coefficients required to perform a single integration step using the sixth-order Adams-Bashforth Adams-Moulton integrator were calculated using the above equations and are presented in Table 4.2 and Table 4.3, respectively.

Table 4.3: Coefficients for the Adams-Moulton method up to six steps, corresponding to an order of seven.

s	b_1	b_0	b_{-1}	b_{-2}	b_{-3}	b_{-4}	b_{-5}
0	1						
1	1/2	1/2					
2	5/12	2/3	-1/12				
3	3/8	19/24	-5/24	1/24			
4	251/720	323/360	-11/30	53/360	-19/720		
5	95/288	1427/1440	-133/240	241/720	-173/1440	3/160	
6	19087/60480	2713/2520	-15487/20160	586/945	-6736/20160	263/2520	-863/60480

Table 4.4: Adams-Bashforth Adams-Moulton Variable Step Size Parameters.

Δt_0	$\Delta t_{\min}$	$\Delta t_{\max}$	Tolerance	$\mathcal{O}_{\text{fixed}}$
0.1s	$0.1 \cdot \frac{1}{2}^{-20}$s	$0.1 \cdot 2^{10}$s	$1 \cdot 10^{-10}$	6

The exact version of the Adams-Bashforth Adams-Moulton method used in this research is a variable step-size fixed order version of the method. Every step it is evaluated if the step-size should be changed. If the errors (after the potential order change) are too large, and the step-size can be halved without exceeding the minimal step-size, it is determined how often the history and the minimal allowed step-size allow for the step-size to be halved. The history required for halving the step-size is than recalculated. For any even node, the value already exists from the previous step-size. For the odd nodes the history is padded by interpolation. As a last step, halving is turned off momentary to ensure that in the next integration step the step-size is not halved again. Similarly, the if the errors are found to be too large, and the step-size can be doubled without exceeding the maximal step-size, the step-size is doubled. The new history is filled with ever other entry from the old history.

4.3.5. Runge-Kutta

Before the Adams-Bashforth Adams-Moulton of desired order can be used, a sufficiently history has to be built up, and for this purpose an Runge-Kutta method is used. Additionally, while using a variable step-size is easier with a Runge-Kutta method, the goal is to obtain a history with consistently spaced nodes. Therefore, a fixed time step is used when generating the history.

The generalised equation for any Runge-Kutta method is

$$y_{n+1} = y_n + h\Sigma_{i=1}^{s} b_i k_i \tag{4.26}$$

where the values for k_i are:

$$\begin{aligned} k1 &= f(t_n, y_n) \\ k2 &= f(t_n + c_2 h, y_n + h(a_{21} k_1)) \\ k3 &= f(t_n + c_3 h, y_n + h(a_{31} k_1 + a_{32} k_2)) \\ &\vdots \\ k_s &= f(t_n + c_s h, y_n + h(a_{s1} k_1 + a_{s2} k_2 + \cdots + a_{s,s-2} k_{s-2} + a_{s,s-1} k_{s-1})) \end{aligned} \tag{4.27}$$

The values of the coefficients a, b, and c, for Runge-Kutta methods are often listed in what is called a Butcher Tableau. A general Butcher table is shown in Table 4.5. The Runge-Kutta method used in Tudat to populate the initial history used by the variable step-size Adams-Bashforth Adams-Moulton method is the Dormand-Prince87 method, for which the coefficients were taken from Montenbruck and Gill (2005). The butcher tableau for this method is presented in Table 4.6.

4.4. Optimisation Routine

An optimisation routine is needed to numerically optimise a process. The goal of optimisation is the find the values of a set of control variables for which a certain objective function $J(\mathbf{x}(t), \mathbf{u}(t), t)$ is minimised. In this form $\mathbf{x}$ denotes the state variables and $\mathbf{u}$ the control variables. For this research J is a function of the total ΔV

Table 4.5: Butcher tableau for a general Runge-Kutta method.

$$\begin{array}{c|ccccc} 0 & & & & & \\ c_2 & a_{21} & & & & \\ c_3 & a_{31} & a_{31} & & & \\ 00\vdots & \vdots & & \ddots & & \\ c_s & a_{s1} & a_{s2} & \cdots & a_{s,s-1} & \\ \hline & b_1 & b_2 & \cdots & b_{s-1} & b_s \end{array}$$

required after atmospheric exit and the peak heat load and load factor experienced by the vehicle during the trajectory. For this research the Non-Dominant Sorting Genetic Algorithm II (NSGA-II) is used.

Some additional nomenclature, each element in the control vector **u** is called a chromosome, and the vector itself is called an individual. A group of individuals is called a population, and every population forms one generation. The generation is evolved by determining the fitness of the individuals within it, and using certain evolutionary operations to create new individuals for the next generation.

4.4.1. Non-Dominant Sorting Genetic Algorithm II

This Non-Dominant Sorting Genetic Algorithm II (NSGA-II) was first proposed by Deb et al. (2000). This proposal mainly deals with specifying how the algorithm ranks the individuals. This proposal does not deal with the evolution of the population, outside of stating that crossover and mutation are used, as is common in all Evolutionary Algorithms (EA). In the NSGA-II algorithm in PaGMO the Simulated Binary Crossover (SBX) method is used for crossover, proposed by the same authors of the original NSGA-II algorithm. For mutation polynomial mutation is used. The descriptions of both these methods was obtained from Deb and Goyal (1996) and by inspecting the PaGMO NSGA-II source code.

Before cross-over and mutation can be discussed, first the method for encoding the values of the chromosomes into a single individual is discussed. Each individual within the population is comprised of j chromosomes. Every chromosomes represents the value of a single control variable. The initial value of a chromosome is determined according to:

$$p_{i,R} = B_{l,R} + \text{rand}(0,1)(b_{u,R} - b_{l,R}) \tag{4.28}$$

where $\mathbf{u}_{i,R}$ represents the R$^{\text{th}}$ chromosome of the i$^{\text{th}}$ individual, $b_{l,R}$ and $b_{u,R}$ represent the upper and lower bound of the variable, and rand(0,1) is a random number generator that provides a random number between 0 and 1, including both 0 and 1.

The new generation is developed by preserving the top individuals of the previous generation, adding a number of entirely new individuals, and performing cross-over and mutation to fill up the generation. Crossover uses the values of the chromosomes in individuals of the current population to determine values of the same chromosomes in a new individual for the next generation. The SBX method works by randomly selecting two parents p_1 and p_2, and their children c_1 and c_2. For each chromosome in the individual, there is a chance CR (default 0.95 in PaGMO) that the chromosome is given a random value according to SBX. If crossover does not happen, the corresponding chromosome of child c_1 inherits the value of parent p_1, and c_2 of parent p_2. If crossover does happen, two values α and β are defined according to:

$$\begin{aligned} \beta &= 1 + (2\frac{p_{1,R} - b_{l,R}}{p_{2,R} - p_{1,R}}) \\ \alpha &= 2 - \beta^{-(\eta_c+1)} \end{aligned} \tag{4.29}$$

where $p_{i,R}$ is the R^{th} chromosome in the i^{th} parent, $b_{l,R}$ is the lower bound of the R^{th} chromosome, and η_c is the distribution index for crossover, 10 per default in PaGMO. The value of the children are than calculated according to

$$c_{i,R} = \frac{1}{2}\left[(p_{1,R} - p_{2,R}) - \beta_q(p_{2,R} - p_{1,R})\right] \tag{4.30}$$

where:

$$\beta_q = \begin{cases} \text{if: rand}(0,1) <= \alpha^{-1} & \text{rand}(0,1)\alpha^{\frac{1}{\eta_c+1}} \\ \text{if: rand}(0,1) > \alpha^{-1} & \frac{1}{2-\text{rand}(0,1)\alpha}^{\frac{1}{\eta_c+1}} \end{cases} \tag{4.31}$$

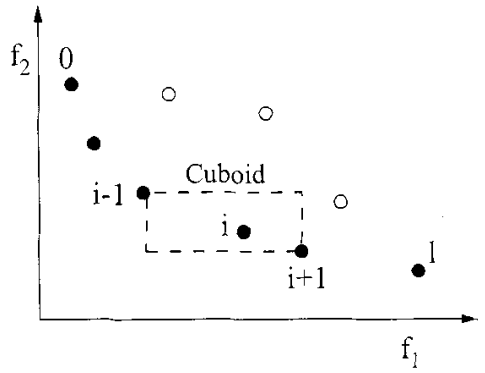

Figure 4.2: Crowding distance calculation. The filled circles are solutions on a single Pareto-front. Deb et al. (2000).

$$x_3 \begin{cases} \frac{x_2 - x_0}{2} & \text{if: } f(x_2) > 0 \\ \frac{x_1 - x_2}{2} & \text{if: } f(x_2) < 0 \end{cases}$$

The last operation performed for crossover is to check if the newly set random chromosome exceeds the boundaries imposed on it. If it does, the value of the chromosome is set equal to the boundary it violated.

Mutation applies to the new individual created by cross-over. The purpose of mutation within the evolution is to create more diversity within the new population. This decreases the chance of the optimiser getting stuck at a local optima, and allows it to explore the full solution space. Each chromosome within the new individual has a chance m to get assigned a value other than what was determined during cross-over. In PaGMO, a mutation probability of 0.01 is default, and will be maintained for this research. The polynomial mutation method used in NSGA-II uses two parameters to perform the mutation. These two parameters are determined by:

$$\begin{aligned} \delta &= \frac{u_{\text{new},j} - B_{l,j}}{B_{u,j} - B_{l,j}} \\ r &= \text{rand}(0,1) \end{aligned} \tag{4.32}$$

if $r \leq 0.5$:

$$\delta_q = [2r + (1-2r)(1-\delta)_m^{\eta}]^{\frac{1}{\eta m}} - 1 \tag{4.33}$$

else:

$$\delta_q = 1 - [2(1-r)(2r-1)_m^{\eta}]^{\frac{1}{\eta m}} \tag{4.34}$$

where η is a distribution index for mutation. This parameter determines how far the mutated value can deviate from the original value, with a larger η keeping the mutation closer to the original. Per default, $\eta = 50$ in PaGMO. The new value of the mutated variable is determined according to:

$$p_{\text{new},R} = p_{\text{new},R} + \delta_q (b_{u,R} - b_{l,R}) \tag{4.35}$$

After the evolution of the first population is allowed to happen, the current and next generation are combined into a single population. The entire extended population is than divided into Pareto fronts. The algorithm than sorts the individuals based on crowding. The crowding level is determined by the dimensions of an n-dimensional rectangle of which the vertices are determined by the closest neighbours on the same front. Crowding is shown schematically in Fig. 4.2. The individuals in the less densely populated parts of the fronts are more desirable than those in the crowded parts. Based on the Pareto front and the crowding level, the N best individuals are moved on to the new population, where N is based on the size of each population.

Table 4.6: Butcher tableau of the Dormand-Prince method.

$\frac{1}{18}$	$\frac{1}{18}$												
$\frac{1}{12}$	$\frac{1}{48}$	$\frac{1}{16}$											
$\frac{1}{8}$	$\frac{1}{32}$	$\frac{3}{32}$											
$\frac{5}{16}$	$\frac{5}{16}$	$-\frac{75}{64}$	$\frac{75}{64}$										
$\frac{3}{8}$	$\frac{3}{80}$	$\frac{3}{16}$	$\frac{3}{20}$										
$\frac{59}{400}$	$\frac{29443841}{614563906}$	$\frac{77736538}{692538347}$	$-\frac{28693883}{1125000000}$	$\frac{23124283}{1800000000}$									
$\frac{93}{200}$	$\frac{16016141}{946692911}$	$\frac{61564180}{158732637}$	$\frac{22789713}{633445777}$	$\frac{545815736}{2771057229}$	$-\frac{180193667}{1043307555}$								
$\frac{5490023248}{9719169821}$	$\frac{39632708}{573591083}$	$-\frac{433636366}{683701615}$	$-\frac{421739975}{2616292301}$	$\frac{100302831}{723423059}$	$\frac{790204164}{839813087}$	$\frac{800635310}{3783071287}$							
$\frac{13}{20}$	$\frac{246121993}{1340847787}$	$-\frac{37695042795}{15268766246}$	$-\frac{309121744}{1061227803}$	$-\frac{12992083}{490766935}$	$\frac{6005943493}{2108947869}$	$\frac{393006217}{1396673457}$	$\frac{123872331}{1001029789}$						
$\frac{1201146811}{1299019798}$	$-\frac{1028468189}{846180014}$	$\frac{8478235783}{508512852}$	$\frac{1311729495}{1432422823}$	$-\frac{10304129995}{1701304382}$	$-\frac{48777925059}{3047939560}$	$\frac{15336726248}{1032824649}$	$-\frac{45442868181}{3398467696}$	$\frac{3065993473}{597172653}$					
1	$\frac{185892177}{718116043}$	$-\frac{3185094517}{667107341}$	$-\frac{477755414}{1098053517}$	$-\frac{703635378}{230739211}$	$\frac{5731566787}{1027545527}$	$\frac{5232866602}{850066563}$	$-\frac{4093664535}{808688257}$	$\frac{3962137247}{1805957418}$	$\frac{65686358}{487910083}$				
1	$\frac{403863854}{491063109}$	$-\frac{5068492393}{434740067}$	$-\frac{411421997}{543043805}$	$\frac{652783627}{914296604}$	$\frac{11173962825}{925320556}$	$-\frac{13158990841}{6184727034}$	$\frac{3936647629}{1978049680}$	$-\frac{160528059}{685178525}$	$\frac{248638103}{1413531060}$				
	$\frac{14005451}{335480064}$	0	0	0	0	$\frac{-59238493}{1068277825}$	$\frac{181606767}{758867731}$	$\frac{561292985}{797845732}$	$\frac{-1041891430}{1371343529}$	$\frac{760417239}{1151165299}$	$\frac{118820643}{751138087}$	$\frac{-528747749}{2220607170}$	$\frac{1}{4}$
	$\frac{13451932}{455176623}$	0	0	0	0	$\frac{-808719846}{976000145}$	$\frac{1757004468}{5645159321}$	$\frac{656045339}{265891186}$	$\frac{-3867574721}{1518517206}$	$\frac{465885868}{322736535}$	$\frac{53011238}{667516719}$	$\frac{2}{45}$	0

5
Software

In this chapter an overview of all the software used, their purpose, and their function is provided. In Section 5.1 the software that was obtained from external sources, and thus did not have to be developed from scratch specifically for this research is discussed. The external software discussed in this chapter is the source of the various numerical methods that were discussed in Chapter 4. In Section 5.2 the general architecture of the software is discussed.

5.1. External Software

Most of the software used during this research, especially the software used for the numerical simulation. was obtained pre-packaged and only had to be connected together using an overarching program. The two libraries that were used exclusively throughout this research for simulation and optimisation purposes, their content, and features are discussed in the following two sections.

5.1.1. Technical University of Delft Astrodynamics Toolbox

The Technical University of Delft Astrodynamics Toolbox, or Tudat, is a collection of C++ libraries, numerical methods, and custom interfaces that are useful for astrodynamical simulations. The toolbox is being actively developed and maintained by members of the Technical University of Delft, specifically the Astrodynamics & Space Mission group of the faculty of Aerospace Engineering. For more information regarding Tudat, the included libraries, interfaces, their functionality, how to use them, and tutorials, the reader is referred to the Tudat website featuring tutorials and documentation[1]. In addition to the various libraries and numerical methods, Tudat also comes with example applications that can be used to familiarise oneself with the various libraries and features of Tudat and to ascertain the correct installation of Tudat

For all the features that are included in Tudat, unit tests are available that can be, should be, and were used to verify the correct implementation of the features. These features are the various numerical methods, but they are also provided for the environmental models. Thanks to the inclusion of these unit tests, the correct installation, and therefore correct implementation of the various features, of Tudat can be verified directly after installation. Only acceptance testing needs to be performed on the elements that are pulled straight from Tudat without modification. For this research, almost everything required was available stock in Tudat as is discussed next.

All numerical methods discussed in the previous section, with the exception of the NSGA2 optimisation algorithm, are available in the Tudat libraries. Due to the inclusion and successful completion of all the unit tests, all these numerical methods can be considered verified in their implementation, and no separate verification effort will be spend on them. The NSGA2 algorithm comes with PaGMO, which will be discussed shortly.

The Tudat libraries include an interface to read data from a file and use it to determine the value of the aerodynamic coefficients based on any number of independent variables. This interface was used to specify the values of the aerodynamic coefficients as a function of Mach number based on the aerodynamic model that will be discussed in Section 3.6.1. This interfaces uses a multi-variable linear interpolator to interpolate values between the discrete values of the independent variables.

[1] TU Delft Astrodynamic Toolbox website available at `http://tudat.tudelft.nl/`

Similarly, the Tudat library includes an interface to specify atmospheric profiles based on data in a file. This is relevant for the inclusion of the Martian and Venusian atmosphere models that are both given as altitude-density profiles read from a file. The details of these models will be discussed in Section 3.6.2, where it will also be shown that the resultant, averaged, altitude-density profile as it was obtained from Tudat after specifying it, is indeed the result of averageing the atmosphere models over both position and time. The atmosphere model for Earth, NRLMSISE-00 is included in Tudat by default.

Furthermore, the coefficients for the spherical harmonics gravity models for Earth and Mars, and the ability to truncate them to obtain the desired accuracy, are included in Tudat, as is a central gravity model interface that is used for Venus, and for Earth and Mars for the simplified environment simulations. the central gravity model requires the specification of a standard gravitational parameter. The values of this parameter were given in Table 3.12.

5.1.2. Parallel Global Multi-Objective Optimiser

The Parallel Global Multi-Objective Optimiser, or PaGMO, library is one of the libraries included in Tudat. According to Biscani et al. (2018), this library is a collection of unified interface optimisation algorithms with the purpose of facilitating multi-objective parallel optimisation. Parallel computing uses multiple processing cores simultaneously so that it can perform multiple tasks such as evaluating a function simultaneously, instead of having to perform every operation sequentially. In PaGMO this parallel computing is used to determine the fitness of multiple individuals in a population simultaneously, significantly decreasing the run time on systems with multiple cores.

The unified interface allows for the user to quickly and easily swap between various optimisation methods by simply specifying the other algorithm and leaving all other code the same, as the interface for the newly swapped to algorithm is the same as the first. A version of PaGMO is also available for Python as PyGMO. This version includes all of the same functionality as the C++ version of the library does.

The PaGMO library comes with its own set of unit tests and optimisation problems that can be, should be, and were used to verify the correct implementation of the library. Additionally, the PaGMO implementation in Tudat comes with a set of example applications where the optimisation algorithms from PaGMO are used in an astrodynamical optimisation problem. Because of these unit tests, the correct implementation of all the optimisation algorithms and problems included in PaGMO can be verified at once by running them. All the unit tests for PaGMO completed successfully, verifying the installation.

In this research, only the NSGA-II algorithm was used from PaGMO. For this algorithm (and all other PaGMO algorithms due to the unified interface ideal), the user needs to specify the population size of a single generation, the maximal number of generations, the boundaries of the input variables, and the number of objectives desired to be minimised.

Similar to all other numerical methods in Tudat, for NSGA-II, unit tests and example applications are available, that were successfully completed, leading to the conclusion that

5.2. Software Architecture

The general architecture of the software is graphically shown in Fig. 5.1. This flowchart depicts the interaction and flow of information between the various elements of the simulator. This general architecture is valid for all types of simulations performed throughout this research. The only differences for specific cases is in how the user defined information, such as the initial state, targets and tolerances, or terminal conditions are set.

When simulating a specific trajectory, all the user defined elements can be set by hand. When using the NSGA-II algorithm, the **Targets and tolerances** block in the **Aerodynamic guidance** block is set by the switch-time and initial bank angle dictated by the evaluated individual of the population. The fitness of the individual depends on the values of ΔV and the peak load factor and heat load. These are returned in the **Save peak load factor, heat flux and ΔV values** block. When performing a grid search over various initial conditions, the **Initial state** is set according the the evaluated grid. When performing root finding, the switch-time is set in the **Targets and tolerances** block in the **Aerodynamic guidance** block.

Additionally, various guidance laws can be defined that all have the same interface and output, making them interchangeable. Two examples of use guidance laws are lift-up lift-down bang-bang, and equilibrium glide guidance.

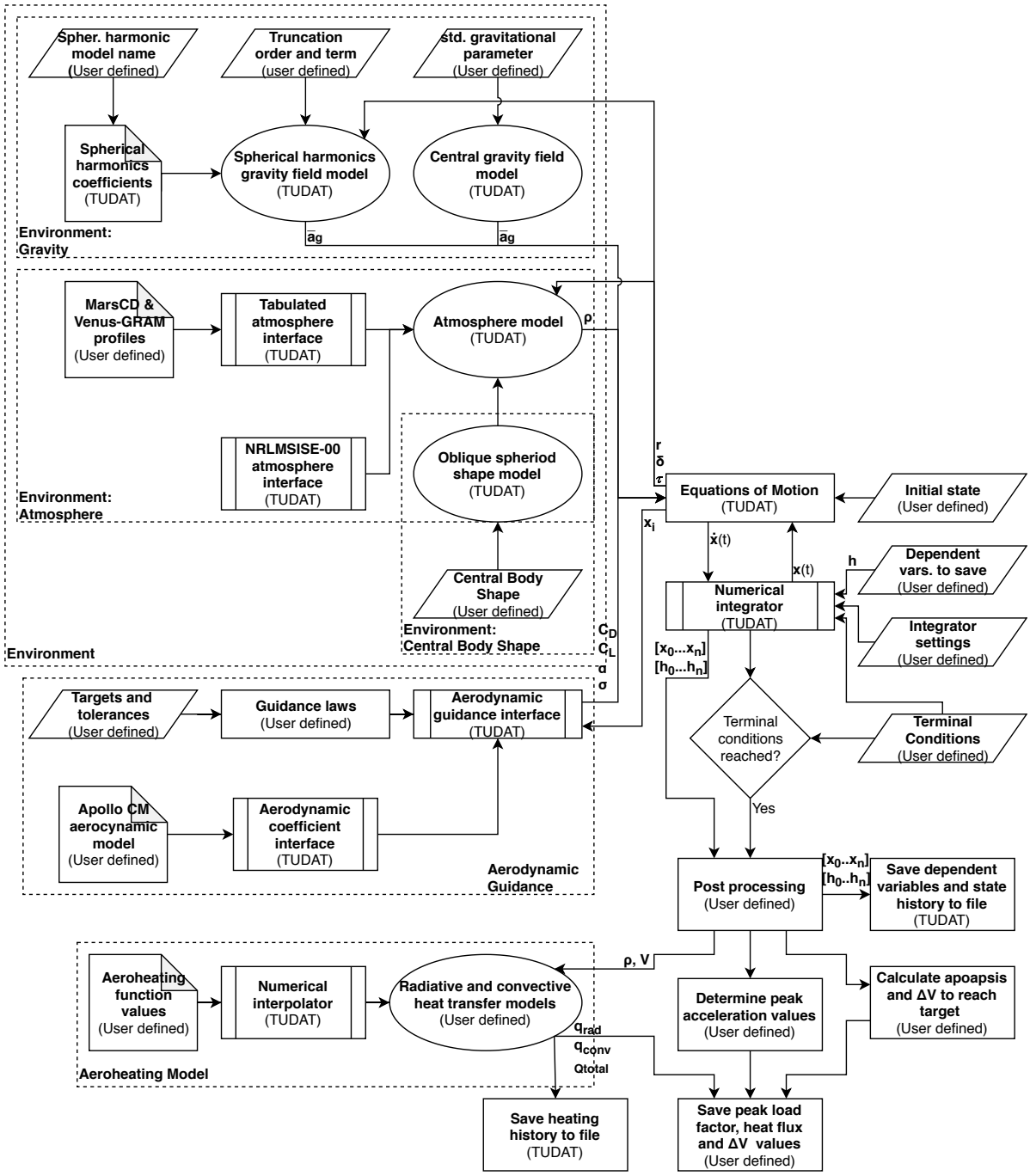

Figure 5.1: Software architecture of the general simulation environment.

6

Verification & Validation

Before any numerical methods or models can be confidently used, it first has to be verified that it has been properly implemented. The verification process determines whether the numerical element has been implemented properly by comparing the output to a known-to-be-correct results.

The numerical methods that are used in this research, and thus have to be verified are the root-finding, interpolation, integration, and optimisation methods. The numerical models that have to be verified are the aerodynamic vehicle model, the atmosphere models, the central body shape model, and the aerodynamic heating model.

Conveniently, a majority of these numerical tools were available pre-packaged in either the Tudat or PaGMO libraries, which come with unit-tests. These unit-tests are pre-defined checks that can be performed to verify that the considered numerical element has been properly installed. All the unit-tests included in Tudat and PaGMO have been successfully completed. However, in this section only those that are directly relevant to the verification process are discussed.

In Section 6.1 the verification process of the numerical methods used throughout this research is treated. Following this, in Section 6.2, the same is done for the numerical models. In the last section

6.1. Verification Numerical Methods

The numerical methods to be verified are the bisection root-finding method, the linear and cubic Hermite spline interpolation methods, the RK87 and ABAM integration methods, and the NSGA-II optimisation method. Since for all of these methods, with the exception of the bisection method, the Tudat or PaGMO version of the numerical method was used, the verification process primarily consisted of running the provided unit-tests. All the tests discussed in this section were completed successfully.

6.1.1. Bisection Root-Finding

The custom implementation of the bisection method was verified by running it against the same unit-tests that are used to verify the Tudat version of the bisection method.

These unit-tests are finding the root of $f(x) = x^2 - 3$ between -1 and 4, finding the root of $f(x) = sin(x)$ between 2 and 4, and $f(x) = cos(x) - x$ between -1 and 2 with a desired accuracy of 10^{-15}. Lastly, it was tested if the implemented method was able to determine if no root was present on the provided interval. This was done by evaluating the first function on the interval [-1,0], where both values for f are negative.

6.1.2. Linear & Cubic Hermite Spline Interpolation

The implementation of the linear and cubic Hermite splite interpolation methods was obtained from Tudat. For each of these methods a unit-test was provided. For the linear interpolation this is *unitTestLinearInterpolator*, and for the cubic Hermite spline interpolation this is *unitTestHermiteCubicSplineInterpolator*.

The linear interpolation unit-test first interpolates the data set [(0,-20), (1,20), (3,21)] to obtain the values at $x = 0.5$ and 2.0, resulting in the expected values of $y = 0$ and $y = 20.5$, respectively.

Next, the interpolation of multiple values simultaneously is tested, by interpolating [0=(10,-10,70),1=(20,-5,80),2=(30,60,90)] to obtain the value at $x = 1.5$, resulting in 1.5=(25,27.5,85).

The last test is to interpolate a data-set loaded from a file consisting of 33 nodes between -3 and 3 to obtain a dataset over the range of a thousand nodes, and to compare the obtained interpolated results to a known-to-be-correct file.

For the cubic Hermite spline interpolation the first test consists of interpolating between nodes given for the function $f(x) = 2 + 3x + 5x^2$ and verifying that the interpolated value is sufficiently close to the analytical value, using a tolerance of $5 \cdot 10^{-3}$.

The next test determines if the implemented method can handle exceptions, such as empty input vectors.

The final two unit-tests interpolate the same data loaded from a file as the linear interpolation unit-test. Again the number of nodes is interpolated to a thousand nodes and compared to a known-to-be-correct file. This test is run twice, one imposing zero first derivatives at the endpoints, and one imposing zero second derivatives at the endpoints.

6.1.3. RK87 & ABAM Numerical Integration

Similar to the interpolator case, both numerical integration methods used were obtained from Tudat. The two unit-test files provided are *"unitTestRungeKutta87DormandPrinceIntegrator"* and *"unitTestAdamsBashforthMoultinIntegrator"*, for the RK87 and ABAM methods, respectively.

The Runge-Kutta method was verified by comparing it to a known-to-be-correct result. In total five different cases are evaluated. First, the initial state is integrated one step ahead in time. Next, the initial state was integrated until a final time using multiple steps. Third, the integration direction was reversed, and the final state is integrated backwards to the initial time. The next test integrates from the initial time to a specified time in a single step. This case differs from the first as in this case the desired time was specified, not the step-size. The final test integrates to a specified time in multiple steps.

For each of these cases, the result obtained from the integration was compared to known-to-be-correct results.

The ABAM numerical integrator was subsequently verified by comparing the results from this method to those obtained from the RKF78 method for various minimal, maximal, and initial step sizes, and relative and absolute tolerance settings.

For completeness, it should be mentioned that the RKF78 method itself was verified in the same manner as the RK87 method described above.

6.1.4. NSGA-II Optimisation

The unit-test for the NSGA-II optimisation method is available in the PaGMO library in the file *nsga2*.

The first test performed is the check if the method properly detects errors in the input variables. Next, it is verified that the method obtains the same results if the seed is set to a particular value.

Additionally, the Tudat library includes several example problems that use the PaGMO library. One of these problems is the Himmelblau function, defined by $f(x,y) = (x^2+y-11)^2+(x+y^2-7)^2$. On the range $-5 \leq x \leq 5, -5 \leq y \leq 5$, this function has four local minima at $f(3.0, 2.0)$, $f(-2.805118, 3.131312)$, $f(-3.779310, -3.283186)$, and $f(3.584428, -1.848126)$.

Using the NSGA-II algorithm, 100 generations, each generation containing 1000 individuals, each of these four local minima was found up to the precious of the roots given above.

6.2. Verification Numerical Models

In addition to the numerical methods, the numerical models used must also be verified. The verification of these models focusses on verifying the correctness of the input parameters of the model. The model interface and the model itself is part of Tudat, and thus always include unit-tests. While these unit-tests have been performed and successfully passed after installing Tudat, their will not be further discussed here.

The numerical models verified in this section are the aerodynamic model, the NRLMSISE-00 model, the Mars and Venus tabulated atmosphere models, the central body shape mode, the central and spherical harmonics gravity field models, and the aerothermal model.

6.2.1. Aerodynamic Model

The aerodynamic model based on the Apollo CM was manually verified. This was done by first verifying that the developed file tabulating the aerodynamic model had the same structure as those already present in

Tudat. subsequently, it was verified that the data in the file was the same as that of the source. This was done by manually checking the Mach numuber and the corresponding angle-of-attack, lift coefficient, and drag coefficient.

6.2.2. NRLMSISE-00 and Tabulated Atmosphere Models

For the verification of the NRLMSISE-00 atmosphere model, the Tudat included *unitTestNRLMSISE00Atmopshere* unit-test was performed. In this test values are requested from the NRLMSISE-00 model and compared to known-to-be correct values.

For the tabulated atmosphere models used for Mars and Venus, the input parameters were manually verified by comparing them to the values obtained from the averaging process of the original models. After this, the density values over a large range of altitudes were requested using the Tudat interface. The obtained values where then again compared to those from the original models. The averaged atmosphere profiles seen in Section 3.6.2 exactly matched the values obtained from Tudat.

6.2.3. Central Body Shape Model

For the central body shape model, the Tudat included unit-test *unitTestBodyShapeModels* was used. This test verifies that the altitude of an object at an arbitrary position in space obtained from the oblate spheroid model is the same as a known-to-be-correct result. Additionally, it was manually verified if the input parameters for the central body shape model were the same as those in the found sources.

6.2.4. Aeroheating model

The equations for the radiative and convective heat flux have been manually verified by comparing the implemented equations to those in the source material. Additionally, the Hayabusa entry was reconstructed based on the work by Fujita et al. (2011).The peak radiative and convective heat loads found from the reconstruction were 2.04 MWm^{-2} and 12.67 MWm^{-2}. The work by Fujita et al. (2011) reports a radiative heat flux and convective heat flux of approximately 2.25 MWm^{-2} and 12.25 MWm^{-2}.

III

Part III: Research

7

Analytical Approach

In this chapter the first- and second-order analytical approximations that were developed in Section 3.5 are evaluated to determine how accurately they approximate the full equations of motion used in the simulation. In addition to evaluating the accuracy, the impact of each assumption made during the derivation of the analytical approximation on the accuracy is evaluated. This was done in an effort to determine the validity of each of the assumptions.

In Section 7.1 the result of evaluating the first-order approximation and the errors induced by the various assumptions is discussed. Following this, in Section 7.2, the same is done for the second-order approximations. In both cases, first the nominal Earth-CRM case is treated, after which the results are attempted to be generalised by evaluating the two other planets and the other vehicle for various initial conditions.

7.1. First-Order Approach

In this section the first-order analytical approximations that were presented in Section 3.5.1 are used to approximate the nominal Earth-CRM trajectory. First the accuracy of this approximation is evaluated by comparing the first-order approximation to the results from the numerical simulation. After this, the potential source of errors is investigated. After this the result of the same investigation performed for the SRM vehicle and the two other planets is discussed.

7.1.1. First Order Evaluation

The entry interface state of the vehicle can be found in Table 2.2, and the properties of the vehicle can be found in Table 2.4. In addition to the information provided in these tables, all trajectories were flown starting from zero latitude and longitude, flying straight east (heading $\chi = 90°$). In Fig. 7.1 the results of both the simulation and the first-order approximation are shown. For now only the full simulation and first-order approximation will be discussed. From the three profiles it can be seen that first-order approximation leaves a lot to be desired in terms of accuracy, specially in the cases of the velocity and flight-path angle. This is to be expected as the two equations governing the change in these two parameters, Eqs. (3.32) and (3.33), respectively, were the equations that got simplified by neglecting the contribution of mass.

Thus far, the equations to obtain first-order approximations for the velocity and altitude at arbitrary point in the trajectory based on entry conditions and local flight-path angle, the flight-path angle at the lowest point in the trajectory, the atmospheric exit, and the point in the trajectory where the peak acceleration occurs, and the magnitude of the peak acceleration have been described.

By using these analytical approximations and the equations of motion an approximation of a trajectory and the values at key points of this trajectory were made. This approximation of the trajectory and the key values was then compared to the simulation results. In contrast to the sophisticated Adams-Bashforth Adams-Moulton numerical integration scheme used in the simulation, the first-order approximations of the equations of motion were integration using a simple Euler scheme.

In Table 7.1, some of the values of interest of the orbit are listed. By combining the overall comparison between the simulated and first-order approximated trajectory shown in Fig. 7.1, and the comparison between the specific parameter values tabulated in Table 7.1, it can be concluded that the first-order approximation is not suitable for the Earth-CRM case.

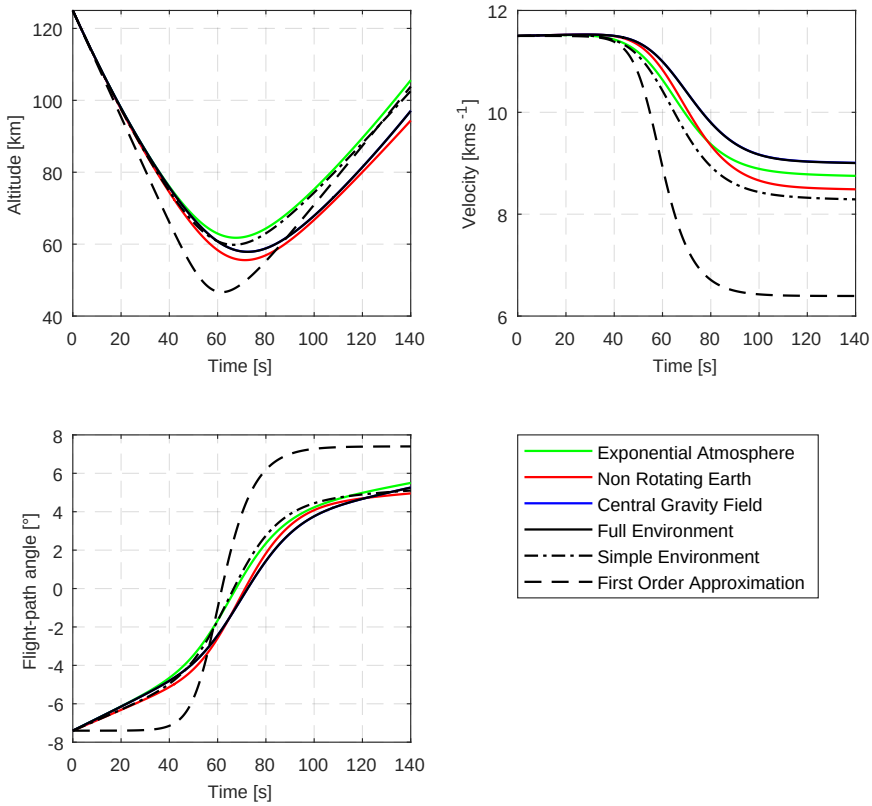

Figure 7.1: Altitude, velocity, and flight-path angle profiles for various numerical simulations and the first-order analytical approximation.

Table 7.1: Tabulation of various variables at three points of interest, taken both from the first-order analytical equations and the numerical simulation.

Point of Interest	Parameter	First Order Approx.	Simulation	Ratio [-]
Lowest Altitude	Altitude [km]	46.6	57.9	0.8
Peak	Flight-path angle [°]	-2.0	-0.6	3.3
Acceleration	Load factor [g]	21.4	7.5	2.9
Atmospheric	Flight-path angle [°]	7.5	5.7	1.3
Exit	Velocity [kms^{-1}]	6.4	9.0	0.7

7.1.2. Error Investigation

From the comparison between the first-order approximations and the simulation output in the previous section it can be concluded that the approximations are not sufficiently accurate to approximate aerocapture for this research. To garnish further insight into the problem, it was investigated how much each of the made assumptions contributed to the inaccuracy of the first-order method. As a start to this investigation, a list of all the assumptions made to obtain the first-order approximations was developed. These assumptions were:

1. The flight is assumed planar, flown with a bank angle of zero degrees (full lift-up, $\theta = 0°$).
2. No apparent forces resulting from a rotating central body are taken into account.
3. The effect of weight in the equations of motion is assumed negligible compared to the effect of the aerodynamic forces (drag and lift)
4. The atmosphere is approximated by an exponential atmosphere model, and the hydrostatic equation is assumed valid.
5. The gravitational acceleration is approximated by a central gravity model.

In this section the results of the effort to isolate and/or eliminate the effects of each of the made assumptions and test their impact on the trajectory is discussed. The first assumption was already eliminated in the previously show results as the flight was simulated using zero bank angle. This does not mean however that the flight is entirely planar as the trajectory was allowed to drift due to the gravity field. However, the effect of this was found to be negligible due to the short duration of the flight. The second assumption could be eliminated by setting the rotational rate of the central body to zero. The fourth assumption could be eliminated by setting the atmosphere model used to the exponential atmosphere model discussed in Section 3.6.2. Lastly, the fifth assumption could be eliminated by setting the gravity model to a central gravity field.

Referring back to Fig. 7.1, the additional four trajectories plotted will now be discussed. It should be noted that it seems that one trajectory is missing from the graph. However, the trajectories simulated using the full environment, and the trajectory using the central gravity field, match almost exactly. This causes their trajectories to be nigh indistinguishable in the graphs. It is therefore concluded that the assumption of a simplified gravity field model has a negligible effect on the accuracy of the trajectory, at least for a flight of this short duration.

Both the use of the exponential atmosphere model and a non-rotating Earth have more significant impacts on the trajectories flown. By comparing the error between the full environment simulation and the non-rotating, exponential atmosphere, and simple environment simulations, and the first-order approximations, it can be concluded that, while the use of a simplified environment has a definite impact on the trajectory, it is by far not the most significant contribution to the inaccuracy. On a side-note, after closer inspection of the error between the full environment simulation and the three other simplified simulations, the error made due to the use of simplified environment seemed additive, as the error made by the simple environment simulation is consistently roughly equal to sum of the error made by the three individual simplified environment simulations.

The only assumption left to investigate is the assumption of negligible mass effect compared the the aerodynamic effect. Unfortunately, no method was found to eliminate this assumption, as an attempt to simulate the trajectory using a non-massive vehicle failed. However, by switching off all other assumptions, it was managed to isolate the effect of the mass-neglect, resulting in the simple environment trajectory. In addition to this, the validity of this assumption for this simulation was tested by determining if the gravity effect (hereinafter also referred to as the mass-effect) is sufficiently small compared to the aerodynamic effect in Eqs. (3.32) and (3.33) to allow for the omission of the gravity terms. To accomplish this, the full environment simulation was taken, and for each data point the mass and aerodynamic contribution were determined. Subsequently the ration of these contributions was determined. This ratio was taken "aerodynamic-over-mass". This means that if the ratio is larger than unity, the aerodynamics are more dominant than the mass.

From this graph it can be concluded that for the CRM vehicle flying through the lower parts of the atmosphere, where the aerodynamic forces are the largest, the mass-effect on the rate of change of the velocity can indeed be neglected. However, for the rate of change of the flight-path angle, both effects contribute roughly the same, and thus cannot be neglected. For the CRM vehicle on Earth the it is therefore concluded that the assumption made at the beginning of this chapter is invalid.

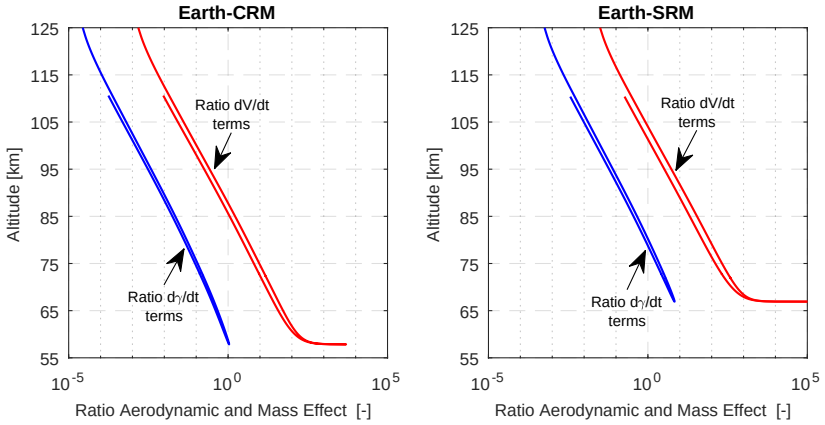

Figure 7.2: Ratio between the aerodynamic and gravitational contributions in the Equations of Motion governing the rate of change of the velocity and flight-path angle.

For the Earth-SRM case a similar conclusion can be drawn. Since the aerodynamic reference area of the SRM vehicle only 14% of the CRM reference area, and the aerodynamic forces are proportional to this area, in the SRM case, only 14% of the aerodynamic force is generated. Additionally, the mass of the SRM vehicle is 0.7% of that of the CRM vehicle. Because of this, the ratio between the mass-effect and aerodynamic effect is decreased by roughly an order of magnitude. Nevertheless, for a majority of the flight, the rates of change of the velocity and the flight-path angle are dominated by the mass-effect. It is therefore again concluded that the made assumption is invalid for this case.

7.1.3. SRM, Mars, and Venus

The above evaluation was all performed for the Earth based case. However, in this research, two other planets are considered. Similar investigations to what has been shown previous have been performed for the other planets. First, the Mars-CRM and -SRM cases were investigated. After this, the Venus-CRM and -SRM case.

On Mars, it was again found that the use of the central gravity field had negligible impact on the trajectory, similar to the Earth case. The error induced by the use of the exponential atmosphere model was smaller compared to Earth. The effect of assuming a stationary planet was comparable, but slightly smaller compared to Earth case due to the slower rotational rate. Lastly, it was found that the aerodynamic-over-mass effect ratio was smaller than when compared to Earth. This is due to the tenuous atmosphere of Mars producing very limited aerodynamic forces, even at the high velocity of aerocapture. This indicates that the assumption of ignoring the mass effect is even more inappropriate for Mars

After this, Venus was examined. As stated in Section 3.6.5, for Venus the central gravity field is already used in the simulation, therefore only the rotation of Venus and the atmosphere model could be examined. It was noted that the error induced by considering a stationary Venus was negligible. This is due to the rotational rate of Venus, which is roughly 240 times slower than Earth's rotational rate, rotating once every roughly 5800 hours. It was also found that the error due to the exponential atmosphere model were significantly smaller than those for Earth when using the custom fit for the middle altitudes developed in Section 3.6.2, namely $\rho_0 = 186765.35$ kgm^{-3} and $H_s = 4.5$ km. However, even in this case, the error due to the neglect of the mass-effect was the most significant. On Venus, due to the increase density, the aerodynamic forces are higher for the same velocity. However, also due to the increase aerodynamic forces, the velocity is lowered quicker. This causes the vehicle to reach the denser parts of the atmosphere with lower velocity. This combined effect cause the ratio between the aerodynamic and mass components to be slightly larger on Venus compared to Earth, but not yet large enough to justify neglecting the mass-effect for the CRM vehicle. For the SRM vehicle on the other hand, where the ratio is already larger compared to CRM, the assumption to neglect the mass compared to the aerodynamics would be applicable. From this analysis it was thus concluded that only in the Venus-SRM case the assumption of ignoring the mass effect can be validly made.

7.2. Second-Order Approach

In this section the second-order analytical approximations that were presented in Section 3.5.2 are used to approximate the nominal Earth-CRM trajectory. First the accuracy of this approximation is evaluated by com-

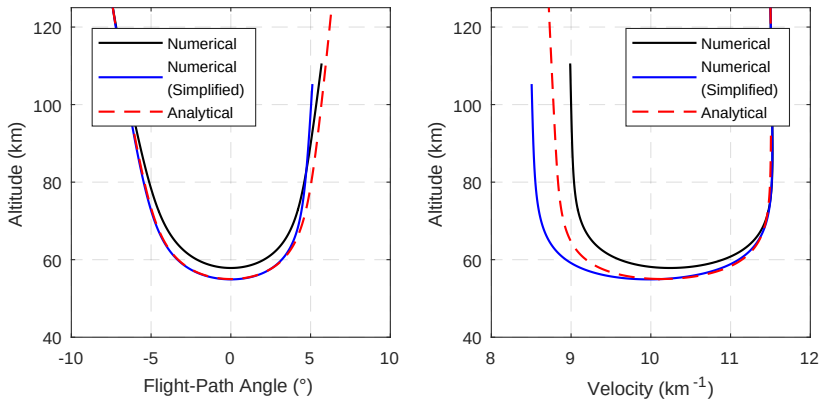

Figure 7.3: Comparison between numerical and second-order analytical results for the trajectory, considering a rotating Earth, an eastward flight, and the CRM vehicle.

paring the second-order approximation to the results from the numerical simulation. After this, the potential source of errors is investigated. After this the result of the same investigation performed for the SRM vehicle and the two other planets is discussed.

7.2.1. Second Order Evaluation

Similar to the previous evaluation section, the results obtained from the second-order approximation will be compared to a simulation of the same trajectory. However, in addition to the simulation where the full environment is taken into account and the equations of motion are integrated using the variable step-size ABAM integration scheme, the analytical results are also compared to the output of a simplified situation. This simplified situation integrates the equations of motion for a flight about a stationary planet, as presented in Eqs. (3.32), (3.33) and (3.35), integrated using simple Euler integration, and considering exponential atmosphere and central gravity. The parameters for the exponential atmospheres and central gravity field models can be found in Section 3.6.2 and Section 3.6.5, respectively.

In Fig. 7.3 the trajectory of the vehicle is plotted both as flight-path-angle-altitude and velocity-altitude. The next figure, Fig. 7.4, shows the lift and drag components of the aerodynamic load. The final figure produced for this case, Fig. 7.5 shows the heat load on the vehicle, split into the convective and radiative heat loading.

Starting with the first figure, Fig. 7.3, it is immediately noted that the analytical expressions match the simplified numerical results almost exactly throughout the downwards leg of the flight. Only when the vehicle starts to climb again do the two start to converge. it is thus concluded that the developed analytical expressions indeed approximate the equations of motion reasonably accurate, especially for the downward slope, and that the use of the second-order analytical equations has improved the accuracy of the model significantly compared to the first-order analytical expressions. The analytical equations still overestimate the penetration depth into the atmosphere, and underestimate the velocity at the atmospheric exit. However, the estimate for the flight-path angle at the atmospheric exit is quite good. In Table 7.2 the values for the penetration depth and the values at atmospheric exit are tabulated for both numerical simulations and the analytical approximation.

In the next figure, Fig. 7.4, the aerodynamic load on the vehicle as a function of altitude is shown. Again the close agreement between the approximate analytical and simplified numerical methods can be observed. Furthermore, it was noticed that that peak aerodynamic g-load was overestimated by the approximate analytical method. While the method lacks accuracy in this situation, as it overestimates the aerodynamic load by approximately 33%, at least it provides an overestimate, and therefore a conservative upper-bound of the peak acceleration experienced by the vehicle during the trajectory. In Table 7.2 the values for the peak aerodynamic load and the flight-path angles at which they occur tabulated for all three trajectories.

In the last figure, Fig. 7.5, the aeroheating is treated. Similar conclusions as for the aerodynamic loading can be drawn. The figure exhibits close agreement between the analytical approximation and simple simulation, while overestimating the Tudat simulation. In this case the overestimate is approximately 28%. Again, since the approximate analytical equations produce an overestimate, they could be used as a conservative

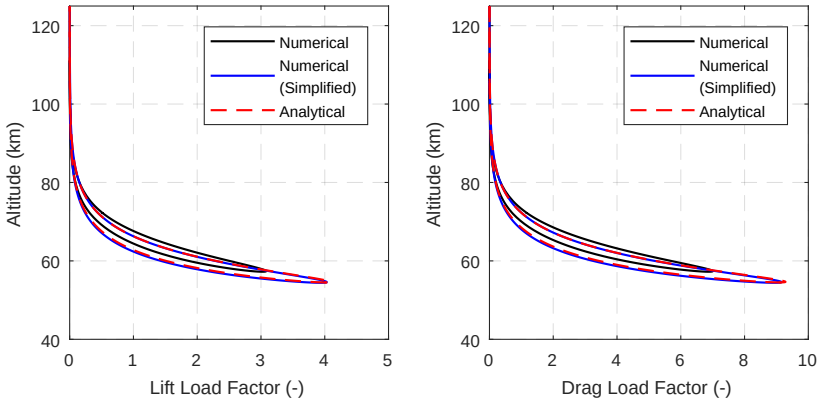

Figure 7.4: Comparison between numerical and second-order analytical results for the aerodynamic load, considering a rotating Earth, an eastward flight, and the CRM vehicle.

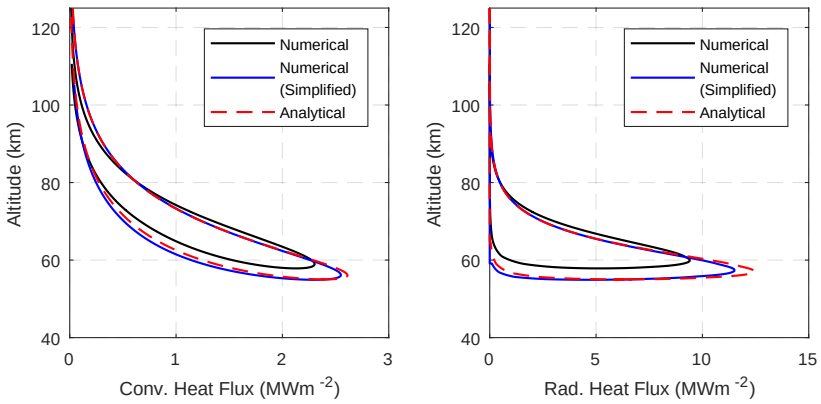

Figure 7.5: Comparison between numerical and second-order analytical results for the heat load, considering a rotating Earth, an eastward flight, and the CRM vehicle.

Table 7.2: Tabulation of various variables at three points of interest, taken from the second-order analytical equations and both numerical simulations.

Point of Interest	Parameter	2^{nd} Order Approx.	Sim. (Simple)	Sim. (Tudat)
Lowest Altitude	Altitude [km]	54.9296	54.9176	57.8588
Peak	Flight-path angle [°]	-0.6429	-0.6710	-0.5762
Acceleration	Lift load factor [g]	3.8502	3.8018	2.8927
Load	Drag load factor [g]	8.7492	8.6391	6.5733
Peak Conv.	Flight-path angle [°]	-1.6859	-1.8145	-1.5435
heat load	Conv. heat load [MWm^{-2}]	2.6119	2.5503	2.3034
Peak Rad.	Flight-path angle [°]	-2.2850	-2.4755	-2.1499
heat load	Rad. heat load [MWm^{-2}]	12.4453	11.5201	9.4055
Peak Total	Flight-path angle [°]	-2.2562	-2.4454	-2.0025
heat load	Total heat load [MWm^{-2}]	15.0208	14.0254	11.6886
Atmospheric	Flight-path angle [°]	6.3201	5.1146	5.6912
Exit	Velocity [kms^{-1}]	8.7211	8.5055	8.9889

upper-bound of the peak-heat load experienced by the vehicle during the flight. In Table 7.2 the values for the peak heat load and the flight-path angles at which they occur tabulated for all three trajectories.

7.2.2. Error Investigation

From the comparison between the second-order approximations and the simulation output in the previous section, it can be concluded that, while this approximation matches closer with the simulation outputs, there are still errors present. Similar to the methodology that was followed for the first-order approximations, each of the assumptions made in the development of the second-order analytical approximations will be attempted to be eliminated or isolated, to determine their impact. The assumptions that apply to the second-order analytical approximations are the following.

1. The flight is assumed planar, flown with a bank angle of zero degrees
2. No apparent forces resulting from a rotating central body are taken into account
3. The atmosphere is approximated by an exponential atmosphere model, and the hydrostatic equation is assumed valid.
4. The gravitational acceleration is approximated by a central gravity field model.
5. The flight-path angle is assumed to be sufficiently small such that $\cos\gamma \approx 1$.

However, the first assumption can be disregarded, as the flight simulated using Tudat is also planar, just as it was in the first-order case. Additionally, it has been shown in Fig. 7.1 that the effect of the central gravity field model on the simulated trajectory is negligible. This leaves three assumptions that could be the cause of the error between the second-order approximations and the simulation. The assumption regarding the use of exponential atmosphere can be eliminated by performing the simulation also using the exponential atmosphere. The effect from apparent forces resulting from a rotating central body can be eliminated by specifying a rotational rate of zero in the simulator. Combining both these simplifications results in the isolation of the last assumption.

First, the effect of rotational rate was investigated. This was done in two ways. The first was to disable the rotational rate from the simulation entirely. The resulting trajectories are presented in Figs. 7.6 to 7.8. The important parameters for the various points of interest are produced in Table 7.3. As nothing changed for the second-order approximation or the simplified simulation, the first two columns of results are the same as in Table 7.2.

By inspecting the figures and consulting the values tabulated in Table 7.3, it can be seen that the analytical approximation, as well as the simplified numerical simulation, has excellent agreement with the non-rotating central body simulation. Additionally, as the error between the simulation and the approximation in the case of the non-rotating central body is incredibly small, it can be concluded that the errors introduced by the small-angle approximation and the approximation of the atmosphere by the exponential model are negligible

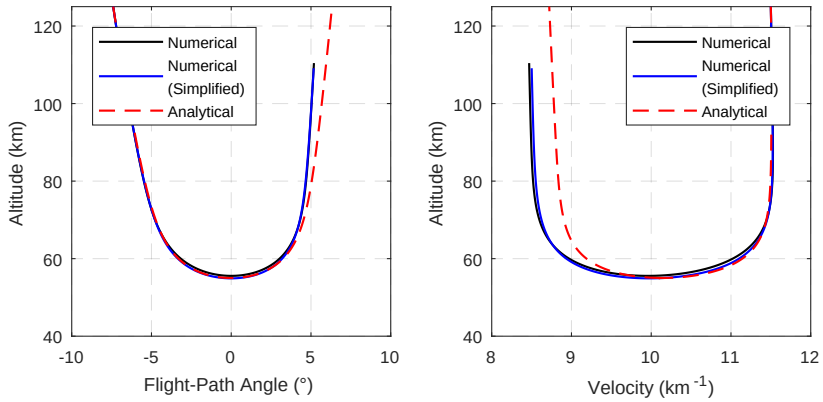

Figure 7.6: Comparison between numerical and second-order analytical results for the trajectory, considering a fixed Earth, an eastward flight, and the CRM vehicle.

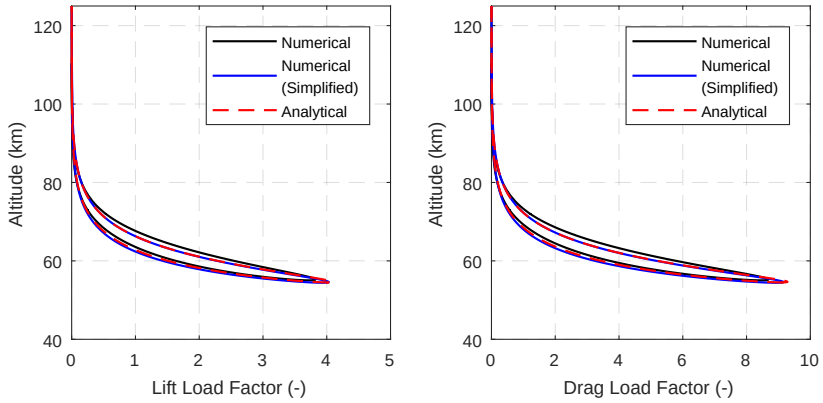

Figure 7.7: Comparison between numerical and second-order analytical results for the aerodynamic load, considering a fixed Earth, an eastward flight, and the CRM vehicle.

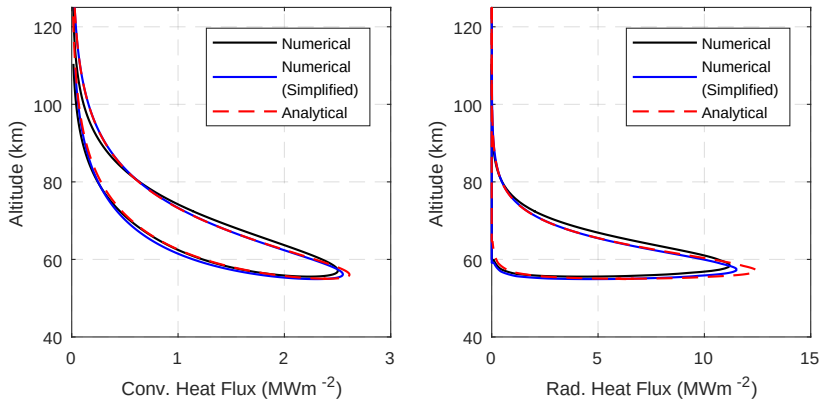

Figure 7.8: Comparison between numerical and second-order analytical results for the heat load, considering a fixed Earth, an eastward flight, and the CRM vehicle.

Table 7.3: Tabulation of various variables at three points of interest, taken from the second-order analytical equations and both numerical simulations.

Point of Interest	Parameter	2^{nd} Order Approx.	Sim. (Simple)	Sim. (Tudat)
Lowest Altitude	Altitude [km]	54.9296	54.9176	55.5604
Peak	Flight-path angle [°]	-0.6429	-0.6710	-0.8370
Acceleration	Lift load factor [g]	3.8502	3.8018	3.6272
Load	Drag load factor [g]	8.7492	8.6391	8.2422
Peak Conv.	Flight-path angle [°]	-1.6859	-1.8145	-1.9439
heat load	Conv. heat load [MWm^{-2}]	2.6119	2.5503	2.5031
Peak Rad.	Flight-path angle [°]	-2.2850	-2.4755	-2.6195
heat load	Rad. heat load [MWm^{-2}]	12.4453	11.5201	11.1983
Peak Total	Flight-path angle [°]	-2.2562	-2.4454	-2.6195
heat load	Total heat load [MWm^{-2}]	15.0208	14.0254	13.6618
Atmospheric	Flight-path angle [°]	6.3201	5.1146	5.1861
Exit	Velocity [kms^{-1}]	8.7211	8.5055	8.4693

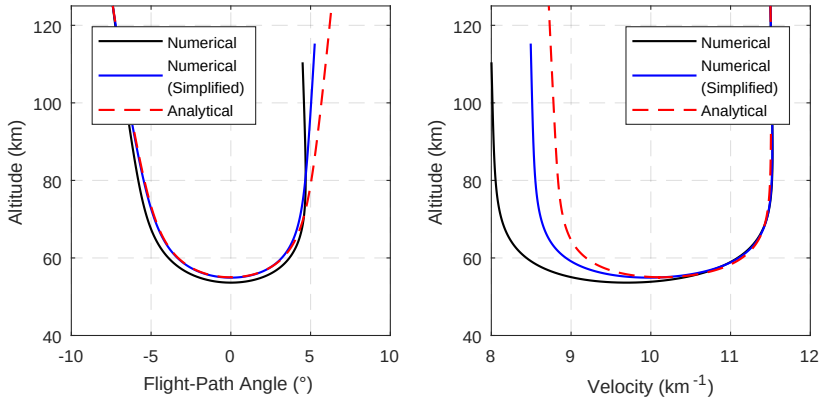

Figure 7.9: Comparison between numerical and second-order analytical results for the trajectory, considering a rotating Earth, Westward flight, and the CRM vehicle.

compared to the error due to the ignored rotation of the Earth, and the neglect of the resultant apparent forces.

Before moving on the other planets, one more element was investigated. It is now know that the analytical approximations approximate the non-rotating central body case accurately, and that they provide a good conservative upper-bound value in the case that the central body is rotating, and the flight is in the direction of the rotation, e.g. eastward flight. However, how well the analytical approximations work when westward flight is performed is not yet know. In the next three figures, Figs. 7.9 to 7.11, as well as in the Table 7.4, the data is presented for the case of westward flight about a rotating Earth.

From these figures it can be seen that the conservative nature of the analytical approximation is no longer present. In the case of westward flight in the atmosphere attached to a rotating Earth, the analytical approximations become slightly optimistic, underestimating the aerodynamic forces and heat load by approximately 12% and 3%, respectively. However, it should be noted that the two cases for rotating Earth tested here are the absolute worst case scenario. The flight is over directly the equator and entirely against or with the rotational velocity of the planet. Considering this, and the ranges of accuracy obtained for the estimation of the peak aerodynamic load and the peak heat load of 30% overestimate or 12% underestimate, and 28% overestimate or 3$ underestimate, respectively, it is concluded these second-order approximations can be quite useful for, for instance, preliminary design. Either one obtains a overestimate, leading to a more conservative design, or one obtains a slight underestimate that should easily be fixed during more detailed design. Another potential application of these equations is the design of a guidance-and-control system, where the results obtained from these analytical equations can be used as first estimates in a predictor-corrector loop.

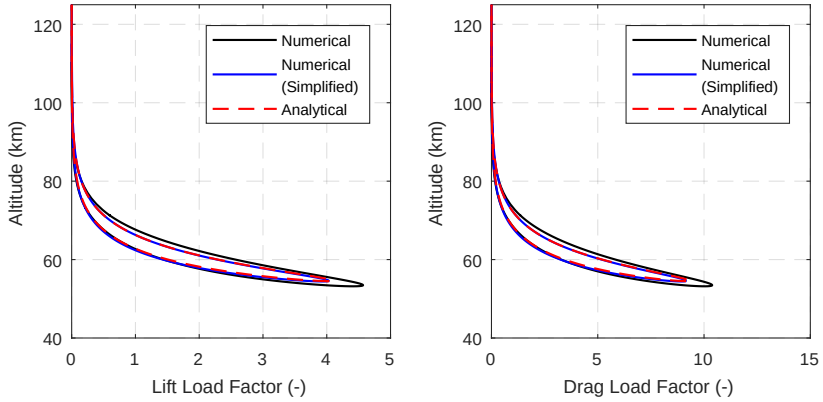

Figure 7.10: Comparison between numerical and second-order analytical results for the aerodynamic load, considering a rotating Earth, Westward flight, and the CRM vehicle.

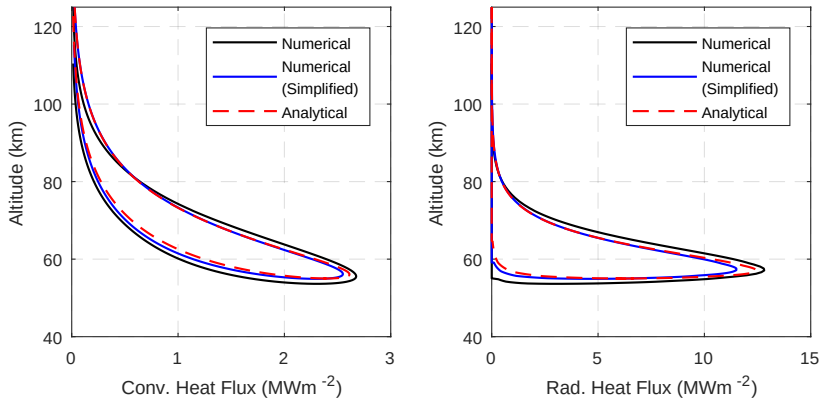

Figure 7.11: Comparison between numerical and second-order analytical results for the heat load, considering a rotating Earth, Westward flight, and the CRM vehicle.

Table 7.4: Tabulation of various variables at three points of interest, taken from the second-order analytical equations and both numerical simulations.

Point of Interest	Parameter	2^{nd} Order Approx.	Sim. (Simple)	Sim. (Tudat)
Lowest Altitude	Altitude [km]	54.9296	54.9176	53.9296
Peak	Flight-path angle [°]	-0.6429	-0.6710	-0.9676
Acceleration	Lift load factor [g]	3.8502	3.8018	4.3714
Load	Drag load factor [g]	8.7492	8.6391	9.9334
Peak Conv.	Flight-path angle [°]	-1.6859	-1.8145	-2.3280
heat load	Conv. heat load [MWm^{-2}]	2.6119	2.5503	2.6753
Peak Rad.	Flight-path angle [°]	-2.2850	-2.4755	-3.0706
heat load	Rad. heat load [MWm^{-2}]	12.4453	11.5201	12.8149
Peak Total	Flight-path angle [°]	-2.2562	-2.4454	-3.0706
heat load	Total heat load [MWm^{-2}]	15.0208	14.0254	15.4413
Atmospheric	Flight-path angle [°]	6.3201	5.1146	4.4990
Exit	Velocity [kms^{-1}]	8.7211	8.5055	8.0018

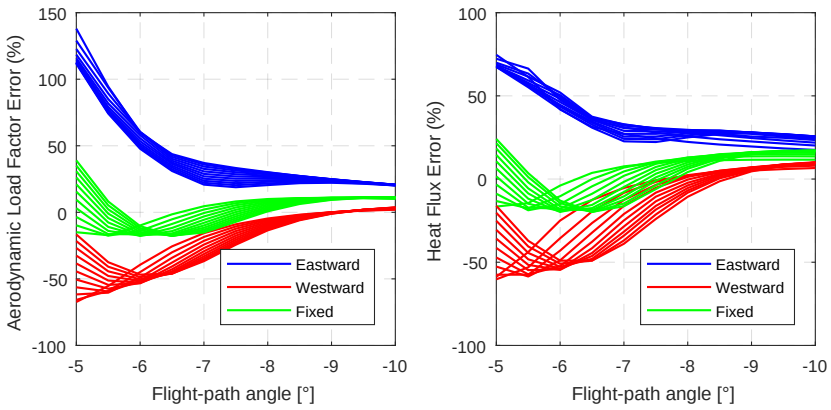

Figure 7.12: Percentual error between the peak values obtained from the second-order analytical approximation and the numerical simulation for the Earth-CRM case for various initial relative velocities and flight-path angles.

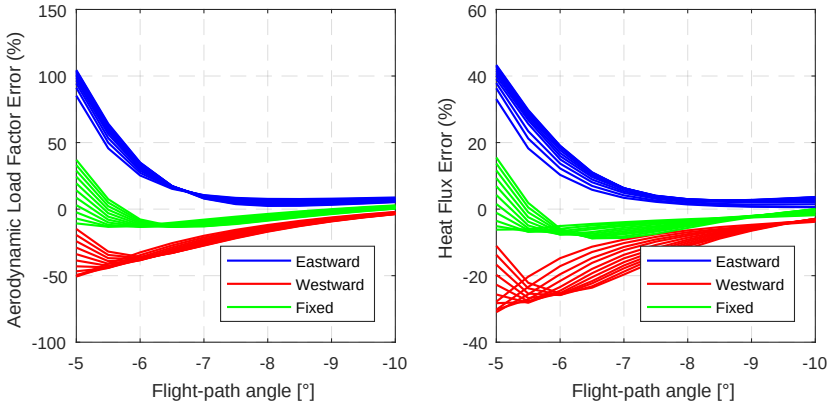

Figure 7.13: Percentual error between the peak values obtained from the second-order analytical approximation and the numerical simulation for the Earth-SRM case for various initial relative velocities and flight-path angles.

7.2.3. SRM, Mars, Venus, and Initial Condition Variation

Thus far the second-order analytical approach has been used to approximate the nominal Earth-CRM case. In this section an overview is given of the results obtained from investigating all planets, using both vehicles, for the full range of potential initial conditions as listed in Section 2.5, for eastward and westward flight about a rotating planet, and eastward flight about a stationary (fixed) planet.

Figs. 7.12 and 7.13 depict the error in the peak aerodynamic load factor and peak heat flux for the Earth-CRM and SRM cases, respectively. A positive error means the analytical approximations overestimates the peak value, a negative error indicates an underestimate. Similarly, Figs. 7.14 and 7.15, and Figs. 7.16 and 7.17 depict the error in the peak aerodynamic load factor and peak heat flux for the Mars-CRM and SRM, and Venus-CRM and SRM cases, respectively.

From these figures several observations can be made. The first observation is that, as the entry becomes steeper, the second-order analytical approximations seems to become more accurate. This is most apparent in the two Earth cases. This is contrary to what was expected however, as the second-order analytical approximations were developed using the small-angle assumption, which should induce a larger error as the flight-path angle increased. The reason for this phenomenon was found to be due to the errors in the exponential atmosphere model used, and not related to the small-angle approximation.

Each of the exponential atmosphere models discussed in Section 3.6.2 was selected for their accuracy around the expected point of deepest penetration. How the values for penetration depth were obtained will be discussed in Section 9.1. In this section it is also shown that for shallow entry, the vehicle penetrates the atmosphere less deep. This means that for a shallow initial flight-path angle, the vehicle does not reach the part of the atmosphere where the exponential model is the most accurate. Otherwise phrased, the entire flight is estimated using the less-accurate portion of the exponential atmosphere model, resulting in larger

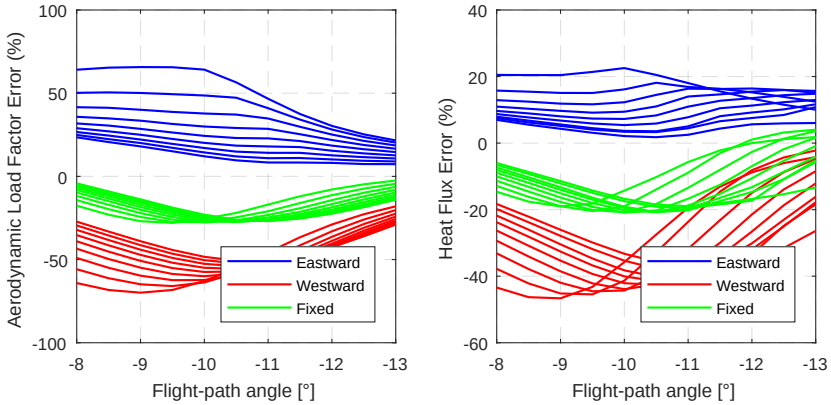

Figure 7.14: Percentual error between the peak values obtained from the second-order analytical approximation and the numerical simulation for the Mars-CRM case for various initial relative velocities and flight-path angles.

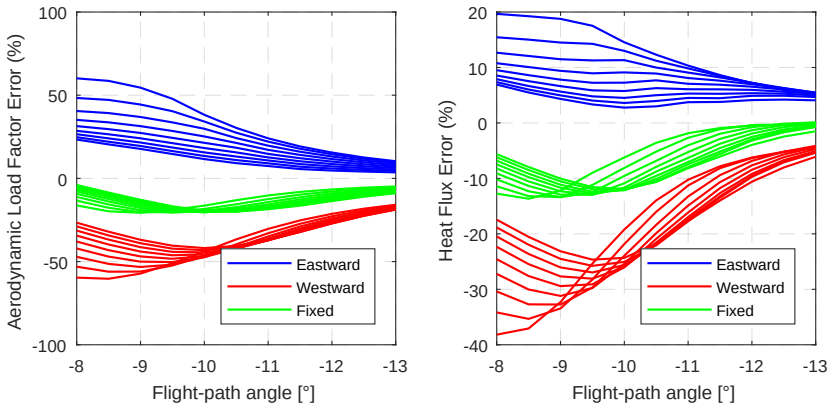

Figure 7.15: Percentual error between the peak values obtained from the second-order analytical approximation and the numerical simulation for the Mars-SRM case for various initial relative velocities and flight-path angles.

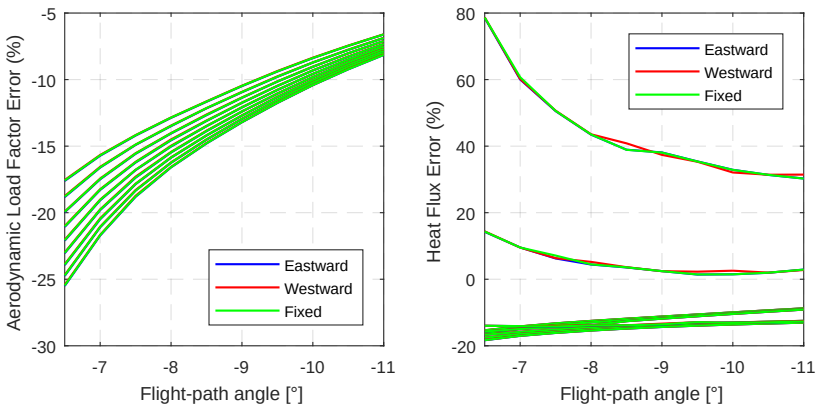

Figure 7.16: Percentual error between the peak values obtained from the second-order analytical approximation and the numerical simulation for the Venus-SRM case for various initial relative velocities and flight-path angles.

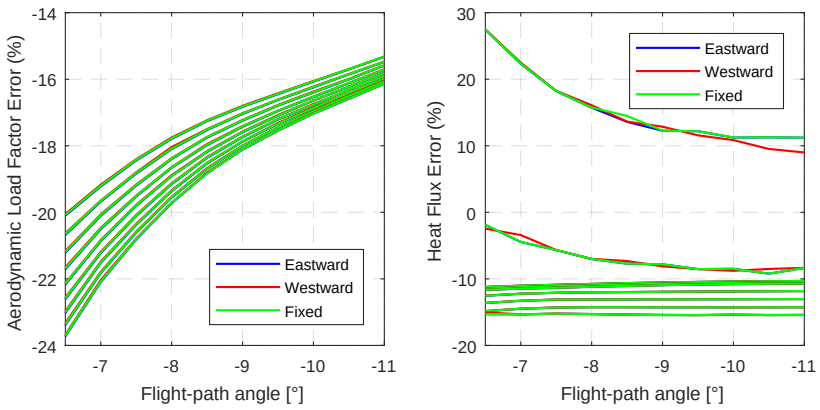

Figure 7.17: Percentual error between the peak values obtained from the second-order analytical approximation and the numerical simulation for the Venus-SRM case for various initial relative velocities and flight-path angles.

errors.

This also explains why the phenomenon is the most pronounced for the Earth cases. Referring back to Section 3.6.2, it can be see that in the upper atmosphere (90 km - 125 km), the error made by the exponential atmosphere for Earth is greater than the error for either Venus or Mars.

One possible method for alleviating this problem would be to fit an exponential atmosphere for the expected part of the atmosphere traversed, the altitudes between the entry interface altitude and the point of deepest penetration, potentially obtained from a first-order approximation. This custom fit would have to be made for each unique velocity and flight-path combination, as the penetration depth depends on both of these parameters, as will be shown in Section 9.1. Additionally, if the atmosphere model exhibits a significant change in slope, such as the Martian and Venusian atmospheres, this fit might be hard to make accurately over the entire range. This process of fitting a new exponential atmosphere for each entry was however not done during this research.

A second observation is that for the Venus case, the difference between westward or eastward flight or flight about a non-rotating planet is negligibly small. This is due to the aforementioned fact that the rotational rate of Venus is much slower than that of either Mars or Earth.

The final observation is that for the eastward flight on both Earth and Mars, the analytical approximation always overestimates the error. For flight about a non-rotating planet, the error fluctuates between over- and underestimate, and the westward flight is underestimated for all but the most steep entries. For Venus these statements are not true. For Venus the aerodynamic load factor is always underestimated, and the status of the heat flux error depends on the velocity with which the entry occurred.

8

Optimal Trajectories

This chapter deals with answering the first research question, by describing, in general, the optimal trajectory for an aerocapture mission. The optimality of the trajectory depends on what is hoped to be achieved with the trajectory. The optimal trajectory discussed here is optimal for an apoapsis-targeting aerocapture. Thus far in the research three aspects have been considered, the ΔV_{total}, which is the culmination of the periapsis and apoapsis alerting ΔV manoeuvres, the value of the peak g-load, and the peak heat load.

In Section 8.1 the theoretically optimal trajectory for ΔV minimisation for a planar aerocapture is presented, based on the work by Lu et al. (2015). Following this, in Section 8.2, the optimal trajectory for load factor and heat flux minimisation, based on the work by Zucchelli (2016) is discussed. The hypothesis by Zucchelli (2016) was numerically evaluated, and the results of this analysis are discussed in Section 8.3. Lastly, in Section 8.4 the relatively simple bank angle guidance laws that were formulated based on the drawn conclusions from the previous three sections are discussed.

8.1. Minimum ΔV Trajectory

The proof for a minimum ΔV trajectory for aerocapture was developed by Lu et al. (2015). In this proof the central body was considered non-rotating, the flight planar, and the gravity modelled by a central gravity field model. These assumptions lead to equations of motion nearly identical to those provided in Eqs. (3.32), (3.33) and (3.35). The only difference is in the expression for the flight-path angle, in which the bank angle σ is taken into account as a variable. The equation for the rate-of-change of the flight-path angle as used by Lu et al. (2015) then becomes

$$V\frac{d\gamma}{dt} = \frac{L\cos\sigma}{m} - g\cos\gamma\left(1-\frac{V^2}{V_c^2}\right) \tag{8.1}$$

where σ is the bank angle. The bank angle is bound according to $0 \leq \sigma_{\min} \leq \sigma \leq \sigma_{\max} \leq \pi$.

Two further assumptions are made before the derivation starts. The first assumption is that the performance index and the constraints on the terminal conditions depend solely on a subset of the terminal vehicle state variables, specifically the longitudinal motion variables r, V, and γ. This subset is referred to by Lu et al. (2015) as $\mathbf{x}_{\text{lon}} = (r, V, \gamma)^T$. Comparing this to the vehicle state given in spherical components in Eq. (3.13), one can see that this is indeed a subset of the full vehicle state, ignoring the variables latitude, longitude, and heading that describe position and lateral motion.

The second assumption is that the bank angle is the only trajectory control variable. The angle of attack is a function of velocity and radial position, and the angle of sideslip is ignored as part of the planar flight assumption. This conveniently matches the assumptions made regarding the angle of attack and sideslip in this research.

It is worth noting that this problem describes a class of aerocapture problems with only in-plane targeting conditions. Any problem with out-of-plane manoeuvres, such as plane changes or landing footprints in entry flight, are not optimised using this method. In these cases the performance index also depends on the lateral motion of the vehicle and its position for position targeting. As these cases are not considered in this research, thThese out-of-plane cases are ignored for this section.

With de definition of $\mathbf{x}_{\text{lon}}$, the performance index of the optimal trajectory is described as $J = \mathbf{x}_{\text{lon}}(t_f)$, and the terminal constraints must satisfy $\mathbf{s}[\mathbf{x}_{\text{lon}}(t_f)] = 0$, where the dimension of $\mathbf{s}$ is k, where $k \leq 3$. The Hamiltonian for this optimisation problem can be written as

$$H = \lambda^T \dot{\mathbf{x}}_{\text{lon}} = \lambda_r V \sin\gamma + \lambda_V \left(-\frac{D}{m} - \frac{\mu}{r^2}\sin\gamma \right) + \lambda_\gamma \frac{1}{V}\left[\frac{L\cos\sigma}{m} - \frac{\mu}{r^2}\cos\gamma\left(1 - \frac{V^2}{V_c^2}\right)\right] \tag{8.2}$$

Lu et al. (2015) continue by using Pontryagin's Maximum Principle to obtain an expression for the optimal bank angle σ^*, for which the Hamiltonian H is maximised. According to Pontryagin's Maximum Principle the derivatives of the costate variables λ_v, λ_r, and λ_γ are

$$\dot{\lambda}_r = -\frac{\delta H}{\delta r} = \lambda_V \left(\frac{1}{m}\frac{\delta D}{\delta r} - \frac{2\mu\sin\gamma}{r^3} \right) - \lambda_\gamma \frac{\delta \dot{\gamma}}{\delta r} \tag{8.3}$$

$$\dot{\lambda}_V = -\frac{\delta H}{\delta V} = -\lambda_r \sin\gamma + \frac{\lambda_V}{m}\frac{\delta D}{\delta r} - \lambda_\gamma \frac{\delta \dot{\gamma}}{\delta V} \tag{8.4}$$

$$\dot{\lambda}_\gamma = -\frac{\delta H}{\delta \gamma} = -\lambda_r V \cos\gamma + \lambda_V \frac{\mu\cos\gamma}{r^2} - \lambda_\gamma \frac{\delta \dot{\gamma}}{\delta \gamma} \tag{8.5}$$

respectively. The expression for the optimal bank angle for which the Hamiltonian is maximised at any point in time is

$$\sigma^* = \underset{\sigma_{\min} \leq \sigma \leq \sigma_{\max}}{\arg\max} \Big(H(\sigma) \Big) \tag{8.6}$$

Because $\cos\sigma$ is monotonic (meaning it either never decreases, or never increases) for $\sigma \in [\sigma_{\min}, \sigma_{\max}] \subset [0, \pi]$ and $L/V > 0$, the value of the optimal bank angle will be

$$\begin{cases} \sigma^* = \sigma_{\min} & \text{if} \lambda_\gamma > 0; \\ \sigma^* = \sigma_{\max} & \text{if} \lambda_\gamma < 0; \\ \sigma^* \in [\sigma_{\min}, \sigma_{\max}] & \text{if} \lambda_\gamma \equiv 0; \end{cases} \tag{8.7}$$

These three cases show that the optimal bank angle differs from its extreme values only if $\lambda_\gamma \equiv 0$.

Lu et al. (2015) uses a proof by contradiction to show that this case is not possible in any of the aeroassist problems defined by the assumptions made in this section. For λ_γ to be constant and zero, both it, and its derivative need to be zero, or $\lambda_\gamma = \dot{\lambda}_\gamma = 0$. By substituting these two equalities in Eq. (8.5) we obtain

$$\lambda_V \frac{\mu\cos\gamma}{r^2} - \lambda_r V \cos\gamma = \lambda_V \frac{\mu}{r^2} - \lambda_r V = 0 \tag{8.8}$$

Note that this only holds in the case $\cos\gamma \neq 0$, which is true for all points in a skipping trajectory between entry and exit, except for the deepest point of the atmospheric flight.

As this problem is a free time problem (no terminal time is imposed, thus t_f is free), the transversality condition $H \equiv 0$ must hold along the entire trajectory, according to Pontryagin's Maximum Principe. With $\lambda_\gamma = 0$, the expression for the Hamiltonian (rewritten slightly for convenience) becomes

$$H = \lambda_r V \sin\gamma - \lambda_V \frac{D}{m} - \lambda_V \frac{\mu}{r^2}\sin\gamma \equiv 0 \tag{8.9}$$

For both Eq. (8.8) and Eq. (8.9) to be valid, it is required that $\lambda_V = 0$, as $D > 0$. However, this results in $\lambda_r = 0$, and that thus all costate variables are zero. This contradicts Pontyagin's Maximum Principe, which states that the costate vector $\lambda \neq \mathbf{0}$. It is thus concluded that this third case for the value of the optimal bank angle is invalid for any point on the trajectory where $\cos\gamma \neq 0$. Therefore, the optimal trajectory for any flight with a free final time and only imposed constrains and objectives at the terminal state is a bang-bang style.

It is reiterated that this proof is for the simplified case of a non-rotating central body considering only planar flight and assuming a central gravity field. However, as already discussed in Chapter 7, the assumption of a central gravity field has a negligible impact on the trajectory. Additionally, the assumption of planar flight can be adhered to by stating $\sigma_{\min} = 0$ and $\sigma_{\max} = \pi$.

8.2. Minimum Peak Load Factor and Heat Flux Trajectory

Normally, the constraints imposed on a trajectory are not minimised. As long as the constraints are respected, their actual value is not of importance. However, by finding the optimal trajectories for which the constraints are minimised, the limit values for the initial conditions can be found. No trajectory that starts with initial conditions beyond this boundary can be flown without violating the requirements. For these trajectories either a pre-entry ΔV manoeuvre needs to be executed to change the initial conditions, or the constrains will be violated.

Zucchelli (2016) presents a derivation for aerocapture trajectories that minimises both the peak load factor and the peak convective heat rate. For the minimisation of the peak load factor, a control history $u(t)$ is attempted to be found such that

$$\min_{u(t)}\left[\max_{t}(\mathbf{q}_\infty)\right] \tag{8.10}$$

In this equation, instead of finding a control history that minimises the peak load factor, it is attempted to minimise the dynamic pressure. For a vehicle with approximately constant L/D, the load factor is proportional to the dynamic pressure according to

$$n = \frac{L^2 + D^2}{mg_0} = \frac{C_L^2 + C_D^2}{mg_0} q_\infty S_{\text{ref}} \tag{8.11}$$

Similarly, for the minimisation of the peak heat flux, instead of taking the full equation, the proportionality to the density and velocity is used to obtain

$$\min_{u(t)}\left[\max_{t}\left(\rho_\infty^b V^M\right) f(V)\right] \tag{8.12}$$

Zucchelli (2016) goes on by stating that parts of his proof is supported by numerical methods, and can therefore not be generalised. The derivation of this proof consists of the following four steps:

1. Prove that the ascending leg can be neglected when regarding peak values of the constraints.
2. Show that the lift-up lift-down bang-bang trajectory, or saturated lift-up trajectory leads to the least negative flight-path angles during the entire descending leg.
3. Prove that having the least negative flight-path angles leads to smaller future dynamic pressure (load factor) and heat flux.
4. Prove that having the least negative flight-path angles minimises the the peak dynamic pressure (load factor) and heat flux.

Only in the proof of the second step does Zucchelli (2016) make use of numerical methods.

The first step can be proved easily by considering the altitude-density profile of at atmosphere, such as presented in Section 3.6.2, and the relation between total, kinematic, and potential energy. During the ascending leg the altitude increases, resulting in decreasing density. Furthermore, both due to aerodynamic drag and energy exchange between kinematic and potential energy, the velocity of the vehicle decreases. As a result, both the dynamic pressure and the proportionality of the heat flux decreases. Additionally, consulting the tables for the heating function f in Section 3.6.4, it can be seen that the value of f also decreases as velocity decreases. Therefore, the peak value for the load factor and heat flux must occur somewhere during the downwards leg.

The second step is proven numerically by Zucchelli (2016) by simulating saturated (Full lift-up, or full lift-down), lift-up lift-down bang-bang, and lift-down lift-up bang-bang trajectories for a wide variety of initial conditions and showing the dynamic pressure as a function of the flight conditions. From this it is concluded that for any flight starting from a particular initial condition the lift-up lift-down bang bang trajectory (or, where possible, the saturated lift-up trajectory) has a least negative flight-path angle over the entire flight.

One additional note that is not made by Zucchelli (2016), but is an important factor for this proof is the notion that, because the flight-path angle is always the least negative for lift-up lift-down bang bang or saturated lift-up trajectories, they reach the deepest point in the trajectory where $\gamma = 0$ at least as quick, but generally quicker, than their lift-down lift-up bang bang or saturated lift-down trajectory equivalent. This means that the downward leg for lift-up trajectories has the shorted flight-time possible.

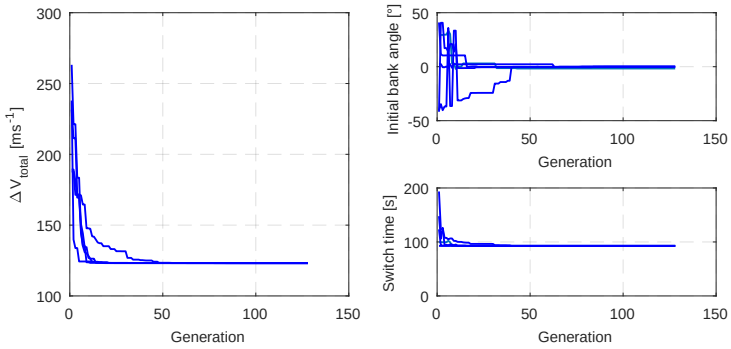

Figure 8.1: Evolution of the optimal ΔV_{total} and the corresponding initial bank angle and switch time.

The third point is proven by Lu (2014), where it is shown that a shallower (less negative) flight-path angles imply smaller derivatives of both dynamic pressure and heat flux. By flying lift-up lift-down bang bang or saturated lift-up trajectories, the flight-path is always the least negative, and the derivatives of the dynamic pressure and the heat flux are kept minimal. This, combined with the fact that the flight-time for the downwards leg, where the peak value must occur, is shorter for lift-up trajectories, results in conclusion that indeed the peak value for the dynamic pressure, and thus the heat flux is lower for lift-up trajectories than it is for lift-down trajectories.

Zucchelli (2016) compared lift-up lift-down bang bang and lift-down lift-up bang bang trajectories for initial conditions where both types of trajectories could be used to reach the target apoapsis. One additional conclusion that can be drawn from his analysis is that, for any initial condition, the trajectory where the load factor and the heat flux are the lowest is a trajectory where the lift is kept full-lift up until the deepest point in the trajectory, $\gamma = 0°$. From this point onwards the bank angle can be set to any value that respects $\frac{\delta\gamma}{\delta t} \geq 0$ without the requirements being violated (Even lift-down, which is required to keep $\gamma = 0°$ if the velocity is larger than the local circular velocity). The situation where the bank angle is set such that $\frac{\delta\gamma}{\delta t} = 0$ is also referred to as equilibrium glide. If horizontal equilibrium glide is sustained, the velocity will eventually be low enough such that $\frac{\delta\gamma}{\delta t} < 0$, even with lift-up. When this occurs, it is expected that sufficient energy has been dissipated such that the peak values of the new descending leg never surpass those of the initial descending leg, as long as the lift is kept lift-up. This however should be investigated case-by-case and is not a generalisation.

8.3. Numerical Verification

In the previous sections proofs have been provided that for simplified cases the optimal trajectory to minimise ΔV and the peak values is lift-up, lift-down bang-bang. However, as this was for simplified cases, it was verified how well these proofs matched with the result of the optimisation of trajectories simulated using more accurate environmental models, and, most significantly, rotating planets. As the results obtained for the various planets and vehicle all featured comparable behaviour, only the Earth-CRM case will be shown and discussed in this section.

The optimisation was done by using the PaGMO library included in Tudat. Specifically, the NSGA2 multi-objective optimisation method was used.. The initial velocities and flight-path angles were spaced out in a grid, with the velocities ranging from 4.0 kms^{-1} to 17.0 kms^{-1} with steps of 3.25 kms^{-1}, and the flight-paths ranging from -3.0° to -16.0° with steps of -3.25°. Additionally, the optimisation was also performed for the nominal initial conditions as described previous, as these were not included on this grid.

For each of the initial conditions the optimisation was performed 5 times, with a population size of 258 for 128 generations. Only the results for the nominal initial condition will be shown here, as the conclusions drawn from these figures are the same for all the initial conditions tested. In Fig. 8.1 and Fig. 8.2 the evolution of the optimal trajectories in terms of δV_{total}, and ΔV_2, respectively, are depicted.

It can be seen that the optimal trajectories converge to a full lift-up, full lift-down bang bang trajectory. In Fig. 8.2 one of the five iterations resulted in a slight outlier that has a non-zero initial bank angle, a delayed switch time, and a ΔV_2 that is an order of magnitude larger than the rest. However, the order of magnitude of ΔV_2 in this case is $\mathcal{O}(10^{-3})$ instead of $\mathcal{O}(10^{-4})$, resulting in a negligible absolute difference. In Table 8.1 the values for ΔV_{total}, ΔV_1, ΔV_2, and their corresponding initial bank angle and switch time are tabulated.

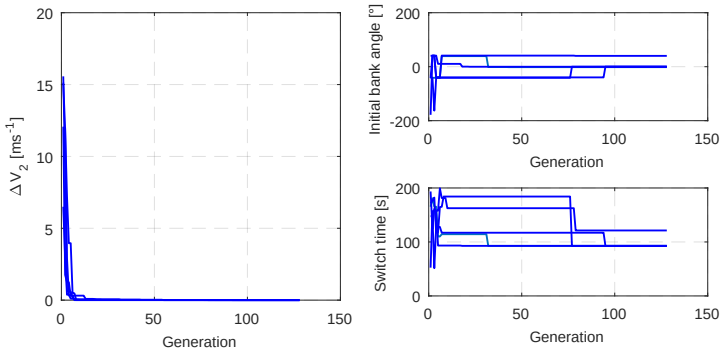

Figure 8.2: Evolution of the optimal ΔV_2 and the corresponding initial bank angle and switch time.

Table 8.1: Values for ΔV_{total}, ΔV_1, ΔV_2, $(a_{res}/g_0)_{peak}$, and q_{peak} and their corresponding initial bank angle and switch time as obtained from the PaGMO optimisation, trajectory optimisation, and full lift-up flight.

	PaGMO			Optimised			Full lift-up		
	Value	σ^* [°]	t_s^* [s]	Value	σ^* [°]	t_s^* [s]	Value	σ^* [°]	t_s^* [s]
ΔV_{total} [ms^{-1}]	123.1463	0.0232	92.7351	123.1456	0	92.5871	-	0	∞
ΔV_2 [ms^{-1}]	-0.0001	0.0232	92.7351	-0.00001	0	92.5871	-	0	∞
$(a_{\text{res}}/g_0)_{\text{peak}}$ [-]	8.2830	179.8720	0.7194	8.2829	0	92.5871	8.2829	0	∞
q_{peak} [MWm^{-2}]	12.5155	179.9927	4.3191	12.5153	0	92.5871	12.5153	0	∞

Additionally, the values obtained from a different method of trajectory optimisation, as will be discussed later, are also shown for comparison. From the data in this table it can be concluded that optimal trajectories to minimise ΔV_{total} and ΔV_2 are the same. This result will be used later for the general optimisation.

Fig. 8.3 and Fig. 8.4 show the evolution of the peak load factor and peak heat flux, respectively. In these figures three types of resultant optimal trajectories can be seen developing. The first style is a trajectory that starts with a bank angle of 0° and and switches sometime after 100s. At this time, the vehicle is already in on the ascending leg in the upper atmosphere about the leave the atmosphere. Effectively, the vehicle performs full lift-up flight. The second and third type of trajectory are physically the same. These types of trajectories start with bank angles of ±180° (lift-down), and switch almost immediately into the flight to lift-up, before the vehicle has significantly penetrated the atmosphere. Again, this type of trajectory is effectively a full lift-up flight. These results match what was expected from the previous analysis. In Table 8.1 the values for the optimal $(a_{\text{res}}/g_0)_{\text{peak}}$, q_{peak}, and their corresponding σ_0 and switch time are tabulated, together with the results from a full full-lift up trajectory for comparison.

From the data in this table two observations can be made. The first observation is that, even in optimal flight, the trajectory for the nominal initial conditions depicted here violate the requirements, specifically the peak heat flux of 7.95 MWm^{-2}. Therefore, it is not possible to design an optimal trajectory for the nominal case without a pre-entry ΔV. The second observation is that the values for the peak load factor and peak heat load are the same for both the full lift-up and the optimised trajectory. This is because the switch from lift-up to lift-down occurs on the ascending leg, after the peak values have been reached. The time after entry when the peak values occurred, together with the switch time and time of deepest penetration are tabulated in Table 8.2.

In this table it can be seen that indeed the values for the peak loads occur on the descending leg. This is a trait shared by all the skip trajectories, and confirms the statement made by Zucchelli (2016). Additionally, it was noted that the peak heat flux always either preceded or coincided with the peak load factor. For high velocity, shallow entries that failed to capture the two points would coincide, otherwise peak heat precedes.

Table 8.2: Values for the various interesting times during the trajectory obtained from the optimised trajectory.

	Switch time	Deepest point	Peak Heat Flux	Peak Load Factor
Time after entry [s]	92.5871	92.0750	62.4750	72.8750

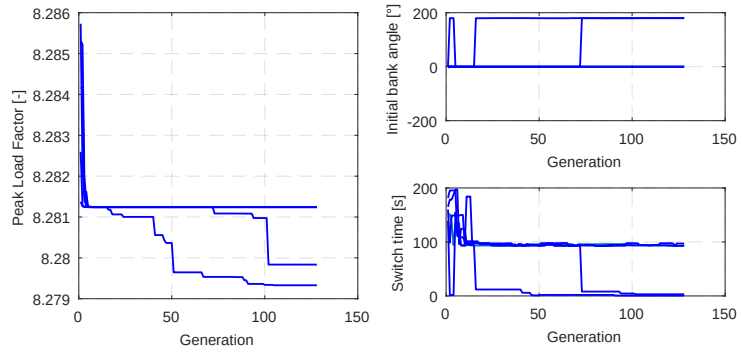

Figure 8.3: Evolution of the optimal peak load factor and the corresponding initial bank angle and switch time.

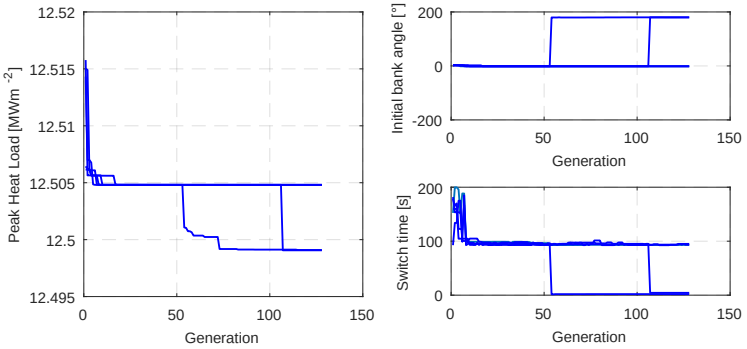

Figure 8.4: Evolution of the optimal peak heat flux and the corresponding initial bank angle and switch time.

8.4. Intermezzo: Bank Angle Laws

As in the previous section and the upcoming chapters trajectories simulated using bank angle control are presented, briefly the laws used to control the bank angle and their implementation will be discussed. Only two relatively simple laws are used throughout this research. The first law is a switch-bank law, and the second law is an equilibrium glide law. For both these laws perfect navigation, guidance, and control are assumed.

8.4.1. Switch-Bank Law

The switch bank law is the simpler of the two laws. This law simply keeps track of the time since atmospheric entry, and switches the bank angle from lift-up (0°) to lift-down (180°) when the time exceeds the specified switch time.

To properly implement this guidance law, and to ensure that the switch occurs exactly on the specified time, the switch time initial acts as a terminal condition for the numerical simulator. If this time is exceeded, the simulation stops and returns the state history. From this state history the epoch from the second to last state (the state that did not yet exceed the switch time) is considered. It is determined what the initial step size required to go exactly from the epoch of this state to the switch epoch is. If this step size falls within the boundaries of the minimal and maximal allowed step sizes, the simulation is restarted using the second to last state as the initial conditions, and the determined step size as the initial step size, resulting in the next epoch coinciding exactly with the switch epoch.

If the time-step required is smaller than the minimal allowed step size, the third to last state is considered. As the step size between the second to last and third to last states will always larger than the minimal allowed step size, the third to last state can be used as the new initial conditions without any further check. In this case the third to last state is used as the initial conditions, and the simulation is restarted.

8.4.2. Equilibrium Glide Law

Equilibrium glide is a flight condition where the flight-path angle does not change. This means that there is a balance between the effects on the flight-path angle due to the aerodynamic lift, gravitational forces,

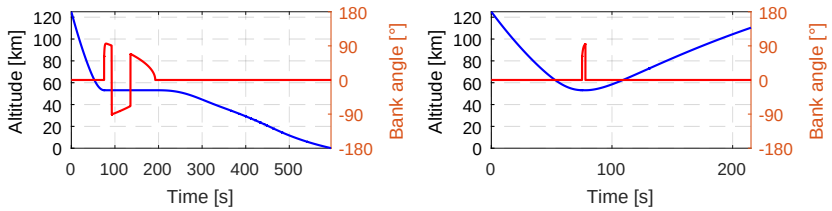

Figure 8.5: Altitude and bank angle profiles for the two versions of the equilibrium glide law.

centrifugal, Coriolis forces, and central body shape. Equilibrium glide can be used to keep the vehicle on a horizontal trajectory for a prolonged period of time.

An expression for the bank angle required to maintain a specific rate-of-change can be obtained by rewriting Eq. (3.33). By including the rate-of-change of the flight-path angle, any errors between the current and desired flight-path angle can be removed. For equilibrium glide, the rate-of-change of the flight-path angle would be set to zero. The approximate expression for the bank angle as a function of the flight-path angle rate-of-change where the apparent forces are omitted is:

$$\cos\sigma_{\text{cmd}} = \frac{2m}{\rho V^2 S C_L}\frac{g-V^2}{r}\cos\gamma + V\frac{\delta\gamma}{\delta t} \tag{8.13}$$

There are three possibilities when this equation is evaluated. $\cos\sigma$ can exceed 1, be below -1, or have a value somewhere in between. In the case that $\cos\sigma > 1$, more lift than is available is required to maintain the desired rate-of-change. In this case the commanded bank angle would be 0°, full lift-up. Similarly, if $\cos\sigma < -1$, more lift, but now pointed downward, is required to maintain the desired rate-of-change. in this case the commanded bank angle is 180°. The last case, where $-1 <= \cos\sigma <= 1$, the bank angle is commanded a value between $0 <= \sigma_{\text{cmd}} <= \pi$.

One consideration with this law is that it sets out-of-plane bank angles, resulting in out-of-plane motion. To control the wedge angle an additional law is added. At every call to the guidance interface, the current inclination is determined from the vehicle state. If the wedge angle between this inclination and the desired inclination exceeds the constraint, a bank reversal is performed.

A bank reversal is the action of mirroring the bank angle about the vertical axis, implemented by controlling the sign of the bank angle. However, after a bank reversal, the wedge angle will likely not fall immediately within the tolerance on the next call. Therefore a grace-period is implemented in which the bank angle cannot be reverse again, even if the wedge angle continues to exceed the tolerance.

A modification made to the general equilibrium guidance law is to only being flying equilibrium glide after horizontal flight has been achieved by full lift-up flight. This modification ensures that the peak heat flux and load factor values experienced during the descending trajectory are minimised. Additionally, instead of maintaining equilibrium glide until $\frac{\delta\gamma}{\delta t} < 0$ with full lift-up, the lift can be switched to lift-up prematurely, resulting in the vehicle being able to skip out of the atmosphere. In Fig. 8.5 the bank angle and altitude profiles for both versions of the equilibrium glide law is shown for a nominal Earth-CRM entry. For the lift-up equilibrium glide lift-up profile the time to switch back to lift up was chosen such that the target apoapsis was reached after atmospheric exit.

An example of the application for the first type of guidance law would be for a direct entry that results in touch- or splashdown. In the current formulation however, there is no control over the landing site. Adding control of the landing site and optimising the direct-entry trajectory is left for future research. While the optimisation is left for future research, in Chapter 10, the entry corridors for this type of trajectory (full-lift up until horizontal flight, followed by endured horizontal flight until touch-/splashdown) are developed. While in this chapter these corridors are given the name direct-entry entry corridor, they also provide insight into the entry corridor for altitude-targeting aerocapture, as will be discussed when relevant. Additionally, the flight-envelopes that ensure save entry into the atmosphere for direct entry are also provided in this chapter.

An example for the application of the second guidance law would be when attempting aerocapture with the desired to perform a plane-change. During the gilding phase instead of using bank-reversals, one could use the out-of-plane bank angle to to control, for instance, the inclination. As can be seen from the example, the duration of the glide phase before switching back to full lift-up is brief, allowing only limited out-of-plane adjustments. Whether this or another method of out-of-plane manoeuvring is optimal is left for future research.

9

Grid Search

With the knowledge established that for planar motion the full lift-up trajectory results in the lowest possible value for the peak load factor and the peak heat flux, and that a lift-up lift-down bang bang trajectory is optimal for obtaining the minimal ΔV trajectory, these two types of trajectories were further investigated. With this investigation it was attempted to determine how the peak loads and the characteristics altitudes responded to changes in the initial conditions and changes in the switch time.

In Section 9.1 the initial conditions are varied over a wide range of values to gather insight into the effect the initial conditions have on the apoapsis, penetration depth, and loads induced on the vehicle. In this section only the impact of varying the initial conditions is regarded. In the next chapter the data obtained from this section and the conclusions drawn are used to develop the entry corridors, and the effect of varying the vehicle configuration on the entry corridor is considered. In Section 9.2 the switch time is varied to gather insight in the effect of the switch time on the required ΔV and peak loads.

9.1. Initial Condition Variations

By determining the impact on varying the initial condition has on the trajectory, a suggestion for the optimal ΔV manoeuvre required to salvage an otherwise impossible trajectory can be made. For instance, the nominal entry condition optimised in the previous section resulted in violated constraints. For this entry a pre-entry ΔV is required modify the initial conditions to lower the peak heat flux to an acceptable values.

From the results presented in this section, it can be concluded that a combination of both velocity and flight-path change would have the best effect. This analysis is restricted to a purely qualitative evaluation, as for a quantitative solution a optimisation problem would need to be solved for every case individually. By formulating the quantitative optimal manoeuvre, the number of control variables for the subsequent optimisation problem can be reduced.

Additionally, the insight gained by this process can be applied when establishing the extreme initial conditions for which optimal flight is possible.

As the simulations performed on Earth, Mars, and Venus, with both the CRM and SRM vehicles all showed the same behaviour, the discussion in this chapter will primarily focus on the Earth-CRM case. For the other 5 cases no figures are presented as they provided no additional insight.

The figures, for example Fig. 9.1 have the following layout. In the top left a 3-dimensional surface is shown providing a complete overview of the behaviour of the considered metric to changes in the initial conditions. In the top right and bottom right, two projections are shown that isolate the behaviour of the metric to changes in velocity and flight-path angle, respectively. The last graph, in the bottom left shows the top-down contour of the surface plot to complete the set of projections.

9.1.1. Apoapsis

In Fig. 9.1 the values for the apoapsis altitude (the altitude of the apoapsis above the surface of the central body) is shown. Note that the apoapsis altitude is given as a fraction of the volumetric radius of the central body, in this case Earth. This is a much larger skip than is desired for this research. However evaluating such a large range of apoapses reveals more information regarding the impact of the initial conditions on the apoapsis altitude.

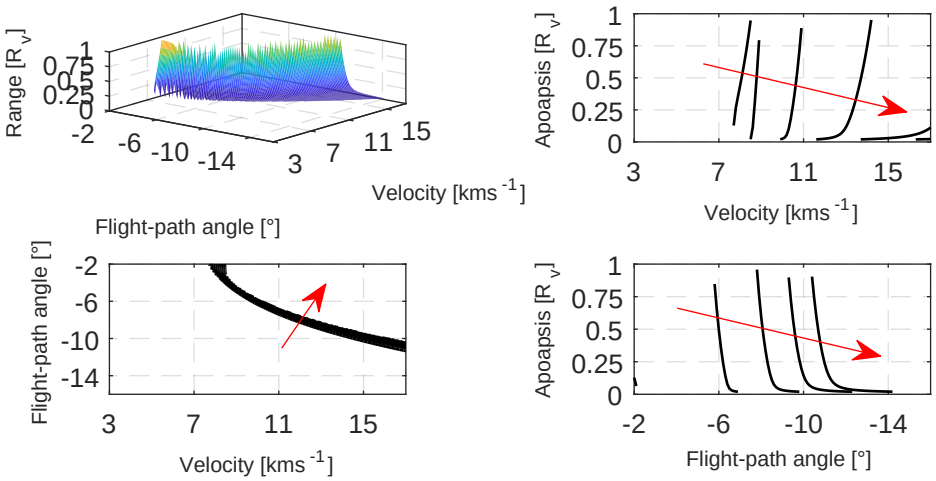

Figure 9.1: Apoapsis altitude from lift-up flight based on varying initial conditions for Earth-CRM. The red arrows indicate the direction of the third variable.

It can be seen that for a wide range of initial conditions no value for the apoapsis altitude is provided. In these cases the vehicle either never skips out of the atmosphere, even with a full lift-up flight, or skips out further than one Earth radius. Only a thin region is available where the apoapsis falls between barely skipping out of the atmosphere, and skipping out further than the radius of the Earth. From this it can be concluded that the apoapsis altitude is highly sensitive to the initial conditions.

From the projections for velocity and flight-path angle dependency, this conclusion is corroborated. Furthermore, the sensitivity to velocity seems to be coupled to the flight-path angle, as the slope of the curves in the top right projection decrease as the flight-path angle decreases (becomes steeper). Conversely, the sensitivity to the flight-path angle seems to be decoupled from the velocity, as no significant change to their shape can be discerned due to increased velocity.

In both cases it can be observed that the apoapsis starts increasing gradually, but suddenly increases its slope significantly. Because of this behaviour, a trajectory that overshoots the target is more likely to significantly overshoot, resulting in a large required ΔV manoeuvre to salvage the trajectory using a post-exit ΔV. However, due the high sensitivity, a much smaller pre-entry ΔV could be used to significantly reduce the apoapsis altitude.

For example consider the third line in the top-right corner ranging from approximately 10 kms^{-1} to 11 kms^{-1}. The pre-entry ΔV manoeuvre to decrease the velocity (disregarding the change in flight-path angle) will be approximately 1 kms^{-1}, while the post-exit ΔV to bring down the apoapsis from 2 Earth volumetric radii (2×6371.0 km) to 500 km above the surface (6871.0 km) will be significantly larger. While this will be discussed further in Chapter 11, it can thus already be concluded that for trajectories that overshoot the target, a pre-entry ΔV manoeuvre will be most effective. Additionally, as the apoapsis altitude is comparably sensitive to both the flight-path angle and velocity, this ΔV manoeuvre is likely a simultaneous change to the initial flight-path and the velocity.

9.1.2. Altitude of Transition Descending to Ascending Leg

In Fig. 9.2 the values for the altitude at which the flight transitions from descending to ascending are shown. This is different from the deepest point in the atmosphere as, technically, the deepest point in the atmosphere for a vehicle that does not exit the atmosphere is 0 m. Sticking to this definition would result in a similarly thin graph as for the apoapsis altitude. To obtain more usable data, it was decided to record the altitude at which the flight-path angle transitioned from negative to positive instead, even if it would transition back to negative later in the flight. For trajectories that skip out of the atmosphere this metric is the same as the penetration depth.

It is interesting to note that a pseudo-minimum altitude exists where the transition from descending to ascending occurs, if it occurs at all, that is relatively constant for the range of initial conditions tested. As can be seen most clearly in the altitude-velocity projection, the data for an initial velocity of 3 kms^{-1} is missing,

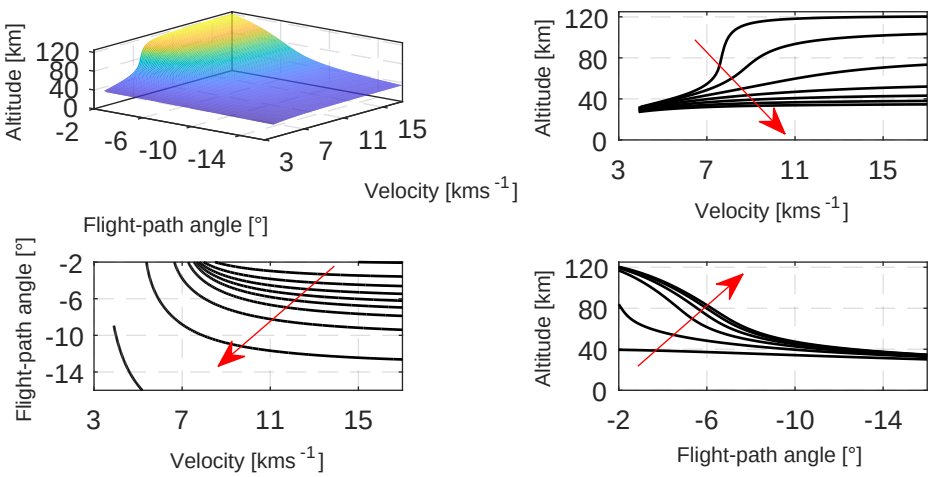

Figure 9.2: Transition altitude from lift-up flight based on varying initial conditions for Earth-CRM. The red arrows indicate the direction of the third variable.

this is because at this velocity the altitude never made the desired transition. The transition altitude primarily depends on the initial flight-path angle, but, especially for the shallower entries, also on the initial velocity.

Lastly, it can be seen that for a combinations of shallow and high velocity entry the vehicle barely enters the atmosphere. This means that barely any aerodynamic forces are generated, and that the trajectory is mostly unperturbed. If the velocity prior to entry was in excess of the escape velocity, this would result in a hyperbolic skip out. If prior to entry the vehicle was already on a closed orbit, the effect would be similar to that of aerobraking, where over time, through repeated passes through the atmosphere, the orbit would decay. The effect this has on the peak load factor and peak heat flux will be discussed in their relevant sections.

9.1.3. Load Factor

In Fig. 9.3 the values for the peak load factor are shown. In this graph the values of the constraint imposed on the load factor is shown as a red plane for the 3-dimensional graph, and as red lines in the three projections. It can immediately be seen that a portion of the initial conditions result in trajectories where this constraint is violated. As the full lift-up trajectory was proven to lead to the lowest value for the load factor, it can be concluded that these initial conditions result in trajectories that cannot be flown without violating the constraints, unless a pre-entry ΔV manoeuvre is conducted.

The fact that the lowest values for the load factor are encountered for shallow high velocity entries is not surprising. These types of entry only pass through the upper layers of the atmosphere, as discussed previously, where there is insufficient density to produce significant aerodynamic forces.

The load factor is sensitive to both velocity and flight-path angle, and the sensitivities are coupled. The faster the entry, the more sensitive the load factor is to the steepness of the entry, and the stepper the entry, the more sensitive the load factor is to the initial velocity.

The red curve in the bottom right graph, indicating the constraint value, appears to approach an asymptote at exceedingly high velocities. In reality the line continues to climb, requiring shallower initial flight-paths for faster entries.

Contrary to the overshoot case, trajectories that violate this constraint cannot be salvaged using a post-exit ΔV manoeuvre, as this will not change the fact that the constraint has been violated. A pre-entry ΔV manoeuvre is required! Considering the shape of the boundary as depicted in the lower-left graph, whether a change in initial velocity, flight-path angle, or both is optimal depends on the initial conditions. However, as the load factor in the Earth-CRM case spans almost the entire tested velocity range at near constant critical flight-path angle, in this case a change in the initial flight-path angle would be suggested.

9.1.4. Heat Load

In Fig. 9.4 the values for the peak heat flux are shown. Again the values for the constraints are shown in the figure. Comparing the boundaries in the bottom left graph of this figure and Fig. 9.3, it can be determined

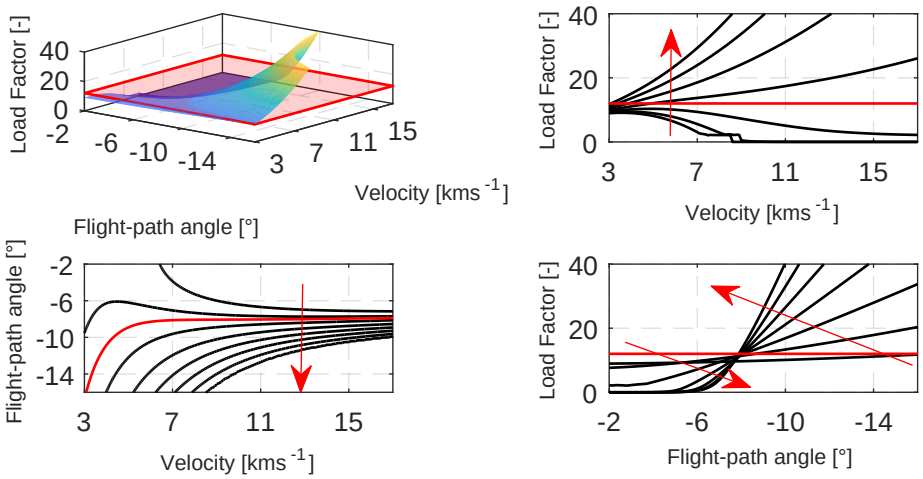

Figure 9.3: Values for the peak load factor from lift-up flight based on varying initial conditions for Earth-CRM. The red arrows indicate the direction of the third variable.

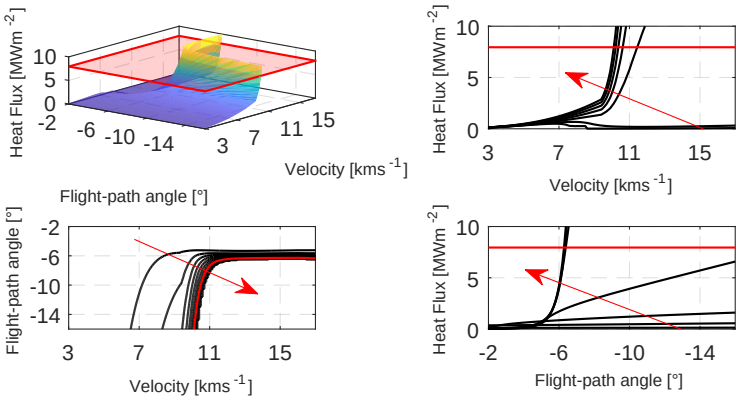

Figure 9.4: Values for the peak heat flux from lift-up flight based on varying initial conditions for Earth-CRM. The red arrows indicate the direction of the third variable.

that for the lower velocities the steepest allowable entry is driven by the peak load factor, whereas for the higher velocities the peak heat load becomes driving.

Similar to the previous case, the lowest values of the peak heat flux are encountered for high velocity shallow entries. While hard to see, this effect can be spotted both on the 3-dimensional surface graph and the heat flux-velocity projection.

The behaviour of the peak heat load is quite strange, as it initially increases slowly, and than suddenly increases exponentially. In the case of the velocity this can be explained by considering the aerothermal heating model for the radiative heat flux discussed in Section 3.6.4. The radiative heat flux is only considered for atmospheric flight with a velocity above 9 kms^{-1}. Viewing the top right graph, showing the velocity projection, it can be seen that indeed the sudden increase in peak heat flux occurs for velocities in excess of this 9 kms^{-1}.

The sudden, nearly exponential increase due to variations in the flight-path angle at these higher velocities can be explained by considering the atmosphere model discussed in Section 3.6.2, and the impact of the flight-path angle on the penetration depth as can be seen in Fig. 9.2. The density in the atmosphere decreases exponentially as the altitude increases. Therefore, the density increases exponentially too as the altitude decreases. As an increase flight-path angle causes deeper penetration, deeper penetration meaning exponentially higher values for the density, and the heat flux being proportional to the density to some power, explains the exponential behaviour of the heat flux to the increasing flight-path angle at higher velocities.

Similar to the case of the apoapsis altitude, the load factor initial increases gradually, but significantly increases its slope as either the initial velocity or flight-path angle increase. Similar to the load factor case, a

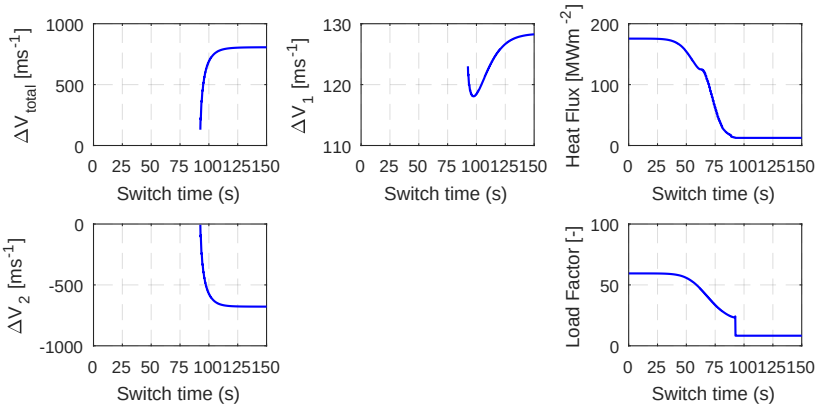

Figure 9.5: Result of the switch time grid search performed for the nominal Earth-CRM case using a wide range of switch times and moderately large step size.

pre-entry ΔV manoeuvre is required when this constraint is violated. Again, dependent on the initial conditions, a change in initial velocity, flight-path angle, or a combination of both can be optimal.

9.2. Switch Time

By investigating the effect of varying the switch time, it is attempted to gain more insight in how the peak values and the terminal conditions react to variations in the time at which the bang-bang manoeuvre is executed. With this insight a more efficient method for optimising the trajectory can be devised. This insight was used to develop the optimisation algorithm that is discussed in Chapter 11. Fig. 9.5 depicts the results for the grid search performed for the nominal Earth-CRM case. This figure graphs the values for ΔV_{total}, ΔV_1, ΔV_2, peak heat flux, and peak load factor as functions of the switch time. A switch time of 0s means that the flight is entirely lift-down, and as the switch time increases, the switch from lift-up to lift-down is delayed. For the first grid search, the switch time was varied over a large range (0s-150s), with moderately large step sizes (1s). The most useful observation that can be made from these graphs is that ΔV_2 is monotonic. It only decreases or stays the same, never increasing. For a short time till switch, the vehicle flies lift-down too long, resulting in either an undershoot or failure to skip. An undershoot results in a positive ΔV_2, and for a failure to skip a positive ΔV_2 is set artificially. This is required as for trajectories that do not skip out of the atmosphere, but instead reach the surface, ΔV_2 cannot be calculated, and a value for it has to be assumed. This is the reason for the lack of data for ΔV before roughly 90s. If the switch occurs too late, the trajectory results in an overshoot, requiring a negative ΔV_2. This monotonic behaviour of ΔV_2 is the key aspect considered when optimising trajectories.

Another observation is that discontinuities are present in the graphs. These discontinuities are due to transitions from one type of trajectory to another. The first type of trajectory is ever decreasing. This trajectory is obtained by switching to lift-down early in the atmospheric flight. The second type of trajectory features an increase in altitude but it does not skip out of the atmosphere. This trajectory is obtained by flying lift-up for a longer time. The third type of trajectory is a skipping flight, which is obtained by delaying the switch to lift-down even further. The transition from one type of trajectory to the next is marked by a discontinuity.

In the figures two discontinuities are present. The first discontinuity is caused by the transition from the monotonic altitude decreasing trajectory to the in-atmosphere altitude increasing trajectory. This discontinuity can be observed easiest in the graph showing the heat flux near the 60s mark. This discontinuity is not marked by a sudden jump in heat flux values, but by an abrupt change in sensitivity to the switch time.

The second discontinuity is due to the transition from fully in-atmosphere flight to skipping flight. This transition can most easily be observed for the load factor graph near the 90s mark. As the vehicle now achieves atmospheric exit, it also marks the start for the graphs showing the ΔV values. The sudden decrease in the load factor is the result of the vehicle no longer reaching the lower atmosphere, and eventually the surface, where the aerodynamic forces are much greater than they are at approximately 40 km, which was found to be the deepest point in the atmosphere for a skipping entry on Earth. As the vehicle no longer reaches these low altitudes, and evidently the peak load factor was measured on this second descending leg, a sudden jump occurs in the load factor.

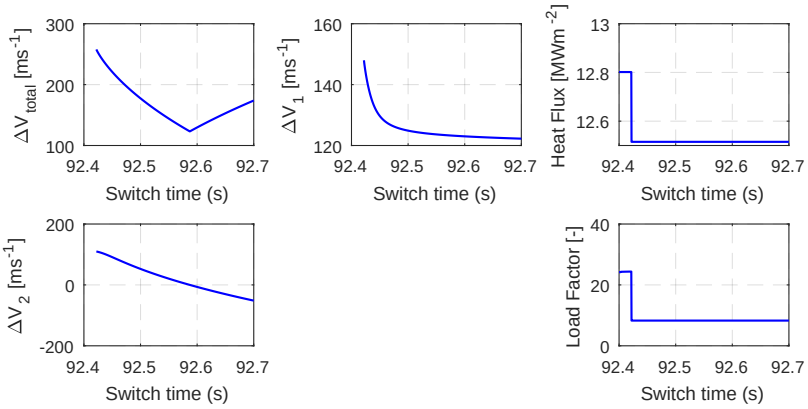

Figure 9.6: Result of the switch time grid search performed for the nominal Earth-CRM case using a narrow range of switch times and small step size.

To get a better look at these discontinuities, and the point where $\Delta V_2 = 0$ and ΔV_{total} is minimised, the range of considered switch times was narrowed to the range of 92.4s-92.7s, and the step size was decreased to 0.0004s. The results of the narrowed grid search is presented in Fig. 9.6. In these graphs the discontinuity effected by the transition to skipping flight can be seen more clearly in both the load factor and the heat flux graphs, where it was not noticeable in the wide version of the latter. Additionally, this narrower view reinforces the statement that this transition coincides with the start of calculateable values for ΔV. It can also be observed that the switch time for which $\Delta V_2 = 0$ is the same as the time for which ΔV_{total} is minimised, and that there indeed is a range of times for which ΔV_2 is positive, as this was not apparent form the wide grid search.

By approximating the curve for ΔV_2 shown in Fig. 9.6 by a linear polynomial, the local sensitivity of ΔV_2 to an error in the switch time can be estimated. Doing this results in a sensitivity of 581 $ms^{-1}s^{-1}$. Approximating the optimal ΔV_{total} by 120 ms^{-1} and applying requirement **GUID-01**, the allowed ΔV_2 is approximately 6 ms^{-1}, resulting a tolerance in switch time of 10.4 ms. To meet requirement **GUID-01** in this case, the guidance algorithm has to be able to command the switch time within this tolerance. An approximation for tolerance can be obtained for the other cases in a similar manner.

The general behaviour shown in Fig. 9.5 and Fig. 9.6 and the discussion of these figures is applicable to both vehicles, and for flight about any of the three planets. Only the exact values change. Therefore, the other cases will not be further discussed here as they provide no additional insight for the research.

10

Entry Corridor & Flight Envelope

This chapter deals with answering the second research questions by determining the limit initial conditions for which aerocapture can be achieved. Based on the results from the two grid-search efforts presented in the previous chapter, the boundaries encompassing the entry corridor for both altitude-targeting and direct entry were defined. For altitude targeting, six boundaries were formulated, for direct entry, five.

In this chapter the entry corridors for both altitude-targeting and direct entry are presented. Altitude-targeting is discussed in Section 10.1, and direct entry in Section 10.2. After this, in Section 10.3, the effect of varying the vehicle configuration on the entry-corridor is discussed. As this effect is similar for both the altitude-targeting and direct entry entry corridors, for both vehicles, on all planets, only the effect on the Earth-CRM case is discussed in detail. In Section 10.4 a method is presented that allows for the definition of the entry corridor at any altitude, based on the developed entry corridor at a particular altitude. In the last section of this chapter, Section 10.5, the flight envelopes that designates the altitude-velocity space usable by the vehicle to ensure safe entry into the atmosphere are presented. The application of these flight envelopes is primarily for direct entry. After discussing the general flight envelope, the effect of varying the vehicle configuration on the flight envelope is discussed.

10.1. Entry Corridor - Altitude Targeting

The entry corridor was in part already discussed in the previous section when the initial condition boundaries for the cases of peak load factor and peak heat flux were established. In this section several additional boundaries are added, creating an fully encompassed entry corridor. In total four new boundaries are added, all related to the terminal conditions of the trajectory.

The first new boundary is formed by the initial conditions for which the vehicle no longer leaves the atmosphere when flying full lift-up, called the no skip-out boundary. Initial conditions exceeding this boundary result in trajectories that never skip out of the atmosphere and require pre-entry ΔV manoeuvres to salvage the trajectory.

The second new boundary is closely related to the first. This boundary is formed by the initial conditions for which the vehicle undershoots the target, but still leaves the atmosphere when flying full lift-up. The vehicle skips out of the atmosphere and is captured, but is not able to reach the desired target. This trajectory requires either a pre-entry ΔV, or a post-exit ΔV to be salvaged.

The third new boundary is the opposite of the previous. This boundary is formed by the initial conditions for which the vehicle overshoots the target when flying full lift-down, but is still captured after leaving the atmosphere. Either a pre-entry ΔV, or a post-exit ΔV is required to salvage this trajectory. Alternatively, aerobraking could be used as a low-propellant cost alternative.

The fourth and last new boundary is formed by the initial conditions for which the vehicle leaves the atmosphere when flying full lift-down without being captured. Trajectories that exceed this boundary skip out of the atmosphere with hyperbolic excess velocity and continue on a perturbed version of their heliocentric trajectory. As the definition of aerocapture is to close the orbit by an atmospheric pass, initial conditions that exceed this boundary fail to aerocapture. Therefore a pre-entry ΔV is required. While technically a post-exit ΔV could be used, this would result in a large propellant requirement, as will be discussed in Section 11.3

It should be noted that these four boundaries only regard the terminal conditions, and not the constraints

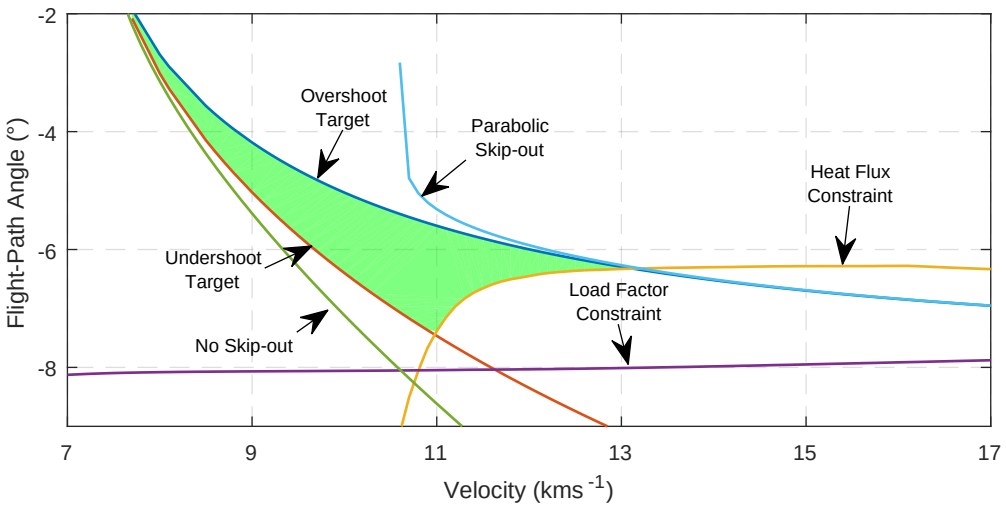

Figure 10.1: Altitude-targeting entry corridor for the Earth-CRM case, flown with nominal vehicle configuration.

throughout the flight. If a set of initial conditions fall within the space dictated by these boundaries. it is not automatically guaranteed that an optimal trajectory is possible. However, being outside of the space dictated by the boundaries does guarantee that an optimal trajectory is impossible without a ΔV manoeuvre either prior to entry, or post-exit.

To illustrate this, consider the point where a boundary flown full lift-up, such as "overshoot target", and a boundary flown full lift-down, such as "heat flux constraint", intersect. At this point the trajectory has to be flown full lift-up to not violate the requirements, but to avoid overshooting or skipping out with hyperbolic excess velocity, the trajectory has to be flown lift-down. These two statements contradict each other, and result in an impossible trajectory requirement.

10.1.1. CRM Entry Corridor

In Fig. 10.1 the entry corridor the Earth-CRM case is shown. In this figure the green area indicates the upper bound for the entry corridor width. Just to reiterate, having initial conditions within this area does not guarantee an optimal trajectory is possible, however, initial conditions outside this area guarantee that an optimal trajectory is impossible. This fact will be used later in the trajectory optimisation algorithm.

As already discovered previous, the nominal initial conditions for the Earth mission fall outside of the entry corridor. The entry corridor indicates that the heat flux constraint will be violated, but no others. This matches the conclusion drawn previously where it was possible to design a trajectory that reached the target, therefore the target is not undershot or overshot, and the load factor was not violated, but the heat flux was. From the sensitivity analysis it can be determined that the optimal strategy for salvaging this trajectory is a pre-entry ΔV that primarily alters the flight-path angle. The exact ΔV required would be the subject of separate optimisation scheme. This is an example how this upper bound can be used to evaluate the ability to design an optimal trajectory.

Entry corridors were also produced for the Mars-CRM and Venus-CRM cases. These can be seen in Fig. 10.2. In addition to the entry corridors, the bottom right graph shows the width of the individual entry corridors as a function of the initial velocity. This facilitates comparing the size of the entry corridors. By showing all the graphs side by side with the same axis limits, one can easily compare the position and size of the entry corridor within the initial condition space. The corridors for Earth and Venus are comparable both in position and size. The Mars corridor is clearly larger, but required steeper entry to prevent overshooting the target or skipping out without capturing.

For entry with low velocity, the flight-path angle boundaries are driven by the full lift-up undershoot and the full lift-down overshoot boundaries. Only when the velocity increases, and thus the peak load factor and heat flux increase, do the constraints imposed on the trajectory become driving. For the Earth-CRM case, the load factor is never a driving constraint. As the velocity increases, the heat flux becomes the driving constraint.

For Mars the opposite conclusion can be drawn. Here the peak heat flux never becomes a driving con-

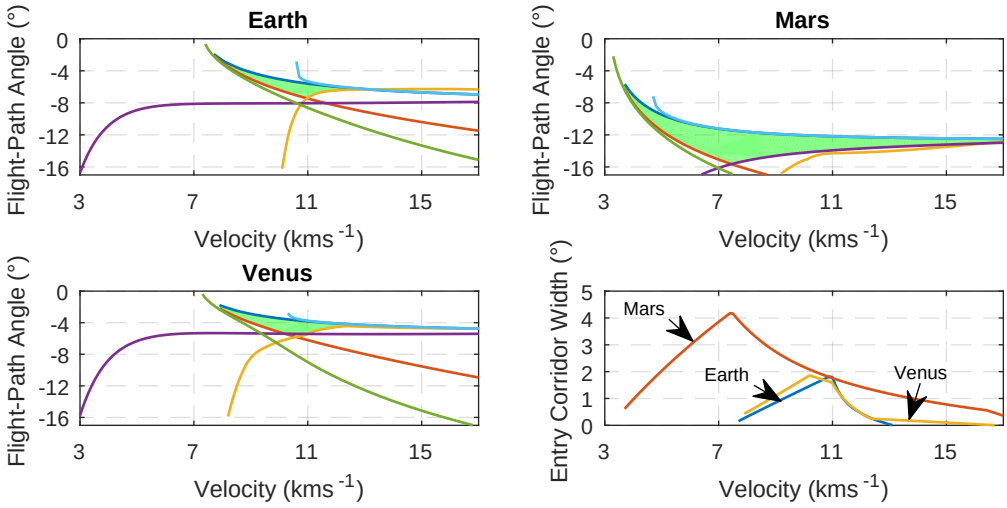

Figure 10.2: Comparison between the altitude-targeting entry corridors for all three planets, flown with nominal CRM vehicle configuration.

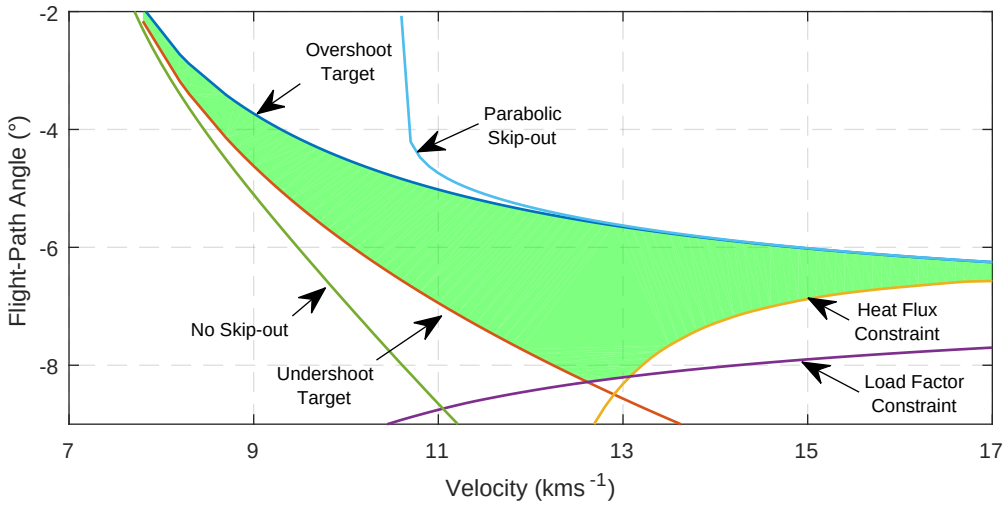

Figure 10.3: Nominal entry corridor for Earth-SRM case with nominal vehicle configuration.

straint, with the peak load factor dictating the maximum steepness of the entry. Venus shows a combination of both. For the low velocities, the undershoot boundary is driving, which gets surpassed by the load factor boundary as the velocity increase, which gets surpassed by the heat load as the velocity continues to increase.

This might be difficult to see in the bottom left graph in Fig. 10.2 depicting the entry corridor for Venus, but it can also be concluded by noticing the discontinuity (kink) in entry corridor width shown in the bottom right graph for Venus near 11 kms^{-1}. This discontinuity indicates that a different curve is driving the entry corridor width. As the upper bound is always dictated by the lift-down overshoot, this must mean that the lower bound changed driving factors, thus that peak load factor is replaced by peak heat flux.

10.1.2. SRM Entry Corridor

In Fig. 10.3 the entry corridor the Earth-SRM case is shown. By comparing this figure to Fig. 10.1, it can immediately be observed that the entry corridor for the SRM vehicle is larger than the corridor for the CRM vehicle. This is primarily due to the smaller nose radius, resulting in lower heat flux, and more relaxed constraints regarding the load factor compared to the CRM vehicle. This trait is not just observed when comparing the CRM and SRM cases for Earth, but also for both Mars and Venus.

Unlike the Earth-CRM case, the initial conditions actually fall well within the entry corridor. Therefore it

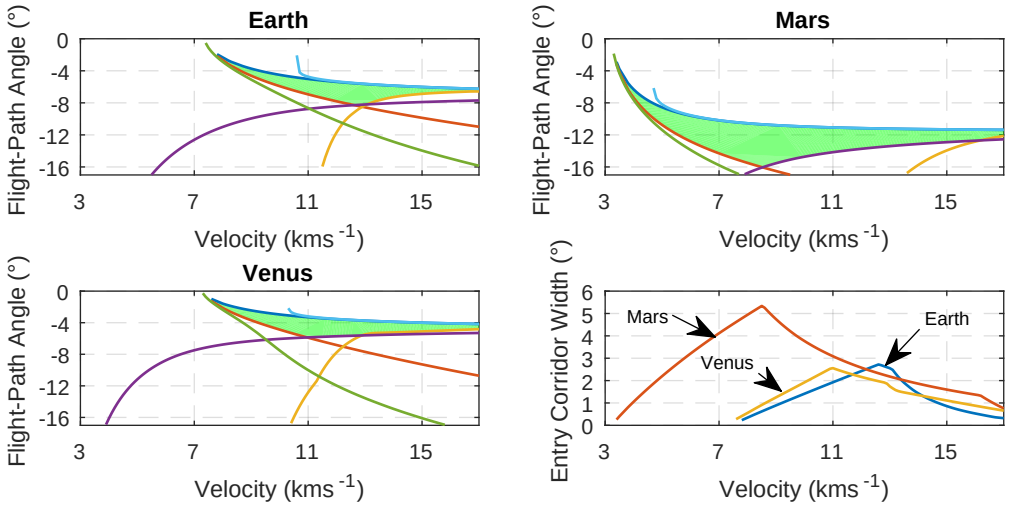

Figure 10.4: Comparison between the altitude-targeting entry corridors for all three planets, flown with nominal SRM vehicle configuration.

is possible that it is possible to develop an optimal trajectory for this case. Another difference is that for the SRM vehicle the peak load factor is driving a small number of initial velocities, before the heat flux becomes the dominant lower boundary.

Similar the the CRM case, the entry corridors were also developed for Mars-SRM and Venus-SRM. These are presented in Fig. 10.4. It can again be seen that the entry corridors for Earth and Venus are comparable in position and size, and that the Mars entry corridor is significantly larger but requires steeper entry. From the corridor width it can easily be concluded that the entry corridors for the SRM vehicle are much larger than for the CRM vehicle.

Unlike the Mars-CRM case, for the Mars-SRM case, at the highest simulated velocities, the peak heat flux becomes a driving constraint. This might be difficult to see in the top right graph in Fig. 10.4 depicting the Mars entry corridor, but can be seen from the discontinuity on the Mars entry corridor width in the bottom right graph.

The Venus-SRM case is similar to the Venus-CRM case in that first the undershoot boundary is dominant, followed by the load factor boundary, followed by the heat flux boundary. The only difference is that the load factor boundary is dominant for a larger range of velocities in the SRM case.

10.2. Entry Corridor - Direct Entry

The entry corridor for direct-entry is defined sightly different than the one used for altitude targeting. Namely, the maximal skip-out altitude and parabolic skip boundaries are defined differently. Both of these boundaries are determined by flying the vehicle lift-up until horizontal flight, and then switching to lift-down, compared to the full lift-down trajectory used for altitude targeting. The entry corridors for the Earth-CRM and Earth-SRM cases are shown in Figs. 10.5 and 10.6, respectively. Note that the no-skip out boundary is not considered driving. This is because whether or not the vehicle skips out of the atmosphere is not important for direct-entry.

By defining the upper limit trajectories as described, the space encompassed by the entry corridor guarantees that direct-entry is possible without skipping out excessively, and, more importantly, that optimal altitude-targeting aerocapture is possible. A trajectory with initial conditions within these boundaries is guaranteed to be able to perform optimal aerocapture. However, in this case a region where aerocapture is potentially possible, but not guaranteed possible, is excluded. Therefore the direct entry entry corridor presented here can be considered a conservative, or guaranteed-safety, entry corridor, where the altitude-targeting entry corridor showed the entire possible region, with no guarantees. The direct entry entry corridors for the other two planets are shown in Figs. 10.7 and 10.8 for the CRM and SRM vehicle, respectively.

The fact that initial conditions within this region are guaranteed to be able to perform aerocapture is attempted to be illustrated with the following example. At the maximal skip-out and parabolic skip-out boundary, the vehicle has both a descending and ascending leg, otherwise the vehicle would not leave the atmo-

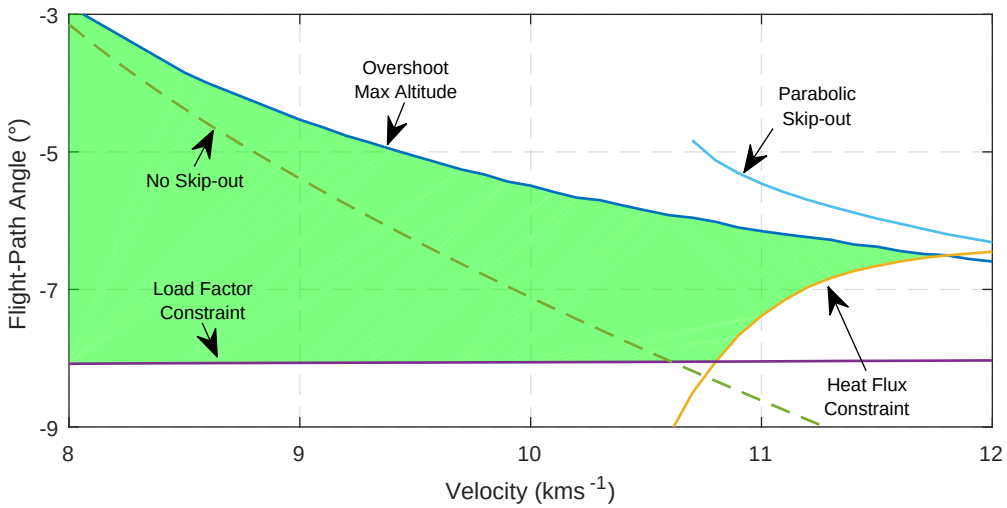

Figure 10.5: Range-targeting and guaranteed-safety altitude-targeting entry corridor for the Earth-CRM case, flown with nominal vehicle configuration.

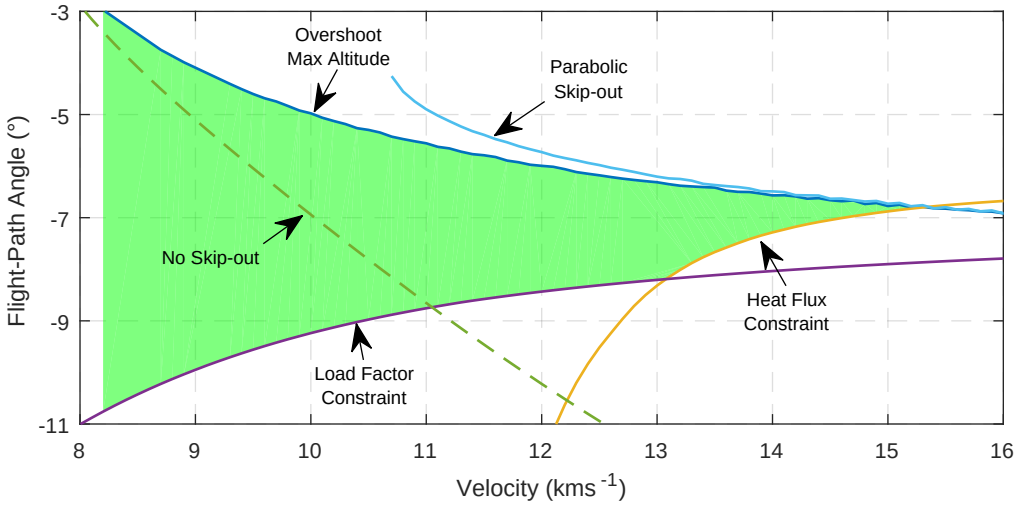

Figure 10.6: Range-targeting and guaranteed-safety altitude-targeting entry corridor for the Earth-SRM case, flown with nominal vehicle configuration.

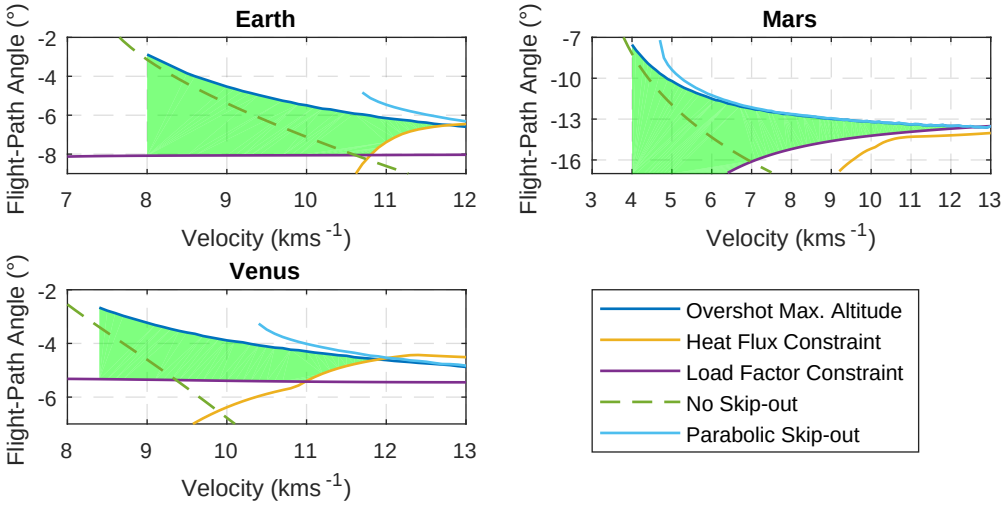

Figure 10.7: Range-targeting and guaranteed-safety altitude-targeting entry corridor for the CRM vehicle for al planets, flown with nominal vehicle configuration

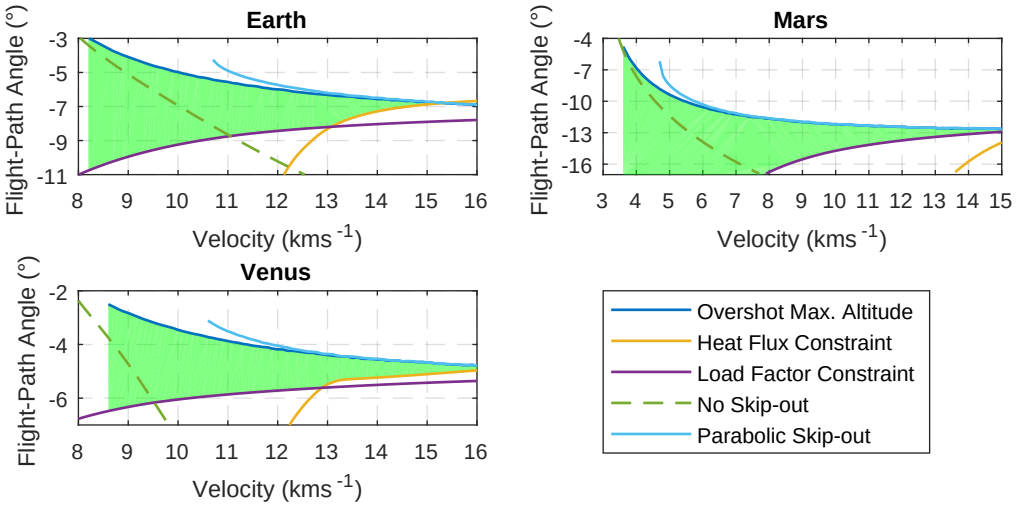

Figure 10.8: Range-targeting and guaranteed-safety altitude-targeting entry corridor for the SRM vehicle for al planets, flown with nominal vehicle configuration

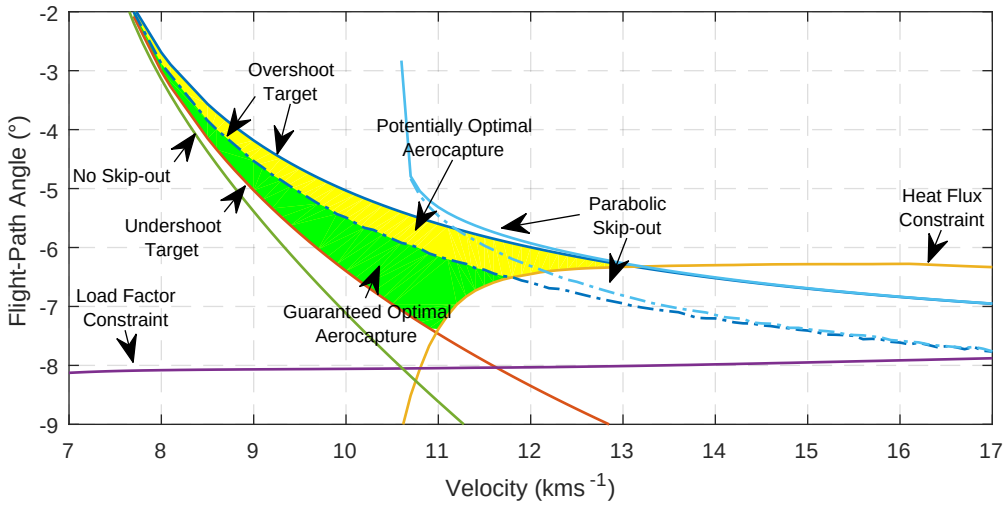

Figure 10.9: Combined entry corridor showing the region that guarantees that optimal aerocapture is possible, and the region for which areocapture is potentially possible.

sphere. It was proven in Chapter 8 that the peak values occur on the descending leg. The entire descending leg is flown lift-up, resulting in the optimal values for the peak load factor and the peak heat load. This means that there no longer is a contradiction at the intersection between the upper parabolic and overshoot boundaries, and the lower peak load factor and heat flux boundaries.

The maximal skip-out altitude to be used for the direct entry was put at 500 km. This is roughly the altitude where the Van Allen radiation belts start for Earth. The added benefit of defining the maximal skip-out altitude like this, is that the entry corridors produced in this section are also valid for altitude-targeting. Therefore the name direct entry entry corridor is not entirely correct, but it was used to distinguish between the two types of corridor.

By combining the information from the altitude-targeting entry corridors presented in the previous section and the direct entry entry corridors presented in this section, it can be determined for any initial state whether aerocapture is impossible (outside altitude-targeting corridor), potentially possible, to be determined from optimisation scheme (inside altitude-targeting corridor but not inside direct entry entry corridor), or guaranteed possible (inside direct entry entry corridor). This is visually shown in Fig. 10.9, where the altitude-targeting and direct entry entry corridors are overlain, and the regions for guaranteed and potentially possible aerocapture are shaded green and yellow, respectively. Similar complete entry corridors were obtained for the remaining five cases too, but these are not reproduced here.

10.3. Entry Corridor Variations

In the previous section the entry corridors for the nominal vehicle configurations were shown. In this section the effect of varying the vehicle configuration on the entry corridor is investigated. The two aspects of the vehicle configuration that are altered are the aerodynamic model and the vehicle mass. As the variation in the vehicle configuration has the same effect for all six cases and for both altitude-targeting and direct entry, at least in a qualitative manner, only the altitude-targeting Earth-CRM case will be shown in detail. For the other cases, only the impact on the area bounded by the entry corridor is shown, as an indication of the effect of the vehicle configuration change. The area bounded by the entry corridor is obtained by integrating the area between the upper and lower bound. By comparing the rates of change of the areas, conclusions can be drawn regarding the sensitivity of the entry corridor to the vehicle configuration.

10.3.1. Impact of Aerodynamic Variation

The first aspect of the vehicle model that was varied was the aerodynamic model. This model was altered in two different manners. The first manner was to scale the lift coefficient up and down by 20%. As the vehicle model discussed in Section 3.6.1 is a variable L/D model, this method retains the variable L/D nature of this model. The effect of increasing and decreasing the lift coefficient on the entry corridor is illustrated in

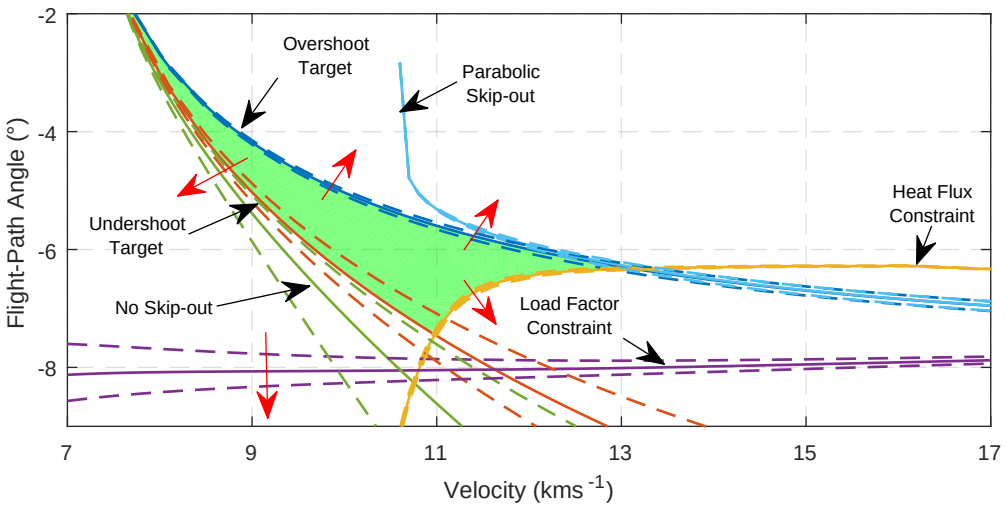

Figure 10.10: Altitude-targeting entry corridor for the Earth-CRM case, flown with lift variations of vehicle configuration. The red arrows indicate the direction of increasing lift.

Fig. 10.10.

The result of increasing the lift-coefficient is an overall wider entry corridor. Because of the increased lift coefficient, the vehicle during lift-up flight remains higher in the atmosphere, lowering the load factor and heat flux, compared to a nominal flight with the same entry angle, thus allowing for steeper entry. As it flies higher in the atmosphere, less aerodynamic forces, mainly drag, are produced compared to the nominal situation, and thus less velocity is lost. The vehicle can therefore enter steeper and still manage to skip out and reach the target. For lift-down flight, as the vehicle generates more lift "pulling" the vehicle down, a shallower entry can be performed that still results in capture. Naturally, the effect of lowering the lift-coefficient is the opposite.

The effect on this lift variation on the size of the entry corridor is shown in Fig. 10.12 for the CRM vehicle, and on Fig. 10.14 for the SRM vehicle. The value for the entry corridor area in these figures have been normalised with respect to the nominal area.

In addition to the effect scaling the lift-coefficient, the effect of varying the L/D ratio was also investigated. By keeping the drag-coefficient dependency on the velocity as prescribed by the aerodynamic model in Section 3.6.1, and making the corresponding lift-coefficient a multiplication of these values, a fixed L/D profile is obtained. The L/D of the vehicle was varied from $L/D = 0$, ballistic entry, to $L/D = 3$. In addition, the L/D ratios of 0.26 and 0.44 were also used. These values were chosen as they represent the minimum and maximum L/D ratio of the variable L/D profile. The effect on the entry corridor area for the CRM and SRM vehicles can be seen in Fig. 10.11 and Fig. 10.13, respectively

From these figures it can be observation that, as the L/D ratio increases, the entry corridor seems to becomes less sensitive to the increase in L/D. This is especially pronounced for the Mars cases. However, for Mars, this is a misleading observation, as the sudden decrease in sensitivity is not due to an actual decrease in sensitivity, but due to the range of initial conditions for which the entry corridor is produced. This range imposes artificial boundaries on the entry corridor size that limit the maximal entry corridor area. As the entry corridor for Mars is much closer to two of these boundaries (steepest flight-path angle and slowest velocity), the entry corridor is not able to increase as much as the Venus and Earth case. For the Venus and Earth cases, these limits are not reached even at $L/D = 3$, and it can thus be concluded that the sensitivity to L/D decreases as L/D increases. It can thus be concluded that, increasing the L/D of a low L/D vehicle has an overall positive effect on the size of the entry corridor, but that the effectiveness of increasing the L/D decreases for vehicles with high L/D ratios.

10.3.2. Impact of Mass Variations

The second investigation was into the effect of the mass on the vehicle on the entry corridor. Similar to the lift variation, the mass was varied by ±15%. The effect of the mass variation on the entry corridor for the Earth-CRM case is shown in Fig. 10.15.

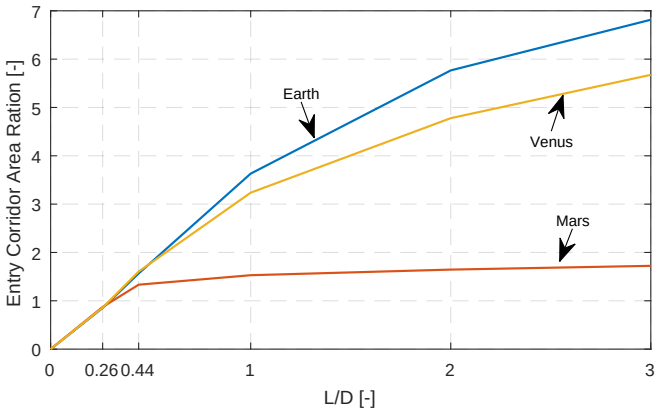

Figure 10.11: Effect on the altitude-targeting entry corridor area due to variation of L/D for the CRM vehicle.

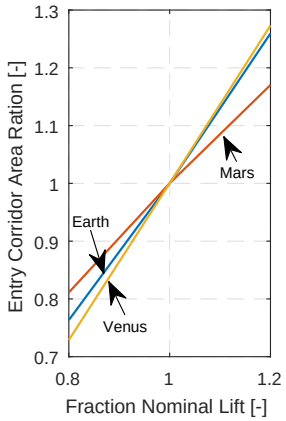

Figure 10.12: Effect on the altitude-targeting entry corridor area due to variations in the lift for the CRM vehicle.

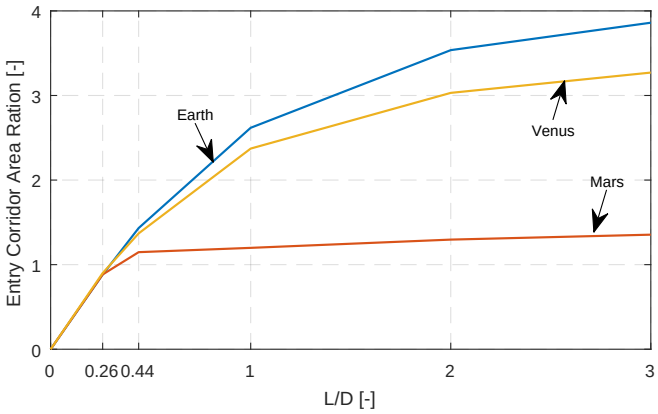

Figure 10.13: Effect on the altitude-targeting entry corridor area due to variation of L/D for the SRM vehicle.

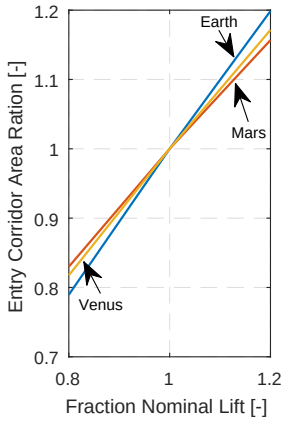

Figure 10.14: Effect on the altitude-targeting entry corridor area due to variations in the lift for the SRM vehicle.

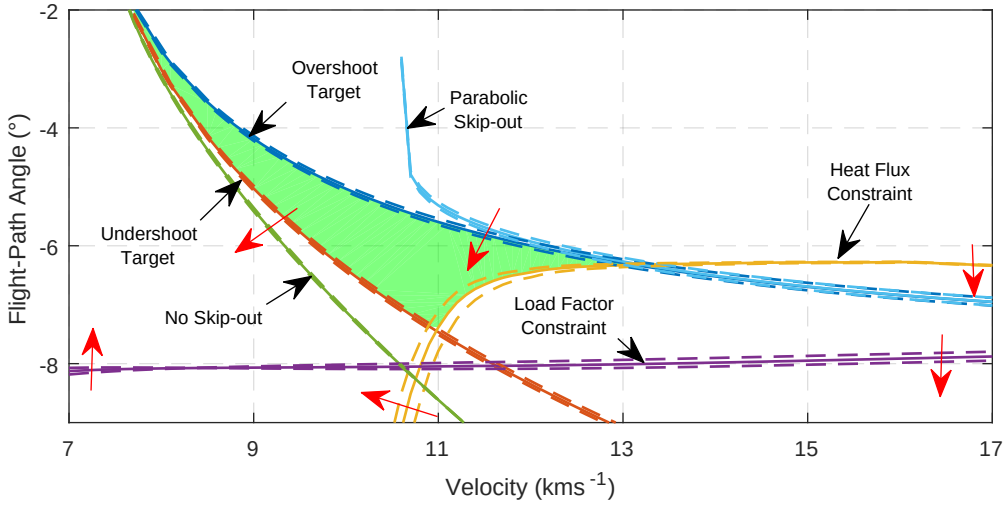

Figure 10.15: Altitude-targeting entry corridor for the Earth-CRM case, flown with mass variations of vehicle configuration. The red arrows indicate the direction of increasing mass.

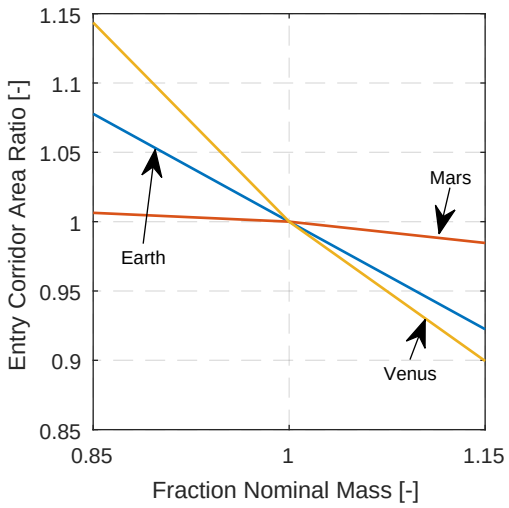

Figure 10.16: Effect on the altitude-targeting entry corridor area due to variations in the mass of the CRM vehicle.

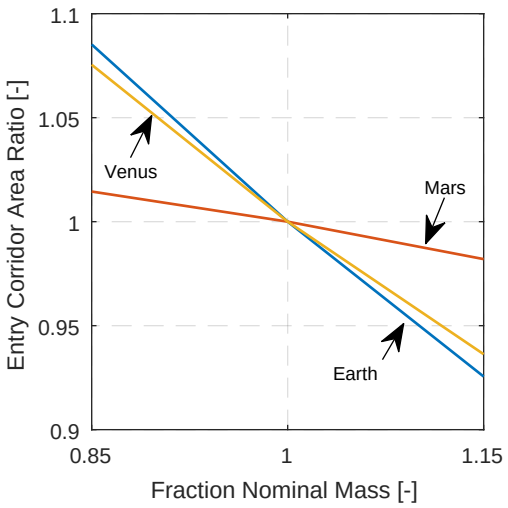

Figure 10.17: Effect on the altitude-targeting entry corridor area due to variations in the mass of the SRM vehicle.

The mass variation affects the entry corridor much different than the lift variation did. The mass variation causes more of a shift of the entry corridor instead of a widening. The no skip, undershoot, overshoot, and parabolic skip boundaries all shift in the same direction, namely steeper entry possible (in case of the former two) or required (in case of the latter two) as the mass increases.

The change in the peak heat flux has the largest impact on the size of the entry corridor area. For the velocities relevant to the entry corridor, the peak heat flux increases compared to the nominal configuration. After investigation this was found to be due to the lowered aerodynamic accelerations, resulting in the vehicle reaching a lower point in the atmosphere with a higher velocity, relative to the nominal situation. As the velocity increases, the effect of mass on the heat flux boundary disappears. At these high velocities, and the flight-path angle indicated by the heat flux boundary, the trajectory does not penetrate deep enough due to the high rate of change of the flight-path angle (see Eq. (3.33)), that the aerodynamic acceleration are negligible, and this the effect of mass on these accelerations disappears.

The effect on this mass variation on the size of the entry corridor is shown in Fig. 10.16 for the CRM vehicle, and on Fig. 10.17 for the SRM vehicle. The value for the entry corridor area in these figures have been normalised with respect to the nominal area. Comparing the entry corridor ratios in these figures to those in Fig. 10.12 and Fig. 10.14, it can be determined that the entry corridor is less sensitive to changes in mass than to changes in lift. Additionally, the sensitivities for the individual planets seems to differ significantly more than they did for lift. It can therefore be concluded that, to increase the entry corridor area, it is more efficient to increase the lift while keeping the mass the same. Even if the mass of the vehicle had to increase, the total effect on the entry corridor might still be positive, although the increase in mass is counter-productive to the purpose of the aeromanoeuvre.

10.4. Intermezzo: Unperturbed Hyperbolic Trajectory

A downside of the entry corridors as discussed in the previous section is that they are only valid at a particular altitude, in this case at 125 km above the volumetric radius of the central body. This means that this representation of the entry corridor, and the entry corridor width established by it, is only useful to a vehicle at this particular altitude. While this representation is good for gaining insight into the entry corridor, the differences between the corridors of various vehicles and planets, and the impact of vehicle configuration variations, its dependency on altitude limits the applicability for, for instance, determining the accuracy required of a guidance applications.

Another method for specifying the entry corridor width is by determining the hypothetical unperturbed hyperbolic trajectories on which the upper and lower bound of the entry corridor particular velocity fall. Based on the periapsis altitudes of these two trajectories, the corridor width can be specified as the distance between them. This is illustrated in Fig. 10.18.

According to Chapman (1960) the value for the periapsis altitude r_p can be determined from Newton's

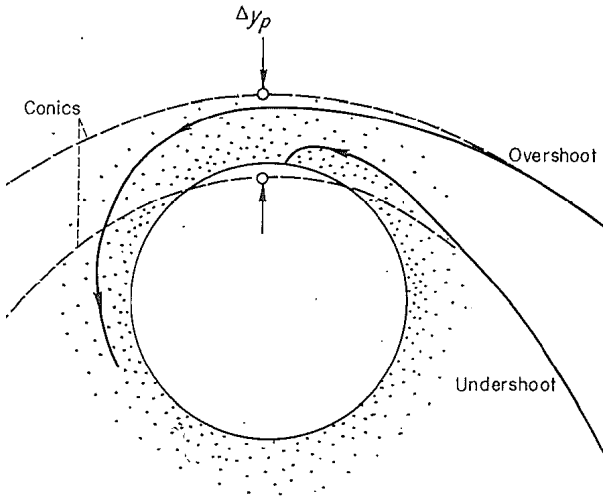

Figure 10.18: Definition of the corridor width Δy_p. This illustration was obtained from Chapman (1960).

equation for a two-body drag-free trajectories:

$$\frac{r_p}{r} = \frac{1 - \sqrt{\left(\bar{V}^2 - 1\right)^2 + \bar{V}^2\left(2 - \bar{V}^2\right)\sin^2\gamma}}{2 - \bar{V}^2} \tag{10.1}$$

where V is the velocity made non-dimensional by dividing by the local circular velocity according to

$$\bar{V} \equiv \frac{V}{V_c} = \frac{V}{\sqrt{gr}} \tag{10.2}$$

With the value for the periapsis radius, the periapsis velocity can be determined using the equation for orbital energy:

$$\epsilon = \frac{v^2}{r} - \frac{\mu}{r} \tag{10.3}$$

and equating the energy at the initial state to the energy at the periapsis, and solving for the velocity.

From this point, the boundary of the velocity and flight-path angle can be found at any radial position away from the central body by applying the same equations. First determine the radial position at which the limit values are desired, and using the orbital energy equation to determine the local velocity. With the local velocity and radial position, Eq. (10.1) can be solved for the limit flight-path angle.

10.5. Flight Envelope

While the entry corridor designates the initial conditions for which optimal trajectory can be achieved, the flight envelope designates the altitude-velocity space usable for re-entry. This type of graph is more important when the goal of the trajectory is to land on the central body, but the lower bound is also relevant for a trajectory with the goal to reach a target apoapsis.

The flight envelope consists of three boundaries. The lower boundaries is determined by the most driving of the load factor and heat flux constraint. Going beyond this boundary will violate one or both of these constraints. The upper bound is the horizontal, lift-up equilibrium glide. If the vehicle state remains underneath this boundary, no skipping flight will occur. This definition shows the reason why these graphs are more useful for entry with the intent to land, as skipping out is desired for apoapsis targeting. Contrary to the previous set of entry corridors, where starting inside the indicated area did not guarantee success, but starting outside of it did guarantee failure, staying within the area indicated in these graphs guarantees safe-passage without skipping, but going beyond the equilibrium glide boundary does not guarantee that a skip will occur.

At and above the local circular velocity, the equilibrium glide boundary is no longer defined as the centrifugal acceleration due to the curvature of the Earth has a positive, or no, effect on the rate of change of the flight-path angle at these velocities. Unless the bank angle is switched to lift-down, equilibrium flight cannot be achieved for supercircular flight

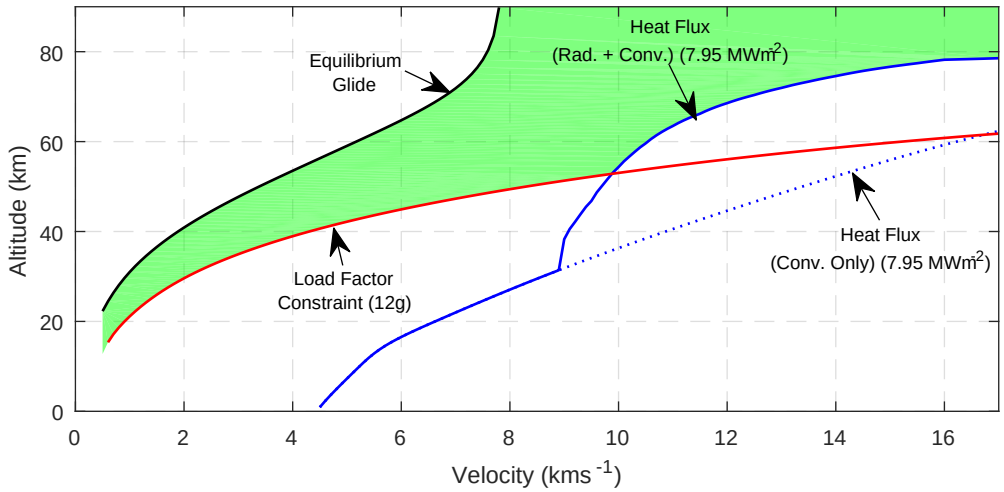

Figure 10.19: Flight envelope for the Earth-CRM case in the nominal configuration.

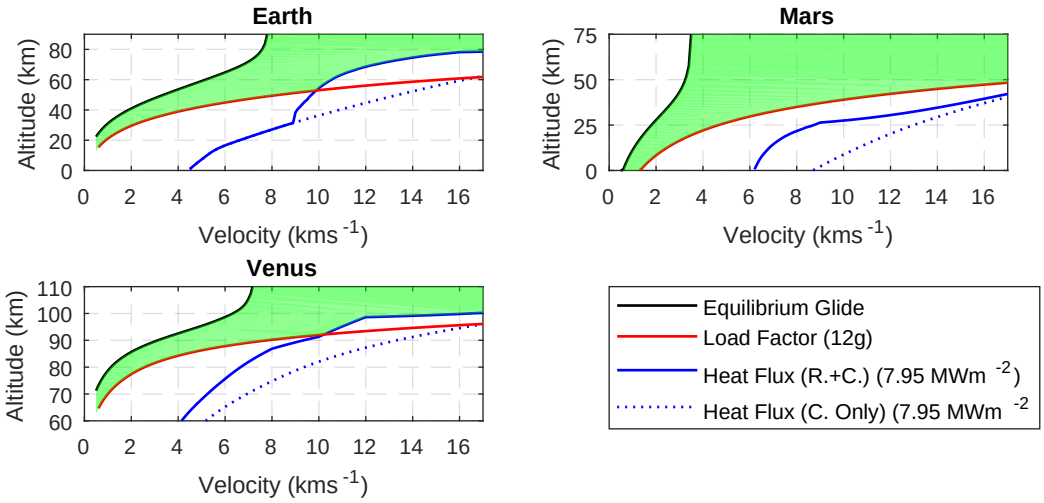

Figure 10.20: Flight envelope for the all planets for the CRM vehicle in the nominal configuration.

Following the methodology used for the entry corridors, first examples of the nominal flight envelope are discussed. Following this the vehicle configuration is altered and the impact of this alteration on the flight envelope is discussed.

10.5.1. Nominal Configuration

The first three figures, Figs. 10.19 to 10.21, show the nominal flight envelope for the Earth-CRM case, all planets flying the CRM vehicle, and all planets flying the SRM vehicle, respectively. Note the kinks in the line for the peak heat flux at 16 kms^{-1}, 9 kms^{-1}, and 12 kms^{-1} for Earth, Venus, and Mars respectively. These discontinuities are due to the limited amount of available data for the radiative heat flux as discussed in Section 3.6.4.

Similar to what was observed for the entry corridors, the flight envelopes of Earth and Venus appear to be quite similar in shape. However, this is deceiving as the altitudes shown for Venus are much higher than those for Earth and Mars. In reality the flight envelope for Venus is positioned significantly higher in the atmosphere and is thinner, in most places below the circular velocity approximately half the width of the envelope for Earth. The Mars envelope is again the widest of the bunch, but requires a much lower velocity and altitude to ensure that the vehicle does not skip out.

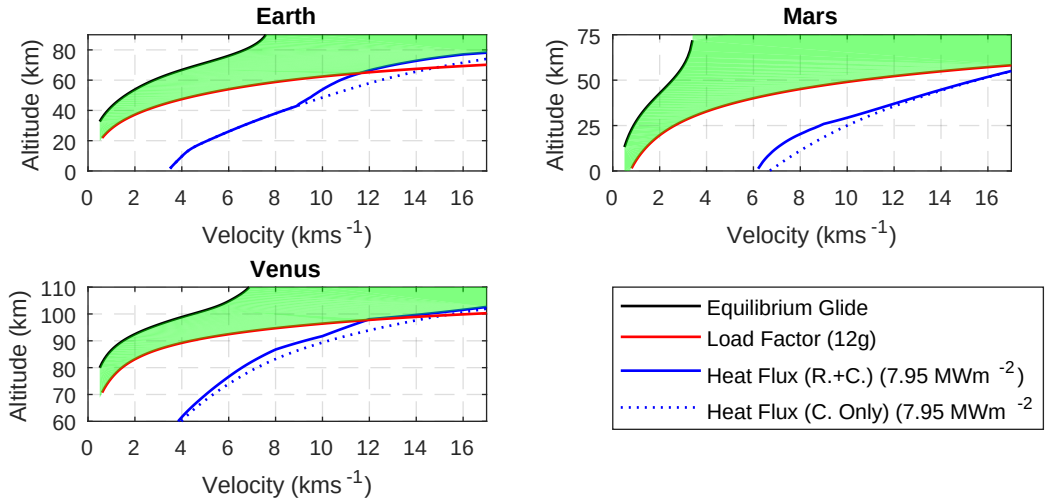

Figure 10.21: Flight envelope for the all planets for the SRM vehicle in the nominal configuration.

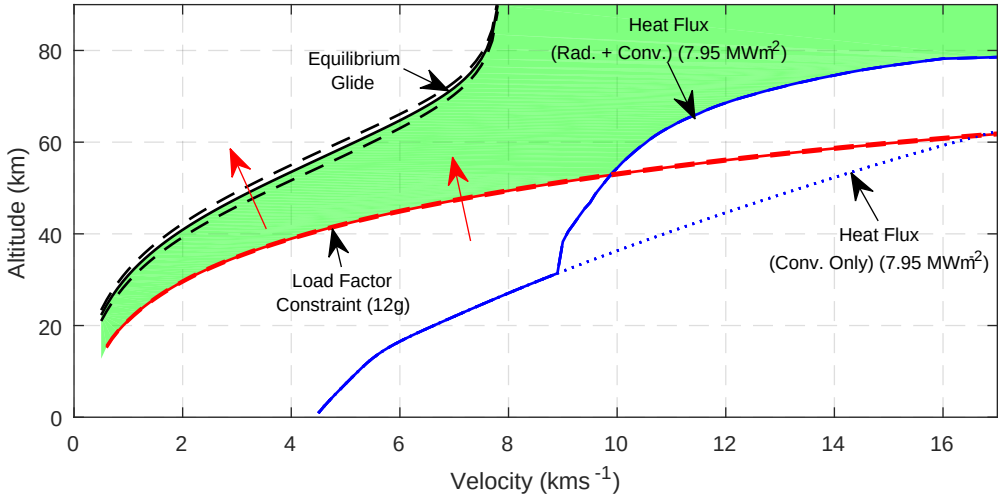

Figure 10.22: Flight Envelope for the Earth-CRM case with lift variations. The red arrows indicate the direction of increasing lift.

10.5.2. Impact of Aerodynamic Variation

Similar to the entry corridor, the aerodynamic model was varied by both multiplying the lift by a factor, and by fixing the L/D and multiplying the drag coefficient by the chosen L/D ratio to obtain the lift coefficient. The effect of the ±20% lift variation is shown in Fig. 10.22, and the effect of using a fixed L/D ratio of 1, 2, and 3, is shown in Fig. 10.23.

Contrary to the effect the increase in lift had on the entry corridor, where the entire corridor is widened, here, the flight envelope is shifted upwards, with the exception of the heat flux boundary, which is not affected. However, as the equilibrium glide boundary is more affected than the load factor constraint, the overall width of the flight envelope does increase. This can be observed easier in Fig. 10.23, where the increase in lift is much more drastic, and thus the effect on the boundaries is more pronounced.

The increase in lift results in equilibrium glide being achieveable in less dense air, allowing for higher altitudes to be reached for the same velocity. Similarly, as the lift is increased, so is the aerodynamic acceleration experienced. For the same velocity the vehicle has to fly higher in the atmosphere where the density is lower to ensure the load factor is not violated.

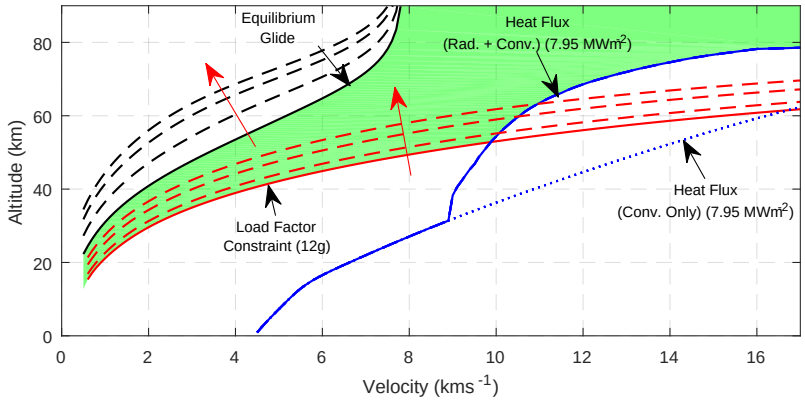

Figure 10.23: Flight Envelope for the Earth-CRM case with variations in the L/D ratio. The red arrows indicate the direction of increasing L/D.

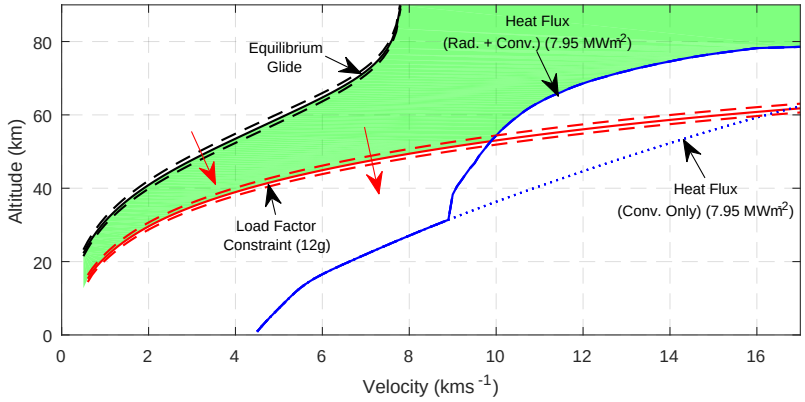

Figure 10.24: Flight envelope for the Earth-CRM case with variations to the vehicle mass. The red arrows indicate the direction of increasing mass.

10.5.3. Impact of Mass Variations

In Fig. 10.24 the impact on the flight envelope due to changing mass is shown. Similar to what was observed in the entry corridor, the mass change shifts the entire envelope. Similar to the aerodynamic variation, the heat flux is unaffected by the change in mass. By comparing Fig. 10.24 to Fig. 10.22, it can be observed that the load factor constraint is more sensitive to changes in mass than it was to the change in lift. This is contrary to the observation made for the entry corridor, which was much more sensitive to lift variation than to mass variations.

The effect that the mass has on the equilibrium glide boundary can be rationalised by considering that for an equal generated aerodynamic force, the effect it has on the flight-path angle, according to Eq. (3.33), is lowered for an increased mas, requiring more density, and this a lower altitude, to achieve equilibrium glide. Similarly, an equally generated aerodynamic force results in a lower acceleration due to the increased mass, allowing deeper flight for the same velocity resulting in larger aerodynamic forces.

11

Optimal Aerocapture Trajectories

In the previous chapter the boundaries for which aerocapture is potentially and guaranteed possible were determined. Using these boundaries, or rather, the type of flight that forms this boundary, a methodology was developed to determine if aerocapture is possible for any set of initial conditions. If it is determined that aerocapture is indeed possible, the final step of the method determines the optimal lift-up lift-down bang bang trajectory to reach the desired target.

This chapter begins with Section 11.1, in which the methodology to ascertain if aerocapture is possible, and if so, to optimise the trajectory, is presented. With the methodology formulated, it was used to analyse a wide range of initial conditions to determine if aerocapture was possible. The results from this analysis are presented in Section 11.2. This analysis was performed for each case considered throughout this report. By comparing the ΔV for the aerocapture trajectories to the ΔV required for propulsive capture, an estimation can be made for the amount of potential propellant, and thus mass, saved by incorporating aerocapture trajectories into the trajectory. This is done in Section 11.3. In this section the fourth and fifth research questions will be answered.

11.1. Optimisation Methodology

Based on the results from the previous part, primarily the results from Chapters 8 and 10, a methodology for determining if an optimal trajectory is possible, determining the required course of action if an optimal trajectory is not possible, and the optimal trajectory itself was developed. The methodology works by first simulating a full-lift up trajectory and checking several characteristics of the flight. If these characteristics satisfy the desired conditions, a full lift-down trajectory is simulated. Again, some conditions are checked. If these too are satisfied, an optimal trajectory is attempted to be made. The details of each of the steps and the conditions that are checked and the implications of each of the conditions are discussed in this section.

11.1.1. Full Lift-up

As a first step in the methodology, a full lift-up trajectory is simulated. The primary reasoning for starting with this trajectory is the fact that the peak load factor and heat flux of this trajectory are the minimal that can be achieved by any trajectory with these specific initial conditions. An added benefit is that it can be verified that the vehicle will leave the atmosphere, and if it does, that the target altitude is reached. These conditions can be though of as representing the lower four lines in the entry corridor figures: Load Factor Constraint, Heat Flux Constraint, No Skip-out, and Undershoot target, respectively.

Depending on whether or not the requirements are violated, whether or not the vehicle skips out of the atmosphere, and whether or not the vehicle overshoots the target, a course of action is determined. As there are three conditions that are checked, all having either a true or falls state, a total of eight scenarios are possible, and the course of action for that scenario can be rationalised.

The course of action for a number of the scenarios is the same. A total of four different courses of action can be distinguished, referred to hereinafter as cases. An overview of the four difference cases, followed by an overview of all eight possible scenarios and the cases resulting from them is presented next. Additionally, a flow-chart using the same logic as presented here for the full lift-up flight is presented in Fig. 11.1.

- **Case 1.1.0** - Continue to full lift-down.

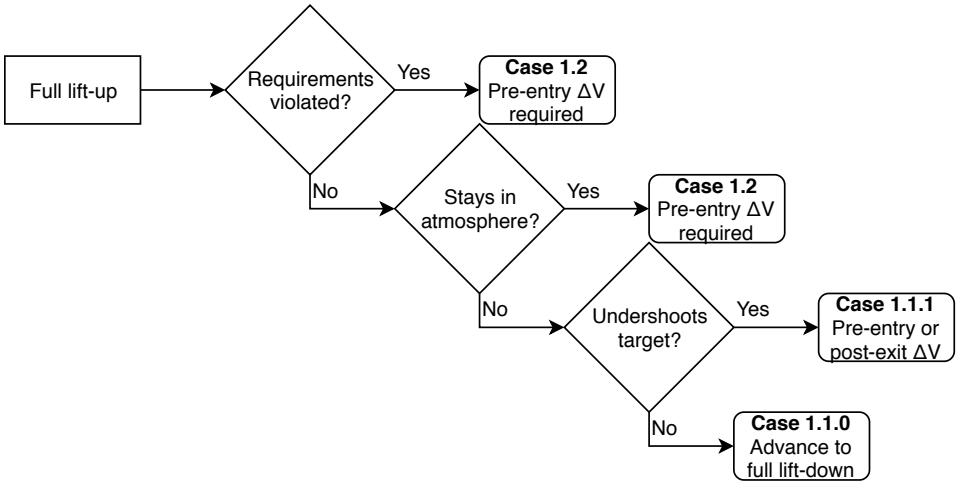

Figure 11.1: Flow chart for the logic behind the full lift-up stage of the optimisation method

- **Case 1.1.1** - Pre-entry and/or post-exit ΔV required, or a combination of both.
- **Case 1.2** - Pre-entry ΔV required, with the possibility of a post-entry ΔV.
- **Case 1.3** - Should not occur (This case can be combined with other cases)

Full-lift up respects requirements, skips out, and overshoots. The vehicle passes through the atmosphere without violating the requirements and reaches the atmospheric exit. Here it skips out of the atmosphere and matches or overshoots the desired target altitude. This is the start of developing the optimal trajectory, and results in **Case 1.1.0**

Full-lift up respects requirements, skips out, and undershoots. The vehicle passes through the atmosphere without violating the requirements and reaches the atmospheric exit. Here it skips out of the atmosphere but does not reach the desired target altitude. If this case is triggered, there are two courses of action that can be taken. Either the initial conditions are modified by using a pre-entry ΔV such that the full lift-up trajectory matches or overshoots the target altitude, resulting in **Case 1.1.0**. Alternatively, a post-exit two-burn ΔV manoeuvre is used to correct the apoapsis altitude and circularise the orbit. Which one of these two options, or a combination of the two options, is optimal has to be determined using additional optimisation scheme. This result is referred to as **Case 1.1.1**

Full lift-up respects requirements, no skip-out, and undershoots. The vehicle passes through the atmosphere without violating the requirements but does not reach the atmospheric exit. If this case is triggered there is only one course of action, and that is to modify the initial conditions using a pre-entry ΔV such that **Case 1.1.0** or **Case 1.1.1** is triggered. Again, to determine which of these options is more optimal has to be determined using an optimisation scheme. This case is **Case 1.2**

Full lift-up violates requirements. The vehicle passes through the atmosphere, violating the constraints. Regardless of the vehicle skipping out, and if over- or undershooting the target, in the four cases containing this condition a pre-entry ΔV manoeuvre is required, and thus **Case 1.2** is triggered.

Full-lift up, no skip-out, and overshoots. The vehicle passes through the atmosphere, but does not reach the atmospheric exit. However, it still manages to match or overshoot the desired target altitude. These last two conditions contradict each other. This is a special case as the two scenario that match this result, should never be encountered. If this situation is encountered, there is a problem in the simulator or post-processing. This case is **Case 1.3**. After debugging, this case was never triggered for the final developed code.

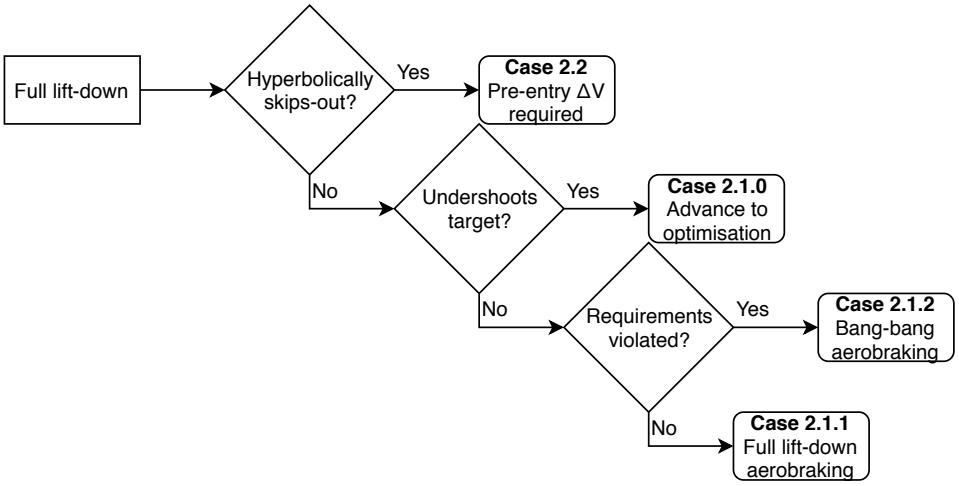

Figure 11.2: Flow chart for the logic behind the full lift-down stage of the optimisation method.

11.1.2. Full Lift-down

The second stage simulates a full lift-down trajectory. With this trajectory it is verified if sufficient energy can be dissipated such that the resultant trajectory undershoots, or if the trajectory always overshoots. It is additionally checked if the vehicle skips out hyperbolically. These conditions represent the two remaining lines in the entry corridor: Overshoot target and hyperbolic skip-out. The full-lift down trajectories that skip out hyperbolically fail to capture regardless of the trajectory used.

At this stage, the conditions considered are whether or not the requirements are violated, whether or not the vehicle undershoots the target, and whether or not the vehicle skips out hyperbolically. As the trajectory is simulateds lift-down, the values obtained for the peak heat flux and peak load factor are the worst that can be obtained. Therefore, whether or not the requirements are violated is not driving, as it was in the full lift-up stage. Similar to before, three conditions, all with two states, results in a total of eight scenarios. Again, the course of action for a number of the scenarios is the same. An overview of the formulated cases, followed by a discussion of the eight scenarios follows, and an diagram following the same logic as discussed is available in Fig. 11.2.

- **Case 2.1.0** - Continue to ΔV Optimisation
- **Case 2.1.1** - Full-lift down followed by aerobraking
- **Case 2.1.2** - Lift-up lift-down bang bang followed by aerobraking.
- **Case 2.2** - Pre-entry ΔV required, with the possibility of a post-entry ΔV.
- **Case 2.3** - Should not occur (This case can be combined with other cases)

Full lift-down, no hyperbolic skip-out, and undershoots. The vehicle passes through the atmosphere. Regardless of the vehicle reaching the atmospheric exit, the vehicle does not reach the desired target altitude. This scenario, combined with the fact that the tested initial conditions passed through the first stage, lead to the conclusion that the initial conditions fall within the boundaries specified by the entry corridor. It can therefore be attempted to develop an optimal trajectory, and thus the two scenarios described by this result fall in **Case 2.1.0**.

Full lift-down respects requirements, no hyperbolic skip-out, and overshoots. The vehicle passes through the atmosphere, respects the requirements, reaches the atmospheric exit, but overshoots the target. In this scenario the trajectory can be kept full-lift down as the requirements are not violated, and full-lift down results in the smallest possible overshoot. After the apoapsis has been reached, aerobraking can be used to decrease the apoapsis of the orbit. This is **Case 2.1.1**. For more information regarding aerobraking manoeuvres the reader is encouraged to read the work by Facchinelli (2019).

Full lift-down violates requirements, no hyperbolic skip-out, and overshoots The vehicle passes through the atmosphere, violating the requirements, reaches the atmospheric exit, overshoots the target but does not skip out hyperbolically. In this case a switch-time can potentially be found that optimises ΔV, while respecting the requirements (as the full lift-up trajectory respects the requirements). The resultant apoapsis will still be above the target apoapsis, but the periapsis will be within the atmosphere, allowing aerobraking to be used to lower the apoapsis down. This is **Case 2.1.2**.

Full lift-down, hyperbolic skip-out The vehicle passes through the atmosphere, and skips out with an hyperbolic trajectory. Full lift-down generates the largest aerodynamic forces. A failure to capture while flying full lift-down means that the vehicle cannot perform aerocapture using the current initial conditions. Therefore a pre-entry ΔV is required to allow for aerocapture, with the possibility of a post-entry ΔV. While technically a post-entry ΔV could be used after the hyperbolic skip out to capture the vehicle, this would resemble a standard capture too much to be of interest to this research. Therefore, post-exit ΔV manoeuvres are not considered for full lift-down hyperbolic skip-out trajectories. This scenario results in **Case 2.2**.

Full lift-down, hyperbolic skip-out, undershoot The vehicle supposedly skips out of the atmosphere hyperbolically but still undershoots the target. These two conditions contradict each other, and should thus never be encountered. If this situation is encountered, there is a problem in the simulator or post-processing. The case for this is **Case 2.3**

11.1.3. Determining Optimal Switch-Time

If the initial entry conditions manage to make it through the first two stages, in this stage the optimal switch-time for the bang-bang trajectory is determined. Since a lift-up lift-down bang-bang style trajectory is determined to be the most optimal, only the switch-time is considered variable. It was shown in Figs. 9.5 and 9.6 that ΔV_2 decrease monotonically as the switch time increased. For a trajectory where the full lift-up trajectory overshoots the target, resulting in a negative ΔV_2, and the full-lift down trajectory undershoots the target, resulting in a positive ΔV_2, two nodes with opposite sign for ΔV_2 are known, satisfying the required data available to use the bisection root-finding method as discussed in Section 4.1.

When the full lift-up trajectory was simulated, five epochs from the resulting orbit were recorder, the initial epoch, the epoch when peak heat flux and peak load factor occurred, the epoch for deepest penetration, and the atmospheric exit epoch. By subtracting the initial epoch from the rest, the time since atmospheric entry can be determined. If the switch time is set equal to the time it takes for the vehicle to reach the atmospheric exit, the entire flight will be flown with full-lift up. If the switch-time is set equal to the initial time, the entire flight is flown lift-down.

Using this, the two boundaries for the bisection method are established. The negative node is located at $t_s = 0$, and the positive node is located at $t_s = t_f$. Using the bisection method, the optimal switch time t_s^* at which ΔV_2, and by association ΔV_{total}, are zero, is approximated. The desired accuracy of the bisection method can be set as accurate as desired. During this research, the desired accuracy of the bisection method was set equal to the minimal simulation time step: $1{\cdot}10^{-6}$. The accuracy of the bisection method doubles every iteration. For a trajectory that lasts approximately 150s, this accuracy is achieved after 28 iterations. Adding the two saturated trajectories to this results in approximately 30 simulated trajectories to obtain the optimal to a sufficient accuracy.

11.2. Optimisation Results

The above methodology was used to analyse if aerocapture was possible for a wide range of initial conditions for every planet and vehicle considered in this research. If it was found that aerocapture was possible, the trajectory was optimised and the required ΔV_2 to obtain the target apoapsis was determined. In case optimal aerocapture was not possible, such as **Case 1.1.1**, **Case 2.1.1**, or **Case 2.1.2**, a post-exit two-burn ΔV manoeuvre was used to obtain a measure for the required ΔV. In the optimal situation $\Delta V_2 = 0$, for an overshoot $\Delta V_2 < 0$, and for an undershoot $\Delta V_2 > 0$. In case optimal aerocapture

In Figs. 11.3 to 11.5, the ΔV_2 is shown for the flight with the CRM vehicle, and in Figs. 11.6 and 11.7 it is shown for the SRM vehicle. Each of these figures contains two graphs. The left graph shows a three-dimensional surface plot of the ΔV_2 required to correct the orbit after aerocapture has been performed. The right graph shows the top-down projection of this surface. Additionally, the altitude-targeting entry corridor

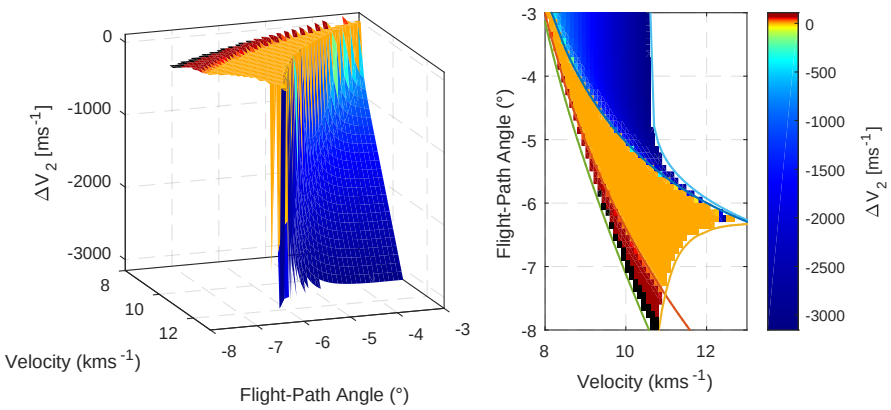

Figure 11.3: ΔV_2 required to reach the target apoapsis for the Earth-CRM altitude targeting case for a wide variety of initial conditions.

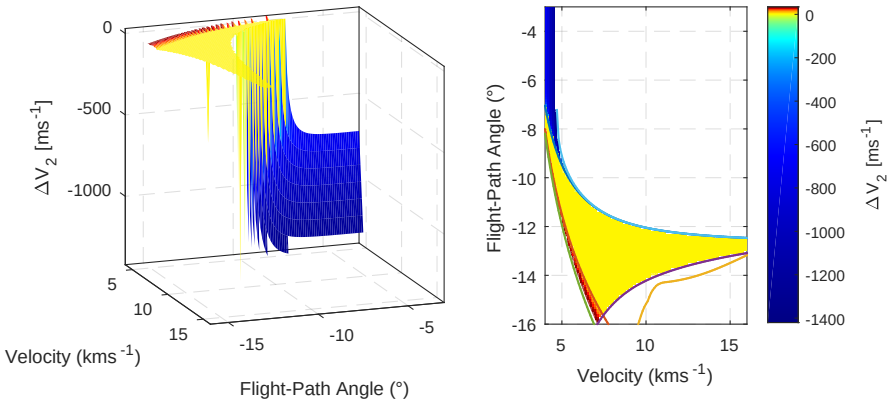

Figure 11.4: ΔV_2 required to reach the target apoapsis for the Mars-CRM altitude targeting case for a wide variety of initial conditions.

boundaries are present in the top-down view. This facilitates comparing the potential area where optimal aerocapture was found possible, and the entry conditions for which optimal aerocapture was obtained.

In these figures the red-shaded area indicates an undershoot, corresponding to a positive ΔV_2, the yellow/orange-shaded area correspond to an optimal aerocapture, with $\Delta V_2 \approx 0$, and lastly the blue shaded-areas indicate an overshoot, corresponding to a negative ΔV_2. As only post-exit ΔV manoeuvers were considered, no values are present for initial conditions that either violate the requirements, fail to skip out, or skip out hyperbolically.

By comparing the entry corridor boundaries and the transitions from undershoot (positive ΔV_2) to optimal ($\Delta V_2 \approx 0$) to overshoot (negative ΔV_2), it can be concluded that the altitude-targeting boundaries approximate the limit initial conditions very well, even though they do not guarantee that entry is possible within their bounds. Additionally, it can be concluded that the methodology described above does indeed result in the development of optimal trajectories, granted that the initial conditions allow for such a trajectory.

These figures corroborate a conclusion that was already drawn in Section 9.1, namely that the post-exit apoapsis is highly sensitive to changes in both initial velocity and flight-path angle, visualised by the steep slope. The ΔV_2 required for a post-exit orbit correction increases significantly faster for the overshoot cases, requiring significantly more ΔV compared to the undershoot corrections.

11.3. Comparison Required Propellent Mass

As was stated in Chapter 1, the ultimate purpose of an aerocapture manoeuvre is to reduce the total mass required to be launched. The aerocapture manoeuvre accomplishes this by lowering the amount of propellent mass required for capture, and thus lowering the launch-mass. In the previous section it has been shown that using the developed methodology, the theoretically optimal aerocapture trajectory can be developed that results in $\Delta V_2 \approx 0$, which corresponds to a minimal ΔV_{total}. In this section, the ΔV_{total} is compared to the ΔV required for propulsive capture in order to evaluate how much fuel can be saved by aerocapture. In order to

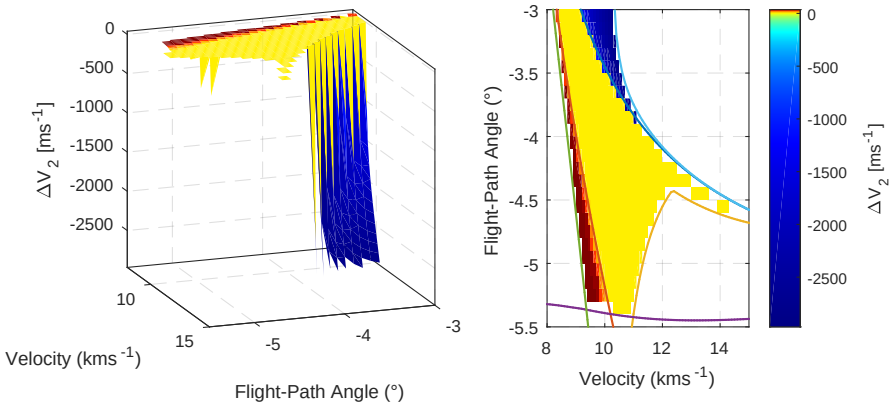

Figure 11.5: ΔV_2 required to reach the target apoapsis for the Venus-CRM altitude targeting case for a wide variety of initial conditions.

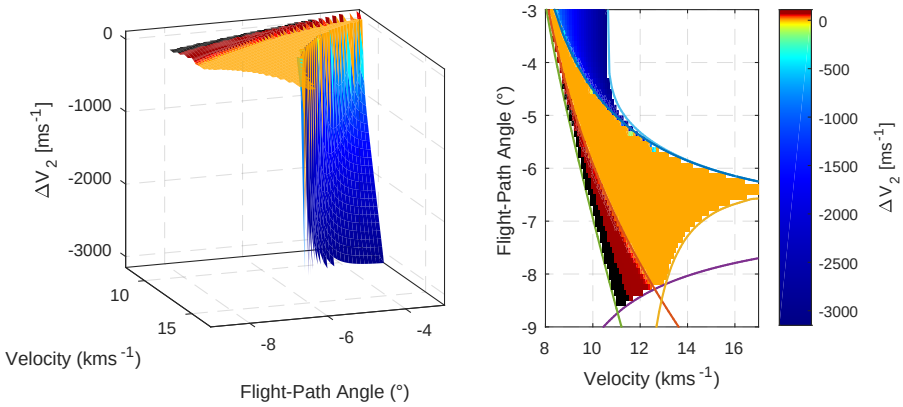

Figure 11.6: ΔV_2 required to reach the target apoapsis for the Earth-SRM altitude targeting case for a wide variety of initial conditions.

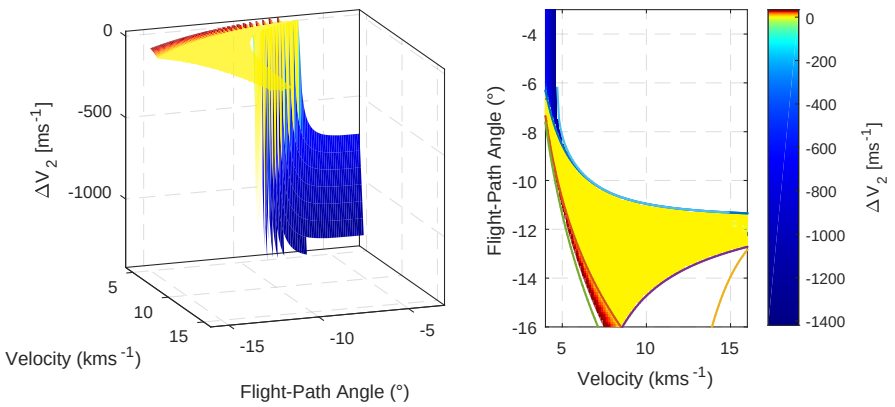

Figure 11.7: ΔV_2 required to reach the target apoapsis for the Mars-SRM altitude targeting case for a wide variety of initial conditions.

determine the propellent mass save however, an estimate has to be made of the propellent mass required to execute the ΔV manoeuvre.

This estimate is obtained by using Tsiolkovsky's rocket equation. This equation provides a relation between the ΔV of a manoeuvre, the mass before and after the manoeuvre, and some characteristics of the propulsive system according to:

$$\Delta V = I_{sp} g_0 \ln \frac{M_0}{M_0 - M_p} \tag{11.1}$$

where M_0 is the mass before the manoeuvre, M_p is the propellent mass, and I_{sp} is the specific impulse, a characteristic of the propulsive system. As an estimate for the specific impulse, the specific impulse of a cold gas thruster is used. According to Anis (2012) the specific impulse of a cold nitrogen gas thruster is approximately 70-75s with a theoretical maximum of 76s. The average of 73s will be used as specific impulse for this estimation. By rewriting, the following expression for the propellant mass needed for a ΔV manoeuvre can be obtained:

$$M_p = M_0 \left(1 - e^{\frac{-\Delta V}{I_{sp} g_0}}\right) \tag{11.2}$$

11.3.1. ΔV for Propulsive Capture

Before it can be determine how much propellent mass is saved by performing aerocapture compared to ordinary propulsive capture, the ΔV required for propulsive capture has to be determined.

For open orbits (parabolic or hyperbolic) the propulsive capture is assumed to occur using a single burn when the vehicle is at the desired altitude. As the initial conditions of the entry throughout this research have been taken at an altitude below the target altitude, the vehicle state at the target altitude was determined using the method described in Section 10.4.

First, the velocity at the target altitude is determined by equating the orbital energy at the entry interface, as per Eq. (10.3), to the energy at the target altitude, and solving for the velocity at the target altitude. Subsequently, Eq. (10.1) is used together with the entry interface state to determine the periapsis radius. Then the same equations is used to with the target altitude radius and velocity to solve for the flight-path angle at the target altitude. Lastly, the ΔV required to obtain the target orbit form a single burn is determined by using the equation for a combined velocity and flight-path altering manoeuvre. From Wakker (2015), this is:

$$\Delta V = \sqrt{V_0^2 + V_1^2 - 2V_0 V_1 \cos \delta\gamma} \tag{11.3}$$

For closed orbits a different approach is taken. Using the vehicle state at the entry interface, the Kepler elements of the corresponding orbit are determined. Using the semi-major axis and eccentricity, the periapsis and apoapsis are determined. Then it is checked if the periapsis is outside of the atmosphere of the central body. If so, a two-burn manoeuvre is executed where the first burn is performed at the periapsis, and the second at the apoapsis. According to Wakker (2015), the ΔV for both burns can be calculated according to:

$$\begin{aligned} \Delta V_1 &= \sqrt{\frac{\mu}{r_p}} \left(\sqrt{\frac{2r_t}{r_p + r_t}} - \sqrt{1+e} \right) \\ \Delta V_2 &= \sqrt{\frac{\mu}{r_t}} \left(1 - \sqrt{\frac{2r_p}{r_p + r_t}} \right) \\ \Delta V_{\text{total}} &= |\Delta V_1| + |\Delta V_2| \end{aligned} \tag{11.4}$$

While this case is not expected to occur at all, as an periapsis outside of the atmosphere would result in the vehicle orbiting instead of entering, it is still considered for robustness. In case that the periapsis falls within the atmosphere, the propulsive manoeuvre must be performed before the vehicle enters the atmosphere, at the apoapsis. In this case, the ΔV values can be calculated using:

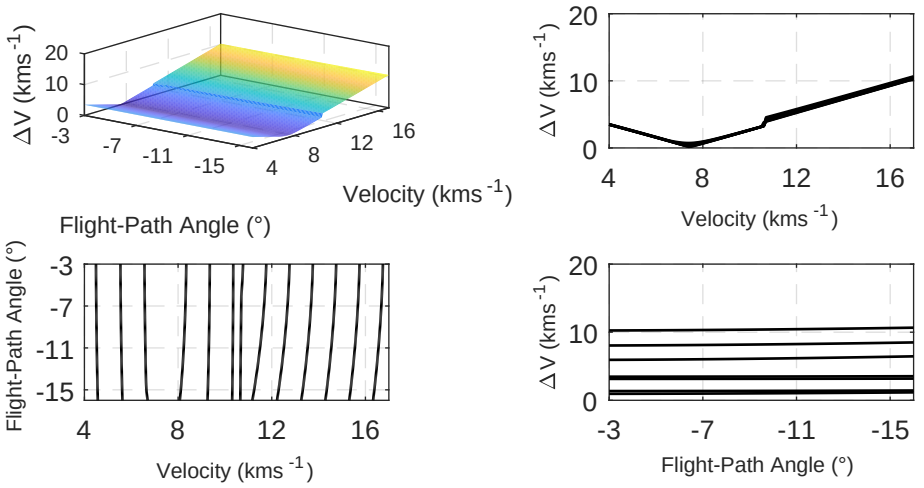

Figure 11.8: 3D, side, and top view of the propulsive ΔV required to reach the target altitude for Earth-CRM for various initial conditions.

$$\begin{aligned} \Delta V_1 &= \sqrt{\frac{\mu}{r_a}}\left(\sqrt{\frac{2r_t}{r_a+r_t}} - \sqrt{1+e}\right) \\ \Delta V_2 &= \sqrt{\frac{\mu}{r_t}}\left(1 - \sqrt{\frac{2r_a}{r_a+r_t}}\right) \\ \Delta V_{\text{total}} &= |\Delta V_1| + |\Delta V_2| \end{aligned} \tag{11.5}$$

Using these equations, estimations for the ΔV required for propulsive captures are made for a wide range of velocities and flight-path angles. The propulsive ΔV distribution for the Earth case is graphed in Fig. 11.8. This figure consists of a 3D graph showing the entire considered initial condition space, the isolated velocity and flight-path angle graphs, and the contours of the 3D graph.

In the top-right graph the effect of altering the velocity is shown. Unsurprisingly, the required ΔV for propulsive capture comes to a minimum if the initial velocity is approximately the same as the circular velocity of the desired apoapsis altitude. The required ΔV increases approximately linearly with the absolute difference in velocity. Near 11 kms^{-1} a small discontinuity in the required ΔV can be observed, this discontinuity is expected to be due to the change from a closed-orbit to an open orbit. From the bottom-right graph, showing the isolated effects of the flight-path angle, it can be concluded that the flight-path angle has a negligible effect on the propulsive ΔV compared to the velocity.

11.3.2. Comparison Required ΔV and Propellent Mass

In the previous section the ΔV_2 obtained from the optimal trajectories was shown. However, to determine the mass saved, the ΔV_{total} is desired. In Fig. 11.9 the total ΔV required for the aerocapture manoeuvre is shown for the Earth-CRM case. By taking the propulsive ΔV values as shown in Fig. 11.8 and subtracting the ΔV values shown in Fig. 11.9, the amount of additional ΔV required from propulsive capture can be determined. The result of this subtraction is shown in Fig. 11.10. Due to the order of the subtraction, a positive difference in ΔV means that more ΔV is required by the propulsive capture.

From Fig. 11.10 it can be concluded that for the entire considered range of entry conditions, the ΔV required for propulsive capture is always in excess of the ΔV required by aerocapture. This same phenomenon was observed for the other cases, and it can therefore be concluded that aerocapture always has a positive effect on the vehicle mass[1]. The most ΔV is saved for the higher energy trajectories (trajectories exceeding the local escape velocity). This brings the report full circle, as in Chapter 1 it was stated that the aerocapture manoeuvre had the most applicability for interplanetary trajectories where the vehicle arrives at a planet from a heliocentric transfer orbit.

[1] This changes if one considers the requirement for a TPS as will be discussed later.

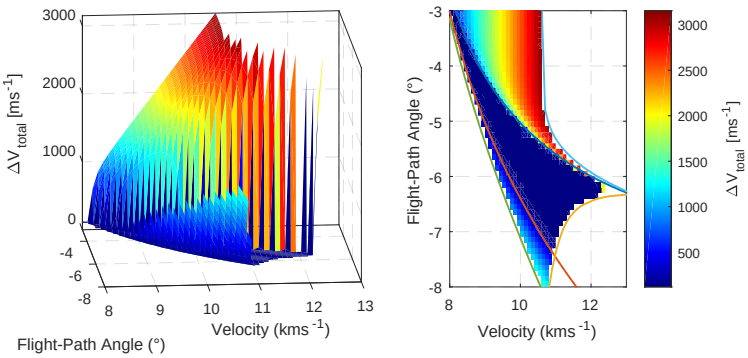

Figure 11.9: Total ΔV required for the aerocapture manoeuvre for the Earth-CRM case.

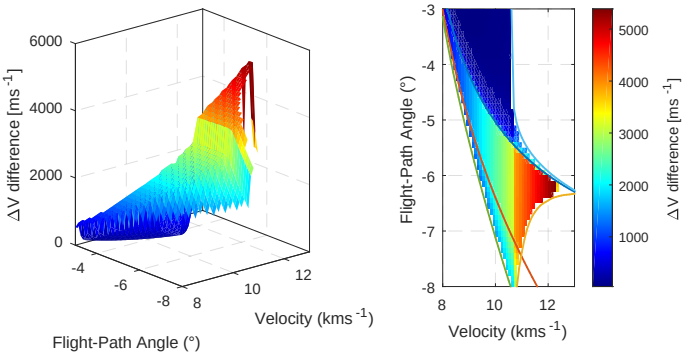

Figure 11.10: Difference in ΔV required between propulsive capture and aerocapture. A positive value indicates that more ΔV is required by propulsive capture.

Using $I_{sp} = 73s$, the mass difference between propulsive capture and aerocapture can be estimated. The result from this is shown in Fig. 11.11 through Fig. 11.15 for all cases. These figures have the same layout as the figures depicting the ΔV_2 surfaces in the previous chapters. The left graph shows the 3D surface plot of the propellent mass difference between aerocapture and propulsive capture. The right graph shows the top-down view of the surface. Again, in the top down view the altitude-targeting entry corridor is superimposed to shown the close agreement between the boundaries established by this entry corridor, and the regions of most propellent mass saved.

From these figures it can be seen that in the region where optimal aerocapture is possible, $\Delta V_2 \approx 0$, the mass difference is significant. For the region bounded by the altitude-targeting entry corridor an average mass differences of approximately 75% the vehicle mass was found for all cases. Note however that this value of mass is dependent on the selected value for the I_{sp}. A different value will result in a different amount of propellent mass saved. A higher value for the specific impulse would result in a lower amount of propellent mass saved, whereas a lower value would result in a larger amount of propellent saved. The value presented here is just one example, and in reality depends on the type of propulsive system available on the vehicle.

From these figures it can again be concluded that the effectiveness of the aerocapture manoeuvre quickly decreases if the trajectory is overshot. In these cases the propellent mass required to correct the orbit was found to be roughly equal to that of the propulsive capture. However, if the vehicle overshoots but is captured, one could use aerobraking to obtain the target apoapsis without requiring the full amount of propellent mass. The analysis and optimisation of a consecutive aerocapture-aerobraking manoeuvre is left for future research.

For the trajectories that undershoot the target, the effectiveness of the aerocapture decreases slower, resulting in a region where aerocapture is a better alternative to propulsive capture even if a post-exit ΔV manoeuvre is required to reach the target apoapsis. As the initial conditions approach the no skip-out boundary, the amount of ΔV increases to roughly equal that of the propulsive capture.

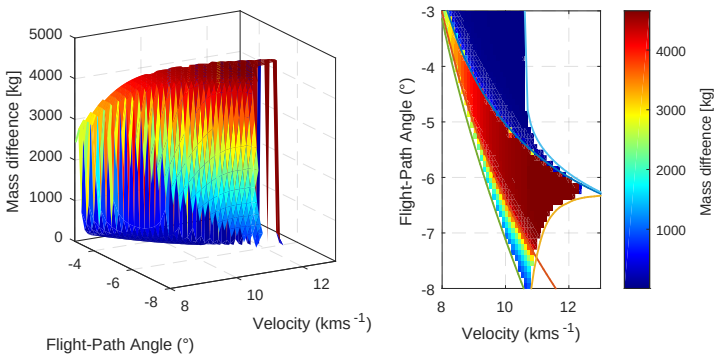

Figure 11.11: Difference in propellent mass required for the Earth-CRM case between propulsive capture and aerocapture. A positive value indicates that more mass is required for the propulsive capture.

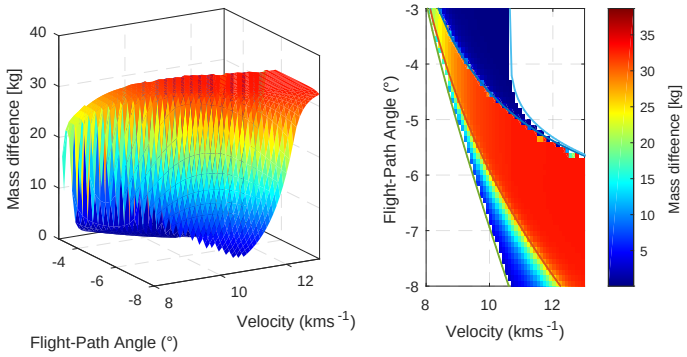

Figure 11.12: Difference in propellent mass required for the Earth-SRM case between propulsive capture and aerocapture. A positive value indicates that more mass is requried for propulsive capture.

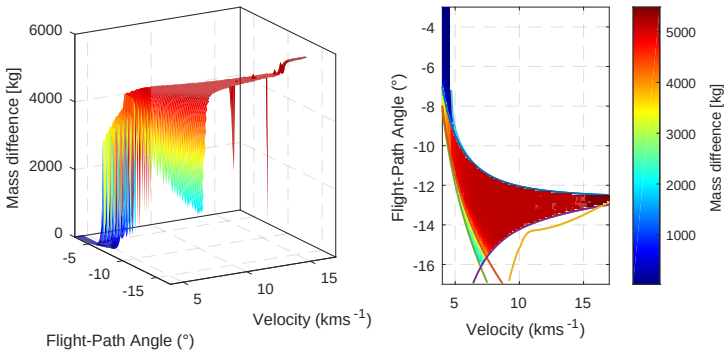

Figure 11.13: Difference in propellent mass required for the Mars-CRM case between propulsive capture and aerocapture. A positive value indicates that more mass is required for the propulsive capture.

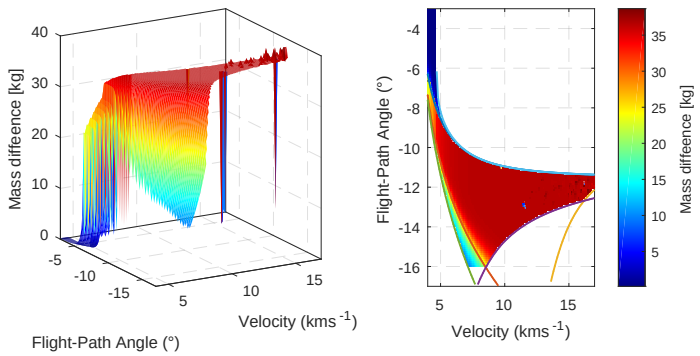

Figure 11.14: Difference in propellent mass required for the Mars-SRM case between propulsive capture and aerocapture. A positive value indicates that more mass is required for the propulsive capture.

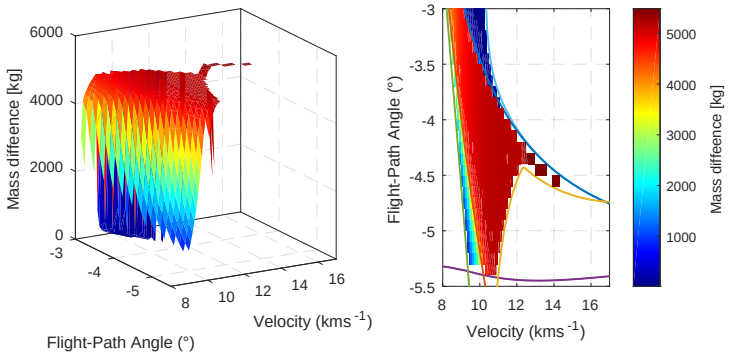

Figure 11.15: Difference in propellent mass required for the Venus-CRM case between propulsive capture and aerocapture. A positive value indicates that more mass is required for the propulsive capture.

Comment on Thermal Protection System Requirement One of the two primary constraints on the vehicle for aerocapture is the heat flux experienced during entry. Not all vehicles for which the aerocapture manoeuvre is of interest natively feature a TPS such as observation or communication satellites.

The amount of launch mass saved by incorporating an aerocapture manoeuvre into the planned trajectory is thus offset by the required TPS. This becomes important for the lighter vehicles, where a 75% mass reduction does not compensate for the TPS. Whether or not the inclusion of aerocapture into the trajectory is beneficial to a vehicle that does not already feature a TPS has to thus be further investigated. This is left however for future research.

IV

Part IV: Conclusions & Recommendations

12

Conclusions & Recommendations

With the optimal trajectories made and the mass saved by aerocapture determined, this research has come to an end. In this final chapter all the conclusions drawn and their implications for the research questions posed in the beginning of this report are discussed. For convenience, the research questions and the sub-questions are repeated here:

1. *"What is the optimal aerocapture trajectory to reach the target apoapsis for the reference vehicle about the central body, arriving with arbitrary entry interface conditions."*
2. *"What are the limit entry interface conditions with which the reference vehicle can arrive at the central body, and still reach the target apoapsis after aerocapture."*
3. *"If the reference vehicle arrives with an entry interface condition outside of the previously defined limits, what is the optimal way to salvage the aerocapture?"*
4. *"How much mass does each of the trajectories save over traditional chemical circularisation?"*
5. *"What is the limit entry interface condition for which traditional chemical circularisation becomes preferable over an aerocapture trajectory?"*

These questions were posed for altitude-targeting trajectories for Earth, Mars, and Venus, using both a vehicle characteristic for Sample Return Missions, and a vehicle for Crew Return Vehicles.

12.1. Conclusions

In this research it has been proven that the assumptions made for the development of the first-order analytical approximations of the equations of motion are invalid. As a follow-up to this, it has been shown that a set of second-order analytical approximations of the equations of motion are more accurate at estimating the peak loads of the trajectory compared to the first order approximations, while taking into account the effect of gravity on the flight-path angle. It is believed that this set of second-order analytical equations of motion make a good basis for the development of a guidance algorithm.

It has been demonstrated that the relatively simple lift-up lift-down bang bang trajectory is the most optimal type of trajectory for altitude-targeting. It has also been shown that the optimal switch-time at which this bang-bang manoeuvre should be executed can be determined by using a relatively simple bisection method of root finding, using ΔV_2 as the parameter to be made zero. With this optimal aerocapture trajectory for altitude-targeting established, the first research question is answered for the case of altitude targeting.

For all vehicles and planets combinations two types of entry corridors have been developed. The first of these corridors marks the limit initial conditions for which aerocapture could potentially be performed. Due to the nature of this first corridor, being inside the boundaries did not guarantee that aerocapture was possible, but being outside of it did guarantee that aerocapture was not possible. A second, more conservative version of the entry corridor was also developed. This entry corridor has the opposite effect of the first. Being

inside the boundaries specified by this corridor guarantees that optimal aerocapture was possible, however being outside of the boundaries does not mean aerocapture is impossible.

A variation on the optimal bang-bang trajectory was developed that still targets altitude. This variation was the lift-up equilibrium glide lift-up trajectory. In this trajectory the vehicle flies lift-up until it reaches the deepest point in the atmosphere, switches to equilibrium glide, and after a certain duration switches back to lift-up to skip back out of the atmosphere. This type of trajectory was optimised using the same bisection root finding method as for the bang-bang trajectory. The downside of using this type of trajectory compared to bang-bang is that it cannot be used for the fastest and shallowest entries, where the bang-bang trajectory switches to full-lift down before the deepest point in the trajectory was reached. A benefit of this method is that it features a non-planar portion of flight through the densest part of the atmosphere, potentially allowing for plane changes.

By investigating the impact of the initial conditions on the peak values and terminal conditions of the trajectories, the optimal salvage strategies were devised. In case the vehicle skips out of the atmosphere hyperbolically, a pre-entry ΔV is required. Technically, this ΔV manoeuvre could also be performed after the atmosphere had been exited. However, as the vehicle skips out with an open orbit, by definition aerocapture has failed. Therefore in this situation a pre-entry ΔV is required, if only to satisfy semantics.

Similarly, in case the vehicle fails to skip out of the atmosphere, or violates a constraint in the full lift-up condition a pre-entry ΔV trajectory must be executed to salvage the trajectory. The ΔV can either alter the initial conditions such that optimal trajectory resulting in $\Delta V_2 = 0$, or in a trajectory where a two-burn manoeuvre is required to obtain the desired circular orbit. Which of these two methods is optimal, together with the magnitudes and directions of the ΔV manoeuvres would be subject to a future research.

In case the vehicle skips out of the atmosphere without skipping out hyperbolically, and either undershoots or overshoots, it was shown that the trajectory can be salvaged by either a pre-entry ΔV, or a post-exit ΔV. Alternatively, for the overshoot case, an aerobraking manoeuvre could be used as an alternative to post-exit ΔV. For trajectories that skip out hyperbolically, do not skip out at all, or undershoot the target, an pre-entry ΔV is required.

With the establishment of methods for salvaging the trajectories, albeit qualitative and not quantitative, the first sub-question is considered answered. Finding the optimal combination between pre-entry ΔV, post-exit ΔV, velocity change, and flight-path change to salvage the trajectory optimally would be a logical continuation of this research.

The last two sub-questions deal with the mass saved by performing aerocapture compared to ordinary propulsive capture. An estimate for the ΔV required for propulsive capture was made using a one- or two-burn ΔV manoeuvre,and Tsiolkovsky's rocket equation.

It was shown by comparing the mass required for propulsive capture and aerocapture, that the amount of mass saved could be as much as the entire mass of the vehicle considered. The most mass was saved for the high energy entries, such as the hyperbolic trajectories. With this the second-to-last sub-question is considered concluded.

Finally, it was determined that for any initial conditions that did not lead to violated constraints, no-skip out, or hyperbolic skip out, aerocapture required less total ΔV than propulsive capture. With this the final sub-question is answered.

12.2. Recommendations

Throughout this report claims have been made for investigations that were left for future research. These included aspects that would be interesting to furthere investigate, or aspects of which the effect was not thoroughly investigated due to time restrictions. Following is a list of the various recommendations for future research made throughout this report.

- In this research the effect of the Knudsen number on the aerodynamics in the Earth atmosphere was investigated. However, a similar analysis was not performed for Mars or Venus. For future work it is therefore recommended to analyse how the tenuous atmosphere of Mars or the dense atmosphere of Venus affect the aerodynamics.

- This work only focussed on the optimisation of altitude-targeting aerocapture. An obvious recommendation for future work is the optimisation of direct entry aerocapture or skipping aerocapture. In this research the flight envelopes for these types of entries have been developed, but an optimal trajectory that would fall within this envelope has not.

- Similarly, a brief comment was made on of out-of-plane manoeuvres, but this was not further considered. A logical continuation of this work is the investigation into the control of non-planar elements, such as the inclination. It has been stated, albeit not shown, that the usage of a lift-up equilibrium glide lift-up trajectory can be used to reach the desired apoapsis. One could used the non-planar bank angle and the prolonged flight time in the lower atmosphere to change, and by extend, control, the non-planar orbital elements.

- For trajectories that did not fall within the entry corridor, in this work qualitative statements have been given regarding the expected optimal method of salvaging the trajectory. This was not fully investigated and optimised. A recommendation for future research would be to further investigate the optimal manoeuvre to salvage a trajectory that does not fall within the entry corridor.

- A brief comment has been made regarding the effect on the total launch mass reduction due to the requirement of a thermal protection system. A quantitative relation between the reference area of the vehicle and the desired peak heat loads should be made. If such a relation is established, the weight added to the vehicle due to the necessity of a thermal protective system which offsets the weight lost by the lowered mass of fuel required can be determined. From this a more complete conclusion regarding the mass saved by aerocapture can be drawn.

- Another recommendation is regarding the second-order analytical approximations. The approximations reproduced in this report work well for single pass through the atmosphere, but fail on anything besides that. An interesting research would be to take these equations, other second-order analytical approximations for ballistic entry and gliding entry, and the analytical expressions for ballistic orbits, and attempt to splice them together to create a framework for the analytical approximation for a general atmospheric flight that smoothly transitions from one type of trajectory to the next.

Bibliography

ACRI/LAN. "Guidance and Control for Moderate Lift/Drag Reentry". Technical report 002-28R7, European Space Agency, May 1992. Under ESA contract 9359/91/NL/JG(SC).

Altman, S.p. "A Unified State Model of Orbital Trajectroy and Attitude Dynamics". *Celestial Mechanics*, 6(4): 425–446, September 1972.

Anderson, Jr, J.D. *Hypersonic and High-Temperature Gas Dynamics - Second Edition.* AIAA Education Series. American Institute of Aeronautics and Astronautics, Inc., 1801 Alexander Bell Drive, Reston, Virginia, United States, second edition, 2006.

Anis, A. "Cold Gas Propulsion System - An ForotIdeal CHoice for Remote Sensing Small Satellites". In Escalante, B., editor, *Remove Sensing - Advanced Techniques and Platforms*, chapter Ch. 20., pages 447–462. InTech, June 2012. DOI:10.5772/37149.

Atkins, K.L., Brownlee, D.E., Duxbury, T.C., Yen, C., Tsou, P., and Vellinga, J.M. "STARDUST: Discovery's Inter-Stellar Dust and Cometry Sample Return Mission". In *Proceedings of the 1997 IEEE Aerospace Conference*, volume 4, pages 229–245, Piscataway, New Jersey, United States, February 1997. IEEE, IEEE Publications. DOI:10.1109/AERO.1997.577510.

Bachrathy, D. and Stepan, G. "Bisection Method in Higher Dimensions and the Efficiency Number". *Periodica Polytechnica, Mechanical Engineering*, 56(2):81–86, January 2012. DOI:10.3311/pp.me.2012-2.01.

Bairstow, S.H. and Barton, G.H. "Orion Reentry Guidance with Extended Range Capability Using PredGuid". In *Proceedings of the AIAA Guidance, Navigation, and Control Conference and Exhibit*, August 2007. DOI:10.2514/62007-6427.

Biscani, F., Izzo, D., and Märtens, M. *"PaGMO Documentation and Source Code"*, 2018. DOI:10.5281/zenodo.1045336.

Boyd, I.D., Trumble, K.A., and Wright, M.J. "Modeling of Stardust Entry at High Altitude, Part 1: Flowfield Analysis". *Journal of Spacecraft and Rockets*, 47(5), September-October 2010. DOI:10.2514/1.37360.

Carandente, V., Savino, R., Iacovazzo, M., and Boffa, C. "Aerothermal Analysis of a Sample-Return Reentry Capsule". *FDMP: Fluid Dunamics & Materials Processing*, 9(4):461–484, 2013. DOI:10.3970/fdmp.2013.009.461.pdf.

Cassel, A.M., Winter, M.W., Allen, Jr, G.A., Grinstead, J.H., Antimisiaris, M.E., Albers, J., and Jenniskens, P. "Hayabusa Re-entry: Trajectory Analysis and Observation Mission Design". In *Proceedings from the 42nd AIAA Thermophysics Conference*, June 2011. DOI:10.2514/6.2011-3330.

Chapman, D.R. "An Approximate Analytical Method for Studying Entry Into Planetary Atmospheres". Technical note 4276, National Advisory Committee for Aeronautics, May 1958. NASA Technical Reports Server Document ID: 19930085059.

Chapman, D.R. "An Analysis of the Corridor and Guidance Requirements for Supercircular Entry into Planetary Atmospheres". Technical report R-55, National Aeronautics and Space Administration, 1960.

Colin, L. "The Pioneer Venus Program". *Journal of Geophysical Research*, 85(A13):7575–7598, December 1980. DOI:10.1029/JA085iA13p07575.

Craig, S. and Lyne, J.E. "A Paramteric Study of Aerocapture for Missions to Venus". In *Proceedings of the AIAA Atmospheric Flight Mechanics Conference*, August 2002. DOI:10.2514/6.2002-4500.

Cruz, M.I. "The Aerocapture Vehicle Mission Design Concept". In *Proceedings of the Conference on Advanced Technology for Future Space Systems*, May 1979. DOI:10.2514/6.1979-893.

Davies, C and Arcadi, M. "Planetary Mission Entry Vehicles - Quick Reference Guide Version 3.0". Technical report SP-2006-3401, National Aeronautics and Space Administration, Jan 2006. NASA Technical Reports Server Document ID: 20070022789.

Deb, K. and Goyal, M. "A combined Genetic Adaptive Search (GeneAS) for Engineering Design". *Computer Science and Informatics*, 26:30–45, 1996.

Deb, K., Agrawal, S., Pratap, A., and Meyarivan, T. "A Fast Elitist Non-Dominated Sorting Genetic Algorithm for Multi-Objective Optimisation: NSGA-II". *IEEE Transactions on Evolutionary Computation*, 6(2):182–197, April 2000. DOI:10.1109/4235.996017.

DeRose, C.E. "Trim Attitude, Lift and Drag of the Apollo Command Module with Offset Centre-Of-Gravity Positions at Mach Numbers to 29". Technical report D-5276, National Aeronautics and Space Administration, June 1969. NASA Technical Reports Document Server ID: 19690020179.

Detra, R.W. and Hidalgo, H. "Generalized Heat Transfer Formulas and Graphs for Nose Cone Re-Entry Into the Atmosphere". *ARS Journal*, 31(3):318–321, January 1961. DOI:10.2514/8.5471.

Diebel, J. "Represeting Attitude: Euler Angles, Unit Quaternions, and Rotation Vectors". Technical report, Stanford University, Stanford, California 94301-9010, October 2006.

Euler, L. "Formulae Generales pro Translatione Quacunque Corporum Rigidorum". *Novi Commentarii Academiae Scientarum Petropolitanae*, 20:189–207, October 1775.

Facchinelli, M. "Aerobraking Navigation, Guidance, and Control - A Comparison of State Variables Performance in Propagation". Diploma thesis, TU Delft, The Netherlands, Faculty of Aerospace Engineering, November 2019. Available at TU Delft Repository at `https://repository.tudelft.nl/`.

Fritsche, F.A. and Carlson, R.E. "Monotone Piecewise Cubic Interpolation". *SIAM Journal on Numerical Analysis*, 17(2):238–246, 1980. DOI:10.1137/0717021.

Fujita, K., Suzuki, T., Matsuyama, M., and Yamada, T. "Numerical Reconstruction of HAYABUSA Sample Return Capsule Flight Environments". *Proceedings from the 42nd AIAA Thermophysics Conference*, June 2011. DOI:10.2514/6.2011-3477.

Gamble, J.D., Cerimele, C.J., Moore, T.E., and Higgins, J. "Atmospheric Guidance Concepts for an Aeroassist Flight Experiment". *Journal of the Astronautical Sciences*, 36(1):45–71, Juny 1988.

Gardini, B., Ongaro, F., Pradier, A., and Vennemann, D. "The Aurora Programme for the Human Exploration of the Solar System". In *Proceedings of the 2003 AIAA Space Conference*, September 2003. DOI:10.2514/6.2003-6236.

González-Galindo, F., Forget, F., López-Valverde, M. A., Angelats i Coll, M., and Millour, E. "A ground-to-exosphere Martian General Circulation Model: 1. Seasonal, diurnal, and solar cycle variation of thermospheric temperatures". *Journal of Geophysical Research*, 114(E4), April 2009. DOI:10.1029/2008JE003246.

Graves, C.A. and Harpold, J.C. "Re-Entry Targeting Philosophy and Flight Results from Apollo 10 and 11". In *Proceedings of the 8th Aerospace Sciences Meeting*, January 1970. DOI:10.2514/6.1970-28.

Graves, C.A. and harpold, J.C. "Apollo Experience Report - Mission Planning for Apollo Entry". Technical report D-6725, National Aeronautics and Space Administration, March 1972. NASA Technical reports Document Server ID: 19720013191.

Grindstead, J.H., Jenniskens, P., Casell, A.M., Albers, J., and Winter, M.W. "Airborne Observation of the Hayabusa Sample Return Capsule Re-entry". In *Proceedings of the 42nd AIAA Thermophysics Conference*, volume 2, pages 845–855, June 2011. DOI:DOI:10.2514/6.2011-3329.

Haemimont Games. *Surviving Mars*. Paradox Interactive, March 2018.

Hall, J.L., Noca, M.A., and Bailey, R.W. "Cost-Benefit Analysis of the Aerocapture Mission Set". *Journal of Spacecraft and Rockets*, 42(2):309–320, March-April 2005. DOI:10.2514/1.4118.

Kahaner, D., Moler, C., and Nash, S. *Numerical Methods and Software*. Prentice-Hall, Inc., Upper Sadle River, New Jersey, United States, 1988.

Kawaguchi, J., Fujiwara, A., and Uesugi, T. "Hayabusa - Its Technology and Science Accomplishment Summary and Hayabusa-2". In *Proceedings of the 57th International Astronautical Congress*, volume 2, pages 1210–1216, October 2006. DOI:10.2514/6.IAC-06-A3.5.02.

Klees, R. and Dwight, R.P. *AE2220-I - Applied Numerical Analysis*. Faculty of Aerospace Engineering, TU Delft, Delft, The Netherlands, 2018.

Kress, R. *Numerical Analysis*. Graduate Texts in Mathematics. Springer Science+Business Media, LLC, New York, New York, United States, 1991.

Loh, W.H.T. *Re-entry and Planetary Entry Physics and Technology Pt. I - Dynamics, Physics, Radiation, Heat Transfer, and Ablation*. Springer-Verlag Inc., New York, New York, United States, 1968.

Lu, P. "Entry Guidance: A Unified Method". *Journal of Guidance, Control, and Dynamics*, 37(3):713–728, 2014. DOI:10.2514/1.62605.

Lu, P., Cerimele, C.J., Tigges, M.A., and Matz, D.A. "Optimal Aerocapture Guidance". *Journal of Guidance, Control, and Dynamics*, 38(4):553–565, April 2015. DOI:10.2514/1.G000713.

Lyne, J. "Parametric Study of Manned Aerocapture. I - Earth return from Mars". *Journal of Spacecraft and Rockets*, 29(6):808–813, Novembe-December 1992. DOI:10.2514/3.25535.

Lyons, D.T. "Aerobraking at Venus and Mars: A Comparison of the Magellan and Mars Global Surveyor Aerobraking Phases". Technical report, National Aeronautics and Space Administration, January 2000. NASA Technical Reports Server Document ID: 20000057306.

Martin, C. and Rayskin, V. "An Improved Bisection Method in Two Dimensions". January 2016.

Millour, E., Forget, F., Spiga, A., Vals, M., Zakharov, V., Montabone, L., Lefevre, F., Montmessin, F., Chaufray, J.Y., López-Valverde, M.A., González-Galindo, F., Lewis, S.R., Read, P.L., Desjean, C.C., and Cipriani, F. "The Mars Climate Database (Version 5.3)". *Scientific Workshop: "From Mars Express to ExoMars"*, February 2018.

Mitcheltree, R.A., Kellas, S., Dorsey, J.T., Desai, P.N., and Martin, C.J. "A Passive Earth-Entry Capsule for Mars Sample Return". In *Proceedings of the 7th AIAA/ASME Joint Thermophysisc and Heat Transfer Conference*, 1998. DOI:10.2514/6.1998-2851.

Montenbruck, O. and Gill, E. *Satellite Orbits: Models, Methods, and Applications*. Springer Science+Business Media, LLC, New York, New York, United States, 2005.

Mooij, E. *The Motion of a Vehicle in a Planetary Atmosphere*. Faculty of Aerospace Engineering, TU Delft, Delft, The Netherlands, 1994.

Mooij, E. *AE4870B - Re-Entry Systems Lecture Notes (2017-2018)*. Faculty of Aerospace Engineering, TU Delft, Delft, The Netherlands, 2017.

Moss, J.N. and Bird, G.A. "Direct Simulation of Transitional Flow for Hypersonic Reentry Conditions". *Journal of Spacecraft and Rockets*, 40(5), January 1984. DOI:10.2514/2.6909.

Moss, J.N., Glass, C.E., and Greene, F.A. "DSMC Simulation of Apollo Capsule Aerodynamics for Hypersonic Rarefied Conditions". In *Proceedings of the 9th AIAA/AS Thermophysics and Heat Transfer Conference*, June 2006. DOI:10.2514/1.30998.

Munk, M.M. and Spilker, T.R. "Aerocapture Mission Concepts for Venus, Titan and Neptune". In *Proceedings of the 6th International Planetary Probe Workshop*. National Aeronautics and Space Administration, June 2008.

NASA. "Constellation Program Human-system Integration Requirements (HSIR), Rev E.". Technical report CxP 70024, National Aeronautics and Space Administration, November 2010. NASA Technical Reports Server Document ID: 20120014522.

NASA. "NASA Tech Brief September 2013". Technical brief, National Aeronautics and Space Administration, September 2013. NASA Technical Reports Server Docuemnt ID: 20140001105.

NASA BUT REALLY IMPROVE THIS ONE. "Aerodynamic Data Manual for Project Apollo", 1965.

Olson, J., Craig, D., Maliga, K., Mullins, C., Hay, J., Graham, R. [Rebecca], Graham, R. [Rachael], Smith, P., Johnson, S., Simmons, A., Williams-Byrd, J., Reves, J.D., Herrmann, N., and Troutman, P. "Voyages - Charting the Course for Sustainable Human Space Exploration", June 2012. Retrieved on May 1, 2018 from `https://www.nasa.gov/exploration/whyweexplore/voyages-report.html`.

O'Neil, W.J. and Cazaux, C. "The Mars Sample Return Project". *Acta Astronautica*, 47(2-9):453–465, 2000. DOI:10.1016/S0094-5765(00)00085-0.

Pavlosky, J.E. and Leger, L.G.St. "Apollo Experience Report - Thermal Protection Sybsystem". Technical report D-7564, National Aeronautics and Space Administration, January 1974. NASA Technical Reports Server Document ID: 19740007423.

Petrosyan, A., Galperin, B., Larsen, S.E., Lewis, S.R., Maattanen, A., Read, P.L., Renno, N., Rogberg, L.P.H.T., Savijarvi, H., Siili, T., Spiga, A., Toigo, A., and Vazquez, L. "The Martian Atmospheric Boundary Layer". *Reviews of Geophysics*, 49, September 2011. DOI:10.1029/2010RG000351.

Revelle, D.O. and Edwards, W.N. "Stardust - An artificial, low-velocity "meteor" fall and recovery". *Meteoritics & Planetary Science*, 42(3):271–299, November 2007. DOI:10.1111/j.1945-5100.2007.tb00232.x.

Robinson, J.S., Wurster, K.E., and Mills, J.C. "Entry Trajectory and Aeroheating Environment Definition for Capsule-Shaped Vehicles". *Journal of Spacecraft and Rockets*, 46(1):74–86, January-February 2009. DIO: 10.2514/1.30998.

Schwehm, G.H. "Rosetta - Comet Nucleus Sample Return". *Advances in Space Research*, 9(6):6185–6190, 1989. DOI:10.1016/0273-1177(89)90228-7.

Serrano-Martinez, J.B. and Hechler, M. "Aerocapture Guidance and Navigation for the Rosetta Comet Nucleus Sample Return Mission". In *Proceeding from the 16th Atmospheric Flight Mechanics Conference*, 1989. DOI:10.2514/6.1989-3381.

Siddiqi, A.A. Challenge to apollo: The soviet union and the space race, 1945-1974. Book SP-2000-4408, National Aeronautics and Space Administration, Washington, District of Columbia, United States, January 2000. NASA Technical Reports Server Document ID: 20000088626.

Singla, P, Mortari, D, and Junkins, J.L. "How to Avoid Singularity When Using Euler Angles?". *Advances in the Astronautical Sciences*, 119:1409–1426, January 2005. Article number: AAS 04-190.

Smith, Jr, J.C. and Bell, J.L. "2001 Mars Odyssey Aerobraking". *Journal of Spacecraft and Rockets*, 42(3):406–415, May-June 2005. DOI:10.2514/1.15213.

Spencer, D.A. and Tolson, R. "Aerobraking Cost and Risk Decisions". *Journal of Spacecraft and Rockets*, 44(6): 1285–1293, November-December 2007. DOI:10.2514/1.24303.

Sutton, K. and Graves, Jr., R.A. "A General Stagnation-Point Convective-Heating Equation For Arbitrary Gas Mixtures". Technical report R-376, National Aeronautics and Space Administration, November 1971. NASA Technical Reports Server Document ID: 19720003329.

Tauber, M.E. and Meneses, G.P. "Aerothermodynamics of Transatmospheric Vehicles". *Journal of Aircraft*, 24 (9):594–605, September 1986. DOI:10.2514/3.45483.

Tauber, M.E. and Sutton, K. "Stagnation-Point Radiative Heating Relations for Earth and Mars Entries". *Journal of Spacecraft and Rockets*, 28(1):40–42, January-February 1991. DOI:10.2514/3.26206.

Tolson, R.H., Prince, J.L.H., and Konopliv, A.A. "An Atmospheric Variable Model for Venus Aerobraking Missions". Technical report NF1676L15939, National Aeronautics and Space Administration, August 2013. NASA Technical Reports Server Document ID: 20140002737.

Uesugi, K. "Results of the MUSES-A "Hiten" Mission". *Advances in Space Research*, 18(11):69–72, 1996. DOI:10.1016/0273-1177(96)00090-7.

Vinh, N.X., Kin, E., and Greenwood, D.T. "Second-Order Analytical Solutions For Re-Entry Trajectories". In *Proceedings from the AIAA Guidance, Navigation, and Control Conference*. n, August 1993. DOI:10.2514/6.1993-3679.

Vittaldev, V. "The Unified State Model - Derivation and Applications in Astrodynamics and Navigation". Diploma thesis, TU Delft, The Netherlands, Faculty of Aerospace Engineering, May 2010. Available at TU Delft Repository at `https://repository.tudelft.nl/`.

Wakker, K.F. *AE4874 - Fundamentals of Astrodynamics*. Faculty of Aerospace Engineering, TU Delft, Delft, The Netherlands, 2015.

Watanabe, S., Tsuda, Y., Yoshikawa, M., Tanaka, S., Saiki, T., and Nakazawa, S. "Hayabusa2 Mission Overview". *Space Science Reviews*, 208:3–16, July 2017. DOI:10.1007/s11214-017-0377-1.

Weir, A. *"The Martian"*. Self-published, Mountain View, California, United States, first edition edition, 2011.

Wertz, J. *"Spacecraft Attitude Detemination and Control"*, volume 73. Springer Science+Business Media, LLC., New York, New York, United States, January 1978. DOI:10.1007/978-94-009-9907-7.

Willcockson, W.H. "Stardust Samlple Return Capsule Design Experience". *Journal of Spacecraft and Rockets*, 36(3):470–474, May-June 1999. DOI:10.2514/2.3468.

Wooster, P.D., Braun, R.D., Ahn, J., and Putnam, Z.R. "Trajectory Options for Human Mars Missions". In *Proceedings of the AIAA/AAS Astrodynamcs Specialists Conference and Exhibit*, August 2006. DOI:10.2514/6.2006-6308.

Zucchelli, E.M. "Aerocapture Guidance - Numerical and Artificial Intelligence Solutions". Diploma thesis, TU Delft, The Netherlands, Faculty of Aerospace Engineering, November 2016. Available at TU Delft Repository at `https://repository.tudelft.nl/`.